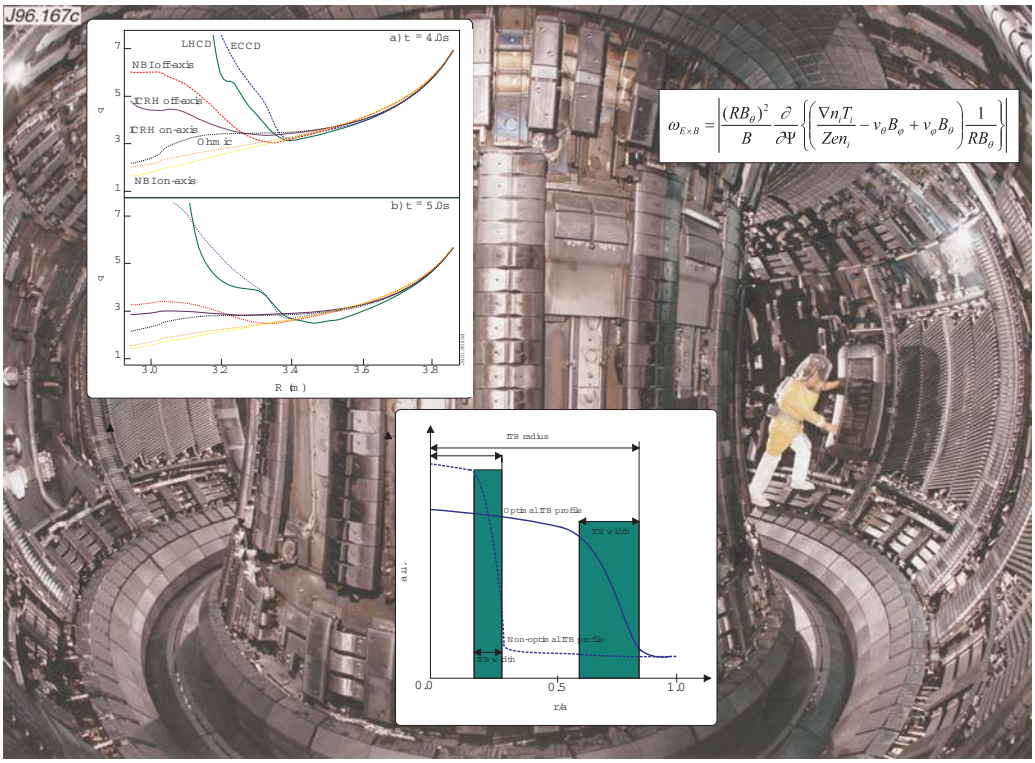

$$\omega_{E\times B} = \left| \frac{(RB_\theta)^2}{B} \frac{\partial}{\partial \Psi} \left\{ \left(\frac{\nabla n_i T_i}{Z e n_i} - v_\theta B_\varphi + v_\varphi B_\theta \right) \frac{1}{RB_\theta} \right\} \right|$$

Tuomas Tala

Transport Barrier and Current Profile Studies on the JET Tokamak

VTT PUBLICATIONS 467

Transport Barrier and Current Profile Studies on the JET Tokamak

Tuomas Tala

VTT Processes

Dissertation for the degree of Doctor of Science in Technology
to be presented with due permission for public examination and debate
in Auditorium F1 at Helsinki University of Technology (Espoo, Finland)
on the 7th of June, 2002, at 12 o'clock noon.

ISBN 951–38–5988–6 (soft back ed.)
ISSN 1235–0621 (soft back ed.)

ISBN 951–38–5989–4 (URL: http://www.inf.vtt.fi/pdf/)
ISSN 1455–0849 (URL: http://www.inf.vtt.fi/pdf/)

JULKAISIJA – UTGIVARE – PUBLISHER

VTT, Vuorimiehentie 5, PL 2000, 02044 VTT
puh. vaihde (09) 4561, faksi (09) 456 4374

VTT, Bergsmansvägen 5, PB 2000, 02044 VTT
tel. växel (09) 4561, fax (09) 456 4374

VTT Technical Research Centre of Finland, Vuorimiehentie 5, P.O.Box 2000, FIN–02044 VTT, Finland
phone internat. + 358 9 4561, fax + 358 9 456 4374

VTT Prosessit, Otakaari 3 A, PL 1404, 02044 VTT
puh. vaihde (09) 4561, faksi (09) 456 6390

VTT Processer, Otsvängen 3 A, PB 1404, 02044 VTT
tel. växel (09) 4561, fax (09) 456 6390

VTT Processes, Otakaari 3 A, P.O.Box 1404, FIN–02044 VTT, Finland
phone internat. + 358 9 4561, fax + 358 9 456 6390

Technical editing Leena Ukskoski

Otamedia Oy, Espoo 2002

Tala, Tuomas. Transport Barrier and Current Profile Studies on the JET Tokamak. Espoo 2002. VTT Publications 467. 71 p. + app. 95 p.

Keywords nuclear fusion, JET tokamak, plasma transport, heat transport, internal transport barriers, current density, modelling, transport models, flow shear, magnetic shear

Abstract

One of the crucial problems in fusion research is the understanding of heat and particle transport in plasmas relevant for energy production. The neo-classical theory of tokamak transport is well-established, but it cannot explain experimental results. Instead, the micro-turbulence driven anomalous transport has been found to be dominant in present tokamak experiments.

There are several mechanisms that can locally suppress micro-turbulence and re- duce significantly the anomalous transport. These regions of reduced transport are called transport barriers. The presence of Internal Transport Barriers (ITBs) is one of the bases in 'Advanced Tokamak Scenarios'. One of the principal goals in the 'Advanced Tokamak Scenarios' is to improve the fusion power density and con- finement with internal transport barriers by controlling the current density profile and maximising the bootstrap current – and ultimately rendering the tokamak compatible with continuous operation.

This thesis reports on studies and modelling of internal transport barriers and current density profiles in the Joint European Torus (JET) tokamak with a fluid transport code. Explanations for the following open questions are sought: what are the mechanisms that govern the formation and dynamics of the ITBs in JET and secondly, how can the current density profile be modified and further, how does it affect ITBs and plasma performance?

On the basis of the empirical study at the ITB transition, the $\omega_{E\times B}$ flow shear and magnetic shear appear as strong candidates in determining the onset time, the radial location and the dynamics of the ITBs in JET. This ITB threshold condition, employed in the semi-empirical Bohm/GyroBohm transport model, has been found to be in good agreement with experimental results in predictive transport simulations. On the other hand, the simulation results from the predictive transport modelling with a theory-based quasi-linear fluid transport model strongly emphasise the importance of the density gradient in the ITB formation.

According to the current density modelling studies, lower hybrid and electron cyclotron current drive are the most versatile current drive methods in terms of the produced q-profile in the preheating phase in JET. With lower hybrid preheating, a core current hole has been found and a physics-based explanation, confirmed by the transport modelling, is given. The predictive transport simulations indicate that application of lower hybrid current drive during the high performance phase can enhance the fusion performance significantly by increasing the ITB radius.

Preface

The work reported in this thesis has been done at the Joint European Torus (JET) in Oxford, the United Kingdom, at VTT (Technical Research Centre of Finland) and at Helsinki University of Technology over a period of three and a half years from summer 1998 until spring 2002. The work has been carried out under the Euratom-TEKES Association Agreement and is a part of the Finnish and European fusion research programs.

I wish to express my deep gratitude to my instructor at JET, Dr. Vassili Parail for his continuous and thorough guidance and encouragement through the thesis. I also want acknowledge Dr. Clive Challis, Dr. Alain Becoulet and Dr. Franz Söldner for many valuable discussions and ideas during my stays at JET.

I am deeply indebted to my instructor at VTT, Dr. Jukka Heikkinen for his continuous guidance and interest in my work and for giving many useful comments through the thesis as well as reading carefully the manuscript. I would also like to acknowledge Dr. Seppo Karttunen for giving me the opportunity to work at JET for two years and the rest of the time at VTT. I also want to thank my supervisor, Prof. Rainer Salomaa, who gave me the first opportunity to work in the field of nuclear fusion.

My special thanks belong to my friends, colleagues and personnel at JET, VTT and Helsinki University of Technology for making my work over these years as pleasurable as it has been.

Financial support from the Fortum Foundation and Euratom is gratefully acknowledged.

I also want to thank my parents for their continuous interest and encouragement during the course of my studies. A large part of the work was carried out within time which would otherwise been spent with my dear wife Satu. I want to express my deep gratitude to her for being there all these years and you will deserve a huge hug right after the dissertation. And last but not least, major thanks to Miika, our dear son, for keeping my thoughts often enough outside the thesis.

Espoo, May 7, 2002

Tuomas Tala

List of Publications

This paper is an introduction to and a review of the main results reported in the following publications (reprinted in the appendices of this thesis):

1. Tala T.J.J., Heikkinen J.A., Parail V.V., Baranov Yu.F. and Karttunen S.J., "ITB formation in terms of $\omega_{E\times B}$ flow shear and magnetic shear s on JET", Plasma Phys. Control. Fusion **43** (2001) 507–523.

2. Tala T.J.J., Parail V.V., Becoulet A., Corrigan G., Heading D.J., Mantsinen M.J., Strand P.I. and contributors to the EFDA-JET workprogramme, "Comparison of theory-based and semi-empirical transport modelling in JET plasmas with ITBs", Plasma Phys. Control. Fusion **44** (2002) in press.

3. Tala T.J.J., Parail V.V., Becoulet A., Challis C.D., Corrigan G., Hawkes N.C., Heading D.J., Mantsinen M.J., Nowak S. and contributors to the EFDA-JET workprogramme, "Impact of different heating and current drive methods on the early q-profile evolution in JET", Plasma Phys. Control. Fusion **44** (2002) in press.

4. Hawkes N.C., Stratton B.C., Tala T.J.J., Challis C.D., Conway G., DeAngelis R., Giroud C., Hobirk J., Joffrin E., Lomas P., Lotte P., Mailloux J., Mazon D., Rachlew E., Reyes-Cortes S., Solano E. and Zastrow K.-D., "Observation of Zero Current Density in the Core of JET Discharges with Lower Hybrid Heating and Current Drive", Phys. Rev. Lett. **87** (2001) 115011-1–4.

5. Tala T.J.J., Söldner F.X., Parail V.V., Baranov Yu.F., Heikkinen J.A. and Karttunen S.J., "Modelling of optimized shear scenarios with LHCD for high performance experiments on JET", Nucl. Fusion **40** (2000) 1635–1649.

6. Heikkinen J.A., Tala T.J.J., Pättikangas T.J.H., Piliya A.D., Saveliev A.N. and Karttunen S.J., "Role of fast waves in the central deposition of lower hybrid power", Plasma Phys. Control. Fusion **41** (1999) 1231–1249.

The work carried out in this thesis is to resolve some of the many questions dealing with the incomplete picture of transport in tokamaks, in particular issues related to internal transport barriers. In Publication 1, the ITB formation mechanisms as

a function of local plasma parameters, i.e. the threshold where the confinement improves and transport reduces in the core region, are sought in plasmas of the JET tokamak. In addition, quantities that govern the further time evolution of the ITBs in JET are investigated.

After having found the empirical ITB formation threshold condition in JET, the threshold condition is implemented into the semi-empirical Bohm/GyroBohm transport model. The condition is then tested against a large database of the JET ITB discharges with JETTO transport code (Publication 1). In Publication 2, the predictions of the empirical ITB model are compared with the predictions from a theory-based fluid transport model (Weiland model).

In Publication 3, a comprehensive analysis and modelling of the impact of different current drive and heating methods on the q-profile evolution in the preheating phase are performed. Very recently, as an extreme example of the current profile modification by LHCD in the preheating phase, a so-called core current hole has been observed in JET. The core current hole has been investigated and modelled in Publication 4.

The effect of LHCD on the current profile and ITB formation in the main heating phase is investigated with transport simulations in Publication 5. Modelling shows that a significant increase in fusion performance in JET can be achieved with a proper current profile control by LHCD.

In Publication 6, the propagation and absorption of the LH waves in different plasma regimes, i.e. different density, temperature and different wave number spectrum of the LH wave, are studied. In addition, the general properties of the FRTC ray-tracing code are investigated in detail.

The author has actively participated in all the work reported in this thesis. He is the principal author in Publications 1–3 and 5. In Publications 1–5, he performed all the transport modelling calculations. He also carried out the empirical data analysis in Publication 1. In Publication 4, he carried out all the numerical transport simulations and contributed to the theoretical ideas behind the core current hole. In addition, he did the transport model and the LH module validation in Publication 5. In Publication 6, he performed all the LH ray-tracing and transport calculations as well as derived the accessibility regions for the LH waves. Other publications related to this thesis with a significant contribution from the author are in Refs. [95, 118, 124].

Contents

Chapter 1

Introduction

Energy consumption in the world is anticipated to double or even to triple within the next 50 years [1]. Firstly, the world population will increase significantly and secondly, the average power consumption per capita will also increase inevitably. However, the proven recoverable reserves of energy will suffice only for a limited time. At the present energy consumption rate, oil and natural gas as well as uranium used in light water nuclear reactors will exhaust within the next 100 years. Furthermore, if the share of fossil fuels remains at the present level, the risk of a major climate change due to the release of CO_2, possibly followed by catastrophic consequences on the environment, is high. Consequently, the development of energy sources with better compatibility with the environment and acceptable to society are needed. However, the number of conceivable non-fossil candidates, which in the long-term could substantially contribute to the energy production, is very limited — renewable energy sources such as solar and wind energy or totally another type of solution, nuclear fusion. Nuclear fusion is an environmentally friendly energy source with inexhaustible resources, well suitable for base load electric production. It is also inherently safe, the worst possible accident in a fusion reactor would not lead to evacuation of people living nearby. However, to exploit fusion, high technology is required, which makes fusion energy expensive compared with conventional energy sources. On the other hand, it is a huge challenge for science and big, almost impossible tasks are always wanted to be solved by scientists. In this thesis, one of the key difficulties in nuclear fusion, heat and particle transport, is explored.

1.1 Nuclear Fusion

In nuclear fusion, two nuclei of light elements are brought together within the range of their strong interactions. As a consequence, the nuclei react and melt together, forming new, heavier elements while also releasing the binding energy of the original nuclei. This reaction is the power source of the sun and other

stars, where confinement and heating occur through compression under enormous gravitational forces. Harnessing the energy of stars on the earth sets demanding requirements for the fuel temperature, density, and confinement in order to force positively charged particles to fuse at a rate that makes energy production possible.

The most accessible and promising reaction for fusion reactors is the one between deuterium D and tritium T. When these two nuclei fuse, the mass of the fusion products, i.e. the mass of a helium nucleus and a neutron is smaller than the mass of the fuel nuclei (deuterium + tritium) and therefore, according to Einstein's famous formula $E = mc^2$, energy is released as

$$ {}^{2}_{1}\mathrm{D} + {}^{3}_{1}\mathrm{T} \rightarrow {}^{4}_{2}\mathrm{He} + {}^{1}_{0}\mathrm{n} + 17.6\ \mathrm{MeV}. \tag{1.1} $$

As shown by Eq. (1.1), even a small amount of fusion fuel produces a huge amount of energy. For this reaction, the necessary requirement for the net energy production, i.e. break-even criterion (fusion gain Q exceeds 1 or $Q = P_{\mathrm{fus}}/P_{\mathrm{in}} > 1$ with P_{fus} and P_{in} being the fusion and input heating powers, respectively), sets the lower limit for the so-called fusion triple product as

$$ T_{\mathrm{i}} n_{\mathrm{i}} \tau_E > 1.0 \times 10^{21}\ \mathrm{keVm^{-3}s}, \tag{1.2} $$

where T_{i} is the ion temperature, n_{i} the ion density and τ_E is the energy confinement time. Worth noting is that in order to have the net energy production criterion valid, T_{i} must be larger than 10 keV. Typically the required ion temperature is of the order of $T_{\mathrm{i}} = 10$–30 keV, i.e. corresponding to about 100 million $^{\circ}C$. The energy confinement time is defined (in steady-state) as the ratio between the energy in the plasma $W = 3/2(n_{\mathrm{i}}T_{\mathrm{i}} + n_{\mathrm{e}}T_{\mathrm{e}})$ and the input heating power P_{in}, i.e. $\tau_{\mathrm{E}} = W/P_{\mathrm{in}}$. The energy confinement time is limited by the energy losses due to thermal conduction and convection processes and due to radiation. When a gas is heated to such a high temperature, atoms in a gas ionise, thus producing two populations, electrons and ionised atoms. This matter is defined to be plasma, sometimes also referred to as the fourth state of matter.

1.2 Plasma Confinement Systems for Nuclear Fusion

Since an extremely high temperature is needed for nuclear fusion, it is obvious that plasma confinement is not a trivial problem. For the present, there exist two main approaches to realise nuclear fusion — inertial and magnetic fusion. In inertial fusion, the Lawson criterion is approached by maximising the density n while having a relatively short energy confinement time τ_E. Inertial fusion consists of micro-explosions of small D–T fuel pellets by means of powerful lasers or particle beams. The fuel pellet reaches the required temperature and finally the burning pellet ignites. In magnetic fusion, hot plasma is confined with magnetic fields. On the contrary to the inertial fusion, density is now moderate, but the confinement time can be much longer, of the order of 1 s in the present fusion devices.

The most promising magnetic fusion device that could solve the confinement problem of the plasma is a tokamak [2, 3]. The basic idea of the tokamak was presented already in 1951 by the Russian physicists Tamm and Sakharov [4, 5]. In the first tokamak experiments, the net energy criterion was by a factor of 10^7 below the break-even condition. During the sixties the tokamak research spread over the whole world and led to rather pure plasmas with electron temperatures around 1 keV, and a confinement time of 7 ms was achieved in the T-3 tokamak [6]. By the seventies the tokamak concept was generally accepted and its significance appreciated. After the seventies the tokamaks have grown in size, and the net energy conditions have become even closer with the confinement time around 100 ms. The discovery of the high confinement mode (H-mode) on the German ASDEX (Axial Symmetric Divertor Experiment) tokamak in 1982 provided a new operating regime where the confinement time was increased significantly and the break-even condition became even closer [7]. So far the best fusion performance has been obtained in the largest currently existing tokamak JET (Joint European Torus) that is located near Oxford in the Great Britain. In the latest H-mode D-T experiments in JET in 1997, the following new records were achieved: transient fusion power of 16.1 MW with a fusion gain $Q = P_{\rm fus}/P_{\rm in} \approx 0.65$, quasi steady-state fusion power of 7 MW and fusion energy of 21 MJ [8]. In JET, the density is typically $\approx 5 \times 10^{19}$ m^{-3} at the ion temperature of 15–20 keV and the confinement time at best ≈ 0.5 s. As a consequence, for the moment JET is only about a factor of 2 separated from the net energy production condition given by the fusion triple product criterion in Eq. (1.2).

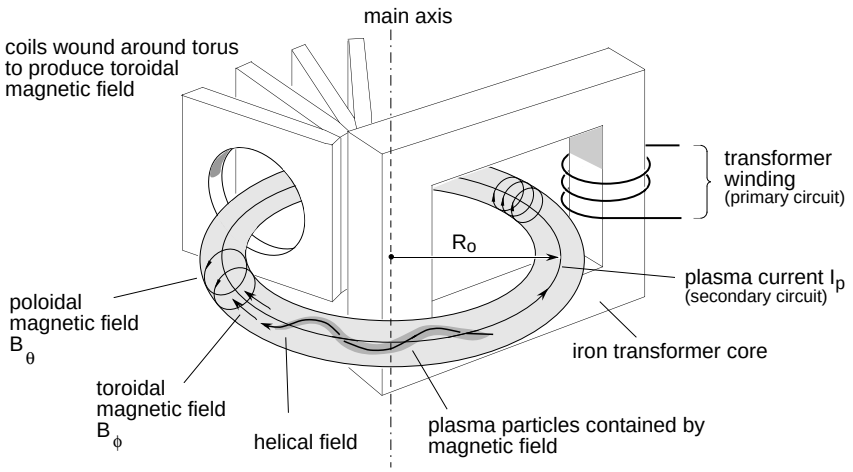

Figure 1.1: The tokamak, its magnetic fields and some of its subsystems. Adapted from Ref. [9].

The tokamak, a toroidal magnetic trap, is based on magnetic confinement where particles are trapped around the closed magnetic field lines as shown in Figure 1.1. The dominant toroidal magnetic field B_ϕ is generated by a toroidal field coil system. In order to prevent particles from drifting out of the plasma, a poloidal magnetic

field B_θ is also required. In a tokamak, this is done by creating a toroidal current I_p into the plasma. In a stellarator, which is the other main approach in magnetic fusion research, both the toroidal and poloidal magnetic fields are produced by external coils. The advantage of a stellarator is that there is no need to drive the toroidal current and thus, steady-state conditions are inherently present. Therefore, no such an event where the current and energy are suddenly lost, called a disruption, can occur. The drawback is an extremely complicated magnetic coil structure, which leads to even more challenging physics to understand than that in tokamaks.

Adding the poloidal magnetic field into the toroidal field in a tokamak, the resultant magnetic field is wound helically (i.e. is spiralled) around the plasma, as sketched in Figure 1.1. The magnetic winding number q expresses the number of toroidal orbits over the number of poloidal orbits, completed by a field line before it closes upon itself. The q-profile turns out to have a great impact on Magneto-Hydro-Dynamic (MHD) stability and transport and therefore, it is often called as the safety factor. It will be also one of the principal issues in this thesis.

1.3 Current Drive and Heating in a Tokamak

Traditionally, the toroidal plasma current is driven inductively so that the plasma operates as secondary circuit of a transformer as shown in Figure 1.1. When a current starts to run in the primary circuit, it induces an electric field in the plasma and further, the electric field creates the toroidal plasma current that is needed for the poloidal magnetic field. The plasma current produced with this method (called induction) is called Ohmic current. In order to maintain the electric field by means of induction, the current in the primary circuit system should be increased continuously. Since this is not realistic, a tokamak has to be driven in a pulsed mode. However, the pulsed tokamak operation mode is not desirable and therefore, large efforts are devoted to developing non-inductive current drive methods that would enable a tokamak fusion reactor to operate continuously. Even if the goal of the continuous tokamak operation is not fully achieved, non-inductive current drive is a necessary tool in modifying the current density profile. By modifying the current density profile, some MHD instabilities and turbulence can be suppressed.

The main idea of current drive is to introduce some kind of asymmetry in the velocity distribution of the electrons or ions in the toroidal direction which then leads to a toroidal current [10]. There are quite a few ways to generate this asymmetry. The methods to modify the current density profile can be divided into three different classes. Neutral Beam Current Drive (NBCD) and Radiofrequency (RF) current drive are based on external current drive and the third option, bootstrap current, is always inherently present in the tokamak operation.

In a tokamak plasma, the current drive and heating methods are closely related together. In all tokamaks, the initial heating comes from the dissipation of the Ohmic plasma current. However, the Ohmic heating decreases rapidly as the tem-

perature increases and temperatures of only 1–2 keV are achievable. Therefore, on top of the external current drive, external heating is also needed. In general, the difference between the external plasma heating and the external current drive is that in heating, both toroidal directions are treated in an equal manner whereas in current drive, one toroidal direction is favoured over the other. It is also to note that the current drive contributes to heating.

The heating by Neutral Beam Injection (NBI) is based on external injection of energetic neutral beam particles into the plasma, and on subsequent ionisation and slowing-down of these beam particles by Coulomb collisions with the background plasma. The ionised beam particles are then confined by the magnetic fields and accordingly, NBI fuels the plasma as well. Directing the beams with a component into one toroidal direction provides the neutral beam driven current. The radiofrequency heating and current drive involves high power electromagnetic waves launched into the plasma, tuned to some natural resonance frequency of the plasma, finally leading to absorption of the wave and transfer of its energy to the plasma particles. The main requirements for the radiofrequency heating are that it should be possible to launch a wave from an antenna or waveguide at the plasma edge and that the wave must be able to propagate to the central region of the plasma and be absorbed there [11]. Similarly to RF current drive, radiofrequency heating is useful in controlling the plasma profiles. The absorption of the RF waves can be localised and the radial position of the absorption is controllable, allowing it to be used to change the temperature or pressure profile. This is sometimes necessary in order to avoid MHD instabilities and suppress turbulence.

The schemes used in radiofrequency heating and current drive fall into three main frequency ranges. Heating in the lowest frequency range at a few tens of MHz is called Ion Cyclotron Resonance Heating (ICRH). This is the scheme that provides most of the RF heating power in present tokamaks, for example more than 10 MW in JET. The frequency of the waves in the Lower Hybrid Current Drive (LHCD) region is a few GHz. LHCD has turned out to have a key role in current drive and current profile modification for example in JET. When the frequency is further increased to about 100 GHz, Electron Cyclotron Resonance Heating (ECRH) and Electron Cyclotron Current Drive (ECCD) can be applied.

1.4 Plasma Transport

In order to achieve thermonuclear fusion conditions in a tokamak, it is necessary to confine the plasma energy for a sufficient time, as shown in Eq. (1.2). Confinement is limited by diffusion, convection and radiation losses. It can be improved by increasing the size of a tokamak or increasing the magnetic field. However, also the cost of a tokamak reactor scales with its volume and with the magnitude of the field. Therefore, understanding why the heat and particles move away from the centre of the tokamak, i.e. heat and particle transport, has a key role in the fusion research. Despite the huge efforts by the fusion scientists during the last decades, many

features of plasma transport still lack theoretical explanation. The diffusivities in all tokamaks exceed by large amount the predictions of the collisional transport theory. The increased transport is most likely due to plasma micro-turbulence, but the details have not yet been verified.

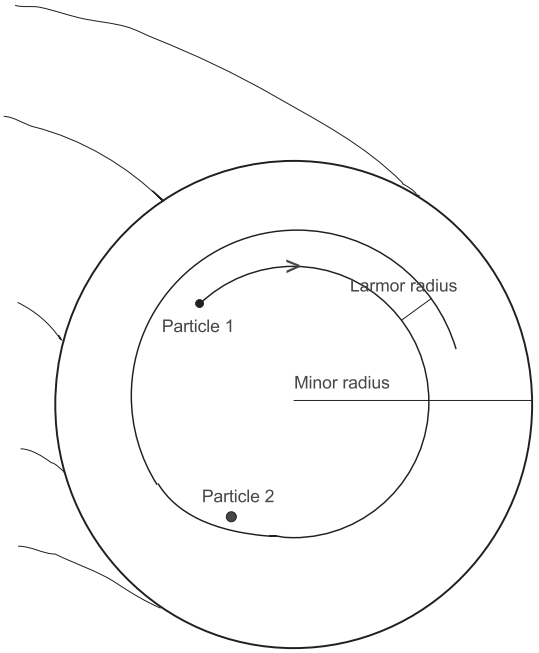

Figure 1.2: A particle experiencing a collision in a simplified cylindrical geometry.

Transport in a tokamak plasma is normally dominated by diffusion processes. The simplest approach to calculate the diffusion coefficients comes from the random-walk model. According to classical transport, which is the simplest model of transport, transport arises from the Coulomb collisions with other particles. In a cylinder with an axial magnetic field without collisions, the particles would move along the magnetic field lines. However, after experiencing a collision with another particle (time between consecutive collisions of a particle is defined as τ), the particles move a distance Δx from their initial field line across to the next field line. This is called transport. This typical random walk process is illustrated in the cross-section of a cylinder in a simplified way in Figure 1.2. Particle 1 moves along the magnetic field line around the cross-section of the cylinder until it comes in the vicinity of another particle 2. Then, it collides or scatters away by a distance of one Larmor radius ($\Delta x \approx r_{\mathrm{L}}$) and continues its trajectory there. The transport coefficient can be estimated by the random walk diffusion coefficient as

$$D_{\mathrm{class}} = (\Delta x)^2/\tau = \nu r_{\mathrm{L}}^2, \tag{1.3}$$

where $\nu = \tau^{-1}$ is the collision frequency of the particles and r_{L} the Larmor or the gyroradius of the particle. Transport by this mechanism in a cylindrical geometry, where the magnetic field lines are straight, is called classical transport

(D_{class}). In a real tokamak plasma, there is a large number of ions and electrons colliding with each other and each collision leads to different scatter and losses. Therefore, the real calculation procedure is very complex. Furthermore, for typical plasma parameters, as for example in JET, the classical diffusion coefficient is several orders of magnitude smaller than the experimentally observed diffusion coefficients. Therefore, classical transport is far from satisfactory to explain the tokamak transport.

The real tokamak geometry is not cylindrical but toroidal, and the toroidal geometry allows the coupling of parallel and perpendicular dynamics. This coupling increases the transport significantly. In addition, the viscosity in a toroidal geometry leads to an additional increase in transport. Transport in a torus, where the magnetic field lines are curved, is called neo-classical transport [12]. In a toroidal tokamak geometry, the particle trajectories remind of the shape of the banana and thus, the particle orbits are called as banana orbits. According to the collisionality, neo-classical transport can be divided into three regimes. In the Pfirsch-Schlüter regime, the collisionality is so high that a particle cannot complete a banana orbit without a collision whereas in the banana regime, collisionality is so low that a particle can well complete the banana orbit. Between the two limiting cases is the Plateau regime.

In the random-walk process, the reason for the enhanced transport comes from the increased step size (Δx) due to trapped particles. The trapped particles are those particles that are trapped on the low field side with their orbits having the shape of the banana. The step size of the trapped particles in the banana regime is larger than the gyroradius. The increase in the neo-classical transport compared with the classical transport due to the toroidal geometry effects can be written as

$$D_{\mathrm{neocl}} = G \times D_{\mathrm{class}} = G \times \nu r_{\mathrm{L}}^2, \tag{1.4}$$

where G stands for the geometry factor. G is either $2q^2$ (in the Pfirsch-Schlüter regime), $2q^2\epsilon^{-3/2}$ (in the Banana regime) or $v_{\mathrm{th}}q^2/(qR\nu)$ (in the Plateau regime), depending on the collisionality of the plasma. Here, ϵ is the inverse aspect ratio $\epsilon = r/R$ with R and r referring to major and minor radii and v_{th} and ν are the thermal velocity and collisionality, respectively. D_{neocl} is typically a factor of 10–100 larger than D_{class}. In a simplified geometry, analytical estimates for the neo-classical transport coefficients exist under certain approximations [12, 13, 14]. Neo-classical theory yields for a tokamak typically the following values: $D_{\mathrm{neocl}} \approx \chi_{\mathrm{e,neocl}} \approx \chi_{\mathrm{i,neocl}}\sqrt{m_{\mathrm{e}}/m_{\mathrm{i}}} \approx 0.01$ m^2/s with m_{e} and m_{i} being the electron and ion mass, respectively. $\chi_{\mathrm{e,neocl}}$ and $\chi_{\mathrm{i,neocl}}$ are the neo-classical electron and ion heat transport coefficients and D_{neocl} the neo-classical particle transport coefficient.

Neo-classical transport is regarded as the minimum level of transport in tokamak plasmas, i.e. values of real diffusivities should be equal to or larger than the neo-classical predictions. Experiments on various tokamaks show that energy losses via the electron channel exceed the neo-classical predictions by one or two orders of magnitude, while the losses via the ions are reported to be roughly one order of magnitude larger than the neo-classical predictions. The transport coefficients in tokamaks are typically of the order 1 m^2/s, rather than 0.01–0.1 m^2/s as predicted

by the neo-classical theory. Micro-turbulence in electric and magnetic fields, not taken into account by the neo-classical theory, is regarded to be responsible for the increased transport. This increased transport is called anomalous transport.

Much effort has been put into the study of the anomalous transport during the last ten years. The ultimate goal of this effort is to understand micro-turbulence and turbulent transport, how to control it and how to achieve important reductions in the anomalous transport. Fortunately, some mechanisms that suppress turbulence and thus reduce the anomalous transport have been found. As already mentioned earlier, the discovery of the high confinement mode (H-mode) in 1982 provided a new operating regime where the turbulence in the edge region of the plasma is suppressed [7]. The discovery of the Edge Transport Barrier (ETB), i.e. H-mode, led to significantly longer confinement times and reduced transport coefficients. In the mid 1990s, several tokamaks, like JT-60U [15], TFTR [16], DIII-D [17], and JET [18, 19] reported confinement levels by a further factor of about two above the standard H-mode level. Turbulence had been suppressed in the core region of the plasma and anomalous transport further reduced besides the ETB — an Internal Transport Barrier (ITB) had been found. After the suppression of turbulence by the internal transport barrier, the transport level, in particular in the ion channel, may be reduced down to the neo-classical level in the plasma core [20, 21, 22, 23, 24]. The characteristics of the ITBs are the reduced heat and/or particle diffusivity and the increased gradients in T_i, T_e and n_e in the core region. This enhanced operation mode with the improved core confinement due to ITBs, together with the modified current density profile, is called as the 'Advanced Tokamak Scenario'.

In the transport theory, the particle transport, the ion and electron heat transport and transport of the toroidal current are coupled. The basic idea in the neo-classical transport theory is to find linear relations between fluxes, such as the heat or particle flux, and thermodynamical forces, like the temperature or density gradient. This coupling can be described in a form of the matrix equation as follows:

$$\begin{pmatrix} \Gamma/n \\ q_\mathrm{e}/(nT_\mathrm{e}) \\ q_\mathrm{i}/(nT_\mathrm{i}) \\ j \end{pmatrix} = \begin{pmatrix} D & L_{21} & L_{31} & L_{41} \\ L_{12} & \chi_\mathrm{e} & L_{32} & L_{42} \\ L_{13} & L_{23} & \chi_\mathrm{i} & L_{43} \\ L_{14} & L_{24} & L_{34} & \sigma \end{pmatrix} \begin{pmatrix} n^{-1}\nabla n \\ T_\mathrm{e}^{-1}\nabla T_\mathrm{e} \\ T_\mathrm{i}^{-1}\nabla T_\mathrm{i} \\ E \end{pmatrix}. \tag{1.5}$$

Here Γ, q_e and q_i are the particle flux and the electron and ion heat fluxes, respectively, and j and E are the toroidal current density and electric field, respectively. The diagonal terms describe the diffusion with D being the particle diffusion coefficient, χ_e and χ_i the electron and ion heat diffusion coefficients and σ the electrical conductivity. The off-diagonal or pinch terms L_{ij} couple for example the particle flux to the temperature gradients and vice versa. In typical tokamak plasmas, these off-diagonal terms are much smaller than the diagonal terms. Some of them are, however, of great importance, like the off-diagonal term L_{14} which indicates that the density gradient drives current. This current is called the bootstrap current which was already mentioned in Section 1.3 (also the temperature gradients drive bootstrap current, thus L_{24} and L_{34} are non-zero). Since up to a suitable normalisation the transport matrix has the onsager symmetry, i.e. $L_{14} = L_{41}$, the electric

field must drive particle flux. This particle flux is called the Ware pinch. The determination of the diffusivities has long been one of the primary goals in transport studies. In determining the transport coefficients, there are three possible ways of making progress — theoretical, numerical simulations and experimental. The methods used in this thesis are concentrated on numerical simulations, but also experimental and theoretical aspects are considered.

1.5 Outline of This Thesis

This thesis is an introduction to and review of Publications 1–6. The two central questions that form the basis of this thesis are the following ones: firstly, how can ITBs be modelled and predicted and secondly, how do different current drive and heating systems affect the q-profile evolution and further the ITB dynamics in the 'Advanced Tokamak Scenarios'. Consequently, the key issues in these publications are modelling of transport and internal transport barriers as well as modelling of current drive and heating.

A schematic view of various interactions constituting a tokamak energy balance is illustrated in Figure 1.3. The grey boxes in the middle describe the energy and particle content of the electrons and ions, and the solid and dashed arrows indicate the energy and particle flows, respectively. The predominant heat and particle loss mechanism in a tokamak is the radial transport or just shortly transport. Transport itself is further dominated by the diffusion processes (diagonal terms in Eq. (1.5)). The work carried out in this thesis is to resolve some of the numerous questions involved in the incomplete picture of the transport, in particular the internal transport barriers, in tokamaks. The ITB formation mechanisms as a function of local plasma parameters, i.e. the threshold where confinement improves and transport reduces in the core region, are sought in plasmas of the JET tokamak (Publication 1). In addition, quantities that govern the further time evolution of the ITBs in JET are investigated.

After having found the empirical ITB formation threshold condition in JET, the threshold condition is implemented into the semi-empirical Bohm/GyroBohm transport model [25, 26]. The empirical ITB threshold condition is then tested against a large database of JET ITB discharges with JETTO [27] transport code. The predictions of the empirical ITB model are also compared with the predictions of the theory-based fluid transport model (Weiland model) [28, 29, 30, 31] in Publication 2. This transport model comparison sheds light on the possibility of having several different ITB formation mechanisms producing fairly similar results.

The source terms for the electron and ion energy are described by the boxes on the left-hand side of the grey boxes in Figure 1.3. The ohmic and externally driven current are also provided by these heat and particle sources. As it was deduced in Publication 1, the magnetic shear s, i.e. the derivative of the safety factor $s \approx (r/q)(dq/dr)$, is one of the key elements in the formation of the ITB in

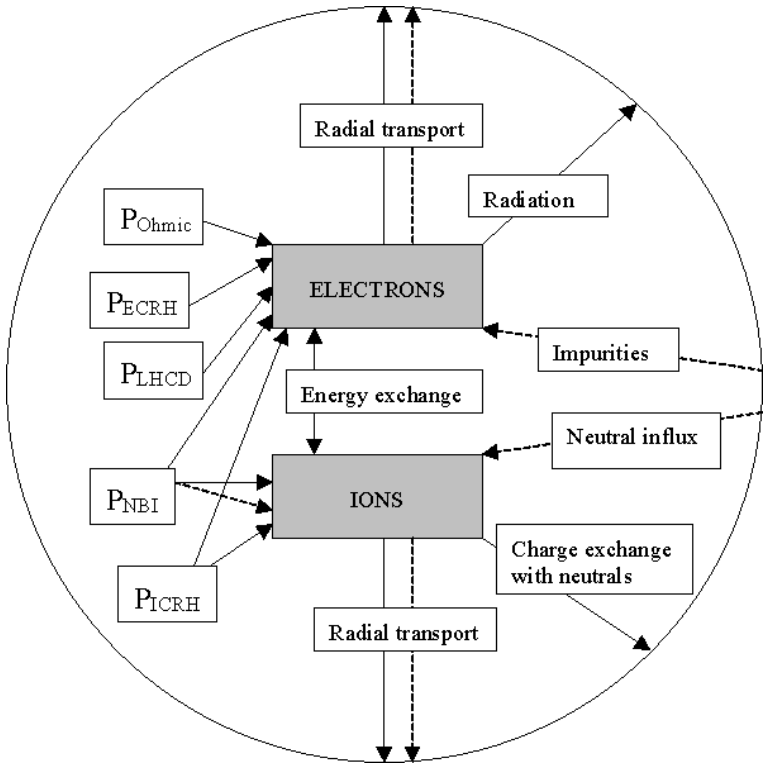

Figure 1.3: A scheme of the various interactions constituting an energy and particle balance in a tokamak.

JET. As a consequence, modifying the current density profile, which determines the q-profile, has a large impact on triggering the ITB. This was the motivation to a comprehensive analysis and modelling of the impact of different current drive and heating methods on the q-profile evolution performed in Publication 3. The modelling is based on JETTO transport code to which different heating and current drive modules, such as FRTC [32] (LHCD ray-tracing code), ECWGB [33] (ECRH beam-tracing code) and PENCIL [34] (NBI code), are coupled. FRTC and ECWGB modules were installed and tested in JETTO during the course of this thesis.

As confirmed by the results in Publication 3, LHCD is very suitable for current drive and current profile modification in JET. Therefore, a more detailed study on the effect of LHCD on the current profile and ITB formation is performed in Publication 5. Modelling shows that a significant increase in fusion performance in JET can be achieved with a proper current profile control by LHCD. Very recently, as an extreme example of the current profile modification by LHCD, a so-called core current hole has been observed in JET (Publication 4). It arises from a fast current ramp-up together with a simultaneous application of LHCD at low electron density. The transport analysis of the core current hole with the coupled JETTO/FRTC code

reported in Publication 4 is in a good agreement with experiments — it shows the wide region ($r/a \leq 0.2$) of zero current density in the plasma core, similarly to experimental measurements. The propagation and absorption of the LH waves in different plasma regimes, i.e. different density, temperature and different wave number spectrum of the LH wave, as well as the general properties of the FRTC code are studied in detail in Publication 6.

This thesis is organised in the following way. The general issues of the 'Advanced Tokamak Scenarios' are illustrated in Chapter 2. In addition, the main transport mechanisms and transport barriers are presented. In particular, the mechanisms that affect the ITB formation, further time evolution and a collapse are discussed in Section 2.3. Moreover, the results from the empirical study of the local plasma parameters governing the ITB formation in JET are shown. In Section 2.4, the numerical codes and transport models used during the course of this thesis are presented. Chapter 3 is devoted to reporting the modelling results from various kinds of transport simulations. In Section 3.1, the main emphasis is in the predictive modelling of the formation and dynamics of the ITBs. The results from the ITB modelling in JET are compared with results from other transport models in other tokamaks. In Section 3.2, the transport simulations of the current density profile, both in the preheating and main heating phases, are presented. Finally, the conclusions with a summary are discussed in Chapter 4.

Chapter 2

Advanced Tokamak Scenarios with Internal Transport Barriers

In the so-called 'Conventional Tokamak Scenarios', the plasma current is driven inductively. It is the most thoroughly investigated tokamak scenario and consequently, it has been chosen as the primary operation mode for the next step tokamak, International Thermonuclear Experimental Reactor (ITER) [35]. There are several reasons why the 'Conventional Tokamak Scenario', often also referred as the 'ELMy H-mode Scenario' has been chosen as the main operation mode. The ELMy H-mode here means the tokamak operation in the H-mode with Edge Localised Modes (ELMs) governing the physics of the edge of the plasma. Firstly, the H-mode is robust, having been seen under a wide variety of conditions in a large number of tokamaks. In addition, the ELMy H-mode scenario has been run in steady-state for as long as 20 s on JET [36]. Here, steady-state means that the temperature, density and current density profiles do not change significantly in time. The ELMy H-mode scenario also exhibits good confinement even in high density cases where the electron and ion temperatures are equilibrated — this is consistent with alpha particle heating and thus needed for ITER. Furthermore, the ELMy H-mode scenario has flat density profiles in the plasma core which are important in order to prevent impurity and helium accumulation in the core, as demonstrated in DIII-D [37]. Finally, the ELMy H-mode scenario requires no special current profile control for long pulse operation, unlike the 'Advanced Tokamak Scenarios'.

On the other hand, the 'Conventional Tokamak Scenario' has its drawbacks as well. Since a large fraction of the plasma current is driven inductively, very long steady-state operation (of the orders of hours or days in a fusion reactor) would not be possible. Moreover, since the device has to operate in a pulsed mode, in a power

plant an energy storage system is required to avoid the loss of the power production capacity during the burn-off phase. In addition, pulsed reactors have large unit size with low fusion power density whereas the utilities would prefer power plants of modest ($\leq$ 500 MW) unit size to match the power production with the demand and to have lower capital investment. In addition, the thermocyclic loads between the burn and burn-off phases become unbearable. Therefore, the 'Conventional Tokamak Scenario' is probably not a feasible operation mode in a commercial fusion reactor. In view of these very serious drawbacks, the fusion community has started to develop more attractive tokamak reactor scenarios, called the 'Advanced Tokamak Scenarios'.

The fundamental ideas in the 'Advanced Tokamak Scenarios' towards an attractive tokamak reactor are to reduce the size of the tokamak (or to increase the margins at a given size), to increase the fusion power density, to improve confinement with internal transport barriers and to drive a large fraction of the total current as bootstrap current to render the tokamak compatible with continuous operation. The main means to achieve these goals are to optimise the shape of the current density (i.e. q-profile) and pressure profiles by external current drive and heating as well as by the optimal alignment of the large fraction of the bootstrap current. A flat or reversed q-profile facilitates the formation of the internal transport barriers which are crucial for significant improvements in confinement and bootstrap current fraction in the 'Advanced Tokamak Scenarios' [16, 17, 19, 38]. Record fusion performance in DIII-D and JT-60U has been achieved utilising the 'Advanced Tokamak Scenarios' [39, 40]. As a consequence, the 'Advanced Tokamak Scenario' research concentrates on the studies of the ITB formation and dynamics as well as the current profile control by external current drive. These two actual topics are also the main issues in this thesis. Other important issues in the studies of the 'Advanced Tokamak Scenario' are the optimisation of the plasma shape as well as the heat and particle exhaust and avoidance and mitigation of detrimental MHD instabilities, like the large-amplitude neo-classical tearing modes and giant ELMs.

2.1 Transport in a Tokamak

Understanding of plasma transport is an issue of paramount importance, both in the 'Conventional' and 'Advanced Tokamak Scenarios', for a design of a future tokamak reactor. Anomalous transport, together with some major MHD instabilities, controls plasma confinement, transport and overall fusion performance. It is universally recognised that transport properties vary a lot across the plasma so that it is constructive to subdivide the plasma volume in radius into five regions with different transport characteristics [41]. The schematic view of such a division is shown in Figure 2.1. All the three most common operation modes, i.e. the L-mode, the 'Conventional Tokamak or the ELMy H-mode Scenario' and the 'Advanced Tokamak Scenario, are illustrated. The difference between the L-mode (dotted line) and the H-mode (dashed line) is the edge transport barrier, which improves the energy confinement by a factor 2–3. The L-mode operation used to

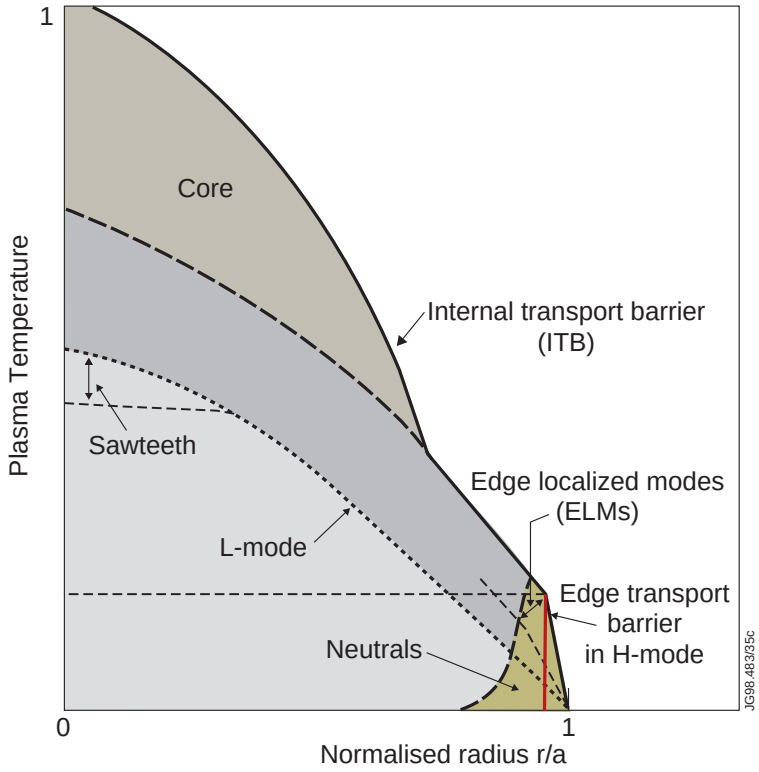

Figure 2.1: Schematic view showing the five different regions with different transport characteristics in a tokamak. Adapted from Ref. [41].

be the most common operation mode, but for the present it is not regarded as an attractive approach towards an economic fusion reactor. An ITB separates the 'ELMy H-mode Scenario' from the 'Advanced Tokamak Scenario' (solid line). The improvement in confinement due to an ITB is typically a factor of 2–3.

Starting from the edge, region 1 is the Scrape-Off-Layer (SOL), which represents the plasma outside the separatrix ($r/a > 1$). Transport properties in this region are dominated by the fast parallel transport and by the atomic physics processes. Region 2 is the Edge Transport Barrier (ETB) region that is a narrow region just inside separatrix. When an ETB exists, i.e. when the H-mode exists, significant reductions in the micro-turbulence level are observed. Transport in region 2 is dominated by the physics of the ETB and by ELMs. The intermediate region 3 ($0.8 \leq r/a \leq 0.95$) links the core plasma to the edge. ELMs, collisional turbulence and cold neutrals dominate transport in region 3. Deeper in the core (between $0.4 \leq r/a \leq 0.8$) is region 4 which is usually free from any strong MHD instabilities. Its transport is dominated by drift type of micro-turbulence [42, 43, 44]. This is also the region where an internal transport barrier normally forms and exists. Finally, transport in the central part of the plasma in region 5 (inside $r/a \leq 0.4$)

is either dominated by MHD events, called sawteeth, in the 'Conventional Tokamak Scenario' or with reduced micro-turbulence and neo-classical transport in the 'Advanced Tokamak Scenario' with ITBs. Sawtooth is usually absent in the 'Advanced Tokamak Scenario' because the standard condition to have sawteeth ($q < 1$) is not fulfilled in those plasmas. In this thesis, the main emphasis in transport modelling and data analysis is focused on the central and core regions (regions 4 and 5, $0.0 \leq r/a \leq 0.8$) although the numerical simulations are extended up to $r/a = 1.0$. Transport in regions 4 and 5 is dominated by the micro-turbulence and ITB physics in the 'Advanced Tokamak Scenarios'. However, both experimental evidence and theoretical considerations suggest that the underlying transport properties are strongly linked between all the five regions. Still, it is quite justified to study anomalous transport in each or in some of the regions independently.

As already mentioned, anomalous transport dominates in regions 4 and 5. There are two main routes in seeking after the explanation of the anomalous energy and particle losses observed in tokamaks. In the first picture, anomalous transport results from fluctuations in the electric field due to fluctuations in density and temperature. The fluctuating electric field leads to small scale $E \times B$ drifts [2, 29, 45, 46]. This is referred to as 'electrostatic turbulence'. The other picture explains the anomalous transport by fluctuations in the magnetic field, referred to as 'magnetic turbulence' that can break the toroidal symmetry and destroy the nested flux surfaces [47]. Since the heat conductivity parallel to the magnetic field is many orders of magnitude higher than perpendicular, the particles flowing along the magnetic field lines reach the plasma edge very fast in the case of broken flux surfaces. It is remarked that even if any physical fluctuation has both the electrostatic and magnetic components, the classification is nonetheless a useful one. Since a tokamak plasma is a combination of several fluids, the plasma turbulence is a result from fluctuations of these multiple turbulent fluids coupled through electromagnetic, friction and energy exchange effects. It is not surprising, therefore, that there is not yet a theory or even a comprehensive approach to this problem.

2.1.1 Heat Transport

The heat transport in the core region of the tokamak is mainly anomalous although the neo-classical transport may be important for the ion heat transport in some special cases. The heat transport caused by the turbulence is driven by the free energy sources of many plasma micro-instabilities, essentially the gradients of the temperature and density [48]. In the plasma core, the micro-instabilities are classified into three categories according to the source of the free energy; instabilities driven by the ion temperature gradient, instabilities driven by the electron temperature gradient and fluid-like instabilities driven by the pressure gradient. The most investigated micro-instability is the Ion Temperature Gradient (ITG) drift mode. It has the longest wavelength amongst the different branches of the micro-instabilities and it is believed to be the main contributor to the ion heat transport in tokamaks, but it is also known to affect the electron heat transport. The importance of the contribution from the ITG turbulence to the ion heat transport

is also recognised in the empirical study in Publication 1. The second category consists of the electron temperature gradient driven instabilities; Trapped Electron Modes (TEM) and Electron Temperature Gradient modes (ETG). The ETG has the shortest wavelength and the wavelength of the TEM is between the ITG and the ETG. The TEM has been found to be the dominant contributor to the heat transport in TFTR [49]. All the main branches of the instabilities, i.e. the ITG, the TEM and the ETG, contribute to the electron heat transport whereas the ETG does not contribute to the ion heat transport nor particle transport [50]. Fluid like instabilities, such as the current diffusive ballooning [51], drift resistive ballooning [52] and neo-classical tearing modes [53] belong to the third category of pressure driven instabilities.

In general, the drift turbulence becomes unstable only if the relevant relative temperature gradient exceeds the corresponding critical value of that instability. For example, the critical temperature gradient length for the ITG in the case of a flat density profile can be written in a simplified form according to Ref. [43] as

$$L_{\mathrm{T_i}}^{\mathrm{crit}} = \left| \frac{T_\mathrm{i}}{\nabla T_\mathrm{i}} \right|_{\mathrm{crit}} \approx R \frac{9}{20} \frac{T_\mathrm{e}}{T_\mathrm{i}}. \tag{2.1}$$

The existence of the critical temperature gradient of the micro-turbulence implies that there is a strong link between the edge and core. It is called as profile stiffness or profile resilience. This phenomenon has been observed on many tokamaks in which the ion and sometimes the electron temperature change in a self-similar way in the core, i.e. the core temperature is proportional to the edge temperature [54, 55]. The dependence of the core ion temperature on the edge temperature for a series of JET discharges with different edge ion temperatures is illustrated in Figure 2.2.

Theoretically stiffness can be explained by the fact that the drift turbulence becomes unstable only if the relevant relative temperature gradient exceeds some critical level $|\nabla T/T| \geq |\nabla T/T|_{\mathrm{crit}}$. In terms of transport or diffusion coefficient, the existence of the critical temperature gradient or stiffness for the ITG turbulence can be illustrated in the following way:

$$\chi_\mathrm{i}^{\mathrm{ITG}} \approx CR/a\rho_\mathrm{i}^2 v_{\mathrm{Ti}} \times \left(\left| \frac{\nabla T_\mathrm{i}}{T_\mathrm{i}} \right| - \left| \frac{\nabla T_\mathrm{i}}{T_\mathrm{i}} \right|_{\mathrm{crit}} \right), \tag{2.2}$$

where the multiplier $CR/a\rho_\mathrm{i}^2 v_{\mathrm{Ti}}$ indicates the widely accepted paradigm that a drift wave turbulence generates GyroBohm type of transport with ρ_i^2 and v_{Ti} being the ion gyro radius and the ion thermal velocity and C is a numerical constant. If $|\nabla T_\mathrm{i}/T_\mathrm{i}| \leq |\nabla T_\mathrm{i}/T_\mathrm{i}|_{\mathrm{crit}}$, no unstable ITG modes exist and $\chi_\mathrm{i}^{\mathrm{ITG}}$ is zero. The critical temperature gradient lengths are distinct for the ITG, TEM and ETG and therefore, typically only either the ion or the electron transport exhibits profile stiffness. Worth mentioning here is that stiffness observed regularly in the ELMy H-mode scenario is broken by the internal transport barriers in the core in the 'Advanced Tokamak Scenarios'. The ITBs will be discussed in detail in Secs. 2.2 and 2.3.

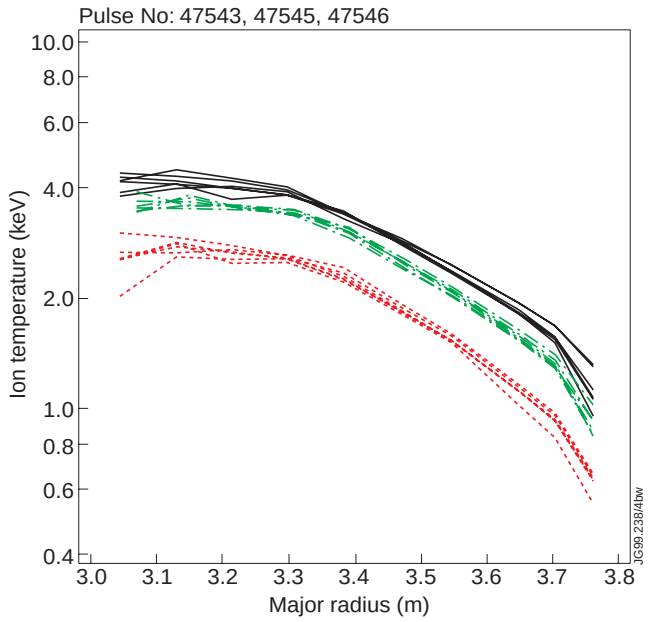

Figure 2.2: Ion temperature profiles for a series of JET shots with different edge ion temperatures indicating the profile stiffness. Adapted from Ref. [55].

Finally, it is instructive to list some experimental characteristics of the heat transport and confinement. The theory of the electrostatic turbulence predicts GyroBohm-like scaling and local transport, but it has been observed that the wavelength of the turbulence increases with increasing size of the tokamak — this is, however, an indication of Bohm-like scaling and non-local transport. Moreover, experiments with inward propagating heat and cold pulses have shown features that cannot be explained within the framework of local transport theory [56]. Consequently, transport has both local and non-local features. Another important observation is that the energy confinement time τ_{E} decreases with auxiliary heating power as $\tau_{\mathrm{E}} \propto P_{\mathrm{in}}^{-0.5}$. Fortunately, it increases with the isotope mass [57].

2.1.2 Particle and Momentum Transport

The particle transport models must be tailored in a different way for each particle species considered. Transport of electrons and deuterium and tritium ions is predominantly anomalous whereas the neo-classical effects play an important role in impurity transport. In this thesis, the electron and the ion particle transport are considered and taken into account in all the simulations and analyses whereas helium and impurity transport are not dealt with. However, still worth mentioning is the fact that in particular in the 'Advanced Tokamak Scenarios', the impurity and helium accumulation (in DT-plasmas) in the plasma core may ultimately be the

most strict condition that determines what kind of temperature, density and current density profiles are feasible in plasmas with ITBs. The impurity accumulation in the plasma centre is due to peaked density profiles arisen from steep pressure gradients of the ITBs.

The particle (electron and ion) transport is much less studied and also much less understood than the heat transport. Theoretically the particle transport is complicated due to ambipolarity, which means that particle diffusion is controlled by the least mobile component, usually electrons. Experimentally the particle transport sets up challenging requirements for the diagnostics in order to have time dependent measurements. Furthermore, cold recycled neutrals from the edge are distributed poloidally asymmetrically and therefore, their behaviour is difficult to measure or calculate.

Even if the particle transport is not well-known, some general remarks can be made. Firstly, plasma confinement degrades when plasma approaches the density limit, called the Greenwald limit [58, 59]. Secondly, the off-diagonal terms in the transport matrix (Eq. (1.5)) may play a larger role than in the overall heat transport [60]. In addition to the neo-classical Ware pinch mentioned in Section 1.4, anomalous pinch, in particular in the outer region of the plasma may be of importance. Furthermore, the role of convection is often significant in the particle transport. Thirdly, experiments indicate a strong correlation between the local thermal and particle transport properties in the core, normally the particle diffusivity aligned more closely with the ion thermal diffusivity ($D/\chi_\mathrm{i} \approx 1$), but sometimes also with the electron thermal diffusivity ($D/\chi_\mathrm{e} \approx 1$) [61].

The study of the toroidal plasma rotation or the toroidal velocity is of interest for several reasons. Firstly, plasma rotation contributes to the suppression of turbulence by the $\omega_{\mathrm{E}\times\mathrm{B}}$ flow velocity shear. This is the topic in Section 2.3.1. Secondly, the toroidal rotation can suppress the growth of the error field instability and improve the stability of low n-kink modes. Thirdly, the toroidal rotation transport studies can provide further knowledge of transport in a tokamak. The rotation in the poloidal direction is also important. According to the neo-classical theory, the magnitude of the poloidal rotation is proportional to the ion temperature gradient and it acts, like the toroidal rotation, as a suppression mechanism of micro-instabilities.

The momentum and energy confinement times have been found to have similar magnitudes on many tokamaks [62]. Experimental values of the toroidal momentum diffusivity χ_ϕ are significantly higher than the neo-classical gyro-viscosity — transport of the toroidal momentum is mainly anomalous. On the contrary, neoclassical transport determines mainly the poloidal rotation [63]. The ITG based gyroBohm theory leads to the equality $\chi_\phi = \chi_\mathrm{i}$ [64]. Experimental results on JET and TFTR also confirm that the radial profiles of the ion heat and toroidal momentum diffusivities are close to each other [65, 66].

2.1.3 Current Diffusion

The diffusion of the plasma current is one of the few transport processes in a tokamak that is believed to be almost purely neo-classical. In a cylindrical plasma, the classical electrical resistivity was derived already 50 years ago by Spitzer [67]

$$\eta_{\mathrm{s}} = 1.65 \times 10^{-9} \ln\Lambda / T_{\mathrm{e}}^{3/2}, \tag{2.3}$$

where the Coulomb logarithm $\ln\Lambda \approx 17$ and is a weak function of density. The classical resistivity is valid only for pure hydrogen plasma without any magnetic field. However, usually tokamak plasmas consist of hydrogen and deuterium with small fractions of impurities, thus having $Z_{\mathrm{eff}} > 1$, where Z_{eff} is defined as

$$Z_{\mathrm{eff}} = \frac{1}{n_{\mathrm{e}}} \sum_{i=1}^{N} n_i Z_i^2. \tag{2.4}$$

Here, n_i and Z_i are the density and charge of the main and the impurity ion species. In addition to the increase of η_{s} by $Z_{\mathrm{eff}} > 1$, trapped particles present in a toroidal device do not carry a current and the Spitzer resistivity is further modified to the neo-classical resistivity η according to [12, 13]

$$\eta \approx N(Z_{\mathrm{eff}}) Z_{\mathrm{eff}} \frac{\eta_{\mathrm{s}}}{[1-(r/R_0)^2]^2}, \tag{2.5}$$

where $N(Z_{\mathrm{eff}})$ decreases roughly from 1 to 0.5 when Z_{eff} increases from 1 to ∞ and $1/[1-(r/R_0)^2]^2$ is an approximation for the trapped particle correction. The simulated current diffusion by using either the Spitzer or the neo-classical resistivity are compared with the experimentally measured current diffusion in Publication 3. The comparison confirmed that the current diffusion on JET can be described very well by the neo-classical resistivity.

There are at least two occasions where the current diffusion is not neo-classical. Firstly, in the case of the sawtooth MHD instability, i.e. when $q < 1$ in the plasma centre, the current is redistributed in the plasma core with a MHD time scale that is much faster than the neo-classical current diffusion time. Secondly, very recently with a deeply reversed q-profile in the plasma core, it has been observed that there is sawtoothlike behaviour appearing in the electron temperature profiles although the condition to have the sawtooth instability active, i.e. $q < 1$, is not fulfilled [68]. This behaviour may lead to a partial redistribution of the current with a very fast time scale. The topic of the deeply reversed q-profile and its impacts are considered in Publication 4.

2.2 Transport Barriers

Progress in reducing the anomalous transport in tokamaks has been dramatic. The improvements in confinement, fusion performance and plasma stability due to

transport barriers have been drastic. Moreover, the richness of the physics revealed by these developments open the possibility of achieving deeper understanding of non-linear turbulent plasma phenomena.

2.2.1 Edge Transport Barrier

The high confinement mode (H-mode) associated with the formation of an edge transport barrier was first discovered in ASDEX in 1982 [7]. The ETB in the H-mode can be seen as steep temperature and density gradients just inside the separatrix at $r/a \approx 0.97$ in Figure 2.1. The H-mode exhibits global energy confinement about a factor of two better than the L-mode. Part of this is due to the formation of the ETB itself, however, another very important part is due to the reduction of the local transport throughout the whole plasma. Reductions in the electron and ion thermal diffusivity as well as in the angular momentum diffusivity have been observed. Although the ETB formation and the physics of the ETB and H-mode are beyond the scope of this thesis, the physics of the ETB and ITB may have similarities. Thus, it is worth mentioning that the leading hypothesis to date for the reappearence of the H-mode is the reduction of turbulent transport by the shear in $E \times B$ flow [69].

2.2.2 Internal Transport Barrier

In the middle of 1990s, many tokamak research groups reported that there is, in addition to the H-mode, also improved confinement in the core of the plasma [15, 16, 17, 18]. This improved core confinement is caused by an internal transport barrier and it is seen as larger temperature, density and pressure gradients in the core region in Figure 2.1 when compared with the standard H-mode.

ITBs and ETBs are now widely achieved in a number of devices with various control schemes, such as NBI heating, ICRF and ECRF heating, LHCD, momentum and mass injection etc. This suggests that there may be several mechanisms that can trigger barriers and affect the dynamics of the barriers. This is discussed in more detail in Section 2.3. Furthermore, there are some similarities in the radial structure of the ETB and ITB, and these similarities point to common physics involved in the formation and sustainment of the barriers. One of them is the qualitatively similar structure of the radial electric field E_r at both the ETB and the ITB [70].

The radial location of the ITB is usually between $0.2 \leq r/a \leq 0.8$. The location can vary with time — roughly speaking the location of the ITB moves inwards when heating is decreased and outwards when heating is increased. Naturally, other quantities, like the q-profile and the radial electric field, affect the actual evolution of the location of the ITB, this is discussed in more detail in Section 2.3.

ITBs have been observed simultaneously in all the four transport channels, i.e. in the ion and electron heat transport as well as in the electron particle and angular

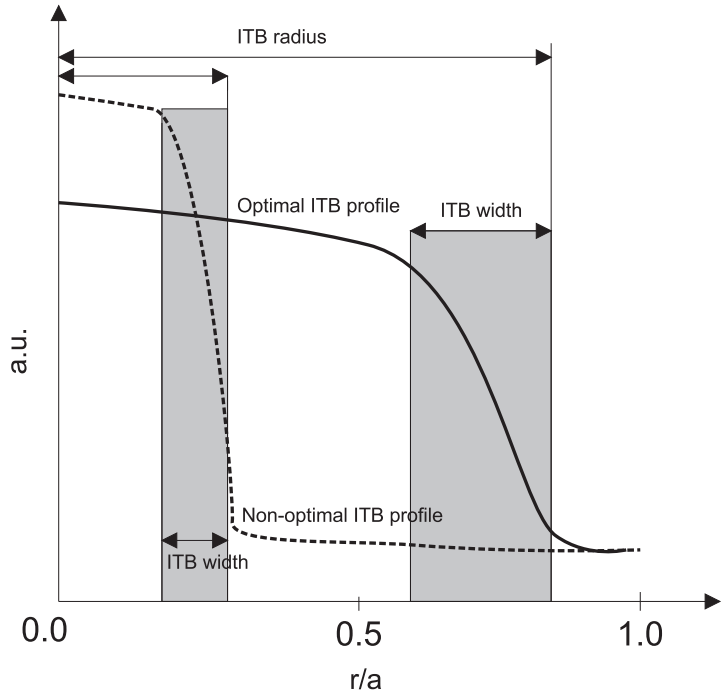

Figure 2.3: A schematic representation of the optimal (broad profiles with moderate gradients) and non-optimal (narrow profiles with steep gradients) ITB profiles.

momentum transport channels, on DIII-D [71, 72], JET [73] and JT-60U [22]. However, there is also a number of cases where one or two transport channels exhibit an ITB while the other ones do not. Sometimes only T_i has an ITB, sometimes T_e and n_e show clear ITBs while the ITB in T_i appears only weak. This phenomenon is not fully understood, but it is probable that the heating scheme, whether it is dominantly ion or electron heating, plays an important role. In addition to this, different transport channels are affected by different micro-turbulence and because the turbulence stabilisation mechanisms become active in different plasma conditions, it is possible that ITBs appear only in some of the transport channels. In the case of simultaneous ITBs in different transport channels, the radial location and time evolution of the ITBs in those channels are similar.

It is not completely clear how the optimal ITB profile should look like. However, some general rules for the optimal ITB profile can be drawn. Firstly, it should provide the largest improvement in fusion performance that can be sustained for a long time. Secondly, good confinement is required; typically a factor of two or higher than the conventional H-mode confinement time indicates good confinement in ITB discharges. Thirdly, the plasma profiles must be stable against MHD instabilities. Fourthly, the ITB must be radially located in the region where the bootstrap current is large and well-aligned with the desired q-profile. A diagram-

matic representation of the optimal and non-optimal ITB profiles (temperature, density or pressure) is shown in Figure 2.3. The optimal ITB profiles lie at a large radius r/a, and possess moderate gradients, whereas the non-optimal ITB profiles are the opposite. A large ITB radius increases confinement. In addition, the fusion performance is improved by the increasing volume of the improved confinement region. MHD modelling indicates that the maximum stable normalised beta, $\beta_{\mathrm{N}} = \beta/(I/aB_{\phi})$, can increase by 60% or more as the ITB radius and width are increased [50]. Moreover, in order to obtain a large bootstrap current fraction that is aligned well with the desired current density profile, the ITB radius should lie at $r/a \approx 0.7 - 0.8$ with moderate ITB gradients.

The most promising way to achieve long-lasting steady-state operation in tokamaks with good confinement is to have two transport barriers simultaneously — plasma that has an ITB with an H-mode (ETB) edge. This double barrier mode has provided promising results in JET [74]. Very recently, a new high performance regime, called the Quiescent Double Barrier (QDB) mode, has been found in DIII-D [50]. The QDB regime combines an ITB with a quiescent, ELM-free H-mode edge, giving rise to good confinement and a possibility to a long-pulse operation with high performance if the density can be increased and the impurity accumulation avoided.

2.3 ITB Formation Dynamics

An ITB often forms in the early phase of the discharge. In many cases, it appears during the current ramp-up phase with only a moderate heating power. These ITBs are most distinct in the electron temperature profiles. The formation of these types of ITBs in JET have been analysed in Publications 3 and 4. Another common way of obtaining ITBs is shortly after the main heating phase or high power phase has started. The formation mechanisms of these ITBs have been investigated in Publications 1, 2 and 5. After the initial formation, an ITB can expand, shrink or disappear depending on the heating power, current density profiles, MHD instabilities etc. What is worth mentioning is that the physics behind the initial formation, i.e. ITB triggering, may differ from the physics that governs the ITB dynamics and evolution later during the discharge. The physical mechanism of the ITB formation has not yet been clearly identified. There are several physical mechanisms that are believed to affect the ITB formation and dynamics of which the most common ones are analysed in detail in Secs. 2.3.1–2.3.5.

2.3.1 $\omega_{E\times B}$ Flow Velocity Shear

The importance of the radial electric field and its shear was already recognised long time ago [75, 76]. For the present, the leading candidate to explain the ITB formation and ITB dynamics in a tokamak seems to be the $E\times B$ velocity shear [77]. It is regarded as a key factor in the ITB formation in most theories [78, 79, 80] and

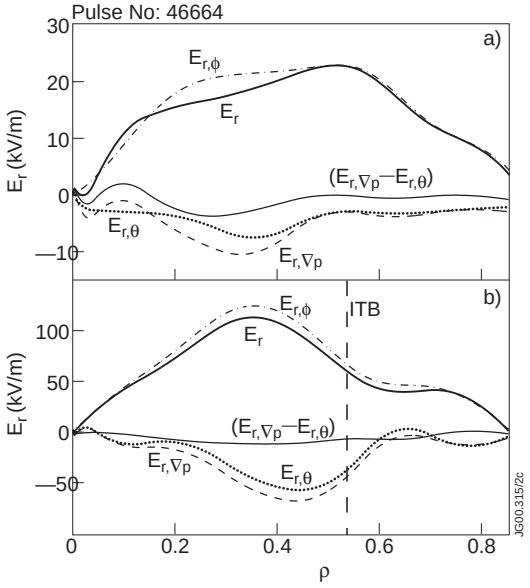

Figure 2.4: E_r and its components 0.6 s before (a) and 0.6 s after (b) the ITB formation as a function of $\rho = \sqrt{\phi/\pi B_\phi}/a_\mathrm{eff}$ with a_eff being the radius of the circle covering the same area as the elongated plasma for JET pulse No. 46664. The footpoint of the ITB is shown by the vertical dashed line in (b).

also found to be essential in most ITB experiments on different tokamaks [21, 70, 81, 82].

The radial force balance equation is written as follows:

$$E_\mathrm{r} = \frac{1}{Zen_i}\frac{\partial p_\mathrm{i}}{\partial r} - v_\theta B_\phi + v_\phi B_\theta, \tag{2.6}$$

where v_θ and v_ϕ are the poloidal and toroidal velocities and B_θ and B_ϕ the poloidal and toroidal magnetic fields, respectively, n_i is the ion density, Z is the ion charge number and e the elementary charge. Equation (2.6) indicates that there is a connection between E_r and the radial heat and particle transport through ∇p_i, toroidal rotation through v_ϕ and poloidal flow through v_θ.

The radial electric field and its different components are shown 0.6 s before the ITB formation in Figure 2.4 (a) and 0.6 s after the ITB formation in Figure 2.4 (b) for a typical 'Advanced Tokamak Scenario' JET discharge (pulse No. 46664). The contribution from the toroidal rotation (dash-dotted curve) is clearly dominant in the total E_r (thick solid), both before and after the ITB formation. The magnitude of E_r and all its components are about 5 times larger after the formation of the ITB than prior to it. The footpoint of the ITB is at $\rho \approx 0.56$ in Figure 2.4 (b). The values for E_r and its different components are found to be of the same order of magnitude and follow the same qualitative behaviour also for other JET ITB

discharges, where the ITB appears in the main heating phase.

In JET, the toroidal rotation produced mainly by the co-rotating NBI gives always a positive contribution to E_r as illustrated in Figure 2.4. However, theoretically, when exploring the interaction of the toroidal rotation with diamagnetic and poloidal rotation contributions, counter-momentum injection was predicted to lower the power threshold to form an ITB and to produce a wider ITB in Ref. [83]. Experimentally NBI counter-injection was demonstrated to be better at sustaining the ITB compared to co-injection on TFTR [70, 84]. However, balanced-injection with $v_\phi \approx 0$ turned out to be enough or even better to sustain and form an ITB on TFTR when the magnetic shear was negative in the core plasma. The advantage of balanced-injection in reversed magnetic shear plasmas has also been reported in JT-60U [81].

In a tokamak geometry, the $\omega_{E\times B}$ shearing rate is usually calculated according to the so-called Hahm-Burrell formula [85]

$$\omega_{E\times B} = \left| \frac{(RB_\theta)^2}{B} \frac{\partial}{\partial \Psi} \frac{E_r}{RB_\theta} \right|, \tag{2.7}$$

where Ψ is the poloidal flux, R the major radius and E_r calculated in Eq. (2.6). Although E_r/RB_θ is constant on a flux surface, $\omega_{E\times B}$ is not because of $(RB_\theta)^2/B$. Consequently, due to the B^{-1} dependence, the $\omega_{E\times B}$ flow shear is larger on the low field side and therefore, turbulence stabilisation occurs more easily there.

The basic theoretical picture of the $\omega_{E\times B}$ flow shear stabilisation relies either on non-linear decorrelation of turbulence [69] or linear stabilisation of unstable modes [86]. In the non-linear electrostatic model, transport (such as ITG, TEM and ETG) is caused by the correlation between the density (or temperature perturbations) and the velocity (or potential perturbations). When the $\omega_{E\times B}$ velocity shear is large enough, the turbulent eddies are distorted and as a consequence, radial transport is reduced. This reduction is due to both changes in the phase relationship between the perturbations and a decrease in the amplitude of the fluctuations. In the linear model, the presence of the $\omega_{E\times B}$ velocity shear results in enhanced damping by coupling the unstable modes to other, nearby lying stable modes, thus reducing transport. In general, turbulence quenching takes place roughly when $\omega_{E\times B}$ velocity shear is larger than the maximum growth rate of the dominant turbulence mode γ_{lin}^{max}, i.e. $\omega_{E\times B} > \gamma_{lin}^{max}$ [86].

Assuming the $\omega_{E\times B}$ shear to be the leading candidate, an ITB should form if the ITB formation threshold condition $\omega_{E\times B} > \gamma_{lin}^{max}$ is fulfilled at a certain radius at a certain time. There is also strong experimental evidence that $\omega_{E\times B}$ is comparable to γ_{lin}^{max} prior to the ITB formation and significantly exceeds it after the formation on JET [87], on DIII-D [23, 77] and on TFTR [49, 84]. Nevertheless, this does not necessarily prove the causality — which one occurs first, turbulence suppression by $\omega_{E\times B}$ shearing rate or transport reduction due to some other turbulence quenching mechanism followed by an increase in $\omega_{E\times B}$. The problem is complicated because when the temperature gradient increases, γ_{lin}^{max} increases, but so does $\omega_{E\times B}$ and usually faster. Consequently, well after the onset of the ITB, it is natural that

$\omega_{E\times B}$ exceeds significantly γ_{lin}^{max}. Nevertheless, for the present the $\omega_{E\times B}$ shearing rate seems to be the most universal mechanism to explain the ITB formation and dynamics in many experiments on many tokamaks.

2.3.2 Magnetic Shear s

There are several ways in which the magnetic shear s, i.e. derivative of the q-profile ($s \approx (r/q)(dq/dr)$), affects transport. The magnetic shear also influences the ITB formation and sustainment. With a negative magnetic shear $s < 0$, ballooning modes enter the second stable region [78, 88] with complete stability to $n = \infty$ ideal MHD ballooning modes [89]. A small or negative magnetic shear also prevents normally the sawtooth instability from becoming active ($q > 1$), thus improving the core confinement and performance. The negative magnetic shear also reduces the geodesic curvature drive of micro-instabilities, such as ITG, TEM and high-n ballooning modes [79, 89] and it also reduces magnetic stress by eliminating perturbations in B [90]. In addition, the threshold of the critical temperature gradient of the ITG turbulence increases due to negative s [91]. Furthermore, it has been also shown that $s < 0$ can reverse the toroidal precession drifts of barely trapped electrons [49]. Even some of the high-k instabilities, such as the ETG turbulence, can be stabilised by a region of the negative magnetic shear [50, 92]. Finally, in the region where $s \approx 0$, the turbulent vortices, initially linked together by toroidicity, are more easily disconnected than with large values of s, thus giving rise to improved plasma confinement [44].

In order to have a negative or small magnetic shear with all its aforementioned beneficial effects during the high performance phase of a tokamak discharge, a successful preparation phase is required to create the appropriate target q-profile. In JET, typically LHCD or sometimes ICRH is used in the preheating phase together with a fast current ramp-up to achieve the negative or small magnetic shear. This is analysed in much more details in Section 3.2 and in Publication 3. On other tokamaks, also ECRH and NBI preheating are applied in order to create the desired magnetic shear profile [38, 93, 94].

One of the key questions with the negative magnetic shear is whether it alone can trigger the ITB or it just facilitates the ITB formation while some other mechanism plays the main role. In some proposals the negative magnetic shear plays the key role [49], while other proposals state that it alone cannot form the ITB [77, 84].

In many proposals, the synergy between the effects by the negative magnetic shear and the $\omega_{E\times B}$ shearing rate is fundamental. In JET, the synergy between s and the $\omega_{E\times B}$ shearing rate is investigated in Figure 2.5. Thirteen ITB pulses in the H-mode and three ITB pulses in the L-mode at the ITB threshold condition are illustrated. There are also three back transitions from an ITB state to an ELMy H-mode plasma included in Figure 2.5. The plasma parameter range of the analysed pulses is very wide, i.e. B_ϕ varies between 1.8–4.0 T, the input power in the range 10–30 MW and the diamagnetic energy in the range 3–12 MJ among the

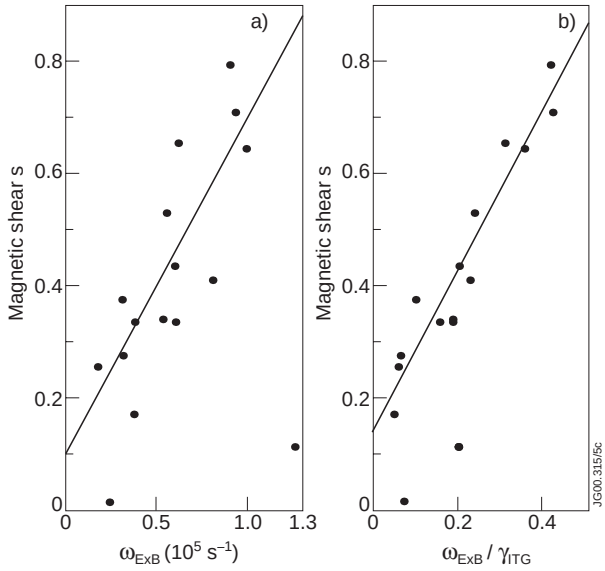

Figure 2.5: (a) Magnetic shear s as a function of $\omega_{\mathrm{E\times B}}$ at the ITB location at the ITB onset for 16 JET 'Advanced Tokamak Scenario' discharges. (b) As in (a), but $\omega_{\mathrm{E\times B}}$ shearing rate divided by the linear estimate of the ITG instability growth rate γ_{ITG}. The straight lines are the best fits calculated with the least-squares method.

investigated pulses. The magnetic shear s is calculated in an interpretative way (predicting q, taking T_{e}, T_{i} and n_{e} from experiments) by JETTO [27] transport code. In Figure 2.5, s is presented at the ITB radius at the onset of the ITB as a function of $\omega_{\mathrm{E\times B}}$ or $\omega_{\mathrm{E\times B}}/\gamma_{\mathrm{ITG}}$ with $\omega_{\mathrm{E\times B}}$ calculated from Eq. (2.7) at the same time and location.

The data points in Figure 2.5 exhibit a linear trend indicating that a linear regression is reasonable. Therefore, by applying the least-squares method to the scatter plots, a straight line in each figure can be estimated. The estimated regression line takes the form $s = 0.60\omega_{\mathrm{E\times B}} + 0.091$ ($\omega_{\mathrm{E\times B}}$ scaled by 10^5) in Figure 2.5(a) and

$$s = 1.47\omega_{\mathrm{E\times B}}/\gamma_{\mathrm{ITG}} + 0.14, \tag{2.8}$$

or by rearranging the terms

$$\omega_{\mathrm{E\times B}} = 0.68s\gamma_{\mathrm{ITG}} - 0.095\gamma_{\mathrm{ITG}}, \tag{2.9}$$

in Figure 2.5(b). The scatter among the different discharges is clearly smaller in the case where the discharges are plotted as a function of $\omega_{\mathrm{E\times B}}/\gamma_{\mathrm{ITG}}$ rather than $\omega_{\mathrm{E\times B}}$. As a consequence, this can be regarded also as an indirect indication that the ITG turbulence and the ITG turbulence suppression play a major role in the ITB formation process with these JET discharges.

There are two distinct regions in the $s - \omega_{\mathrm{E\times B}}/\gamma_{\mathrm{ITG}}$ space, separated by the straight

line from Eq. (2.8) in Figure 2.5(b). The ITB formation threshold condition is interpreted as follows: when and where $\omega_{\mathrm{E\times B}} > 0.68 s\gamma_{\mathrm{ITG}} - 0.095\gamma_{\mathrm{ITG}}$ is fulfilled, an ITB does exist whereas when and where $\omega_{\mathrm{E\times B}} < 0.68 s\gamma_{\mathrm{ITG}} - 0.095\gamma_{\mathrm{ITG}}$, an ITB does not exist. The ITB forms or collapses, depending on the direction, when the straight line given by Eq. (2.8) is crossed. The same rule is valid for all discharges in a wide range of parameters B_ϕ, P_{in} and W_{dia} [95].

The empirical threshold condition found for the ITB formation provides the first clear indication of the strong correlation between s and $\omega_{\mathrm{E\times B}}$ at the ITB transition in JET. The physics interpretation of the ITB formation in the s–$\omega_{\mathrm{E\times B}}/\gamma_{\mathrm{ITG}}$ space could be the following: the $\omega_{\mathrm{E\times B}}$ flow shear must be large enough to tear apart the turbulent eddies thus decreasing the growth rate of the long wave length ITG turbulence (γ_{ITG}) while at the same time the small (or negative) magnetic shear s helps to disconnect the turbulent vortices (e.g. ballooning modes) initially linked together by toroidicity. Another point worth mentioning is the intercept term in $s = 1.47\omega_{\mathrm{E\times B}}/\gamma_{\mathrm{ITG}} + 0.14$. A positive intercept implies that a negative or zero magnetic shear should be a sufficient condition for an ITB to exist in JET. Recent results from the previous JET experimental campaigns with LHCD preheating, considered thoroughly in Publications 3 and 4, support the idea. Using only LHCD in the preheating phase, the discharge has a very clear ITB in the electron transport channel and the magnetic shear is negative while the $\omega_{\mathrm{E\times B}}$ shearing rate and the Shafranov shift are very small, almost negligible. The above result would suggest that the negative magnetic shear alone would be a sufficient condition to form an ITB (at least in the electron transport channel in JET). In addition, in some experiments the footpoint of the ITB has been also found to follow the q_{min}-surface in JET [74]. Similar results of the special role of the negative magnetic shear has been reported from other tokamaks [96, 97]. However, there is also some evidence from other tokamaks that may contradict the aforementioned statement [70, 77].

2.3.3 Integers and Rationals of the q-profile

There is evidence on JET [98], RTP [99], JT-60U [15] and DIII-D [23] that integer and possibly also rational surfaces of the q-profile affect ITB triggering and in some cases may also have an influence on the later time evolution of the ITB. In JET, an ITB is often formed when the $q = 2$ surface appears in the core region. In addition, in many cases the footpoint of the ITB seems to follow the outward propagation of the $q = 2$ surface.

One of the proposed ideas behind the ITB triggering by an integer q surface is a link between the MHD activity on the integer q surface and the MHD activity at the edge [98]. This coupling of the magnetic perturbations with different poloidal mode numbers results via toroidicity and via the shaping of the flux surfaces [100]. The strong toroidal coupling of the external ($n = 1$) kink mode at $q_{\mathrm{edge}} = 5$ or $q_{\mathrm{edge}} = 4$ to the $q = 2$ or $q = 3$ surface in the core indicates the potential for modifying transport. The modified enhanced transport at the q integer island ($n = 1$ and $m = 2$ or $m = 3$) can locally increase or decrease the pressure and toroidal rotation

at adjacent points around the integer q surface. Therefore, the integer q surface can act as a trigger for an ITB although the actual turbulence suppression occurs via the increased $\omega_{\mathrm{E}\times\mathrm{B}}$ shearing rate. Another explanation relies on the density of the rational q surfaces; near a simple rational q surface, there are less low order rational resonant surfaces [44]. This idea works very well in the turbulence simulations. Other experimental and theoretical studies to explain the ITB formation due to the integer and rational surfaces in the q-profile have suggested different mechanisms. They rely either on a local reduction in transport associated with low order rational q surfaces or on some other topological modifications of the flux surface structure resulting from the internal MHD occurring at the rational q surfaces [101].

2.3.4 Shafranov Shift

The Shafranov shift Δ is a displacement of the magnetic axis (and flux surfaces) due to pressure and current density profiles with respect to the magnetic axis in the vacuum field. The flux surfaces in a plasma are more densely populated on the outer mid-plane and less densely on the inner mid-plane than those in the vacuum field without the plasma. The Shafranov shift has a twofold effect on the ITB formation. Firstly, it enhances the $\omega_{\mathrm{E}\times\mathrm{B}}$ shearing rate on the low field side on the outer mid-plane. This originates from Eq. (2.7); the Shafranov shift compresses the flux surfaces closer to each other on the outer midplane and thus, E_{r} is larger because the potential is constant on a flux surface. This results further in larger $\omega_{\mathrm{E}\times\mathrm{B}}$ shearing rates. Secondly, the Shafranov shift can directly affect the growth rate of the micro-turbulence, for example the growth rate of the TEM and ETG reduces significantly with a large Shafranov shift [49, 92].

The effect of the Shafranov shift on the turbulence suppression and on the ITB formation via the increased $\omega_{\mathrm{E}\times\mathrm{B}}$ shearing rate has been investigated in Publication 1. The local increase in the $\omega_{\mathrm{E}\times\mathrm{B}}$ shearing rate on the outer mid-plane as compared with the inner mid-plane was found to be very small for typical JET 'Advanced Tokamak Scenario' ITB pulses. However, although the effect of the Shafranov shift on the ITB formation via the increased $\omega_{\mathrm{E}\times\mathrm{B}}$ shearing rate may be small (at least in JET), its effect on the instability growth rate has been reported to be of great importance on TFTR [49]. The stabilisation mechanism is based on the favourable precession of the trapped electrons due to the large Shafranov shift. Transport by the TEM can be decreased significantly and even suppressed completely in the case of a large Shafranov shift. This stabilisation effect is enhanced by the small or negative magnetic shear.

The Shafranov shift stabilisation is a positive feedback mechanism — a larger Shafravov shift leads to reduced transport and steeper pressure gradient which then, in principle, can lead to even larger Shafranov shift and in turn, steeper pressure gradient. As a consequence, the Shafranov shift could be a possible trigger for the sudden transition to an ITB. Another practical issue with turbulence stabilisation by the Shafranov shift is that it has more favourable scaling to reactors than for example the $\omega_{\mathrm{E}\times\mathrm{B}}$ shearing rate because it is less dependent on the machine size.

2.3.5 Density Gradient

Certain drift waves in tokamaks, such as the ITG and the ETG, have the property that they become unstable when the temperature gradient exceeds a critical value, as already discussed in Section 2.1.1. This critical temperature gradient threshold, like the critical temperature length for the ITG $L_{\mathrm{T_i}}^{\mathrm{crit}}$, depends on the density gradient. Accordingly, an increase in the density gradient may stabilise the ITG or the ETG and thus lead to a bifurcation to a reduced transport state [78, 102]. Therefore, a local particle source can act as a trigger mechanism to the ITB formation. With a moderate or steep density gradient, equation (2.1) in Section 2.1.1, which is the simple approximation of the critical temperature gradient of the ITG with a flat density profile, is not valid any longer. On the other hand, even if the ITG and the ETG may be quenched by the density gradient, the TEM may be destabilised by the density gradient. Thus, anomalous transport can be suppressed completely with the density gradient mechanism only in the plasma centre and in a highly collisional edge region where trapped particles are absent.

The role of the density gradient in the ITB formation in JET is analysed in Publication 2. The simulation results indicate that indeed, the density gradient can form the ITB, independently of the $\omega_{\mathrm{E\times B}}$ shearing rate stabilisation. The onset of the ITB is based on the suppression of the ITG turbulence by the large density gradient inside $r/a \approx 0.5$. In general, the ITG turbulence is believed to be the main source of the anomalous transport in the core region of the JET ITB plasmas and as a consequence, the turbulence suppression by the density gradient mechanism should be taken into account.

2.3.6 Interplay of the Different ITB Formation Mechanisms

As already shown in Section 2.3.2, it is not necessarily only one mechanism at a time that triggers and governs the dynamics of the ITB. Rather, it is probable that at least two of them interact with each other so that the micro-turbulence is suppressed, transport reduced and an ITB can form. Identification and evaluation of the relative importance of the different mechanisms are difficult since various types of micro-instabilities affect different transport channels and furthermore, various types of micro-instabilities are suppressed by different stabilisation mechanisms. It is also difficult to diagnose the contribution from the different stabilisation mechanisms since they are not independent of each other. For example, raising the density increases the Shafranov shift and density gradient and increases or decreases, depending on the direction of the toroidal rotation, the $\omega_{\mathrm{E\times B}}$ shearing rate. Similarly, raising the temperature affects both the $\omega_{\mathrm{E\times B}}$ shear and the Shafranov shift. The aforementioned complicated interaction among the different transport mechanisms affecting different transport channels, together with the stabilisation mechanisms, is illustrated in Figure 2.6.

It is important to note in Figure 2.6 that even if it seems to be possible to decrease or suppress the ITG with all turbulence stabilisation mechanisms, it can be still

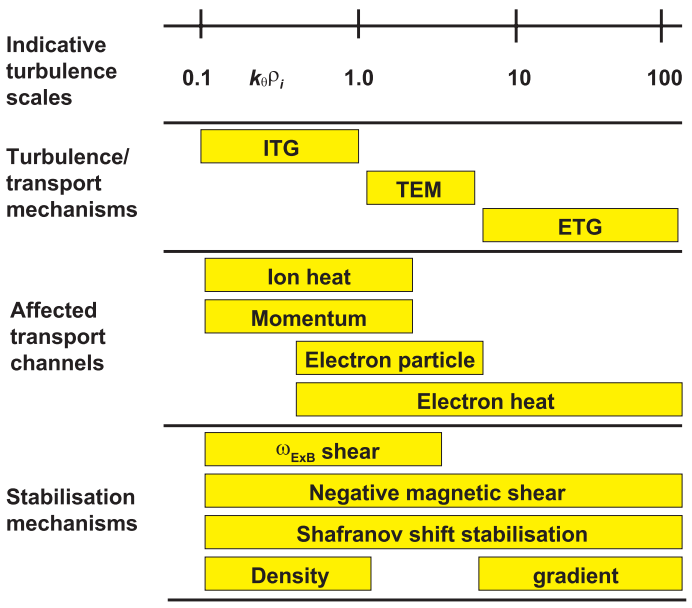

Figure 2.6: An outline summary of different transport mechanisms, how they affect different transport channels and how they can be stabilised.

regarded as the worst instability. This is due to the fact when the ITG is unstable, it also the predominant instability. Using the simple mixing length estimation, i.e. $\chi \sim \gamma / k_\theta^2$, the ITG gives the largest transport because of the longest wavelength although the growth rate γ of the ETG is much larger. As a consequence, the $\omega_{\mathrm{E}\times\mathrm{B}}$ shearing rate could be still the main turbulence stabilisation mechanism because it can efficiently suppress the ITG. The role of the rational q-surfaces is not illustrated in Figure 2.6 because it most probably affects transport indirectly via the other mechanisms, like increasing locally the $\omega_{\mathrm{E}\times\mathrm{B}}$ flow shear or the density gradient.

It might be expected that it is easiest to obtain ITBs in the ion heat and momentum transport channels, somewhat harder in the particle transport channel, and hardest in the electron heat channel. This tendency is consistent with observations on DIII-D [50]. In JET, with strong LHCD during the current ramp-up in the preheating phase, a clear ITB appears in the electron heat channel. However, no ITB in the ion heat or electron particle transport channels can be observed. Therefore, an interesting question remains whether this is just a measurement problem due to the low ion temperature and electron density or whether there is a contradiction with the results from DIII-D.

2.4 Numerical Codes and Transport Models

In this thesis, all the transport simulations have been performed with the JETTO transport code [27]. JETTO is a one and a half dimensional general transport code solving the time-dependent plasma diffusion equations averaged over the magnetic flux surfaces. In addition to solving the transport equations, JETTO has an internal equilibrium solver, several heating and current drive packages, calculation of the radial electric field, calculation of the fusion power and so on. Furthermore, JETTO transport code has several transport models, both empirical and theory-based ones.

2.4.1 JETTO Transport Code

The transport equations for the particle transport channel (Eq. (2.10)), for the electron heat transport channel (Eq. (2.11)), for the ion heat transport channel (Eq. (2.12)) and for the poloidal magnetic flux (current density) (Eq. (2.13)) can be written as follows:

$$\frac{1}{V'}\frac{\partial}{\partial t}(V' n_j) + \frac{1}{V'}\frac{\partial}{\partial \rho}(V'\langle(\nabla\rho)^2\rangle\Gamma_j) = \langle S_{\mathrm{n}_j}\rangle, \qquad j = 1, ..., n_H \quad (n_H < 3) \tag{2.10}$$

$$\frac{3}{2}(V')^{-5/3}\frac{\partial}{\partial t}\left[(V')^{5/3} n_{\mathrm{e}} T_{\mathrm{e}}\right] + \frac{1}{V\prime}\frac{\partial}{\partial \rho}\left\{V'\langle(\nabla\rho)^2\rangle\left[q_{\mathrm{e}} + \frac{5}{2}T_{\mathrm{e}}\Gamma_{\mathrm{e}}\right]\right\} = \langle P_{\mathrm{e}}\rangle \tag{2.11}$$

$$\frac{3}{2}(V')^{-5/3}\frac{\partial}{\partial t}\left[(V')^{5/3}\sum_{j=1}^{n_H} n_j T_{\mathrm{i}}\right] + \frac{1}{V'}\frac{\partial}{\partial \rho}\left\{V'\langle(\nabla\rho)^2\rangle\left[\sum_{j=1}^{n_H} q_j + \frac{5}{2}T_{\mathrm{i}}\Gamma_j\right]\right\} = \langle P_{\mathrm{i}}\rangle \tag{2.12}$$

$$\frac{\partial\psi}{\partial t} - \frac{A\eta_{||}}{\rho\mu_0}\frac{\partial}{\partial\rho}(K\frac{\partial\psi}{\partial\rho}) + \frac{V'\eta_{||}}{2\pi\rho}(j_{\mathrm{bs}} + j_{\mathrm{cd}}) = 0, \tag{2.13}$$

where the toroidal flux surface label ρ is defined as $\rho = \sqrt{\phi/\pi B_\phi}$ with ϕ being the toroidal flux and ψ is the poloidal flux. V is the volume and V' denotes the differentiation with respect to ρ. The brackets $\langle\rangle$ denotes the flux surface average, A and K are geometrical factors and μ the permeability of the vacuum. The electrical resistivity $\eta_{||}$ is a slightly modified version of Eq. (2.5). The particle and heat fluxes are denoted with Γ_j and q_j, respectively. S_{n_j}, P_{e} and P_{i} represent sources and sinks due to auxiliary heating and fuelling, energy exchange between different species, charge exchange losses, radiation, losses due to background neutrals and ionisation etc. j_{bs} and j_{cd} are the bootstrap current and externally driven current, respectively. The contribution from the transport models enter the equations (2.10)–(2.12) into the terms Γ_j and q_j. These terms are calculated from the transport matrix in Eq. (1.5) with the diffusion coefficients given by the transport models. In addition, there is a momentum balance equation in order to follow the time evolution of the toroidal rotation in JETTO.

The transport equations, i.e. the energy, particle and current balance equations, (2.10)–(2.13) form a complex integro-differential system. As a consequence, an

appropriate set of initial and boundary conditions is required in order to predict the time evolution of the simulated unknown quantities, such as n_e, T_e, T_i and B_θ. In JETTO, the initial profiles of all the unknown quantities that are to be modelled are read from an external file at the first time step. The initial profiles are constructed either from the experimental data or from some prescribed formula. For the initial condition in the poloidal magnetic field equation, an initial q-profile from EFIT [103] is used. EFIT is an equilibrium reconstruction code which calculates, among other, the equilibrium, the flux surfaces and the q-profile. The boundary conditions are needed both in the centre and at the separatrix. In the centre, the boundary condition of all the unknown quantities takes the form $\partial u/\partial \rho = 0$, where u is the unknown quantity to be modelled. At the separatrix, the boundary conditions are employed with the aid of time polygons, indicating the time evolution of the unknown quantity at the edge. Typically, experimental values at the plasma edge are imposed in JETTO. For example in JET, when the H-mode appears, the boundary value for T_e or T_i rises from about 300 eV up to 1.2 keV within some tens of milliseconds. The boundary condition for the poloidal magnetic field equation is the total plasma current. In addition, the value of Z_{eff} is needed in the simulations and normally, the experimentally measured value is used.

There are several other numerical modules than the transport equation solver coupled to JETTO. Several heating and current drive packages, neutral particle calculation package, fusion power calculation package etc. are implemented and coupled to JETTO. One of the most fundamental ones is the equilibrium package ESCO. ESCO takes the pressure and current density profile as input from JETTO and then solves the Grad-Schlüter-Shafranov equation in order to calculate the equilibrium and flux surfaces. The plasma boundary is normally taken from the experiment, i.e. from the EFIT output. Another way to introduce the equilibrium in JETTO is to use directly the EFIT equilibrium. The equilibrium is always calculated at the beginning of the JETTO transport simulation and can be recalculated later during the transport calculation as many times as needed.

The power deposition and current density profiles of LHCD in JETTO are calculated with the Fast Ray Tracing Code (FRTC) [32], which is coupled to JETTO. FRTC includes a fast ray-tracing package and the calculation of the power deposition and current density profiles by iteration between the evaluation of the quasi-linear diffusion coefficient and a 1D Fokker-Planck equation for the electron distribution function. A comprehensive study of its properties has been done in Publication 6. Since FRTC is coupled to JETTO, self-consistent simulations between transport and Lower Hybrid (LH) power and current calculation can be achieved. The coupled JETTO/FRTC code has been validated and tested in Publication 5.

In order to calculate the NBI power deposition and current density profiles in JETTO, the NBI code PENCIL [34] is used. PENCIL is also coupled to JETTO. It solves a simplified Fokker-Planck equation that is used to describe the fast ion dynamics. Fast ion self-collisions and the effects of the toroidal electric field on the fast ion dynamics are neglected. The resulting bounce averaged Fokker-Planck equation is then solved using an eigenfunction expansion in the pitch angle variable. On-axis/off-axis power deposition profiles are produced by an appropriate selection

between the normal and tangential PINIs, normal PINIs producing NBI power perpendicular to the toroidal direction (on-axis power deposition) and tangential PINIs at angles smaller than 90° with respect to the toroidal direction (off-axis power deposition).

The calculation of ECRH and ECCD is done with the 3D code ECWGB [33]. ECWGB calculates the propagation and absorption of the electron cyclotron waves injected as collimated microwave gaussian beams in toroidal geometry. The ECRH power absorbed and the ECCD current generated by highly collimated gaussian beams are evaluated using the equilibrium from JETTO and the relativistic treatment of the wave propagation and driven current. In addition, the effects of the trapped particles are taken into account. The toroidal and poloidal angles of the ray launching direction can be steered to change radially the location of the power absorption and the amount of the generated current.

The only heating method that is not dealt with in a self-consistent way in JETTO is ICRH. The power deposition profiles for electrons and ions are calculated with the ICRH code PION [104]. The PION code calculates the Ion Cyclotron Resonance Frequency (ICRF) heating power deposition profiles by taking into account the time evolution of the distribution functions of the resonating ions. In the 'Advanced Tokamak Scenario' discharges on JET, typically the hydrogen minority scheme (hydrogen concentration typically 2–4 %) is applied with frequencies in the range of 42–51 MHz to obtain on-axis and off-axis power deposition. The driven ICRH current is negligible for this ICRH scheme.

2.4.2 Transport Models in JETTO

There are three different transport models implemented in JETTO to predict the heat and particle transport. They are called the Bohm/GyroBohm model [25] which is semi-empirical, the Weiland model [28] and the Multi-Mode Model (MMM) [105] which are both theory-based transport models. Moreover, JETTO has a sawtooth model, a model for ELMs physics and an ablation model for pellet injection which are not considered in this thesis.

The Bohm/GyroBohm semi-empirical model has been tested against several different plasma discharges from DIII-D, TFTR, JT-60U, ASDEX-U, START and JET in the L-mode and against many different plasma shots performed on JET in the H-mode [20, 26, 25]. This transport model has been used in Publications 1–5. The set of the heat and particle transport coefficients in the Bohm/GyroBohm model

can be written in the following form:

$$\chi_{\mathrm{e}} = 1.0\chi_{\mathrm{gB}} + 2.0\chi_{\mathrm{B}} + \chi_{\mathrm{neo-al}} \tag{2.14}$$

$$\chi_{\mathrm{i}} = 0.5\chi_{\mathrm{gB}} + 4.0\chi_{\mathrm{B}} + \chi_{\mathrm{i}}^{\mathrm{neo}} \tag{2.15}$$

$$D = [0.3 + 0.7\rho]\frac{\chi_{\mathrm{e}}\chi_{\mathrm{i}}}{\chi_{\mathrm{e}} + \chi_{\mathrm{i}}}, \tag{2.16}$$

$$\text{where} \quad \chi_{\mathrm{gB}} = 5 \times 10^{-6}\sqrt{T_{\mathrm{e}}}\left|\frac{\nabla T_{\mathrm{e}}}{B_{\phi}^{2}}\right| \tag{2.17}$$

$$\chi_{\mathrm{B}} = \chi_{\mathrm{B}_0} \times \Theta(-0.14 + s - 1.47\omega_{\mathrm{E\times B}}/\gamma_{\mathrm{ITG}}) \tag{2.18}$$

$$\text{with} \quad \chi_{\mathrm{B}_0} = 4 \times 10^{-5} R\left|\frac{\nabla(n_{\mathrm{e}}T_{\mathrm{e}})}{n_{\mathrm{e}}B_{\phi}}\right| q^2 \times \left(\frac{T_{\mathrm{e}}(0.8\rho_{\max}) - T_{\mathrm{e}}(\rho_{\max})}{T_{\mathrm{e}}(\rho_{\max})}\right) \tag{2.19}$$

$$\text{and} \quad \chi_{\mathrm{neo-al}} = \frac{c^2 v_{\mathrm{th}}}{\omega_{\mathrm{pe}}^2 q R}\epsilon. \tag{2.20}$$

In Eqs. (2.17)–(2.20), T_{e} and T_{i} are the electron and the ion temperatures, respectively, n_{e} is the electron density, B_{ϕ} the toroidal magnetic field, c the speed of light, v_{th} and ω_{pe} are the electron thermal velocity and plasma frequency as well as R is the major radius and ϵ the inverse aspect ratio. The non-locality in the Bohm transport appears in the last term where ρ is the flux surface label defined by $\rho = \sqrt{\Phi/\pi B_{\phi}}/a_{\mathrm{eff}}$ with a_{eff} being the radius of the circle covering the same area as the elongated plasma. Φ is the toroidal magnetic flux and $\rho_{\max}$ is the value of ρ at the separatrix in the L-mode and on top of the barrier in the H-mode. All the units appearing in Eqs. (2.14)–(2.20) are in SI units except T_{i} and T_{e} whose unit is eV. $\chi_{\mathrm{i}}^{\mathrm{neo}}$ is the neo-classical term for the ion heat transport [12]. $\chi_{\mathrm{neo-al}}$ term represents transport arising from the ETG turbulence and has the similar form to one proposed already long time ago by Ohkawa [106]. Recently, this form of ETG transport has been supported by non-linear gyro-kinetic calculations and found to match experiments reasonably well [92].

The Θ-function multiplying the Bohm transport in Eq. (2.18) is the Heaviside step function. The controlling parameter inside its argument is the empirical ITB formation threshold condition that was found in Publication 1 and presented in Eq. (2.8). When the argument x in the step function $x = -0.14+s-1.47\omega_{\mathrm{E\times B}}/\gamma_{\mathrm{ITG}}$ changes its sign, the ITB either forms $[\Theta(x < 0) = 0]$ or collapses $[\Theta(x > 0) = 1]$ in the model. $\omega_{\mathrm{E\times B}}$ stands for the flow shearing rate defined in Eq. (2.7) and γ_{ITG} is an approximation for the linear growth rate of the ITG instability, defined as $\gamma_{\mathrm{ITG}} = v_{\mathrm{th,i}}/R$ with $v_{\mathrm{th,i}}$ being the ion thermal velocity. The toroidal velocity is calculated from the momentum balance equation using the torque from the neutral beam injection as the source term. The anomalous toroidal viscosity coefficient is assumed to be equal to the ion heat transport coefficient given in Eq. (2.15). The poloidal rotation is assumed to be neo-classical.

The other core transport model used in this thesis (Publication 2) is based on the fluid theory where the fluid equations are solved for each plasma species. Then, the fluid equations are linearized, with taking into account the magnetic drifts for each plasma species. The eigenvalues and eigenvectors from these equations are

computed for a given Fourier harmonic of the perturbed variables. Using the quasi-linear approximation, the saturation level is approximated by taking the mixing length estimate and balancing the linear growth. Then, the heat and particle fluxes can be calculated. The diffusion coefficients are calculated by taking the finite difference derivatives of the fluxes with respect to the temperature and density gradients. The model does not calculate the entire spectrum of the turbulence with respect to poloidal mode number k_θ, but a value of $k_\theta \rho_s = 0.316$ representing the middle of the spectrum is used (ρ_s is the larmor radius). This assumption produces a GyroBohm transport model. In this thesis, we call this transport model as the Weiland model [28, 29, 30, 31, 43]. The Weiland model includes electromagnetic effects as well as the effects of electron-ion collisions, impurities and fast ions.

The transport coefficients in JETTO with the implemented Weiland model have the following form:

$$\chi_e = \chi_{e,weil} + \chi_{neo-al}, \tag{2.21}$$

$$\chi_i = \chi_{i,weil} + \chi_i^{neo}, \tag{2.22}$$

$$D = D_{weil}, \tag{2.23}$$

where $\chi_{e,weil}$, $\chi_{i,weil}$ and D_{weil} are the transport coefficients from the ITG and TEM micro-turbulence, calculated by the Weiland model. Both the diagonal, off-diagonal and convective terms in the transport matrix (Eq. (1.5)) are calculated. There are two important issues worth mentioning in the present implementation of the Weiland model in JETTO. Firstly, there is no numerical fitting parameter in the present version and secondly, there is no additional term giving some extra transport in the edge region as in most of the other transport codes where the Weiland model has been implemented. Therefore, the ITB formation and the overall transport predictions can be regarded as rather theory-based predictions.

Chapter 3

Modelling of ITB Dynamics and Current Profile Evolution in JET

All the main results from the numerical modelling of the 'Advanced Tokamak Scenarios' performed during this thesis are presented in this Chapter. The predictive simulations of the 'Advanced Tokamak Scenarios' in this thesis concentrate on two subtopics. The first topic in Section 3.1 focuses more on predictive transport modelling of the ITB dynamics in JET (Publications 1, 2 and 5) whereas the second one in Section 3.2 concentrates on issues related to the modelling of the current density profile (or q-profile) evolution with respect to different heating and current drive scenarios in JET (Publications 3, 4 and 5).

3.1 Predictive Modelling of Discharges with Internal Transport Barriers

The predictive accuracy of most of the one-dimensional transport models in the ELMy H-mode scenarios is of the order of 20% [35]. As a consequence, when modelling the 'Advanced Tokamak Scenario' discharges, a better agreement between the experimental and predicted ITB dynamics can hardly be expected. In this thesis, the predictive simulations are defined to be simulations where the ion and electron temperatures, the density and usually also the toroidal rotation as well as the current density evolution are predicted by a transport model. Since the ITB formation and dynamics is not yet understood, no fully theory-based model based on first- principles and without any fitting parameters for explaining the physics of the ITBs exists for the moment. However, phenomenological transport models

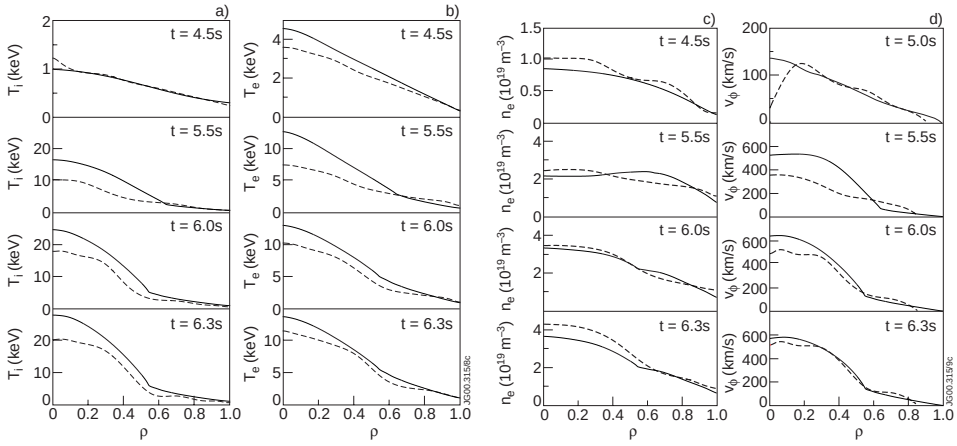

Figure 3.1: The ion (a) and the electron (b) temperatures as well as the density (c) and toroidal velocity profiles (d) at $t = 4.5$ s, $t = 5.5$ s, $t = 6.0$ s and $t = 6.3$ s. Dashed curves correspond to the experiment (Pulse No. 46664) and solid curves are calculated by the transport model.

have been successful at reproducing qualitative and numerous quantitative features in the ITB dynamics. The goodness of the empirical ITB formation threshold condition presented in Eq. (2.8) is tested in Section 3.1.1 and the applicability of the Weiland model to predict the behaviour of the ITB plasmas in Section 3.1.2. Results from the ITB modelling performed in this thesis are compared with predictions calculated by other ITB models in Section 3.1.3.

3.1.1 ITB Formation with the Empirical Transport Model

In order to demonstrate how the empirical transport model, together with the found threshold condition for the ITB formation, is able to predict the profiles of the temperatures, density and toroidal rotation, the simulation results of the JET 'Advanced Tokamak Scenario' pulse No. 46664 are illustrated in Figure 3.1. The magnetic field and the plasma current are $B_\phi = 3.4$ T, $I_\mathrm{p} = 3.4$ MA (peak). The simulation starts at $t = 3.0$ s while the NBI and ICRH heating begins at $t = 4.6$ s. The discharge ends up with a disruption due to the emergence of a pressure driven kink instability at $t = 6.5$ s. This pulse was selected here because it has a very strong and clear ITB formation, both in time and space, and also the time evolution of the ITB can be tracked with small experimental errors. The ITB forms at $t = 5.6$ s and the H-mode appears earlier at $t = 5.1$ s. The q-profile is monotonic but flat with the magnetic shear being almost zero over a large region in the plasma core. The q-profile calculated by JETTO is in good agreement with the q-profile reconstructed by EFIT.

Table 3.1: The prediction uncertainties of the transport simulations.

JET Pulse Number	47843	49196	47170	46664	47413	46998
B_ϕ [T]	1.8	2.5	3.0	3.4	3.4	4.0
$P_{\rm in}$ [MW]	14	16	25	22	30	20
$W_{\rm dia}$ [MJ]	3	4	11	10	12	6
Experimental ITB onset time [s]	2.1	4.4	5.6	5.6	6.2	6.3
Simulated ITB onset time [s]	2.3	4.1	5.4	5.2	6.1	5.7
Exper. ITB width at onset [r/a]	0.42	0.28	0.50	0.44	0.53	0.32
Simul. ITB width at onset [r/a]	0.44	0.28	0.42	0.48	0.42	0.38
Experimental ITB location [r/a]	0.30	0.29	0.54	0.56	0.58	0.33
Simulated ITB location [r/a]	0.41	0.40	0.57	0.57	0.52	0.34
$\sigma_{\rm T_i}$ [%]	23	17	18	20	17	29
$\sigma_{\rm T_e}$ [%]	24	9	7	16	15	12
$\sigma_{\rm n_e}$ [%]	13	11	6	6	7	17
$\sigma_{\rm v_\phi}$ [%]	$--$	9	16	10	19	17

As is seen, the simulation clearly predicts the existence of the ITB. However, the temperatures, in particular the ion temperature, are overestimated by the transport model. This is mainly due to the ITB threshold condition that triggers the ITB by 0.4 s too early at $t = 5.2$ s for this discharge. This is illustrated by the second time slices at $t = 5.5$ s in Figure 3.1 (ITB does not yet exist in the experiment). The last two time slices describe the highest performance phase where the ITB also exists in the experiment. The model overestimates the location of the barrier by 5–7 cm at $t = 6.0$ s, but later before the disruption at $t = 6.3$ s, the experimental location of the ITB is in agreement with the prediction. The simulated and experimental density and toroidal velocity profiles are presented at the same instants as the temperatures in Figure 3.1(c) and (d).

A comprehensive predictive analysis (in Publication 1) includes several JET 'Advanced Tokamak Scenario' discharges from a wide plasma parameter range of $B_\phi = 1.8$–4.0 T, $P_{\rm in} = 14$–30 MW and $W_{\rm dia} = 3$–12 MJ. The transport model with the ITB threshold condition is identical for all the analysed discharges. The statistics shown in Table 3.1 indicates that the temperature profiles $T_{\rm i}$ and $T_{\rm e}$ generally match the experimental data with prediction errors of the order of 10–25 %, thus being roughly of the same order as the experimental measurement errors that are within 5–20 % in JET. The accuracy in $n_{\rm e}$ and v_ϕ profiles is even better, typically the time averaged prediction errors are in the range of 10–20 %. The pulse No. 46664 that was illustrated in Figure 3.1 turned out to have the poorest agreement with the experiment among the chosen discharges. There is also a trend that the model triggers the ITB too early (pulse No. 47843 is an exception) whereas no similar trend can be observed in the location of the ITB. Furthermore, the magnitude of the overall simulation error does not seem to depend on the magnetic field nor on any other global plasma parameter.

3.1.2 ITB Formation according to the Theory-Based Weiland Transport Model

In the ITB formation, the Weiland model takes into account the $\omega_{\mathrm{E\times B}}$ shearing rate, the magnetic shear and the density gradient stabilisation mechanisms. The following issues can be concluded when the Weiland model is applied to the same pulse as illustrated in Figure 3.1. Firstly, the Weiland model produces an ITB. The onset time of the ITB is reproduced within 0.1 s accuracy, thus more accurately than the Bohm/GyroBohm model does. On the other hand, the location of the ITB is clearly better reproduced with the Bohm/GyroBohm model than with the Weiland model. The Weiland model overestimates the density and the electron temperature, in particular in the L-mode. The agreement in the location of the ITB and in the temperature profiles between the experimental and modelling results would be better if the density were taken from the experiment rather than modelled. However, this would reduce the self-consistency and make the transport model comparison more biased.

The next obvious question is that because the Weiland model produces an ITB, what is the dominating formation mechanism. The analysis of the effect of the $\omega_{\mathrm{E\times B}}$ shearing rate on the ITB formation and temperature profiles is done in Publication 2. Surprisingly, practically no difference between the case with the actual shearing rate, where the shearing rate is calculated from [85], and the case with zero shearing rate is found. However, both cases exhibit a clearly visible ITB. Therefore, the importance of the $\omega_{\mathrm{E\times B}}$ shearing rate in the ITB formation seems to be questionable according to the Weiland model and thus, there must be something else that governs the ITB dynamics in the model.

The next study concerns the effect of the density gradient on the ITB formation. Two predictive simulations are compared, one with the actual NBI power and particle source and another one with the same NBI power but with no particle source. The results from the simulations are illustrated in Figure 3.2.

The threshold of the critical ion temperature gradient length $L_{\mathrm{T_i}}^{\mathrm{crit}}$ to turn on the ITG turbulence depends on the density gradient. Then, even with a moderate density gradient, equation (2.1) is not valid but depends on the density gradient. Therefore, having a larger density gradient allows one to have also a larger temperature gradient while simultaneously preventing the ITG micro-turbulence from becoming unstable. Consequently, a large density gradient can act as an ITB formation mechanism provided that the drive due to the TEM is small enough. Interestingly, the good confinement in the so-called Pellet Enhanced Performance (PEP) mode observed in JET 10 years ago was also explained to be due to the favourable effects provided by the large density gradient [107].

The following conclusions from Figure 3.2 can be drawn: because the density gradient is much larger with the NBI particle source (solid curves), the critical temperature gradient length $L_{T_{\mathrm{i}}}^{\mathrm{crit}}$ of having the ITG unstable is smaller. Therefore, the ITG turbulence is suppressed and as a consequence, an ITB can form. This will

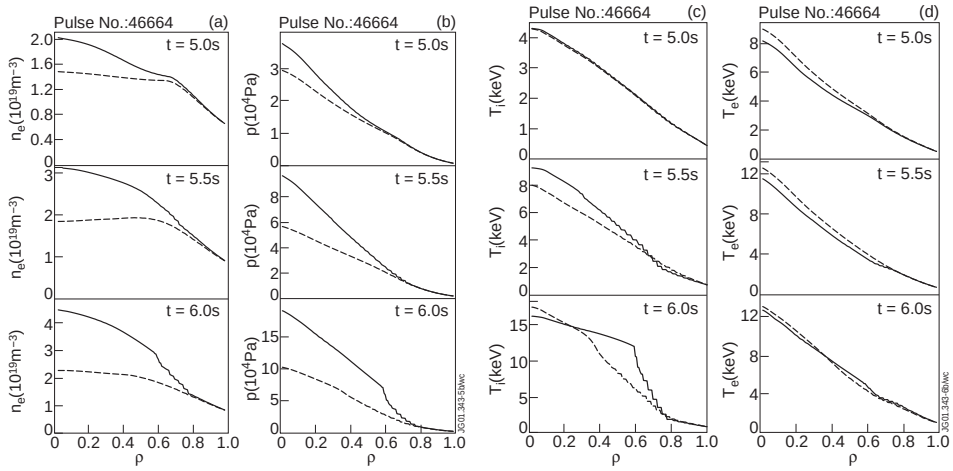

Figure 3.2: Electron density (a), pressure (b), ion temperature (c) and electron temperature (d) profiles at $t = 5.0$ s (L-mode), $t = 5.5$ s (H-mode) and $t = 6.0$ s (H-mode + ITB). The solid curve corresponds to the modelling with the NBI particle source and the dashed one without it.

then lead inevitably to significantly better confinement and larger pressure (shown in Figure 3.2(b)). As can be seen in Figure 3.2(c), the ITB clearly exists with the NBI particle source (solid curve) and is missing without the NBI particle source (dashed curve). Consequently, according to the Weiland model, the importance of the density gradient seems to dominate the effect of the $\omega_{\mathrm{E}\times\mathrm{B}}$ shearing rate in governing the dynamics of the ITB. This is quite contrary to what was found in Secs. 3.1.1 and Publication 1, i.e. where the ITB formation threshold condition was found to depend strongly on $\omega_{\mathrm{E}\times\mathrm{B}}$ and s.

3.1.3 Comparison of ITB Dynamics Calculated by Other Transport Models

The Multi-Mode Model (MMM) is a combination of theory-based transport models used to predict the temperature and density profiles in tokamaks [105]. MMM consists of the Weiland model [28, 29, 30, 31, 43] for the ITG and TEM modes, the Guzdar-Drake model for drift resistive ballooning modes [52] as well as smaller contributions from the kinetic ballooning modes and neo-classical transport. It has been found that the MMM transport model predicts temperature and density profiles that match the experimental data more closely (within 15% accuracy) than any other theory-based model currently available [105]. The formation of the ITB is interpreted as a combination of the $\omega_{\mathrm{E}\times\mathrm{B}}$ flow shear and magnetic shear mechanisms [108]. In order to match the location and timing of the ITB onset, a factor of 3–5 is required to multiply the calculated $\omega_{\mathrm{E}\times\mathrm{B}}$ flow shear for JET plasmas

whereas for DIII-D, no such a factor is needed. This large variation in the fitting factor between different tokamaks is an indication of significant uncertainties in the ITB formation mechanism in the model.

The Gyro-Landau-Fluid (GLF) transport model is developed from 3D gyro-kinetic stability calculations for the linear growth rates of the instabilities and from 3D gyro-Landau fluid simulations to determine the saturation levels [109]. It yields quasi-linear estimates of diffusivities of the particle, heat and momentum transport and includes turbulence suppression mechanisms of $\omega_{\mathrm{E}\times\mathrm{B}}$ flow shear, Shafranov shift and magnetic shear. The model can be characterised as a stiff model and, as a distinguishing feature the model includes the physics of the ETG mode. The ITB formation in the GLF model occurs normally in two stages; when the $\omega_{\mathrm{E}\times\mathrm{B}}$ flow shear approaches the maximum linear growth rate of the turbulence, the profiles begin to dither between the phase with an ITB and without it [110]. Finally, the $\omega_{\mathrm{E}\times\mathrm{B}}$ flow shear exceeds the growth rate and a clear ITB can be observed. According to the model, the $\omega_{\mathrm{E}\times\mathrm{B}}$ flow shear is the key mechanism in the ITB formation. In order to have an agreement with experiments, a multiplier 1.1 for the $\omega_{\mathrm{E}\times\mathrm{B}}$ flow shearing rate in DIII-D plasmas is needed while the same multiplier has to be 2.65 for JET plasmas. The model is able to predict the steady-state temperatures and densities within 20% accuracy.

The theory-based Current-Diffusive Ballooning Mode (CDBM) transport model is based on self-sustained turbulence of current-diffusive ballooning modes [111]. The $\omega_{\mathrm{E}\times\mathrm{B}}$ flow shear, magnetic shear and Shafranov shift are taken into account in the ITB formation. The $\omega_{\mathrm{E}\times\mathrm{B}}$ shearing rate seems to be the dominating mechanism. The CDBM also includes a model for the collapse of the ITB; if the critical pressure gradient limit is exceeded, the electron viscosity is selectively enhanced, and this results in enhanced turbulence and transport and finally, in the collapse of the ITB. Good agreement with ITB experiments on JT-60U has been achieved with CDBM, but in order to reproduce the long sustainment of the ITB, however, further improvement of the transport model is necessarily required [112].

There are also various other theory-based transport models capable of predicting the dynamics of the ITBs. One of them exhibits an oscillatory or bursty behaviour close to the ITB transition [113]. The diffusion coefficients are proportional to the density fluctuation level whose evolution is modelled separately. There is also a model, called Transport Barrier Dynamics (TBD) model, that is based on bifurcations due to the sharp radial gradients and the fast time dynamics occurring in the radial transport [114]. Another bifurcation model for the ITB formation that is based on the local fluctuation intensity of the density explains the onset of the ITB as the synergism between the $\omega_{\mathrm{E}\times\mathrm{B}}$ shearing rate and the magnetic shear [79]. The model is able to predict the favourable dependence on the temperature ratio ($T_{\mathrm{i}}/T_{\mathrm{e}}$) and on the density profile peakedness as well as the unfavourable scaling with the density. There are also semi-empirical transport models that have been used to predict the ITB evolution. The q-comb model explains the electron diffusivity as a direct function of the safety factor q [101]. Low values of χ_{e} exist at low order rational surfaces of the q-profile and on the contrary, high values of χ_{e} between them. Consequently, ITBs are formed at low order rational surfaces of

the q-profile. The model works well in RTP tokamak and it is also in good agreement with many JET ITB pulses [115]. However, the q-comb model is not able to explain the ion thermal transport or ion ITBs. Simulations of ASDEX Upgrade plasmas with ITBs have shown that the Weiland model is capable of reproducing sufficiently well the experimental results [116]. The other transport models tested on ASDEX-U, i.e. IFS/PPPL [117], CDBM and Bohm/GyroBohm transport models, tend to underestimate the central values of both T_i and T_e and often also fail to form the ITB.

To conclude this section, the accuracy of the present Bohm/GyroBohm transport model with the empirical ITB model in predicting JET 'Advanced Tokamak Scenario' discharges is at least as good as that of the other models. The extensive use of the found empirical ITB formation threshold condition during the course of this thesis gives confidence in the belief that the $\omega_{\mathrm{E}\times\mathrm{B}}$ shearing rate and the magnetic shear play the major role in governing the ITB dynamics. However, the results from the Weiland model concerning the ITB formation in JET are rather contradicting. The Weiland model is also the basis for the MMM model and in order to reproduce ITBs in JET with MMM, an additional multiplier of 3–5 for the $\omega_{\mathrm{E}\times\mathrm{B}}$ shearing rate is needed. This observation is in agreement with present results from the Weiland model, stating that the $\omega_{\mathrm{E}\times\mathrm{B}}$ shearing rate, at least without any additional multiplier like in MMM, is not enough to form an ITB in JET. One conclusion could be that the importance of the $\omega_{\mathrm{E}\times\mathrm{B}}$ flow shear has been overestimated by many transport models. Another conclusion could be that the fluid theory used in deriving the Weiland model underestimates the importance of the $\omega_{\mathrm{E}\times\mathrm{B}}$ shearing rate and possibly also the effect of a small or negative magnetic shear. However, since the MMM model can produce ITBs in TFTR and DIII-D without an additional multiplier, one could also conclude that the importance of the $\omega_{\mathrm{E}\times\mathrm{B}}$ shearing rate in governing the ITB dynamics in JET is less important than found in TFTR and DIII-D.

3.2 Simulations of the Current Profile Evolution

As it has been demonstrated in Secs. 2.3 and 3.1 as well as in Publication 1, the current density profile is a key issue in governing the formation and dynamics of the ITB. As a consequence, detailed modelling of the current or the q-profile evolution must be inherently integrated to the studies of the 'Advanced Tokamak Scenarios' and the physics of the ITBs. The behaviour of the current profile evolution can be divided into two separate phases; into the preheating or prelude phase, when the plasma current is ramped-up at low density, and into the main heating or high performance phase. In the preheating phase the current density profile can be tailored relatively easily to the desired one by means of Ohmic current ramp-up and external current drive as well as electron heating. In the main heating phase on the contrary, tailoring of the current density profile is difficult due to the large density inhibiting efficient external current drive and due to high T_e resulting in the long current diffusion time. Consequently, the current density profile, achieved

in the preheating phase, is rather tried to keep fixed than significantly modified in the high performance phase. This is very difficult since the current diffusion time although long, is not infinite, being typically of the orders of tens of seconds in JET. Thus, minimising the unwanted changes by means of the external current drive and proper alignment of the bootstrap current is the best one can do.

The current density profile evolution in the preheating phase with respect to different heating and current drive methods is studied in Section 3.2.1 (Publication 3). As a fascinating special case of this, a so-called core current hole obtained with LH heating and current drive together with a fast current ramp-up is analysed in Section 3.2.2 (Publication 4). The effect of the efficient current profile control in the main heating phase on plasma performance, fusion power and the physics of the ITB is presented in Section 3.2.3 (Publication 5).

3.2.1 Impact of Different Heating and Current Drive Methods on the Early q-profile Evolution

The current profile evolution during the preheating phase in JET has been studied in a systematic way with the JETTO transport code. The following preheating methods are considered and compared: Ohmic, LHCD, on-axis and off-axis ICRH, on-axis and off-axis NBI as well as ECCD. The basic principle used in this study is that the power deposition and external current density profiles are calculated in a self-consistent way (except ICRH). Consequently, the codes to calculate the power deposition profiles are coupled to JETTO to allow a self-consistent simulation cycle between the transport and power deposition (plus current density) calculation with time. The start time of the simulation is at $t = 1.0$ s. In the simulations, the main plasma parameters ($B_\phi = 3.4$ T, $I_\mathrm{p} = 0.7$ MA at $t = 1.0$ s and $I_\mathrm{p} = 2.3$ MA at $t = 5.0$ s) as well as the initial and boundary conditions for T_e are taken from JET 'Advanced Tokamak Scenario' discharge No. 51897. The initial q-profile is from EFIT. The external heating power is 5 MW except in the case of LHCD when the power is 3 MW. Thus, the simulations are identical except in terms of the heating and current drive methods.

The q-profiles at $t = 4.0$ s and $t = 5.0$ s produced by the different preheating methods are compared in Figure 3.3. On the basis of the modelling calculations, the preheating methods can be divided into three categories in terms of the created q-profile at the end of the preheating phase [118]. LHCD and ECCD form category 1 as being the only methods that can produce deeply reversed q-profiles. Quantitatively the q-profiles produced by LHCD and ECCD are quite similar. However, the central values of q are distinct. With LHCD, q tends to increase to very high values, such as $q_0 \approx 30$–50 whereas in the case of ECCD, q_0 remains between 10 and 20. This difference comes mainly from the amount of driven off-axis current; LHCD driven current is of the order of 500–900 kA whereas ECCD current is only 70–160 kA. The large off-axis current can transiently drive the total current density in the core to zero, as has been recently observed in JET. This is investigated in more detail in Section 3.2.2 and Publication 4. Category 2 consists of off-axis NBI

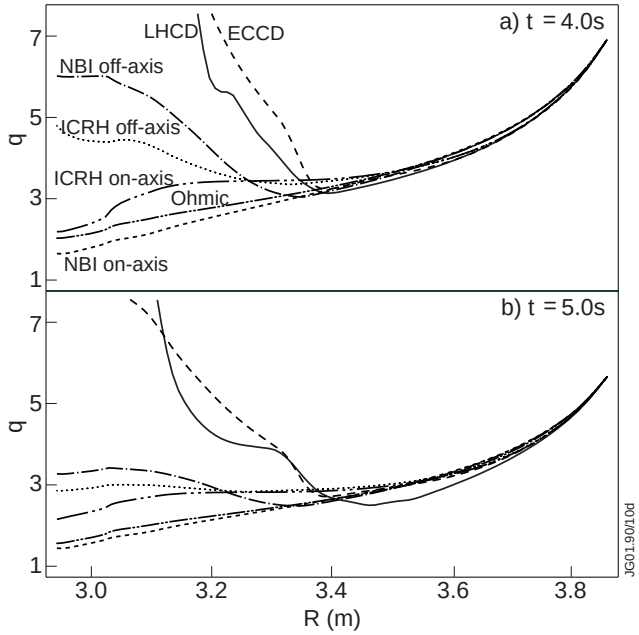

Figure 3.3: Simulated q-profiles produced with different preheating methods at $t = 4.0$ s (a) and $t = 5.0$ s (b). Category 1: LHCD (solid curve) and ECCD (dashed curve); category 2: off-axis NBI (dash-dotted curve) and off-axis ICRH (dotted curve); category 3: on-axis NBI (short dashed curve), on-axis ICRH (long double dot-dashed curve) and ohmic (short double dot-dashed curve).

and off-axis ICRH heating which create weakly reversed q-profiles with $q_{\min}$ located inside $R = 3.4$ m. On-axis NBI, on-axis ICRH and ohmic preheating belong to category 3 as they can only create monotonic q-profiles. Experimental results on LHCD, ICRH and Ohmic preheating on JET, presented in Publication 3 and Ref. [118], have verified the aforementioned predictive modelling results.

One of the main conclusions in this study is that the external current driven by LHCD and ECCD, not the decreased current diffusion by the direct electron heating, is the crucial factor in producing deeply reversed target q-profiles in the preheating phase. Also, the NBI driven current turned out to be very important in the off-axis NBI preheating scheme. Other important factors affecting the q-profile evolution in the preheating phase are the width of the power deposition profile and the start time of the preheating with respect to plasma initialisation. A narrow off-axis power deposition profile is able to slow down the ohmic current diffusing from the plasma periphery to the centre much more efficiently than a wide one. Moreover, the earlier the preheating is started, the more the current diffusion is slowed down. Since ICRF preheating has wider power deposition profiles than ECRH and it also has an additional slowing down time of the fast ions colliding with the electrons (≈ 0.5 s in JET) that is missing in the ECRH scheme, it is

understandable that ECRH preheating (even without any ECCD current) turned out to be a more efficient tool to modify the q-profile evolution in the preheating phase than ICRH.

How well the desired target q-profile can be sustained later in the main heating phase depends on the applied heating and current drive methods and the power levels. Bootstrap current and its alignment with the desired current density profile becomes an important issue. The current density evolution in the main heating phase has been analysed in Section 3.2.3 and Publication 5. It should be noted that the experimental results on the q-profile evolution in the preheating phase from other tokamaks may differ from the present results. These differences originate from the different machine sizes and heating systems with different power densities.

3.2.2 Core Current Hole with LHCD Preheating in JET

An observation of zero current density within measurement errors in the core ($r/a \leq 0.2$) of JET 'Advanced Tokamak Scenario' plasmas with LHCD preheating is reported in Publication 4. This is the first time ever in any tokamak when a so-called core current hole has been observed. Theoretically it has been predicted earlier that a region of zero or even negative $j(R)$ in the core can exist [119, 120]. According to the theory, the total magnetic flux, and therefore the total current, in the core of a highly conductive plasma cannot be rapidly modified due to the slow radial diffusion of the parallel electric field. It can be seen from the following expression, obtained by combining in a cylindrical geometry the radial derivative of the Faraday's law with the time derivative of the Ampère's law and then eliminating the axial electric field using the Ohm's law:

$$\frac{\partial j_{\mathrm{tot}}}{\partial t} = \mu_0^{-1} \left(\frac{\partial^2}{\partial r^2} + \frac{1}{r}\frac{\partial}{\partial r} \right) \eta_{||}(j_{\mathrm{tot}} - j_{\mathrm{ext}}). \tag{3.1}$$

Here, j_{tot} is the total parallel current density, j_{ext} is the externally driven (non-inductive) parallel current density, and $\eta_{||}$ is the parallel resistivity. Initially the external current drive is switched off ($j_{\mathrm{ext}} = 0$). When the external off-axis current drive turns on, regions of positive radial curvature ($\frac{\partial^2}{\partial r^2}\left[\eta_{||}(j_{\mathrm{tot}} - j_{\mathrm{ext}})\right]$) on either side of the peak in j_{ext} transiently decrease j_{tot}. With sufficient external current, this effect can locally drive the current density to zero or even negative. This situation can persist for many seconds in hot JET plasmas due to the long current diffusion time.

The experimentally observed core current hole can be seen in a simulation of the evolution of the current density performed with JETTO. Measured values of the densities, temperatures, Z_{eff}, plasma current and magnetic field are used. The simulation is started at $t = 1.0$ s and the initial q-profile is taken from the EFIT equilibrium.

Figure 3.4 shows the simulated current density profiles at two times, during the LHCD prelude at $t = 3.0$ s and immediately afterwards that at $t = 4.0$ s. The

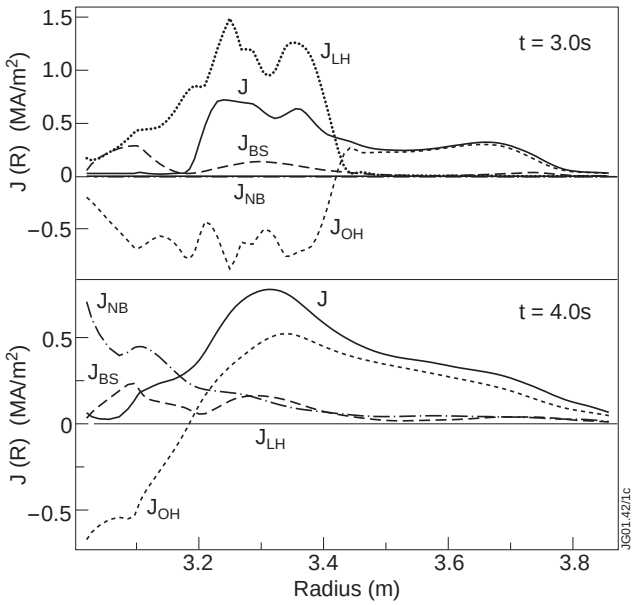

Figure 3.4: JETTO *simulation of $j(R)$ during the LHCD preheating phase ($J_{\rm NB} = 0$) at $t = 3.0$ s and immediately after ($J_{\rm LH} = 0$) at $t = 4.0$ s. The contributions to the total current due to LHCD ($J_{\rm LH}$), Ohmic current ($J_{\rm OH}$), bootstrap current ($J_{\rm BS}$) and beam-driven current ($J_{\rm NB}$) are shown. The region of the core current hole is clearly visible at $t = 3.0$ s.*

contributions to the total current due to LHCD, Ohmic current, bootstrap current, and beam-driven current are shown. The region of zero current density in the core region ($r/a \leq 0.2$) at $t = 3.0$ s created in response to the strong off-axis LHCD is illustrated in Figure 3.4. At $t = 4.0$ s the region of zero current begins to fill in after the LHCD turns off, leaving a small region of zero current density similar to that deduced from the Motional-Stark Effect (MSE) measurements. Shrinking of the region of zero current is significantly enhanced by the on-axis current driven by the neutral beams present at $t = 4.0$ s but not at $t = 3.0$ s. The modelling is qualitatively consistent with the MSE measurements.

The resistivity, LHCD power deposition and bootstrap current profile calculations are not valid in the regime where the toroidal current vanishes, while the profiles away from the zero current region will still be valid. In the JETTO simulations, this situation is avoided by enforcing $q < 60$. However, the fact that this condition of the zero current, i.e. $q \to \infty$, in the core is attained in the JETTO simulation is a confirmation of the mechanism suggested as responsible for the zero axis current. In addition, the use of the $q < 60$ is justified by the experimental measurements which indicate that the current in the core is not negative, but seems to be clamped at zero. This observation suggests that a separate physical mechanism acts to prevent a negative core current density to exist. It is possible that the sawtoothlike MHD

modes present during the LHCD prelude could redistribute the current from the periphery to the zero $j(R)$ region, thus preventing formation of a negative $j(R)$ region [121], but this has not yet been experimentally verified.

3.2.3 Improved Fusion Performance with Current Profile Control

The performance of the 'Advanced Tokamak Scenarios' is investigated and optimised with JETTO transport code modelling calculations, using LHCD for current profile control. As found in Publication 3, LHCD can create hollow current density profiles and a wide region of negative magnetic shear. Therefore, as the empirical studies in Publication 1 indicated, wider ITBs with a steep pressure gradient producing large amount of bootstrap current can be achieved. However, there is only a very limited number of high performance 'Advanced Tokamak Scenario' experiments with current profile control by LHCD performed on JET. The main reason for this is due to the problems in the coupling of the LHCD with the H-mode plasma edge. It is therefore crucial to investigate how LHCD, applied to high performance discharges, affects the sustainability of the ITB and plasma performance on JET.

The starting point for the modelling calculations of the high performance discharges is the pulse No. 40542. In the experiment, the high performance phase lasted from $t = 5.0$ s until $t = 7.5$ s, but the modelling calculation is extended by 5.5 s until $t = 13.0$ s. The reason for choosing this pulse is that it has suitable steady-state like features and benign properties against MHD instabilities. The initial and boundary conditions for T_i, T_e, n_e and plasma current are taken from the experiment. The plasma current is as for the actual discharge No. 40542 until $t = 7.5$ s after which it is ramped-up up to 3.9 MA at the same speed. The magnetic field is taken from the experiment ($B = 3.4$ T) as well as Z_eff. The heating power and the deposition profiles of NBI and ICRH are kept fixed since the last experimental power deposition profiles calculated by TRANSP [122]. The LH power deposition profiles, which are the key issue in the modelling calculations, are calculated self-consistently by JETTO/FRTC. This new coupled code combination is validated in Publication 5. The transport model is the same as shown in Eqs. (2.14)–(2.20) with the exception of some differences in the argument of the step function in the ITB formation condition (see Publication 5).

The time evolution of the fusion power is shown in Figure 3.5 (a) (upper half). As can be seen, fusion power in the range 20–30 MW is predicted for $I_\mathrm{p} = 3.9$ MA, $B_\mathrm{t} = 3.4$ T discharges. There are three types of uncertainties in the modelling; uncertainties coming from the experimental data, like the initial q-profile and the boundary values for T_i and T_e, uncertainties coming from the LHCD module, such as the amount of LH driven current and those ones coming from the transport model, like the empirical fitting parameter used in the ITB formation threshold condition. The shaded area illustrates the modelling uncertainties; the upper curve is a prediction with the present transport model using the experimental data as it is

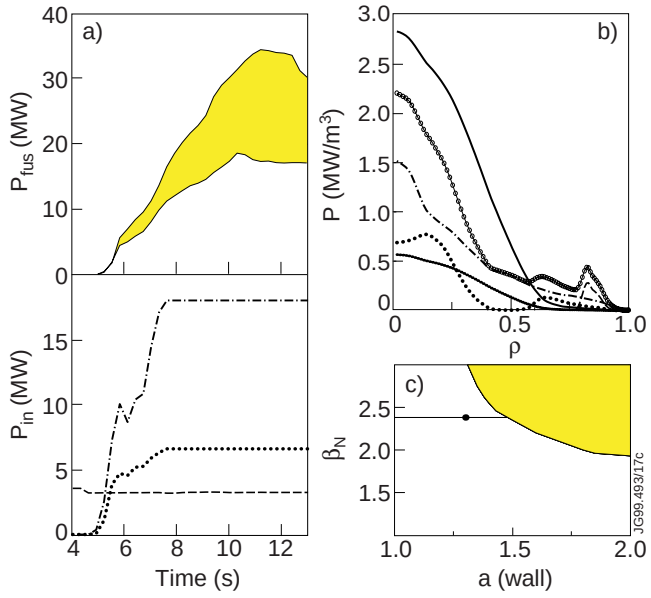

Figure 3.5: (a) Time evolution of the fusion power with modelling uncertainties predicted by JETTO/FRTC *and the input heating powers (NB=dash-dotted, RF=dotted, LH=dashed). (b) The radial profiles of the input heating powers (NB=dash-dotted, RF=dotted, LH=dashed, NB+RF+LH=solid curve with circles) and produced fusion (solid curve) and alpha heating powers (densely dotted) at $t = 13.0$ s. (c) MHD stability analysis of the scenario with the largest fusion power at $t = 13.0$ s. The shaded area is unstable against the $n = 1$ kink instability as being the limiting factor.*

while the lower curve represents a conservative prediction assuming lower recycling coefficient for the neutrals penetrating back to the plasma at the edge and lower edge temperatures. The case with the larger fusion power is stable against MHD instabilities with a beta value $\beta_N \approx 2.4$, as illustrated in Figure 3.5(c). The most limiting MHD instability is the pressure driven global $n = 1$ kink instability which is a typical limiting factor for the high performance 'Advanced Tokamak Scenario' discharges on JET [123]. Worth mentioning is that the MHD stability analysis does not consider neo-classical tearing modes nor $q = 2$ snakes which often limit the high performance in JET. Therefore, the fusion power may be overestimated. The input heating powers of $P_{NB} = 18$ MW, $P_{RF} = 6.5$ MW (composed of 2/3 on-axis and 1/3 off-axis deposition) and $P_{LH} = 3.5$ MW are illustrated in Figure 3.5(a) (bottom) and the power deposition profiles in (b), respectively.

The quasi-stationary regimes for electron and ion temperatures as well as for densities, pressure and the location of the ITB are reached at $t \approx 10$ s. The current diffusion time is around 40–50 s. The magnetic shear is negative inside about 60–70 % of the plasma radius. The safety factor at the edge (q_{95}) is between 3 and 4

and settles during the steady state phase down to 3.1. Worth noticing is also the large contribution (≈ 50 %) from the bootstrap current which is produced in the large pressure gradient region, i.e. in the same region where the footpoint of the ITB is located, thus giving rise to larger current and smaller magnetic shear in that region. An interesting question remains whether this scenario could be extended to true steady-state, i.e. being independent of the current diffusion time. It would require enough off-axis current produced by the bootstrap current together with LHCD to compensate the slow current diffusion.

The same two simulations as shown in Figure 3.5 are also performed without LHCD. In each run, the ITB is formed slightly later and its width stays about 10 cm narrower until $t = 7.0$ s than in the simulation with LHCD. After $t = 7.0$ s the ITB starts to shrink and finally at $t \approx 8$ s, the width of the ITB settles down to $\rho \approx 0.4$. The fusion power is only about 50–60 % of the fusion power with LHCD and the average ion temperature about 80 %. The reason for the degraded fusion performance and confinement is that the q-profile remains monotonic (positive magnetic shear) throughout the discharge, thus inhibiting the ITB to lie on a larger radius [124].

Different current ramp-up schemes are also analysed for 'Advanced Tokamak Scenario' plasmas with JETTO. In the core region the current density profiles are not affected, but at $\rho > 0.4$ they are strongly modified. ITBs are wider with a larger current and with a faster current ramp-up speed. In conclusion, shrinking of the ITBs seems to be caused by higher edge shear, i.e. higher q_{a} (smaller I_{p}). Consequently, the best fusion performance for the 'Advanced Tokamak Scenario' plasmas is expected to be obtained with the highest current and the fastest stable current ramp-up speed.

Chapter 4

Summary and Conclusions

This thesis is about transport modelling of 'Advanced Tokamak Scenarios' in the Joint European Torus (JET). Answers to and explanations for the following questions have been sought: what are the mechanisms that govern the formation and dynamics of the ITBs in JET and how can the current density profile be modified and further, how does the current density profile affect ITBs and plasma performance? In order to reliably predict the performance perspectives in future 'Advanced Tokamak Scenarios' in JET and ITER, it is crucial to know and understand the answers to the aforementioned questions.

On the basis of the results from the transport analyses carried out during the course of this thesis, two possible scenarios for the ITB formation and for the time evolution of the ITB in JET can be illustrated. The first one (scenario 1) is based on the empirical studies of the $\omega_{\mathrm{E}\times\mathrm{B}}$ flow shear and magnetic shear, together with predictive modelling with the Bohm/GyroBohm transport model, whereas the second scenario (scenario 2) is based on the results from the Weiland fluid theory. In scenario 1, the onset of the ITB occurs provided that the threshold condition $s \leq 1.47\omega_{\mathrm{E}\times\mathrm{B}}/\gamma_{\mathrm{ITG}} + 0.14$ given in Eq. (2.8) is fulfilled. Triggering of the ITB is probably initiated around a magnetic island at an integer q surface when the condition in Eq. (2.8) is approached, and the $\omega_{\mathrm{E}\times\mathrm{B}}$ shearing rate is locally enhanced because of the island. In the ITB formation, according to the found empirical ITB threshold condition, the following interaction between the $\omega_{\mathrm{E}\times\mathrm{B}}$ shearing rate and s could occur: the $\omega_{\mathrm{E}\times\mathrm{B}}$ flow shear must be large enough to tear apart the turbulent eddies, thus decreasing the growth rate of the long wave length ITG turbulence (γ_{ITG}). At the same time the small (or negative) magnetic shear s helps to disconnect the turbulent vortices (e.g. ballooning modes) initially linked together by toroidicity and enables the plasma to enter the second stable ballooning stability region. The found empirical threshold condition for the ITB formation provides the first clear indication of the strong correlation between s and $\omega_{\mathrm{E}\times\mathrm{B}}$ at the ITB transition in JET. The modelling results from the extensive predictive transport analyses with the found empirical ITB threshold condition in Eq. (2.8)

support the strong interplay between $\omega_{\mathrm{E}\times\mathrm{B}}$ and s in governing the dynamics of the ITB in JET.

The ITB formation scenario 2 is based mainly on the density gradient stabilisation. The threshold of the critical ion temperature gradient length $L_{\mathrm{T_i}}^{\mathrm{crit}}$ to have the ITG turbulence unstable depends on the density gradient. Therefore, having a larger density gradient allows one also to have a larger temperature gradient while preventing the ITG micro-turbulence from becoming unstable at the same time. Consequently, a large density gradient can act as an ITB formation mechanism. Again, the onset of the ITB may be initiated at an integer q surface around which the density gradient locally increases. Furthermore, a small or negative magnetic shear facilitates the ITB formation, probably in a similar way as in the ITB formation scenario 1. In addition, after having formed an ITB, the significantly enhanced $\omega_{\mathrm{E}\times\mathrm{B}}$ flow shear may help to stabilise TEM which may be otherwise destabilised by the density gradient. The modelling results from the predictive transport simulations with the Weiland model emphasise strongly the importance of the density gradient over the $\omega_{\mathrm{E}\times\mathrm{B}}$ shearing rate in governing the dynamics of the ITB. In addition, the good confinement in the so-called Pellet Enhanced Performance (PEP) mode observed in JET 10 years ago was also explained to be due to the favourable effects provided by the large density gradient [107].

There are two major problems in analysing the ITB formation mechanisms — the interplay and the coupling of the different mechanisms with each other. Due to the interplay, it may be difficult to identify which mechanism is the dominant one, as in the case when one employs the empirical ITB threshold condition in Eq. (2.8). The coupling problem can be seen when one increases for example n_{e} by NBI fuelling or pellets, both the density gradient and the Shafranov shift increase and in addition, the $\omega_{\mathrm{E}\times\mathrm{B}}$ shearing rate may increase or decrease. Therefore, due to the coupling of the different ITB formation mechanisms, diagnosing the principal mechanism is tricky. Consequently, the causality, i.e. the classical "which was first, hen or egg" problem, is difficult to resolve. In the ITB formation scenario 1, the $\omega_{\mathrm{E}\times\mathrm{B}}$ shearing rate seems to be the cause of the ITB, together with s whereas in scenario 2, the density gradient seems to be the cause while the $\omega_{\mathrm{E}\times\mathrm{B}}$ shearing rate is rather the effect of the ITB than the cause.

At first glance, it is quite astonishing that the two aforementioned scenarios 1 and 2, which are based on completely different physics mechanisms, seem both to be able to explain the ITB formation and time evolution in JET. One of the most plausible reasons for this coincidence is that in JET, the NBI is the main source for both the $\omega_{\mathrm{E}\times\mathrm{B}}$ flow shear through the toroidal momentum injection and for the increase of the density gradient through the core particle fuelling. As a consequence, when one increases the NBI power, one increases the toroidal momentum and particle fuelling simultaneously. Due to the relatively inflexible NBI system in JET, keeping the same NBI power and thus the same fuelling, the amount of the toroidal momentum is difficult to change [125]. By replacing a part of the NBI power with the ICRH power, one encounters the same problem; both the fuelling and the toroidal momentum injection are decreased in a similar way. One way to resolve the problem would be to increase the density gradient in the

core with pellets as in the PEP mode [107] and see whether an ITB appears in this 'Advanced Tokamak Scenario'. Launching a significant amount of pellets in the core, the density gradient should rise while the $\omega_{\mathrm{E}\times\mathrm{B}}$ flow shear should not change significantly, only the pressure gradient term in Eq. (2.6) may change a little, but it should not affect the $\omega_{\mathrm{E}\times\mathrm{B}}$ shearing rate very much.

One common thing that is not controversial among the ITB formation mechanisms is that the small or negative magnetic shear facilitates the ITB formation. Still, it is not clear in which way the magnetic shear affects the ITB formation. The ITB formation scenario 1 would suggest that zero or negative s is enough to form an ITB. However, the effect of the magnetic shear could also be only that the smaller is the magnetic shear, the smaller $\omega_{\mathrm{E}\times\mathrm{B}}$ shearing rate or the smaller density gradient is needed to stabilise micro-turbulence and to form an ITB. In addition, it is still not clear whether the value $s = 0$ has a special role in the ITB physics or whether the condition reads rather like $s \lessapprox 0$.

The second main topic in this thesis considered the modelling of the current density profile and its impacts on the ITB formation and plasma performance. On the basis of the transport simulations in the preheating phase, the heating and current drive methods could be divided into three categories in terms of the produced q-profiles. LHCD and ECCD formed category 1 since they were the only methods which created deeply reversed q-profiles in JET. Accordingly, in order to have the maximum flexibility for creating the desired q-profile in the preheating phase, either the LHCD or the ECCD system is to be installed in future tokamaks. Category 2 consisted of off-axis NBI and off-axis ICRH preheating which produced weakly reversed q-profiles with q_{min} located inside $R = 3.4$ m. On-axis NBI and on-axis ICRH and ohmic preheating belonged to category 3 as they created only monotonic q-profiles. Experimental results on LHCD, ICRH and Ohmic preheating on JET verified the predictive modelling results (Publication 3).

It has been argued for a long time, for example in the case of LHCD, whether it is the effect of the direct electron heating that decelerates the ohmic current diffusion or whether it is the external off-axis current driven by LHCD which is the main contributor in modifying the current density profile in JET. In this thesis, the external current driven by LHCD, ECCD or NBI was found to be the most crucial factor in giving the best flexibility to modify q-profiles in the preheating phase. Other important factors affecting the q-profile evolution in the preheating phase were found to be the width of the power deposition profile and the start time of the preheating with respect to plasma initialisation. A narrow off-axis power deposition profile was able to slow down the ohmic current diffusing from the plasma periphery to the centre much more efficiently than a wide one. Moreover, the earlier was the preheating started, the more was the ohmic current diffusion slowed down.

As a fascinating special case of LHCD preheating, the so-called core current hole was introduced in this thesis. The existence of the core current hole can be explained by combining the Faraday's, Ampere's and Ohm's laws. Then, a sufficient amount of off-axis current can locally and transiently drive the current density to zero in the core. In JET, this situation can persist for many seconds due to the

long current diffusion time. Predictive JETTO simulations confirmed the presented physical picture as the condition $q \to \infty$ ($j \to 0$) in the core was attained in the JETTO calculations. Even if it seems possible and even probable that a plasma with the core current hole is not an optimum way to operate the 'Advanced Tokamak Scenario', it may be very enlightening from physics' point of view. This new plasma regime with a region of the core current hole found in Publication 4 poses several new challenges and requirements on transport modelling. The new regime also suggests interesting experiments with promising perspectives of finding new physics. Firstly, it enforces the neo-classical theory used in transport models to be modified since the present neo-classical transport theory is not valid when B_θ is close to zero. Secondly, it will allow studies on the dependence of the $\omega_{\mathrm{E}\times\mathrm{B}}$ on B_θ and a possible further impact on the ITB formation because B_θ is almost zero in the region of the current hole and outside the region has a large gradient. Thirdly, the calculation of the equilibrium must be updated. For example EFIT and ESCO reconstruct the equilibrium as a function of the poloidal magnetic flux whose definition will not be single-valued with the core current hole. Therefore, the equilibrium reconstruction does not converge towards an unique equilibrium and the flux surfaces remain undefined.

It is not yet known exactly what the optimal q-profile in the 'Advanced Tokamak Scenarios' will be. One of the most important criteria is that it should facilitate the formation of the optimal ITB profile, which was sketched in Figure 2.3, and prevent the non-optimal ITB profile from arising. As a consequence, the optimal q-profile should assist the ITB to form as wide as possible in r/a (broad T_i, T_e and n_e profiles) and with moderate gradients. The optimal q-profile should also provide the largest sustainable improvement in the fusion performance and a good confinement while at the same time it should be MHD stable against large-scale MHD instabilities.

Obviously in the optimal 'Advanced Tokamak Scenario', the optimal ITB profile should be somehow combined with the optimal q-profile. However, achieving the optimal 'Advanced Tokamak Scenario' is not trivial for at least two basic reasons; firstly, it is not yet known precisely what the optimal ITB and q-profiles are and secondly, reaching experimentally the optimal ITB and q-profiles is a difficult task. As found in Publication 5, application of LHCD during the high performance phase helps in achieving the optimal ITB and q-profiles. With LHCD, s is smaller and an ITB can more easily expand. A larger ITB radius leads then to a larger fraction of the bootstrap current, which further decreases the magnetic shear. At the same time the plasma performance is enhanced. In addition, a larger ITB radius is more benign against MHD instabilities. Although LHCD and NB current drive may be of importance in optimising the q-profile, the importance of the bootstrap current and its alignment with the optimal q-profile is probably even greater, in particular in future large tokamaks like in ITER.

A large ITB radius implies also a moderate or steep density gradient at a large radius. In the light of the modelling results in Publication 2, obtaining moderate or steep density gradients may be crucial if it can stabilise the ITG since the ITG is the worst possible branch of turbulence in terms of the amount of transport it

drives. Having stabilised the ITG and possibly the ETG with the density gradient, it may be then easier to stabilise the TEM, which is not stabilised by the density gradient, through the $\omega_{\mathrm{E}\times\mathrm{B}}$ flow shear, the Shafranov shift or the negative magnetic shear.

In the integrated modelling of the ITB dynamics and current density profile in the 'Advanced Tokamak Scenarios', it should be noted, however, that certain important aspects have not been considered in this thesis. Firstly, as it has been indicated in Publication 2, a moderate or steep density gradient may stabilise micro-turbulence, like the ITG and enable the optimal ITB profile to be born. However, according to neo-classical theory, the impurity accumulation in the core due to the density gradient is a very serious problem. The impurity accumulation in the 'Advanced Tokamak Scenarios' with a moderate and steep density gradient has been also verified in the experiments in JET [126]. This may limit significantly the range of the feasible density gradients in the 'Advanced Tokamak Scenarios'. Secondly, as it has been demonstrated in Publications 3 and 4, LHCD is a very useful tool in modifying the current density profile. However, there are serious problems in the coupling of the LH waves from the grill to the plasma in the H-mode discharges with ELMs. Thus, the LH power and current may be overestimated in the modelling calculations. Thirdly, large scale MHD events, such as NTMs and ELMs, are not taken into account in the modelling. These may change the behaviour of the ITBs and limit significantly the feasible pressure, temperature, density and current density profiles in the 'Advanced Tokamak Scenarios'.

Bibliography

[1] Ongena J. and van Oost G., "Energy for Future Centuries", Transactions of Fusion Technology **37** (2000) 3.

[2] Kadomtsev B.B., *Tokamak plasma, a complex physical system*, Institute of Physics Publishing, Bristol, 1992.

[3] Wesson J., *Tokamaks*, Oxford Science Publications, Oxford, 1997.

[4] Golowin I.N. and Schafranov W.D., *Die Anfänge der Kontrollierten Kernfusion (in Andrej D. Sacharow, Leben und Werk einers Physikers)*, Spektrum Akad. Verlag, Heidelberg, 1991, p. 45.

[5] Tamm I.E. and Sakharov A.D., *Plasma Physics and the Problem of Controlled Thermonuclear Reactions*, edited by M.A. Leontovich, Pergamon Press, London, 1961, Vol. 1.

[6] Artsimovich L.A. et al., "Experiments in tokamak devices", Plasma Physics and Controlled Nuclear Fusion Research (Proc. Int. Conf., Novosibirsk, 1968), IAEA, Vienna, **1** (1969) 157.

[7] Wagner F. et al., "Regime of improved confinement and high beta in neutral-beam heated divertor discharges of the ASDEX tokamak", Phys. Rev. Lett. **49** (1982) 1408.

[8] Keilhacker M. et al., "High fusion performance from deuterium-tritium plasmas in JET", Nucl. Fusion **39** (1999) 209.

[9] de Baar M.R., *Electron Transport Barriers in Tokamak Plasmas*, PhD Thesis, FOM Institute, The Netherlands, (1999).

[10] Fisch N.J., "Theory of current drive in plasmas", Reviews of Modern Physics **59** (1987) 175.

[11] Cairns R.A., *Radiofrequency Heating of Plasmas*, Institute of Physics Publishing, Bristol, 1991.

[12] Hinton F.L. and Hazeltine R.D., "Theory of plasma transport in toroidal confinement systems", Rev. Mod. Phys. **48** (1976) 239.

[13] Hirshman S.P. and Sigmar P.D., "Neoclassical transport of impurities in tokamak plasmas", Nucl. Fusion **21** (1981) 1079.

[14] Taguchi M., "A method for calculating neoclassical transport coefficients with momentum conserving collision operator", Phys. Fluids B **4** (1992) 3638.

[15] Koide Y. et al., "Internal Transport Barrier on $q = 3$ Surface and Poloidal Plasma Spin Up in JT-60U High-β_p Discharges", Phys. Rev. Lett **72** (1994) 3662.

[16] Levinton F.M. et al., "Improved Confinement with Reversed Magnetic Shear in TFTR", Phys. Rev. Lett. **75** (1995) 4417.

[17] Strait E.J. et al., "Enhanced Confinement and Stability in DIII-D Discharges with Reversed Magnetic Shear", Phys. Rev. Lett. **75** (1995) 4421.

[18] The JET Team (presented by C. Gormezano), "Optimisation of JET Plasmas with Current Profile Control", Proc. 16th Int. Fusion Energy Conf. Montreal, Canada, 7–11 October 1996, **1** IAEA, Vienna (1997) 487.

[19] Söldner F.X. et al., "Shear optimization experiments with current profile control on JET", Plasma Phys. Control. Fusion **39** (1997) B353.

[20] Parail V.V. et al., "Predictive Modelling of JET Optimised Shear Discharges", Nucl. Fusion **39** (1999) 1743.

[21] Baranov Yu.F. et al.,"Current profile, MHD activity and transport properties of optimised shear plasmas in JET", Nucl. Fusion **39** (1999) 1463.

[22] Shirai H. et al., "Recent experimental and analytic progress in the Japan Atomic Energy Research Institute Tokamak-60 Upgrade with W-shaped divertor configuration", Phys. Plasmas **5** (1998) 1712.

[23] Greenfield C.M. et al., "Behaviour of electron and ion transport in discharges with internal transport barrier in the DIII-D tokamak", Nucl. Fusion **39** (1999) 1723.

[24] Gruber O. et al., "Stationary H-Mode Discharges with Internal Transport Barrier on ASDEX Upgrade", Phys. Rev. Lett. **83** (1999) 1787.

[25] Erba M. et al., "Validation of a New Mixed Bohm/gyro-Bohm Transport Model on Discharges of the ITER Data-Base", JET Report JET-R(96)07 (1996).

[26] Erba M. et al., "Development of a non-local model for tokamak heat transport in L-mode, H-mode and transient regimes", Plasma Phys. Control. Fusion **39** (1997) 261.

[27] Genacchi G. and Taroni A., "JETTO: A free boundary plasma transport code (basic version)", Rapporto ENEA RT/TIB 1988(5).

[28] Jarmen A., Andersson P. and Weiland J., "Fully toroidal ion temperature gradient driven drift modes", Nucl. Fusion **27** (1987) 941.

[29] Nordman H., Weiland J. and Jarmen A., "Simulation of toroidal drift mode turbulence driven by temperature gradients and electron trapping", Nucl. Fusion **30** (1990) 983.

[30] Weiland J. and Hirose A., "Electromagnetic and kinetic effects on the ion temperature gradient mode", Nucl. Fusion **32** (1992) 151.

[31] Strand P., Nordman H., Weiland J. and Christiansen J., "Predictive transport simulations of JET L and H mode gyro-radius scaling experiments", Nucl. Fusion **38** (1998) 545.

[32] Esterkin A.R. and Piliya A.D., "Fast ray tracing code for LHCD simulations", Nucl. Fusion **36** (1996) 1501.

[33] Nowak S., Lazzaro E. and Ramponi G., "Self-diffraction effect of electron cyclotron Gaussian beams on noninductively driven current in the International Thermonuclear Experimental Reactor tokamak", Phys. Plasmas **3** (1996) 4140.

[34] Challis C.D. et al., "Non-inductively driven currents in JET", Nucl. Fusion **29** (1989) 563.

[35] ITER Physics Basis Editors, et al., "Plasma confinement and transport", Nucl. Fusion **39** (1999) 2175.

[36] JET TEAM (presented by D. Stork), "The new experimental phase of JET and prospects for future operation", in Plasma Physics and Controlled Nuclear Fusion Research 1994 (Proc. 15th Int. Conf. Seville, 1994), **1**, IAEA, Vienna (1995) 51.

[37] Wade M. et al., "Helium Exhaust Studies in H-Mode Discharges in the DIII-D Tokamak Using an Argon-Frosted Divertor Cryopump", Phys. Rev. Lett. **74** (1995) 2702.

[38] Koide Y. et al., "Study of internal transport barriers by comparison of reversed shear and high-$\beta_{\rm p}$ discharges in JT-60U", Plasma Phys. Control. Fusion **40** (1998) 641.

[39] Lazarus E.A. et al., "Higher Fusion Power Gain with Current and Pressure Profile Control in Strongly Shaped DIII-D Tokamak Plasmas ", Phys. Rev. Lett. **77** (1996) 2714.

[40] Ishida S. and JT-60U Team, "JT-60U high performance regimes", Nucl Fusion **39** (1999) 1211.

[41] Parail V.V., "Energy and particle transport in plasmas with transport barriers", to be published in Plasma Phys. Control. Fusion (2002).

[42] Horton W., Hong B.-G. and Tang W.M., "Toroidal electron temperature gradient driven drift modes", Phys. Fluids, **31** (1988) 2971.

[43] Weiland J., *Collective Modes in Inhomogenous Plasma*, Institute of Physics Publishing, Bristol, 2000.

[44] Garbet X. et al. "Turbulence in fusion plasmas: key issues and impact on transport modelling", Proc. 28th European Physical Society Conf. on Controlled Fusion and Plasma Physics, Madeira, Portugal, 18-22 June, 2001 A251.

[45] Hasselberg G. and Rogister A., "Drift wave transport and origin of the disruption phenomenon — a theoretical model", Nucl. Fusion **23** (1983) 1351.

[46] Waltz R.E., Dominguez R.R. and Perkins F.W., "Drift wave model tokamak ignition projections with a zero-dimensional transport code", Nucl. Fusion **29** (1989) 351.

[47] Rechester A.B. and Rosenbluth M.N., "Electron Heat Transport in a Tokamak with Destroyed Magnetic Surfaces", Phys. Rev. Lett. **40** (1978) 38.

[48] Kadomtsev B.B. and Pogutse O.P., "Turbulence in Toroidal Systems", Reviews of Plasma Physics (ed. M.A. Leontovich) Consultants Bureau, New York, **5** (1970) 249.

[49] Beer M.A. et al., "Gyrofluid simulations of turbulence suppression in reversed-shear experiments on the Tokamak Fusion Test Reactor", Phys. Plasmas **4** (1997) 1792.

[50] Doyle E.J. et al., "Progress towards increased understanding and control of internal transport barriers (ITBs) on DIII-D", Proc. 18th Int. Fusion Energy Conf. Sorrento, Italy, 4–10 October 2000, paper IAEA-CN-77/EX6/2.

[51] Itoh K. et al., "L-mode confinement model based on transport-MHD theory in tokamaks", Plasma Phys. Control. Fusion **35** (1993) 543.

[52] Guzdar P.N., Drake J.F., McCarthy D. and Hassam A.B., "Three-dimensional fluid simulations of the nonlinear drift-resistive ballooning modes in tokamak edge plasmas", Phys. Fluids B **5** (1993) 3712.

[53] Connor J.W. and Chen L., "Resistive ballooning modes in an axisymmetric toroidal plasma with long mean free path", Phys. Fluids **28** (1985) 2201.

[54] Stober J. et al., "Effects of triangularity on confinement, density limit and profile stiffness of H-modes on ASDEX upgrade", Plasma Phys. Control. Fusion **42** (2000) A211.

[55] Horton L.D. et al., "Performance near operational boundaries", Plasma Phys. Control. Fusion **41** (1999) B329.

[56] Mantica P. et al. "Non-local plasma response induced by peripheral perturbations in the RTP tokamak", Proc. 24th European Physical Society Conf. on Controlled Fusion and Plasma Physics, Berchtesgaden, Germany, 9–13 June 1997, **1V** (1997) 1853.

[57] Hawryluk R.J. et al., "Confinement and Heating of a Deuterium-Tritium Plasma", Phys. Rev. Lett. **72** (1994) 3530.

[58] Greenwald M. et al., "A new look at density limits in tokamaks", Nucl. Fusion **28** (1988) 2199.

[59] Saibene G. et al. "The Effect of Plasma Shape on Density and Confinement of ELMy H-mode in JET", Proc. 28th European Physical Society Conf. on Controlled Fusion and Plasma Physics, Madeira, Portugal, 18-22 June, 2001 933.

[60] Efthimion P.C. et al., "Observation of Temperature-Dependent Transport in the TFTR Tokamak", Phys. Rev. Lett. **66** (1991) 421.

[61] Greenwald M. et al., "Transport experiments in Alcator C-Mod", Phys. Plasmas **2** (1995) 2308.

[62] Zastrow K.-D. et al., "Transfer rates of toroidal angular momentum during neutral beam injection", Nucl. Fusion **38** (1998) 257.

[63] Kim Y.B., Diamond P.H. and Groebner R.J., "Neoclassical poloidal and toroidal rotation in tokamaks", Phys. Fluids B **3** (1991) 2050.

[64] Mattor N. and Diamond P.H., "Momentum and thermal transport in neutral-beam heated tokamaks", Phys. Fluids **31** (1988) 1180.

[65] De Esch H.P.L., Stork D. and Weisen H., "Toroidal plasma rotation in JET", Proc. 17th European Physical Society Conf. on Controlled Fusion and Plasma Physics, Amsterdam, The Netherlands, 25–29 June 1990, **14 B, part I** (1990) 90.

[66] Scott S.D., "Correlations of heat and momentum transport in the TFTR tokamak", Phys. Fluids B **2** (1990) 1300.

[67] Spitzer L. and Härm R., "Transport phenomena in a completely ionized gas", Physical Review **89** (1953) 1953.

[68] Challis C.D. et al., "Effect of q-profile modification by LHCD on internal transport barriers in JET", Plasma Phys. Control. Fusion **43** (2001) 861.

[69] Biglari H., Diamond P.H. and Terry P.W., "Influence of sheared poloidal rotation on edge turbulence", Phys. Fluids B **2** (1990) 1.

[70] Synakowski E.J., "Formation and structure of internal and edge transport barriers", Plasma Phys. Control. Fusion **40** (1998) 581.

[71] Burrell K.H. et al., "Effects of $E \times B$ velocity shear and magnetic shear in the formation of core transport barriers in the DIII-D tokamak", Plasma Phys. Control. Fusion **40** (1998) 1585.

[72] Doyle E.J. et al., "Observation of simultaneous internal transport barriers in all four transport channels and correlation with turbulence behaviour in NCS discharges on DIII-D", Plasma Phys. Control. Fusion **42** (2000) A237.

[73] Sips A.C.C. et al., "Operation at high performance in optimized shear plasmas in JET", Plasma Phys. Control. Fusion **40** (1998) 1171.

[74] Söldner F.X. et al., "Approach to steady state high performance in DD and DT plasmas with optimized shear in JET", Nucl. Fusion **39** (1999) 407.

[75] Budger T., *Plasma Physics and the Problem of Controlled Thermonuclear Reactions*, edited by M.A. Leontovich, Pergamon Press, New York, 1951, Vol. 1, p .78.

[76] Lehnert B., "Short-Circuit of Flute Disturbances at a Plasma Boundary", Phys. Fluids **9** (1966) 1367.

[77] Burrell K.H., "Effects of $E \times B$ velocity shear and magnetic shear on turbulence and transport in magnetic confinement devices", Phys. Plasmas **4** (1997) 1499.

[78] Staebler G.M., "Theory of internal and edge transport barriers", Plasma Phys. Control. Fusion **40** (1998) 569.

[79] Diamond P.H. et al., "Dynamics of Transition to Enhanced Confinement in Reversed Magnetic Shear Discharges", Phys. Rev. Lett. **78** (1997) 1472.

[80] Ernst D.R. et al., "Unifying Role of Radial Electric Field Shear in the Confinement Trends of TFTR Supershot Plasmas", Phys. Rev. Lett. **79** (1998) 2454.

[81] Shirai H. et al., "Role of radial electric field and plasma rotation in the time evolution of internal transport barrier in JT-60U", Plasma Phys. Control. Fusion **42** (2000) A109.

[82] Gruber O. et al., "Internal transport barrier discharges on ASDEX upgrade: progress towards steady state", Plasma Phys. Control. Fusion **42** (2000) A117.

[83] Staebler G.M., Waltz R.E. and Wiley J.C., "The role of rotation in tokamak internal transport barriers", Nucl. Fusion **37** (1997) 287.

[84] Synakowski E.J. et al, "Roles of Electric Field and Shafranov Shift in Sustaining High Confinement in Enhanced Reversed Shear Plasmas on the TFTR Tokamak", Phys. Rev. Lett. **78** (1997) 2972.

[85] Hahm T.S. and Burrell K.H., "Flow shear induced fluctuation suppression in finite aspect ratio shaped tokamak plasma", Phys. Plasmas **2** (1995) 1648.

[86] Waltz R.E., Kerbel G.D., Milowich J. and Hammet G.W., "Advances in the simulation of toroidal gyro-Landau fluid model turbulence", Phys. Plasmas **2** (1995) 2408.

[87] Crisanti F. et al., "Analysis of the $E \times B$ flow shearing rate in JET ITB discharges", Nucl. Fusion **41** (2001) 883.

[88] Turnbull A.D., Taylor T.S., Lin-Liu Y.R. and St. John H., "High Beta and Enhanced Confinement in a Second Stable Core VH-Mode Advanced Tokamak", Phys. Rev. Lett. **75** (1995) 718.

[89] Kessel C., Manickam J., Rewoldt G. and Tang W.M., "Improved Plasma Performance in Tokamaks with Negative Magnetic Shear", Phys. Rev. Lett. **72** (1994) 1212.

[90] Shaing K.C., Aydemir A.Y., Houlberg W.A. and Zarnstorff M.C., "Theory of Enhanced Reversed Shear Mode in Tokamaks", Phys. Rev. Lett. **80** (1998) 5353.

[91] Guo S.C. and Weiland J., "Analysis of η_{i} mode by reactive and dissipative descriptions and the effects of magnetic q and negative shear on the transport", Nucl. Fusion **37** (1997) 1095.

[92] Dorland W., Jenko F., Kotschenreuther M. and Rogers B.N., "Electron Temperature Gradient Turbulence", Phys. Rev. Lett. **85** (2000) 5579.

[93] Greenfield C.M. et al., "Understanding and control of transport in Advanced Tokamak regimes in DIII-D", Phys. Plasmas **7** (2000) 1959.

[94] Wolf R.C. et al., "Response of internal transport barriers to central heating and current drive on ASDEX Upgrade", Phys. Plasmas **7** (2000) 1839.

[95] Tala T.J.J. et al., "ITB Formation in Terms of $\omega_{\mathrm{E}\times\mathrm{B}}$ Flow Shear and Magnetic Shear s on JET", Proc. 27th European Physical Society Conf. on Controlled Fusion and Plasma Physics, Budapest, Hungary, 12-16 June, 2000 1493.

[96] Koide Y. and JT-60U Team, "Progress in confinement and stability with plasma shape and profile control for steady-state operation in the Japan Atomic Energy Research Institute Tokamak-60 Upgrade", Phys. Plasmas **4** (1997) 1623.

[97] Litaudon X. et al., "Stationary magnetic shear reversal experiments in Tore Supra", Plasma Phys. Control. Fusion **38** (1996) 1603.

[98] Joffrin E., Challis C.D., Hender T.C., Howell D.F. and Huysmans G.T.A., "MHD Internal Transport Barrier triggering in low positive shear scenario in JET", Nucl. Fusion **42** (2002) 235.

[99] Lopes Cardozo N.J. et al., "Electron thermal transport in RTP: filaments, barriers and bifurcations", Plasma Phys. Control. Fusion **39** (1997) B303.

[100] Fitzpatrick R., Hastie R.J., Martin T.J. and Roach C.M., "Stability of coupled tearing modes in tokamaks", Nucl. Fusion **33** (1993) 1533.

[101] Hogeweij G.M.D., Lopes Cardozo N.J., de Baar M.R. and Schilham A.M.R., "A model for electron transport barriers in tokamaks, tested against experimental data from RTP", Nucl. Fusion **38** (1998) 1881.

[102] Staebler G.M., "Density gradient bifurcation in tokamaks", Nucl. Fusion **39** (1999) 815.

[103] Lao L. et al., "Reconstruction of current profile parameters and plasma shapes in tokamaks", Nucl. Fusion **25** (1985) 1611.

[104] Eriksson L.-G., Hellsten T. and Willen U., "Comparison of time dependent simulations with experiments in ion cyclotron heated plasmas", Nucl. Fusion **33** (1993) 1037.

[105] Bateman G. et al., "Predicting temperature and density profiles in tokamaks", Phys. Plasmas **5** (1998) 1793.

[106] Ohkawa T., "A transport model for alcator scaling in tokamaks", Phys. Lett. A **67** (1978) 35.

[107] Tubbing B.J.D. et al., "H-mode confinement in JET with enhanced performance by pellet peaked density profiles", Nucl. Fusion **31** (1991) 839.

[108] Zhu P., Bateman G., Kritz A.H. and Horton W., "Predictive transport simulations of internal transport barriers using the Multi-Mode model", Phys. Plasmas **7** (2000) 2898.

[109] Waltz R.E. et al., "A gyro-Landau-fluid transport model", Phys. Plasmas **4** (1997) 2482.

[110] Kinsey J.E., Waltz R.E., Staebler G.M. and St. John H., "Dynamic Modeling of Multi-channel Transport Bifurcations Using Ion Temperature Gradient Based Models for Tokamak Plasmas", Proc. 26th European Physical Society Conf. on Controlled Fusion and Plasma Physics, Maastrict, The Netherlands, 14-18 June, (1999) 1205.

[111] Itoh S.-I. et al., "Self-sustained turbulence and H-mode confinement in toroidal plasmas", Plasma Phys. Control. Fusion **38** (1996) 1743.

[112] Fukuyama A., Takatsuka S., Itoh S.-I., Yagi M. and Itoh K., "Transition to an enhanced internal transport barrier", Plasma Phys. Control. Fusion **40** (1998).

[113] Lopez-Bruna D., Newman D.E., Carreras B.A. and Diamond P.H., "Fluctuation level bursts in a model of internal transport barrier formation", Phys. Plasmas **6** (1999) 854.

[114] Horton W. and Zhu P., "Transport barrier dynamics", Phys. Plasmas **7** (2000) 4534.

[115] Schilham A.M.R., Hogeweij G.M.D., Lopes Cardozo N.J., Parail V.V. and Gormezano C., "Application of the RTP transport model to the JET tokamak", submitted to Nucl. Fusion (2001).

[116] Pereverzev G. et al., "Simulation of ASDEX Upgrade Plasmas with Internal Transport Barrier", Proc. 26th European Physical Society Conf. on Controlled Fusion and Plasma Physics, Maastrict, The Netherlands, 14-18 June, (1999) 1429.

[117] Kotschenreuther M. et al., "Quantitative predictions of tokamak energy confinement from first-principles simulations with kinetic effects", Phys. Plasmas **2** (1995) 2381.

[118] Tala T.J.J. et al. "Impact of Different Preheating Methods on q-profile Evolution in JET", Proc. 28th European Physical Society Conf. on Controlled Fusion and Plasma Physics, Madeira, Portugal, 18-22 June, 2001 541.

[119] Kolesnichenko Ya. et al., *Reviews of Plasma Physics* edited by B.B. Kadomtsev, Plenum, New York, **17** (1992) 1.

[120] Strand P.I. and Houlberg W.A., "Magnetic flux evolution in highly shaped plasmas", Phys. Plasmas **8** (2001) 2782.

[121] Huysmans G.T.A., Hender T.C., Hawkes N.C. and Litaudon X., "MHD stability of Advanced Tokamak Scenarios with reversed central current: An Explanation of the 'Current Hole"', submitted to Phys. Rev. Lett. (2001).

[122] Budny R.V. et al., "Simulations of deuterium-tritium experiments in TFTR", Nucl. Fusion **32** (1992) 429.

[123] Hyusmans G.T.A. et al., "MHD stability analysis of optimised shear discharges in JET", Proc. 24th European Physical Society Conf. on Controlled Fusion and Plasma Physics, Berchtesgaden, Germany, 9–13 June, (1997) **21A** 21.

[124] Tala T.J.J. et al. "Modelling of LHCD Profile Control for High Performance DT Experiments on JET", Proc. 13th Topical Conf. on Radio Frequency Power in Plasmas (AIP Conference Proceedings 485), Annapolis, Maryland, USA, 12-14 April, 1999 207.

[125] Challis C.D. et al., "Influence of the q-profile shape on plasma performance in JET", submitted to Plasma Phys. Control. Fusion in 2002.

[126] Dux R. et al. "Analysis of Impurity Behaviour in ITB Discharges with Reversed Shear on JET", Proc. 28th European Physical Society Conf. on Controlled Fusion and Plasma Physics, Madeira, Portugal, 18-22 June, 2001 505.

PUBLICATION 1

ITB formation in terms of $\omega_{\mathbf{E\times B}}$ flow shear and magnetic shear *s* on JET

In: Plasma Physics and Controlled Fusion 2001. Vol. 43, pp. 507–523.
Reprinted with permission from the publisher.
http://www.iop.org/journals/ppcf

INSTITUTE OF PHYSICS PUBLISHING PLASMA PHYSICS AND CONTROLLED FUSION

Plasma Phys. Control. Fusion **43** (2001) 507–523 www.iop.org/Journals/pm PII: S0741-3335(01)18561-1

ITB formation in terms of $\omega_{\mathbf{E}\times\mathbf{B}}$ flow shear and magnetic shear s on JET

T J J Tala[1], J A Heikkinen[1], V V Parail[2], Yu F Baranov[2] and S J Karttunen[1]

[1] Association Euratom-Tekes, VTT Chemical Technology, PO Box 1404, FIN-02044 VTT, Finland
[2] EURATOM/UKAEA Fusion Association, Culham Science Centre, Abingdon, OX14 3EA, UK

Received 2 November 2000, in final form 29 January 2001

Abstract

A linear empirical threshold condition $\omega_{\mathrm{E}\times\mathrm{B}}/\gamma_{\mathrm{ITG}} > 0.68s - 0.095$ has been found for the onset of the ion internal transport barriers in the JET optimised shear database. Here, s is the magnetic shear, $\omega_{\mathrm{E}\times\mathrm{B}}$ the flow shearing rate and γ_{ITG} is an approximate of the linear growth rate of the ion temperature gradient instability. The present empirical threshold condition for the ITB formation will provide a first clear indication of the strong correlation of s and $\omega_{\mathrm{E}\times\mathrm{B}}$ at the ITB transition. The empirical analysis consists of ITB discharges from a wide plasma parameter range; the toroidal magnetic field varies between 1.8–4.0 T, the auxiliary heating power between 10–30 MW and the diamagnetic energy between 3–12 MJ. The predictive simulations of several ITB discharges with the empirical ITB threshold condition reproduce the experiments with time averaged prediction errors of the order of 10–25% in T_{i} and T_{e} profiles and 10–15% in n_{e} profiles as well as the toroidal flow velocity with errors of the order of 10–20%. The simulated times of the onset of the ITB compared to the experimental ones are typically within 0.4 s and the simulated ITB widths within 0.1 in r/a throughout the whole simulations.

1. Introduction

Internal transport barriers (ITBs) have now been recognized as having the potential to operate fusion machines in an improved confinement mode where the pressure gradients can drive the required bootstrap current [1, 2, 3, 4]. At present, there is an urgent need to understand the parameter dependence of the threshold for the ITB formation, the dynamics of the barrier and the collapse of the barrier.

The physical mechanism of the ITB formation has not yet been clearly identified. The $\omega_{\mathrm{E}\times\mathrm{B}}$ flow shear is commonly regarded as a very crucial factor in the ITB formation in most theories [5, 6, 7] and also found to be important in most ITB experiments on different tokamaks [8, 9, 10, 11]. Another crucial factor possibly contributing to the ITB formation is the weak or negative magnetic shear in the plasma core region, demonstrated also on many

0741-3335/01/040507+17$30.00

tokamaks [1, 12, 13, 14]. The combined effects of $\omega_{E\times B}$ velocity shear and magnetic shear s on turbulence suppression and transport in magnetic confinement devices have been investigated in [15]. A third possible factor affecting the ITB formation are the low order rational q-surfaces, reported on JET and RTP in [16, 17, 18]. Other explanations for the ITB formation consider Shafranov-shift-induced turbulence stabilization [19] and turbulence suppression by the turbulence generated zonal flows [20]. The role of the inhomogeneity in the plasma, i.e. the ion temperature gradient (ITG) and electron temperature gradient (ETG) modes can be of major significance. The possible mechanisms listed above are not independent of each other and most probably, the ITB formation is an interplay of two or more physical mechanisms.

ITBs have been identified either separately in the ion and electron channels or, as is often the case, with both ion and electron transport suppression occurring at the same barrier position, although not necessarily simultaneously [21]. Typically on JET after the onset of the ITB, χ_e drops approximately by a factor of 5 while χ_i falls by more than an order of magnitude, almost to the neo-classical level in the plasma core. In the absence of any satisfactory theory that is based on the first principles for the onset of the ITB, empirical predictive transport models describing the suppression of the microturbulence and the further evolution of the ITB have been developed [22, 23, 24]. Here, the standard transport equations for the ion and electron temperatures, density, flow velocities and magnetic flux as well as various types of turbulence models have been amended by the inclusion of an ITB transition model. In [23], the ITB transition has been described as a jump from ELMy H mode or L mode to an improved core confinement with a linear combination of a Hahm–Burrell flow shearing rate $\omega_{E\times B}$ [25] and magnetic shear. An alternative method to the Hahm–Burrell flow shear model takes into account the effect of the weak magnetic shear in addition to $\omega_{E\times B}$ flow shear mechanism. There one has introduced a flow shearing rate factor which is called the Hamaguchi–Horton shear parameter [26]. This has been used in the simulation of ITBs in [22], taking also into account the magnetic shear effect as presented in Weiland model in [27]. Various numerical techniques in order to allow time-dependent transport codes to dynamically follow bifurcations to enhanced confinement regimes by self-consistently computing the effect of $E \times B$ shear stabilization are investigated in [24].

In this paper, the $\omega_{E\times B}$ flow shear and the magnetic shear s are determined from the JET optimized shear (OS) experiments at the ITB transition. These values are used to construct an empirical ITB transition threshold condition in terms of the shear quantities $\omega_{E\times B}$ and s. This empirical condition is further employed in predictive simulations to describe the ITB onset, evolution and a possible collapse. The present empirical fit of s and $\omega_{E\times B}$ for the ITB transition provides the first clear indication of the strong correlation of s and $\omega_{E\times B}$ at the ITB transition. It will be further shown that the statistical error in the fit reduces significantly if instead of $\omega_{E\times B}$ flow shear a quantity $\omega_{E\times B}/\gamma_{ITG}$ is used. This indicates the significant role of ITG turbulence in the ITB formation in JET. $\gamma_{ITG} = v_{th}/L_T$ approximates the linear growth rate of the ITG type of plasma turbulence, where $v_{th} = \sqrt{2k_B T_i/m_i}$ is the ion thermal velocity with T_i being the ion temperature and m_i the ion mass, and $L_T = T_i/(\partial T_i/\partial R)$ is the ion temperature scale length.

In finding the values of s and $\omega_{E\times B}$ at the ITB transition from the experimental data, special attention must be paid to determining the location and time of the onset of the ITB. This is complicated by the limited accuracy in spatial and temporal resolution of the charge exchange spectroscopy (CXS) (temporal resolution $\approx$ 50 ms, spatial resolution $\approx$ 10 cm), electron cyclotron emission (ECE) and magnetic measurements. Motional Stark effect (MSE) measurements are not available for the JET OS discharges considered in this analysis and, as a consequence, the magnetic shear calculated by EFIT [28] without MSE measurements has large error bars. Therefore, s is inferred from interpretative JETTO [29] simulations,

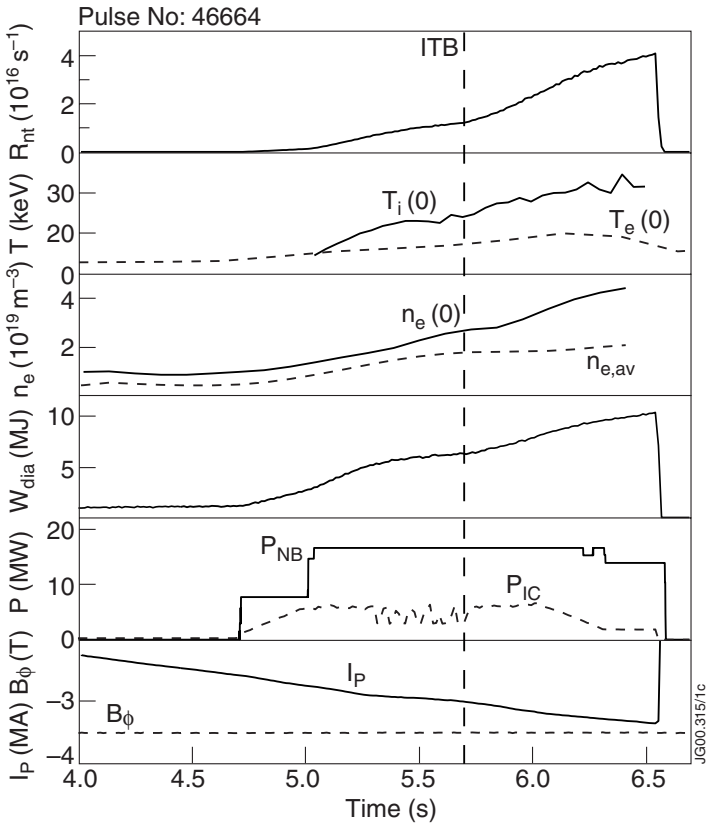

Figure 1. Time traces of the neutron rate R_{nt}, the central ion T_i and electron T_e temperatures, the central and volume averaged electron density n_e, the diamagnetic energy W_{dia}, the heating powers P_{NB} and P_{IC} and the plasma current I_p and toroidal magnetic field B_ϕ for the OS discharge pulse No 46664. ITB appears at $t = 5.6$ s (shown by the vertical dashed line) and L–H mode transition occurs after $t = 5.1$ s.

i.e. only Faraday's equation is solved for the current by using the neo-classical conductivity and external sources for current, but all the other quantities (temperatures, densities, plasma current, toroidal magnetic field, Z_{eff}, etc.) are taken from the experiment. The time for the onset of the ITB is inferred from the sudden increase in the $\tau_{ITER-97}$ confinement time. The possibility of the increase in the confinement time being due to the L–H transition can be excluded by checking the D_α signal. After determining the time for the onset of the ITB, the radial location is inferred from the large gradients in the temperature profiles. A dimensionless criterion for characterising ITBs was reported very recently in [30]. That method, also based on the similar determination of the temperature gradients, is not used here, but it gives similar results.

Figure 1 shows time traces of typical plasma parameters from a $B_\phi = 3.4$ T, $I_p = 3.4$ MA (peak) OS discharge No 46664. This pulse was selected because it has a very strong and clear ITB formation, both in time and space, and also the time evolution of the ITB can be tracked with small experimental errors. The ITB forms at $t = 5.6$ s and this can be seen as a sudden increase in R_{nt} signal at the same time in figure 1. The discharge ends up with a disruption due to the emergence of a pressure driven kink instability at $t = 6.5$ s.

The paper is structured in the following way. Section 2 illustrates the calculation of the

radial electric field E_r and its different components with and without ITBs in JET. In section 3, the ITB formation is studied in terms of $\omega_{E\times B}$ shearing rate and magnetic shear s. An empirical threshold condition for the ITB formation is found. That empirical ITB transition condition is applied in predictive simulations to an extensive set of JET OS plasmas in section 4. The maximum simulation errors in T_i, T_e, n_e and the toroidal rotation velocity v_ϕ as well as ITB formation time and location are also estimated. Finally, we summarize and discuss the results in section 5.

2. Calculation of the radial electric field E_r

The radial electric field for the main plasma ions is calculated as follows:

$$E_r = \frac{1}{Zen_i}\frac{\partial p_i}{\partial r} - v_\theta B_\phi + v_\phi B_\theta, \tag{1}$$

where v_θ and v_ϕ are the poloidal and toroidal velocities and B_θ and B_ϕ the poloidal and toroidal magnetic fields, respectively, n_i is the ion density, Z is the ion charge number and e the elementary charge. Experimentally measured values for all other quantities except v_θ are available in the calculation of E_r, and due to the lack of measurements of v_θ in JET, it is assumed to be neo-classical. The validity of this assumption has been discussed in [31] and it was concluded that anomalous viscosity can be neglected compared to neo-classical viscosity provided that the typical scale length of the poloidal rotation is much longer than the poloidal Larmor radius of the ions. Within the present model for v_θ, we do not consider either ripple- or turbulence-originated sources of torque for poloidal rotation, although such mechanisms may play a role in the ITB formation in some configurations [20, 32]. Toroidal rotation velocity v_ϕ is measured by charge exchange spectroscopy using the carbon impurity. The difference between the toroidal rotation of the carbon impurity and the main ion for plasmas with NBI (large momentum input) is found to be at most of the order of 10–15% at radii where the ITBs take place. The correction has been calculated with an equation given in [33].

The radial electric field and its different components are shown 0.6 s before the ITB transition in figure 2 (a) and 0.6 s after the ITB formation in figure 2 (b) for the JET discharge No 46664. The contribution from the toroidal rotation (dash-dotted curve) is clearly dominant in the total E_r (thick solid), both before and after the ITB formation. The dominance of $E_{r,\phi} = v_\phi B_\theta$ in E_r becomes even more pronounced because the poloidal velocity term $E_{r,\theta} = v_\theta B_\phi$ (dotted curve) almost cancels out the pressure gradient term $E_{r,\nabla p} = \frac{1}{Zen_i}\frac{\partial p_i}{\partial r}$ (dashed curve), the difference being indicated also in figure 2. The partial cancellation of these two terms is a direct consequence of the used neo-classical model for v_θ in the banana-regime. The magnitude of E_r and its all components are about 5 times larger after the formation of the ITB than before it. The footpoint of the ITB is at $\rho \approx 0.56$ in figure 2 (b). The values for E_r and its different components are found to be of the same order of magnitude and follow the same qualitative behaviour for other JET OS discharges as well.

In JET, the toroidal rotation produced mainly by the co-rotating neutral beam injection (NBI) always gives a positive contribution to E_r as illustrated in figure 2. For co-injected NBI, the dominant contribution from the toroidal rotation term $E_{r,\phi}$ to the radial electric field and its gradient is reduced by the sum of the two remaining terms, i.e. pressure gradient and poloidal rotation terms as $(E_{r,\nabla p} - E_{r,\theta})$. Then if the pressure gradient is increased, E_r and its gradient is decreased, thus hindering the formation and expansion of the ITB. However, in the case of counter-injection the toroidal rotation term and the remaining two terms add to each other, increasing E_r with increasing pressure gradient. Consequently, there is a reason to expect that the ITBs would be wider for discharges with the counter-injected NBI because increasing the

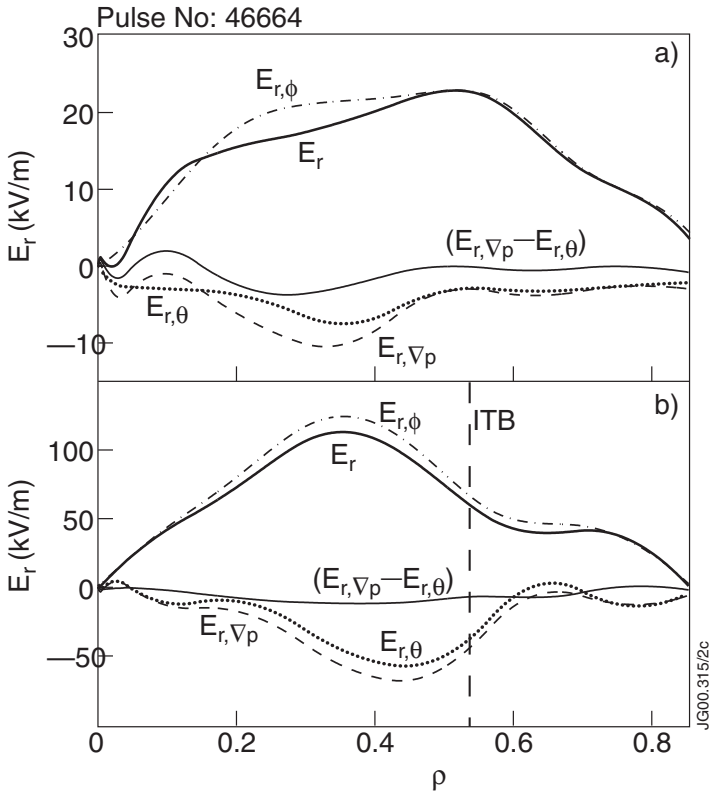

Figure 2. E_r and its components 0.6 s before (a) and 0.6 s after (b) the ITB formation as a function of $\rho = \sqrt{\Phi/\pi B_\phi}/a_{\text{eff}}$ with a_{eff} being the radius of the circle covering the same area as the elongated plasma for JET pulse No 46664. The footpoint of the ITB is shown by the vertical dashed line in (b).

gradient of the radial electric field will reinforce the positive effect of $\omega_{E\times B}$ shearing rate on the turbulence suppression and further on the ITB formation. In addition, the counter-injected current in the plasma core produced by NBI could help in decreasing the magnetic shear in the plasma centre, thus further facilitating wider ITBs.

Theoretically counter-momentum injection was predicted to lower the power threshold to form an ITB and produce a wider ITB in [34]. Experimentally NBI counter-injection was demonstrated to be better at sustaining the ITB compared to co-injection on TFTR [19, 36]. However, balanced-injection turned out to be enough or even better to sustain and form an ITB on TFTR when the magnetic shear was negative in the core plasma. The advantage of balanced-injection in reversed shear (RS) plasmas was also reported in JT-60U [9]. In DIII-D negative central shear (NCS) plasmas, discharges with NBI counter-injection exhibited wider ITBs compared to those with co-injection [35]. NBI co-injection produced a positive E_r hill which then gradually lead to the formation of relatively narrow ITBs with a very small power threshold whereas with counter-injection, wider ITBs were obtained but with a higher power threshold [35, 36]. In addition, the recently found promising steady state operating mode, so-called quiescent double barrier (QDB) mode requires necessarily a counter NBI [37]. When comparing the time behaviour and the profiles of the different components of the radial electric field before and after the ITB formation between different tokamaks, DIII-D plasmas with NBI

co-injection are found to remind most of the present situation on JET.

To actively control the width and strength of the ITB, a flexible NBI system is needed. Recent results from JT-60U indicate that changing the toroidal momentum injection, i.e. toroidal rotation, by changing from co- to balanced or counter-injection or vice versa, the width and strength of the ITB can be controlled [38].

3. $\omega_{\mathrm{E}\times\mathrm{B}}$ flow shear versus magnetic shear s in ITB formation

The $\omega_{\mathrm{E}\times\mathrm{B}}$ shearing rate is calculated following [25]

$$\omega_{\mathrm{E}\times\mathrm{B}} = \left| \frac{RB_\theta^2}{B_\phi} \frac{\partial}{\partial \Psi} \frac{E_\mathrm{r}}{RB_\theta} \right|, \tag{2}$$

where Ψ is the poloidal flux, R the major radius and E_r calculated as in section 2. In figure 3, we plot 13 ITB pulses in H mode, 3 ITB pulses in L mode and 3 pulses where no ITB was observed for the ITB formation threshold condition of JET optimized shear discharges. The plasma parameter range of the analysed pulses is very wide, i.e. B_ϕ varies between 1.8–4.0 T, the input power in the range 10–30 MW and the diamagnetic energy in the range 3–12 MJ among the investigated pulses. The magnetic shear s, calculated in an interpretative way by JETTO [29], is presented before and after the ITB formation as a function of $\omega_{\mathrm{E}\times\mathrm{B}}$ in figure 3. The diamonds denote the values of s and $\omega_{\mathrm{E}\times\mathrm{B}}$ ~50 ms before the ITB formation and the stars ~50 ms after it for OS pulses with ELMy H-mode edge. For L-mode plasma edge discharges, the triangles symbolize s and $\omega_{\mathrm{E}\times\mathrm{B}}$ ~50 ms before the ITB transition and the plus signs ~50 ms after the transition. The reason for using the instants ~50 ms before or after the ITB formation is the temporal resolution (50 ms) from CXS mesurements for T_i and v_ϕ. The values of s and $\omega_{\mathrm{E}\times\mathrm{B}}$ are taken at the location of the footpoint of the ITB. Thus, there are two sets of pairs that belong to the same discharge, i.e. each diamond has a corresponding star that has originated from the same discharge, calculated ~100 ms later after the onset of the ITB (H mode), and each triangle has a corresponding plus-sign that has come from the same discharge (L mode) in a similar way. For the three discharges marked with circles, no ITB was observed. In these cases, the values of s and $\omega_{\mathrm{E}\times\mathrm{B}}$ are taken at the most likely location and instant for an ITB to take place. There are also three back transitions from an ITB state back to an ELMy H-mode plasma included in the ITB transitions presented in figure 3.

There seems to be a trend in figure 3 that larger values of the magnetic shear require a larger $\omega_{\mathrm{E}\times\mathrm{B}}$ shearing rate for an ITB to be formed. This trend can be seen as all the points with larger s tend to be located more on the right-hand side, thus indicating larger $\omega_{\mathrm{E}\times\mathrm{B}}$ to be needed to trigger the ITB for those cases. Also, there seems to be another trend in figure 3, an obvious separation of diamonds and stars (H-mode discharges) and triangles and plus signs (L mode discharges), i.e. values of $\omega_{\mathrm{E}\times\mathrm{B}}$ and s are different before and after the appearence of the ITB. This separation is mainly horizontal, indicating that the $\omega_{\mathrm{E}\times\mathrm{B}}$ shearing rate increases significantly within 100 ms time interval around the ITB formation whereas the magnetic shear remains almost unchanged at the same time. In order to see whether the trend is clearer when taking into account the turbulence growth rate we define a dimensionless ratio of the $\omega_{\mathrm{E}\times\mathrm{B}}$ shearing rate to the maximum linear growth rate of the ITG type of plasma turbulence γ_{ITG}, $\Omega = \omega_{\mathrm{E}\times\mathrm{B}}/\gamma_{\mathrm{ITG}}$ where the linear ITG instability growth rate is $\gamma_{\mathrm{ITG}} \propto v_{\mathrm{i,th}}/R$ with $v_{\mathrm{i,th}}$ being the ion thermal velocity. To reach the maximum accuracy for the estimation of the growth rates, more sophisticated models for the calculation of the ITG turbulence, such as Weiland's model [27, 39], should be used, but within the scope of this simplified empirical work we will use only the simplified expression. Inclusion of the Weiland's turbulence model is left for future work.

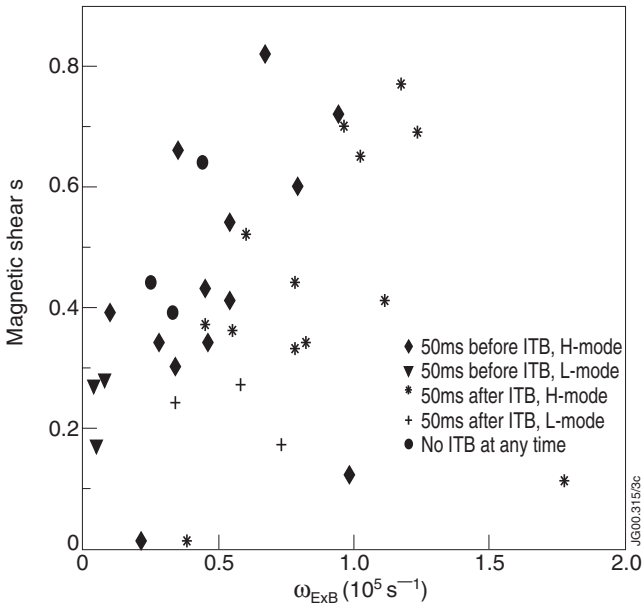

Figure 3. Magnetic shear and $\omega_{E\times B}$ at the ITB location for the ITB formation threshold condition.

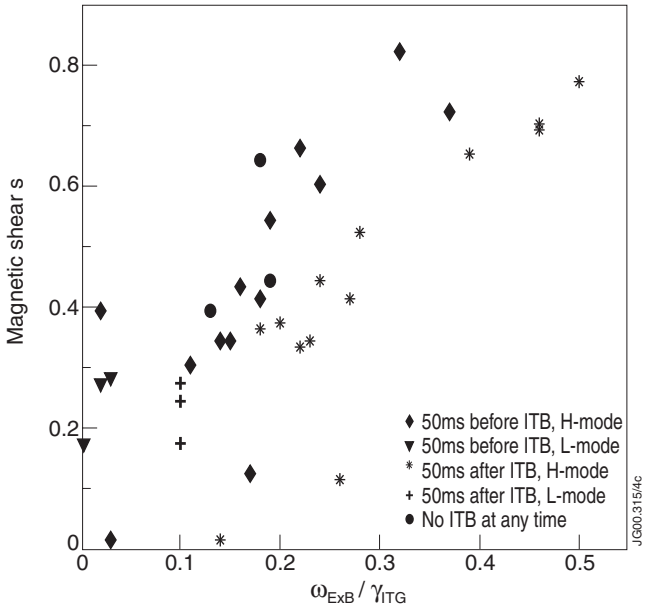

Figure 4. As in figure 3, but $\omega_{E\times B}$ shearing rate is divided by the ITG instability growth rate γ_{ITG} (x axis).

Figure 4 illustrates again the same ITB pulses for ITB formation threshold conditions, with the only exception that now $\omega_{E\times B}$ flow shear is divided by the ITG instability growth rate γ_{ITG}. Now the separation of the discharges before the ITB formation (diamonds in H mode and triangles in L mode) and after the formation (stars in H mode and plus signs in L mode) is more

systematic than without dividing $\omega_{E\times B}$ by γ_{ITG} as presented in figure 3. As a consequence, this can be regarded also as an indirect indication that the ITG turbulence and the ITG turbulence suppression play a major role in the ITB formation process with these JET OS discharges.

Since measurements of T_i and v_ϕ are not always available at the instant of the ITB formation because of the temporal resolution of CXS diagnostic, we will estimate more accurate values for the shear quantities (s and $\omega_{E\times B}$) at the onset of the ITB. The procedure takes the mid-point of each two points that belong to the same discharge in figures 3 and 4, i.e. linear interpolation of the points that are definitely before (∼50 ms) and definitely after (∼50 ms) the ITB formation. The resulting mid-points then depict the shear quantities at the onset of the ITB within the experimental measurement accuracy in the s–$\omega_{E\times B}$ and in the s–Ω spaces. Figure 5 presents the values of s and $\omega_{E\times B}$ in figure 5(a) and s and Ω in figure 5(b) for the same discharges as in figures 3 and 4, respectively. Naturally, the three discharges with no ITB are excluded in figure 5.

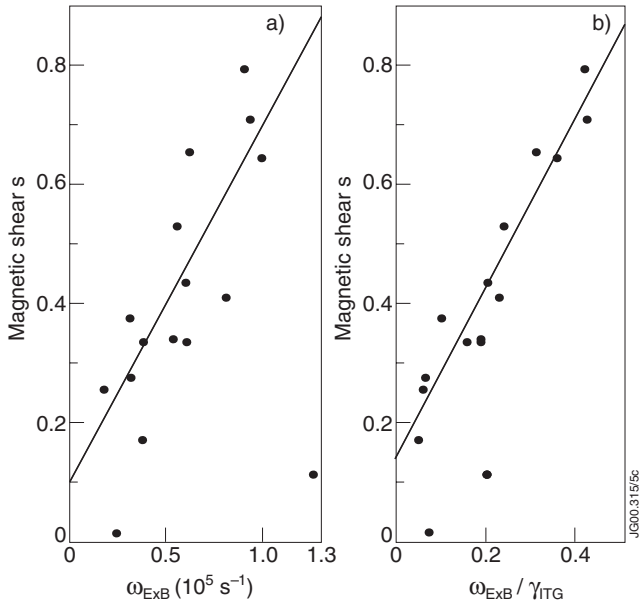

Figure 5. As in figures 3 and 4, but linearly interpolated values for s, $\omega_{E\times B}$ and Ω are used. Shown also are the straight lines, i.e. the best fits calculated with the least-squares method.

Both scatter plots in figure 5 exhibit a linear trend indicating that linear regression is reasonable. Therefore, by applying the least-squares method to the scatter plots in figure 5 a straight line in each figure can be estimated. The estimated regression line takes the form $s = 0.60\omega_{E\times B} + 0.091$ ($\omega_{E\times B}$ scaled by 10^5) in figure 5(a) and $s = 1.47\Omega + 0.14$ in figure 5(b). The standard deviations for the slope and intercept terms are 0.14 and 0.081 in figure 5(a), respectively and 0.13 and 0.031 in figure 5(b), respectively. Relatively small values for the standard deviations of the estimators compared to the actual values of the estimators are found, thus indicating small confidence intervals for the fit and further of an accurate fit of the straight lines. Especially the curve $s = 1.47\Omega + 0.14$ shown in figure 5(b) exhibits very small relative standard deviations compared to its estimators.

The interpretation of the ITB formation in the s–Ω space could be the following: the $\omega_{E\times B}$ flow shear must be large enough to tear apart the turbulent eddies thus suppressing the long-wavelength ITG turbulence (γ_{ITG}) while at the same time small magnetic shear s

helps to disconnect the turbulent vortices (e.g. ballooning modes) initially linked together by toroidicity. Other possible mechanisms why the small magnetic shear is favourable to yield an ITB at significantly smaller $\omega_{E\times B}$ shearing rate are the splitting of some global modes [40] and some other topological modifications in the flux surface geometry [41]. This can be better understood by rearranging the terms in the estimated regression curve as $\omega_{E\times B} > s\gamma_{ITG}/1.47–0.14\gamma_{ITG}/1.47 = 0.68s\gamma_{ITG}–0.095\gamma_{ITG}$. Consequently, there are two distinct regions in the s–Ω space, separated by the line $s = 1.47\Omega + 0.14$ in figure 5(b). Above the line an ITB does not exist, whereas below it an ITB does exist. The ITB is formed or collapsed, depending on the direction, when the line is crossed. The same rule is valid for all discharges in a wide B_ϕ, P_{in} and W_{dia} parameter range when the ITB is formed at typical radii in the range $\rho = 0.35$–0.55. Furthermore, both the ELMy H-mode and L-mode plasmas obey the same rule, although the required Ω to compensate the magnetic shear is smaller due to smaller s at the footpoint of the ITB with an L mode edge. Moreover, the three ITB back transitions included in the analysis fit well in the same straight line.

Another point worth mentioning is the intercept term in $s = 1.47\Omega + 0.14$. A positive intercept implies that a negative or zero magnetic shear should be a sufficient condition for an ITB to exist. It is known from the theory that negative magnetic shear has a beneficial effect on curvature driven instabilities [42, 43]. Recent results from the ongoing JET experimental campaign with LHCD used also during the main heating phase to sustain negative s support the theory of the turbulence suppression, ITB formation and enhanced high performance by negative magnetic shear [44].

The time evolution of three ITB discharges in s–Ω parameter space is shown in figure 6. Diamonds, interconnected with a dotted line, indicate that no ITB yet exists whereas stars, interconnected with a dashed line, denote an existing ITB. The time interval between the consecutive points is 250–400 ms, depending on the discharge. The values of s and Ω before the ITB formation are calculated at the location where the ITB later appears. After the ITB formation the actual footpoint is followed. The thin solid lines between the last diamond and first star mark the time interval during which the ITB is formed. The thick solid line is the line $s = 1.47\Omega + 0.14$ estimated with the least-squares method, and shown in figure 5.

Both s and Ω are small at the beginning of the discharges, s because of the early phase of the current ramp-up and Ω because NBI is not yet switched on. The magnetic shear starts to increase immediately because of the current penetration. When NBI is switched on after 2–3 s, Ω also starts to increase, finally leading to the formation of the ITB. After the onset of the ITB, it typically expands in radius and goes far from the $s = 1.47\Omega + 0.14$ ITB formation threshold curve, as is the case with pulses No 47413 and 46664. Pulse No 47413 is the longest steady-state OS high performance DD discharge achieved on JET so far. Only the technical restrictions on the high power NBI system were limiting the duration of the discharge. Discharge No 47413 is a pulse with an argon puff that was used to control the ELM activity at the edge and thus, the measurements of T_i and v_ϕ have some uncertainties, further leading to larger uncertainties than normally measured by CXS in the toroidal velocity and pressure gradient (T_i) terms [45]. Pulse No 46664 has a very rapidly increasing neutron yield in the beginning, but it ends prematurely with a disruption due to the pressure-driven kink instability. The time traces of this discharge are shown in figure 1 and the radial electric field in figure 2. The empirically estimated curve $s = 1.47\Omega + 0.14$ can predict the ITB formation in s–Ω space relatively well for both discharges. However, as an opposite case to the previous pulses where full beam power were used, NBI power is decreased from 16 MW to 10 MW after the ITB formation for the shot No 48971. Therefore, the power threshold for the ITB to exist is no longer fulfilled and consequently, the ITB is lost only 1 s after its onset. This back transition is also shown in figure 6 and predicted very well by the estimated ITB formation threshold.

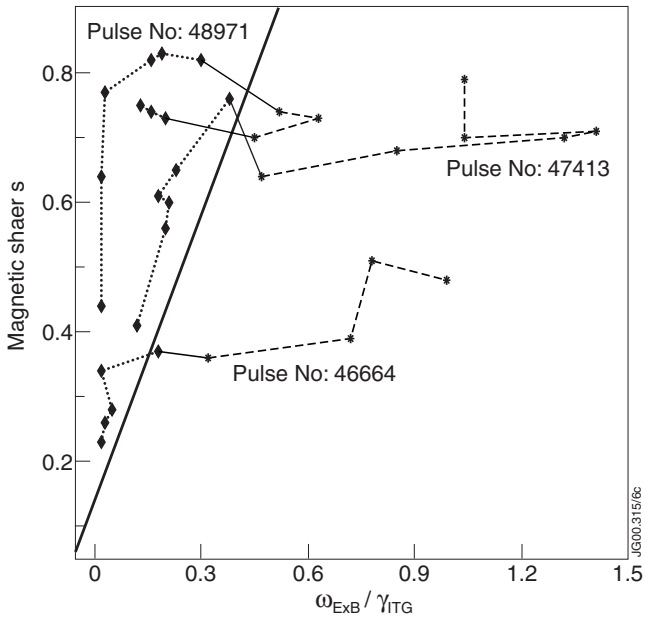

Figure 6. The time evolution of the magnetic shear as a function of Ω for 3 OS discharges. The same solid line, $s = 1.47\Omega + 0.14$, as in figure 4 is also shown.

It should be noted that in evaluation of $\Omega = \omega_{E\times B}/\gamma_{ITG}$ no account for the poloidal dependence of that quantity has been taken. As Ω here is defined, it is a flux-surface averaged quantity. Thus, the effect of Shafranov-shift is not included. However, by redefinition of $\omega_{E\times B}/\gamma_{ITG}$, its value on the outboard equator was determined and found to be about 10% larger for the present JET OS discharges than the values calculated from equation (2). Firstly due to the dominant role of ITG turbulence on JET, and secondly due to the relatively small Shafranov-shifts of JET discharges, the effect of the Shafranov-shift-induced turbulence suppression cannot be regarded as important as has been found, e.g. for the trapped electron mode turbulence in TFTR experiments [19].

4. Predictive simulations by using $s = 1.47\Omega + 0.14$ as the ITB formation condition

Predictive transport simulations of ITBs have been recently performed with several transport models and codes by many authors [22, 23, 24, 46, 47, 48]. Modelling the formation and dynamics of ITBs differs to some extent between the different transport models. At present, we will test the empirical ITB formation threshold condition $s = 1.47\Omega + 0.14$ found in section 3 for several JET OS discharges. The mixed Bohm–gyro-Bohm transport model [49] and validated in [23, 46, 49, 50] has been amended to include the ITB threshold condition. The amended set of transport coefficients can be written in the following form:

$$\chi_e = 1.0\chi_{gB} + 2.0\chi_B, \tag{3}$$

$$\chi_i = 0.5\chi_{gB} + 4.0\chi_B + \chi_i^{neo}, \tag{4}$$

$$D = [0.3 + 0.7\rho]\frac{\chi_e\chi_i}{\chi_e + \chi_i}, \tag{5}$$

where

$$\chi_{\mathrm{gB}} = 5 \times 10^{-6} \sqrt{T_{\mathrm{e}}} \left| \frac{\nabla T_{\mathrm{e}}}{B_{\phi}^{2}} \right|, \tag{6}$$

$$\chi_{\mathrm{B}} = \chi_{\mathrm{B}_0} \times \Theta(-0.14 + s - 1.47\Omega) \tag{7}$$

and

$$\chi_{\mathrm{B}_0} = 4 \times 10^{-5} R \left| \frac{\nabla (n_{\mathrm{e}} T_{\mathrm{e}})}{n_{\mathrm{e}} B_{\phi}} \right| q^2 \times \left(\frac{T_{\mathrm{e}}(0.8\rho_{\max}) - T_{\mathrm{e}}(\rho_{\max})}{T_{\mathrm{e}}(\rho_{\max})} \right). \tag{8}$$

In equations (6), (7) and (8), T_{e} and T_{i} are the electron and the ion temperatures, respectively, n_{e} is the electron density, B_{ϕ} the toroidal magnetic field, R the major radius and q is the safety factor. $\chi_{\mathrm{i}}^{\mathrm{neo}}$ is the neo-classical term for the ion heat transport [51]. The non-locality in the Bohm transport appears in the last term where ρ is the flux surface label defined by $\rho = \sqrt{\Phi/\pi B_{\phi}}/a_{\mathrm{eff}}$ with a_{eff} being the radius of the circle covering the same area as the elongated plasma. $\rho_{\max}$ is the value of ρ at the separatrix in the L mode and on top of the barrier in the H mode. Φ is the toroidal magnetic flux. All the quantities appearing in equations (3)–(8) are expressed in SI units except the temperatures T_{e} and T_{i} whose unit is eV. The Θ-function multiplying the modified Bohm transport in equation (7) is the Heaviside step function with the controlling parameter given by the ITB formation threshold condition found in section 3. When the argument in the step function $-0.14 + s - 1.47\Omega = 0$ changes its sign, the ITB either forms ($\Theta(x < 0) = 0$) or collapses ($\Theta(x > 0) = 1$) as already shown in figure 5. Physically, the Bohm-type of anomalous transport χ_{B} is fully suppressed in equations (3)–(5), and the internal transport barrier forms.

The toroidal velocity is calculated from the momentum balance equation using the torque from neutral beam injection as the source term. The anomalous toroidal viscosity coefficient is assumed to be equal to the ion heat transport coefficient as in equation (4). There is experimental evidence on JET and other tokamaks that in the NB heated plasmas, the toroidal viscosity coefficient coincides with the ion heat diffusion coefficient, both radially (at least inside $r/a = 0.8$) and with time [52].

The initial and boundary conditions for the ion and electron quantities as well as the plasma current are taken from the experiment. The initial q-profile is calculated by EFIT and Z_{eff} and P_{rad} are taken from the TRANSP analysis. Also, the power deposition profiles of NBI and ICRH, and the torque are calculated by TRANSP. The standard Monte Carlo model was used for calculating the NB power deposition profiles. For the calculation of the ICRH power deposition profiles, the bounce-averaged Fokker–Planck code [53] was applied in TRANSP calculations.

The time evolution of the average ion and electron temperatures and the volume averaged electron density are shown in figure 7 for the JET OS pulse No 46664. This discharge was chosen here because it is one of the worst cases when compared to the experimental data among the analysed ITB pulses, especially in terms of the ITB formation produced by our model. Thus, it gives some insight into the order of magnitude in the maximum errors calculated by the present transport model with the ITB formation threshold condition. The temperatures, in particular the ion temperature, are overestimated by the transport model. This is due to the ITB threshold condition that triggers the ITB by 0.4 s too early for this discharge.

That the ITB is triggered too early by the model for that particular shot can be seen more clearly in the temperature profiles shown in figure 8. The first time slice at $t = 4.5$ s is before the main heating starts at $t = 5.0$ s and with an L-mode plasma edge. The L–H mode transition occurs at $t = 5.1$ s and the ITB appears at $t = 5.6$ s. However, the present transport model with the ITB threshold condition triggers the barrier already at $t = 5.2$ s, as illustrated by the

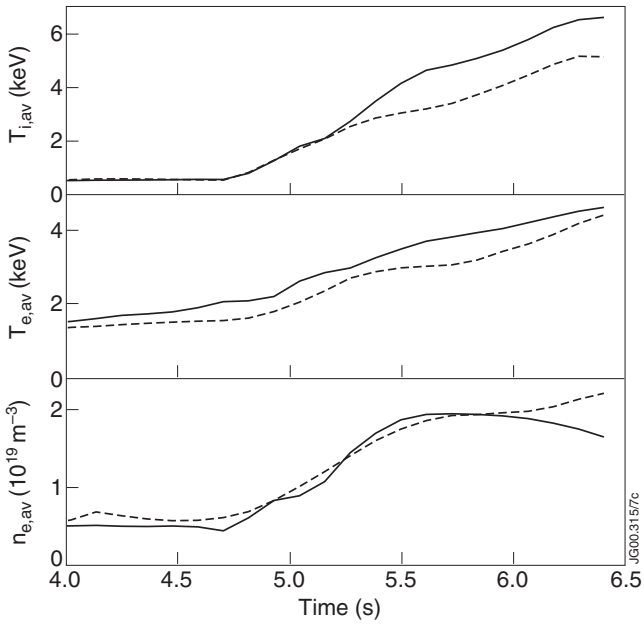

Figure 7. Reproduction of the JET discharge No 46664. Dashed curve corresponds to the experiment and solid curve is calculated by the transport model. The time evolution of the average ion and electron temperatures and the volume averaged electron density are shown.

second time slice in figure 8. Both the temperatures are overestimated and the ITB clearly exists in the simulation curves. The last two time slices describe the highest performance phase where the ITB also exists in the experiment. The model overestimates by 5–7 cm the width of the barrier at $t = 6.0$ s, but later before the disruption at $t = 6.3$ s, the location of the ITB is in agreement with the prediction.

The simulated and experimental density and toroidal velocity profiles are presented at the same instants as the temperatures in figure 9. The simulated toroidal velocity is zero at $t = 4.5$ s because the source term in the toroidal momentum balance equation in the transport model is the torque which is zero before the NBI heating.

A comprehensive predictive analysis includes several JET OS discharges from a wide plasma parameter range of $B_\phi = 1.8$–4.0 T, $P_{\rm in} = 14$–30 MW and $W_{\rm dia} = 3$–12 MJ. The transport model with the ITB threshold condition is identical for all the analysed discharges. To quantify the agreement between the modelling and the experiments, a statistical approach to the simulation results is applied according to the following equations:

$$\sigma_{\rm Y}^2 = \sum_{i=1}^{K} \left(\frac{\sum_{j=1}^{N} [(Y_{\rm exp}(x_j) - Y(x_j))/Y(x_j) - m_{\rm Y,i}]^2}{N} \right) / K, \tag{9}$$

where $m_{\rm Y,i}$ is defined as

$$m_{\rm Y,i} = \sum_{j=1}^{N} \frac{(Y_{\rm exp}(x_j) - Y(x_j))}{Y(x_j)} / N. \tag{10}$$

The quantity $\sigma_{\rm Y}^2$ stands for the variance between the experimental measurement and the modelling result of the quantity Y, which can be in the present case either $n_{\rm e}$, $T_{\rm e}$, $T_{\rm i}$ or v_ϕ. The

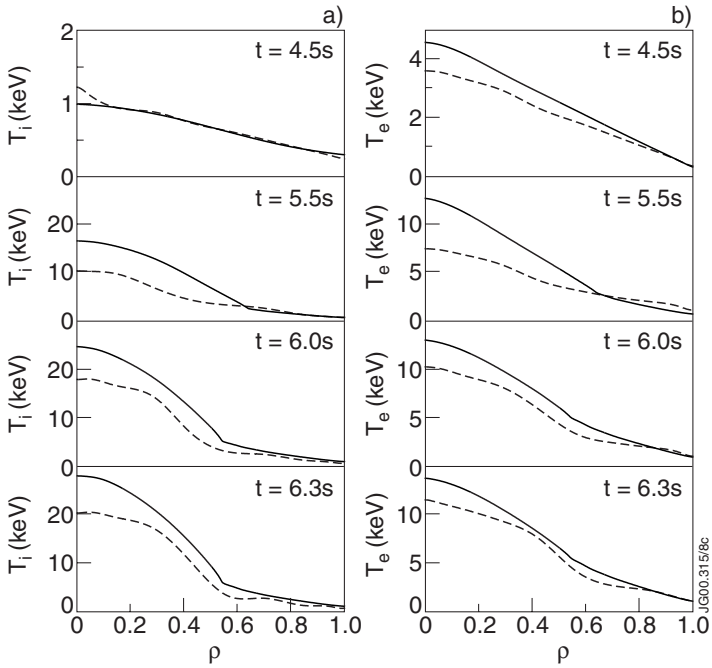

Figure 8. The ion (a) and the electron (b) temperatures at $t = 4.5$ s, $t = 5.5$ s, $t = 6.0$ s and $t = 6.3$ s. Dashed curve corresponds to the experiment and solid curve is calculated by the transport model.

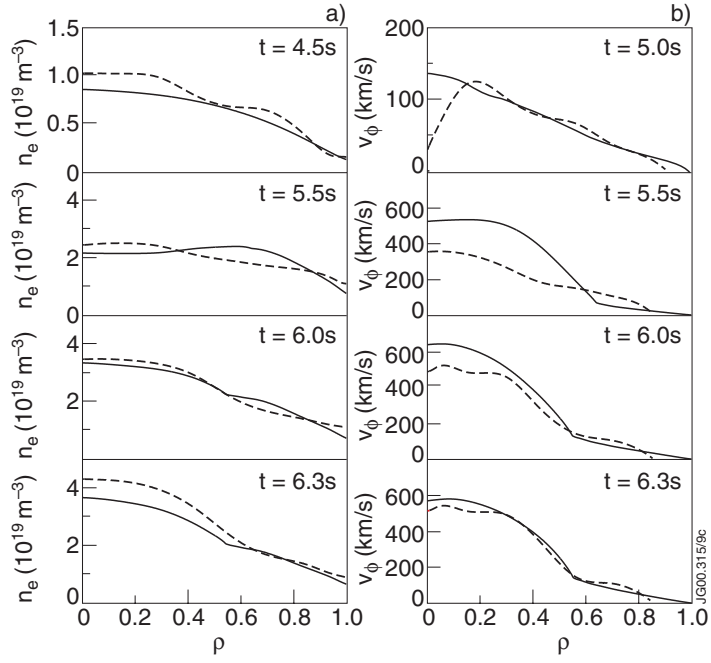

Figure 9. As in figure 8, but for density and toroidal velocity.

calculated quantity $m_{Y,i}$ symbolizes the modelling offset of the quantity Y at time t_i. The inner summation from $j = 1$ to N in equation (9) is over the radial grid points ($N = 301$) from $\rho = 0.0$ to $\rho = 0.8$ and the outer summation $i = 1$ to K is over evenly distributed K time points within the time interval of the simulation, i.e. the instants where the radial profiles have been taken. The reason for using $\rho = 0.8$ as the outermost point in the statistical analysis is that no reliable CXS measurements for v_ϕ are available beyond that radius in JET. $Y_{exp}(x_j)$ is the measured value of the given quantity at the radial point x_j and $Y(x_j)$ is the simulated one at the same point. Consequently, m_Y and σ_Y characterize the time averaged modelling offset and the time-averaged standard deviation, respectively, compared to the measured quantities over the whole duration of the simulation.

Table 1. The prediction uncertainties of the transport simulations.

JET Pulse Number	47843	49196	47170	46664	47413	46998
B_ϕ [T]	1.8	2.5	3.0	3.4	3.4	4.0
P_{in} [MW]	14	16	25	22	30	20
W_{dia} [MJ]	3	4	11	10	12	6
Experimental ITB onset time [s]	2.1	4.4	5.6	5.6	6.2	6.3
Simulated ITB onset time [s]	2.3	4.1	5.4	5.2	6.1	5.7
Exp. ITB width at onset [r/a]	0.42	0.28	0.50	0.44	0.53	0.32
Sim. ITB width at onset [r/a]	0.44	0.28	0.42	0.48	0.42	0.38
Exp. ITB width in highest perf. [r/a]	0.30	0.29	0.54	0.56	0.58	0.33
Sim. ITB width in highest perf. [r/a]	0.41	0.40	0.57	0.57	0.52	0.34
σ_{T_i} [%]	23	17	18	20	17	29
σ_{T_e} [%]	24	9	7	16	15	12
σ_{n_e} [%]	13	11	6	6	7	17
σ_{v_ϕ} [%]	—	9	16	10	19	17

The statistics shown in table 1 indicates that the temperature profiles T_i and T_e generally match the experimental data with prediction errors of the order of 10–25%, thus being of the same order as the experimental measurement errors that are typically within 20% in JET. The accuracy in n_e and v_ϕ profiles is even better, typically the time averaged prediction errors are in the range of 10–20%. There is also a trend that the model triggers the ITB too early (pulse No 47843 is an exception) whereas no similar trend can be observed in the width of the ITB either when it is formed or later during the highest performance phase. Furthermore, the magnitude of the overall simulation error does not depend on the magnetic field nor on any other plasma parameter.

5. Summary and discussions

The physical mechanisms of the ITB formation have been investigated with a significant number of JET OS discharges. The analysis consisted of two different parts. The first one concentrated on studying the experimental ITB data base, determination of the radial electric field and the calculation of the $\omega_{E\times B}$ flow shear and the magnetic shear. The most important result was the derivation of the empirical ITB formation threshold condition in terms of $\omega_{E\times B}$ and s. In the second part, the ITB formation condition was implemented into the JETTO transport code and the ITB formation was tested in a predictive way against several JET OS discharges from a wide plasma parameter range.

The contribution from the toroidal rotation was found to be always the dominant component in the radial electric field in JET. It produces a positive E_r with co-injected NBI, as

is typically the case in JET. When the magnetic shear was plotted as a function of the $\omega_{E\times B}$ flow shear at the onset of the ITB, a clear linear trend, i.e. the ITB formation threshold condition was found. The statistical error of this trend was smaller when the $\omega_{E\times B}$ shearing rate was divided by γ_{ITG}, thus indicating the evident role of the ITG turbulence in the ITB formation. The empirical ITB formation threshold condition takes the form $s = 1.47\omega_{E\times B}/\gamma_{ITG} + 0.14$. By rearranging the terms in the equation one obtains $\omega_{E\times B} > 0.68s\gamma_{ITG} - 0.095\gamma_{ITG}$. This empirical ITB formation condition is valid for flat, weakly positive and positive magnetic shear regions such as found in the JET OS plasmas, but not necessarily for negative magnetic shear plasmas, as is the case with NCS plasmas in DIII-D or RS plasmas in JT-60U or TFTR. The role of Shafranov-shift in the ITB formation on JET turned out to be modest, giving only about a 10% local increase in $\omega_{E\times B}/\gamma_{ITG}$ which is well within the measurement accuracy.

The physical picture of the ITB formation could be the following one: $\omega_{E\times B}$ flow shear must be large enough to tear apart the turbulent eddies thus suppressing the long wave length ITG turbulence (γ_{ITG}) while at the same time the magnetic shear s must be small enough to disconnect the turbulent vortices initially linked together by toroidicity. In addition to toroidal decoupling by small magnetic shear, it can split some global modes and can also make some other beneficial topological modifications in the flux surface geometry. It is also known from theory that negative magnetic shear has a favourable effect on curvature driven instabilities.

The comprehensive predictive analysis included several JET OS discharges from a wide plasma parameter range. The Bohm–gyro-Bohm transport model was amended with the empirical ITB formation condition in JETTO transport code. The predictive simulations reproduce the experiments with time averaged prediction errors of the order of 10–25% in T_i and T_e profiles while the uncertainties in n_e and v_ϕ are in the range of 10–20%. The simulated times of the onset of the ITB compared to the experimental ones are typically within 0.4 s and the simulated ITB widths within 0.1 in r/a throughout the whole simulations. The initial q-profile from EFIT and torque from TRANSP turned out to be the most sensitive input parameters. When the simulations are started early enough, the plasma current has enough time to evolve self-consistently and, as a consequence, the sensitivity to the initial q-profile can be eliminated. The sensitivity of the simulation predictions on the slope (=1.47) in the ITB formation condition $s = 1.47\omega/\gamma_{ITG} + 0.14$ was rather weak. By increasing or decreasing the slope by 40%, advanced or delayd, respectively, the ITB formation time by 0.10-0.25 s, and correspondingly the width of the ITB by 0.05–0.10 in r/a. The sensitivity on the intercept term (= 0.14) was somewhat larger.

Future efforts will be aimed at extending the model to include a treatment of the ETG mode, which may affect the electron transport [54]. In the present work, the ITB formation threshold condition was derived mainly from the ion transport channel, but the same ITB triggering condition was also applied to the electron transport. However, it is likely that the electron temperature profiles would be in better agreement with experiments when the ion and electron transport channels are separated. An important and useful way to proceed in future is to test the ITB formation threshold condition found in this study for discharges from other tokamaks where the plasma parameters and experimental settings, in particular the magnetic shear, are similar to that of the present JET OS operation mode.

Acknowledgments

The authors are grateful to Claude Gormezano for many fruitful discussions during the project. The authors also thank Arthur Peeters for giving useful ideas on approaching the problem. We are also grateful to Carine Giroud for her help in the calculation of the rotation velocities. Special thanks also belong to David Heading and Gerard Corrigan for technical assistance.

References

[1] Levinton F M *et al* 1995 *Phys. Rev. Lett.* **75** 4417
[2] Rice B W *et al* 1996 *Phys. Plasmas* **3** 1983
[3] Fujita T *et al* 1997 *Phys. Rev. Lett.* **78** 2377
[4] Söldner F X *et al* 1999 *Nucl. Fusion* **39** 407
[5] Staebler G M 1998 *Plasma Phys. Control. Fusion* **40** 569
[6] Diamond P H *et al* 1997 *Phys. Rev. Lett.* **78** 1472
[7] Ernst D R *et al* 1998 *Phys. Rev. Lett.* **79** 2454
[8] Synakowski E J 1998 *Plasma Phys. Control. Fusion* **40** 581
[9] Shirai H *et al* 2000 *Plasma Phys. Control. Fusion* **42** A109
[10] Baranov Yu F *et al* 1999 *Nucl. Fusion* **39** 1463
[11] Gruber O *et al* 2000 *Plasma Phys. Control. Fusion* **42** A117
[12] Strait E J *et al* 1995 *Phys. Rev. Lett.* **75** 4421
[13] The JET Team *Plasma Phys. Control. Fusion* **39** B353
[14] Koide Y 1998 *Plasma Phys. Control. Fusion* **40** 641
[15] Burrell K H 1997 *Phys. Plasmas* **4** 1499
[16] Challis C D *et al* 2001 Effect of q-profile modification by LHCD on internal transport barriers in JET *Plasma Phys. Control. Fusion* submitted
[17] Challis C D *et al* 1999 *Proc. 26th European Physical Society Conf. on Controlled Fusion and Plasma Physics (Maastrict, The Netherlands, 14–18 June, 1999) (ECA vol 23J)* p 69
[18] Hogeweij G M D *et al* 1998 *Nucl. Fusion* **38** 1881
[19] Synakowski E J *et al* 1997 *Phys. Rev. Lett.* **78** 2972
[20] Hahm *et al* 2000 *Plasma Phys. Control. Fusion* **42** A205
[21] Conway G D *et al* 2000 *Phys. Rev. Lett.* **84** 1463
[22] Zhu P *et al* 2000 *Phys. Plasmas* **7** 2898
[23] Parail V V *et al* 1999 *Nucl. Fusion* **39** 429
[24] Kinsey J E *et al* 1999 *Proc. 26th European Physical Society Conf. on Controlled Fusion and Plasma Physics (Maastrict, The Netherlands, 14–18 June, 1999) (ECA vol 23J)* p 1205
[25] Hahm T S and Burrell K H 1995 *Phys. Plasmas* **2** 1648
[26] Hamaguchi S and Horton W 1992 *Phys. Fluids B* **4** 319
[27] Weiland J and Hirose A 1992 *Nucl. Fusion* **32** 151
[28] Lao L *et al* 1985 *Nucl. Fusion* **25** 1611
[29] Genacchi G and Taroni A 1988 JETTO: A free boundary plasma transport code (basic version) *Rapporto* ENEA RT/TIB 1988(5)
[30] Tresset G, Litaudon X and Moreau D 2000 A dimensionless criterion for characterising internal transport barriers in tokamaks *Report* DRFC/CAD EUR-CEA-FC-1700 July 2000
[31] Rozhansky V and Tendler M 1992 *Phys. Fluids B* **4** 1877
[32] Shaing K C *et al* 1999 *Phys. Rev. Lett.* **83** 3840
[33] Kim J *et al* 1994 *Phys. Rev. Lett.* **72** 2199
[34] Staebler G M, Waltz R E and Wiley J C 1997 *Nucl. Fusion* **37** 287
[35] Greenfield C M *et al* 2000 *Phys. Plasmas* **7** 1959
[36] Synakowski E J *et al* 1999 *Nucl. Fusion* **39** 1733
[37] Doyle E J *et al* 2000 *Proc. 18th IAEA Fusion Energy Conference (Sorrento, 4–10 October, 2000) IAEA-CN-77/EX6/2*
[38] Sakamoto Y *et al* 2000 *Proc. 18th IAEA Fusion Energy Conference (Sorrento, 4–10 October, 2000) IAEA-CN-77/EX6/4*
[39] Nordman H, Weiland J and Jarmen A 1990 *Nucl. Fusion* **30** 983
[40] Kishimoto Y *et al* 1998 *Plasma Phys. Control. Fusion* **40** A663
[41] Beer M A *et al* 1997 *Phys. Plasmas* **4** 1792
[42] Sydora R D *et al* 1996 *Plasma Phys. Control. Fusion* **38** A281
[43] Dong J Q *et al* 1996 *Phys. Plasmas* **3** 3065
[44] Challis C D *et al* 2001 *Proc. 28th European Physical Society Conf. on Controlled Fusion and Plasma Physics (Madeira, Portugal, 18–22 June, 2001)* in press
[45] Zastrow K-D *et al* 1999 *Proc. 26th European Physical Society Conf. on Controlled Fusion and Plasma Physics (Maastrict, The Netherlands, 14–18 June, 1999) (ECA vol 23J)* p 217
[46] Tala T J J *et al* 2000 *Nucl. Fusion* **40** 1635
[47] Pereverzev G *et al* 1999 *Proc. 26th European Physical Society Conf. on Controlled Fusion and Plasma Physics*

(Maastrict, The Netherlands, 14–18 June, 1999) (ECA vol 23J), p 1429
[48] Voitsekhovitch I *et al* 1999 *Proc. 26th European Physical Society Conf. on Controlled Fusion and Plasma Physics (Maastrict, The Netherlands, 14–18 June, 1999) (ECA vol 23J)*, p 957
[49] Erba M *et al* 1997 *Plasma Phys. Control. Fusion* **39** 261
[50] Erba M *et al* 1996 Validation of a new mixed Bohm/gyro-Bohm transport model on discharges of the ITER data-base *JET Report* JET-R(96)07
[51] Hinton F L, Hazeltine R D 1976 *Rev. Mod. Phys* **48** 239
[52] de Esch H P L, Stork D, Weisen H 1990 *Proc. 17th European Physical Society Conf. on Controlled Fusion and Plasma Physics (Amsterdam, The Netherlands, 25–29 June, 1990) (ECA vol 14B)* p 90
[53] Smithe D N *et al* 1989 *Proc. 8th Topical Conf. on Radio-Frequency Power in Plasmas (AIP, New York)* p 338
[54] Jenko F *et al* 2000 *Phys. Plasmas* **7** 1904

PUBLICATION 2

Comparison of theory-based and semi-empirical transport modelling in JET plasmas with ITBs

Accepted for publication in Plasma Physics and Controlled Fusion
2002. Vol. 44. 6 p.

http://www.iop.org/journals/ppcf

INSTITUTE OF PHYSICS PUBLISHING PLASMA PHYSICS AND CONTROLLED FUSION

Plasma Phys. Control. Fusion **44** (2002). 6 p. PII: S0741-3335(02)34449-X

Comparison of theory-based and semi-empirical transport modelling in JET plasmas with ITBs

T J J Tala[1], V V Parail[2], A Becoulet[3], G Corrigan[2], D J Heading[2], M J Mantsinen[4], P I Strand[5] and contributors to the EFDA-JET Workprogramme[6]

[1] Association Euratom-Tekes, VTT Chemical Technology, PO Box 1404, FIN-02044 VTT, Finland
[2] Euratom/UKAEA Fusion Association, Culham Science Centre, Abingdon, Oxon OX14 3DB, UK
[3] Association Euratom-CEA, CEA-Cadarache, F-13108, St Paul lez Durance, France
[4] Association Euratom-Tekes, Helsinki University of Technology, FIN-02015 TKK, Finland
[5] Oak Ridge National Laboratory, Oak Ridge, TN 37831, USA

Received 5 September 2001
Published
Online at stacks.iop.org/PPCF/44

Abstract

The theory-based Weiland transport model has been applied to JET discharges with internal transport barriers (ITBs) for the first time. The agreement of the modelling results with the experiments has been found to be comparable with the agreement of the modelling results produced by the semi-empirical Bohm/gyro-Bohm transport model. Weiland model overestimates the width of the ITB and the electron temperature. There is evidence that the density gradient in the Weiland model plays a more important role in governing the ITB formation dynamics for JET discharges than the suppression of turbulence by the $\omega_{E\times B}$ flow shearing rate.

1. Introduction

The internal transport barrier (ITB) formation and dynamics have been modelled in a detailed way with the Bohm/gyro-Bohm semi-empirical transport model [1] in JET [2–4]. The modelling results have been found to be in good agreement with the experiments. In order to further improve the understanding of the ITB physics, theory-based transport modelling of JET plasmas with ITBs is needed. In this paper, the theory-based Weiland transport model [5–8] is used to predict the physics of optimized shear (OS) discharges with ITBs. Furthermore, a comparison of the modelling results between the two models and experiments is presented.

Several mechanisms, such as $\omega_{E\times B}$ flow shear, negative or small magnetic shear s, rational surfaces of q, Shafranov shift, density gradient versus temperature gradient, etc, are known

[6] See Annex of Pamela J *et al* 2001 Overview of recent JET results and future perspectives, Fusion Energy 2000 *Proc. 18th Int. Conf. Sorrento, 2000* (Vienna: IAEA).

to have a contribution to the ITB physics. In the Bohm/gyro-Bohm transport model, the ITB formation and dynamics are interpreted with the combination of the $\omega_{E\times B}$ flow shear and the magnetic shear s [4]. In this paper, the main contributors to the ITB formation in JET plasmas given by the Weiland model are sought.

2. Weiland and Bohm/gyro-Bohm transport models

The empirical Bohm/gyro-Bohm transport in JETTO can be written in the following way:

$$\chi_{\rm e} = 1.0\chi_{\rm gB} + 2.0\chi_{\rm B} + \chi_{\text{neo-al}}, \tag{1}$$

$$\chi_{\rm i} = 0.5\chi_{\rm gB} + 4.0\chi_{\rm B} + \chi_{\rm i}^{\rm neo}, \tag{2}$$

$$D = [0.3 + 0.7\rho]\frac{\chi_{\rm e}\chi_{\rm i}}{\chi_{\rm e} + \chi_{\rm i}}, \tag{3}$$

where

$$\chi_{\rm gB} = 5 \times 10^{-6}\sqrt{T_{\rm e}}\left|\frac{\nabla T_{\rm e}}{B_\phi^2}\right|, \tag{4}$$

$$\chi_{\rm B} = \chi_{\rm B_0} \times \Theta\left(-0.14 + s - \frac{1.47\omega_{E\times B}}{\gamma_{\rm ITG}}\right), \tag{5}$$

with

$$\chi_{\rm B_0} = 4 \times 10^{-5} R\left|\frac{\nabla(n_{\rm e}T_{\rm e})}{n_{\rm e}B_\phi}\right| q^2\left(\frac{T_{\rm e}(0.8\rho_{\rm max}) - T_{\rm e}(\rho_{\rm max})}{T_{\rm e}(\rho_{\rm max})}\right) \tag{6}$$

and

$$\chi_{\text{neo-al}} = \frac{c^2 v_{\rm th}}{\omega_{\rm pe}^2 q R}\epsilon. \tag{7}$$

In equations (4)–(7), $T_{\rm e}$ and $T_{\rm i}$ are the electron and the ion temperatures, respectively, $n_{\rm e}$ is the electron density, B_ϕ is the toroidal magnetic field, c is the speed of light, $v_{\rm th}$ and $\omega_{\rm pe}$ are the electron thermal velocity and plasma frequency as well as R is the major radius and ϵ is the inverse aspect ratio. $\chi_{\rm i}^{\rm neo}$ is the neoclassical term for the ion heat transport [9] and $\chi_{\text{neo-al}}$ term represents transport arising from ETG modes and has a similar form to one proposed by Ohkawa [10]. $\omega_{E\times B}$ is the flow shearing rate by Hahm–Burrell [11] and $\gamma_{\rm ITG}$ is the linear growth rate defined as $\gamma_{\rm ITG} = v_{\rm th,i}/R$ with $v_{\rm th,i}$ being the ion thermal velocity. The Θ function multiplying the Bohm transport in equation (5) is the Heaviside step function with the controlling parameter given by the ITB formation threshold condition found in [4].

The transport coefficients in JETTO with the implemented Weiland model have the following form:

$$\chi_{\rm e} = \chi_{\rm e,weil} + \chi_{\text{neo-al}}, \tag{8}$$

$$\chi_{\rm i} = \chi_{\rm i,weil} + \chi_{\rm i}^{\rm neo}, \tag{9}$$

$$D = D_{\rm weil}, \tag{10}$$

where $\chi_{\rm e,weil}$, $\chi_{\rm i,weil}$ and $D_{\rm weil}$ are the transport coefficients from the ITG and TEM turbulence calculated by the Weiland model [5–8]. There are two important issues worth mentioning in the present implementation of the Weiland model in JETTO. First, there is no numerical fitting parameter in the present implementation and second, there is no additional term giving some extra transport in the edge region as in the most implementations of the Weiland model.

The initial and boundary conditions for the ion and electron quantities as well as the plasma current are taken from the experiment. The initial q-profile is calculated by EFIT because the

simulations start well before NBI and no MSE measurements are available, and $Z_{\rm eff}$ and $P_{\rm rad}$ are taken from the TRANSP analysis. Also, the power deposition profiles of NBI and ICRH, and the torque are calculated by TRANSP. Experimental values for the toroidal velocity are used. The poloidal rotation is assumed to be neoclassical.

3. Comparison of the modelling results calculated by the two transport models

The time evolution of a typical JET OS discharge is illustrated in figure 1. The magnetic field was 3.4 T, and the plasma current (peak) 3.4 MA. This pulse was selected because it had a very strong and clear ITB formation (ITB formation criterion taken from [12]), both in time and space. The discharge ended up with a disruption due to the emergence of a pressure-driven kink instability at $t = 6.5$ s.

The modelling results are compared with the experiment in figure 2. The following issues can be concluded. Both models produce an ITB, the onset time of the ITB is reproduced within 0.1 s accuracy with the Weiland model, but only within 0.3 s accuracy with the Bohm/gyro-Bohm model. On the other hand, the width of the ITB is clearly better reproduced with the Bohm/gyro-Bohm model than with the Weiland model. The Bohm/gyro-Bohm model overestimates the central ion temperature, whereas the Weiland model overestimates the density. The overestimated density by the Weiland model can be one reason for the overestimation of the width of the ITB. Both models overestimate the electron temperature. In addition, the Weiland model overestimates all the quantities in Ohmic state before $t = 4.7$ s when NBI heating starts and the plasma goes to L mode. In L mode, the Weiland model reproduces the ion temperature very well, but overestimates the density. These discrepancies are likely due to the absence of the edge transport mechanism in the present simulations.

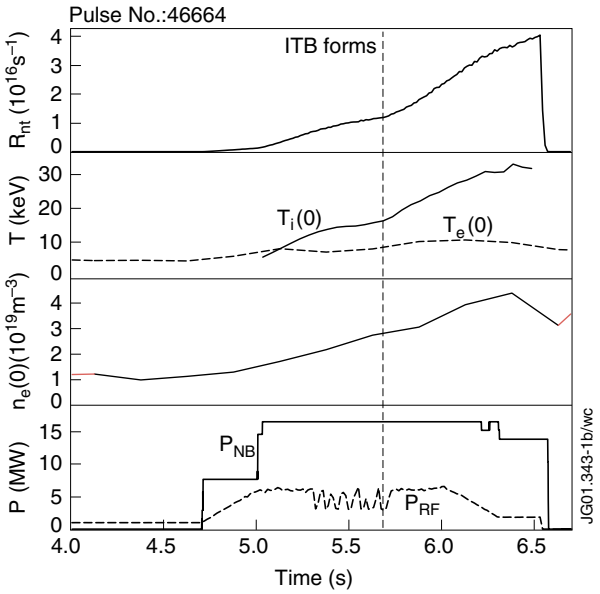

Figure 1. Time traces of the neutron rate $R_{\rm nt}$, the central ion $T_{\rm i}$ and electron $T_{\rm e}$ temperatures, the central electron density $n_{\rm e}$ and the heating powers $P_{\rm NB}$ and $P_{\rm RF}$ for the OS discharge pulse no 46664. ITB appears at $t = 5.6$ s (shown by the vertical dashed line) and L–H mode transition occurs at $t = 5.1$ s.

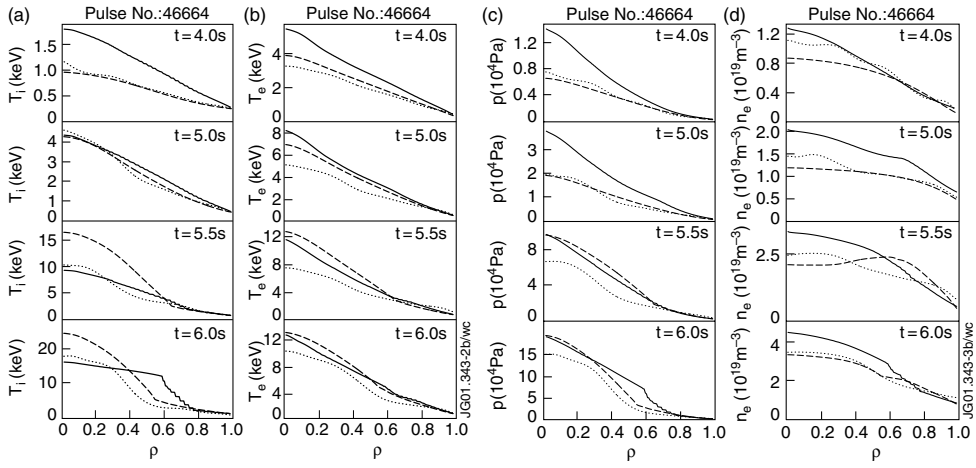

Figure 2. Ion temperature (*a*), electron temperature (*b*), pressure (*c*) and electron density (*d*) profiles at four different instants. The dashed curve corresponds to the modelling predictions by the Bohm/gyro-Bohm model, the solid one by the Weiland model and the dotted curve is the experiment.

The transport coefficients tend to peak at 80–90% of the minor radius and then decrease due to their $T_e^{1.5}$ dependence. An additional edge transport mechanism is likely to offset the overprediction of the temperatures in Ohmic state and density in L mode. The agreement in the width of the ITB and in the temperature profiles between the experimental and modelling results would be better if the density were taken from the experiment rather than modelled. However, this would reduce the self-consistency and make the transport model comparison less fair.

4. The main mechanisms of the ITB formation for JET pulses according to the Weiland model

The effect of the $\omega_{E\times B}$ shearing rate on ITB formation and temperature profiles calculated with the Weiland model is studied in figure 3. What is surprising is that there is almost no difference between the case with the actual shearing rate (solid curve) where the shearing rate is calculated from [11] using experimental data and the case with zero shearing rate (dotted curve). However, both cases exhibit a clearly visible ITB. Moreover, with five times larger shearing rate (dashed curve, the actual shearing rate multiplied by 5), the ITB appears earlier, but it is not significantly wider. Therefore, the importance of $\omega_{E\times B}$ shearing rate seems to be questionable according to the Weiland model; thus, there must be something else that governs the ITB dynamics in the Weiland model.

The next study concerns the effect of the density gradient on ITB formation. The first simulation is the same simulation with the actual $\omega_{E\times B}$ shearing rate as the solid curve in figure 3 and the second one is identical except the NBI particle source is switched off (NBI power is still the same). The comparison is illustrated in figure 4. The staircase feature on the outer side of the ITB, evident in particular in T_i profiles in figures 2(*a*), 3(*a*) and 4(*c*), has a limit cycle character and stems from the model balancing at marginality over the barrier region.

The following conclusions can be drawn: because the density gradient is much smaller without the NBI particle source, ITG and TEM turbulence is not suppressed and as a consequence, an ITB does not form which then leads to significantly poorer confinement

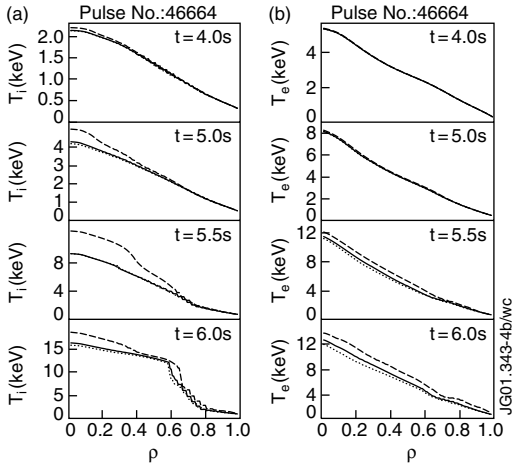

Figure 3. Modelled ion (*a*) and electron (*b*) temperature profiles at four different instants. The solid curve corresponds to the simulation with the actual shearing rate, the dotted one with $\omega_{E\times B} = 0$ and the dashed one with five times larger shearing rate than the actual one.

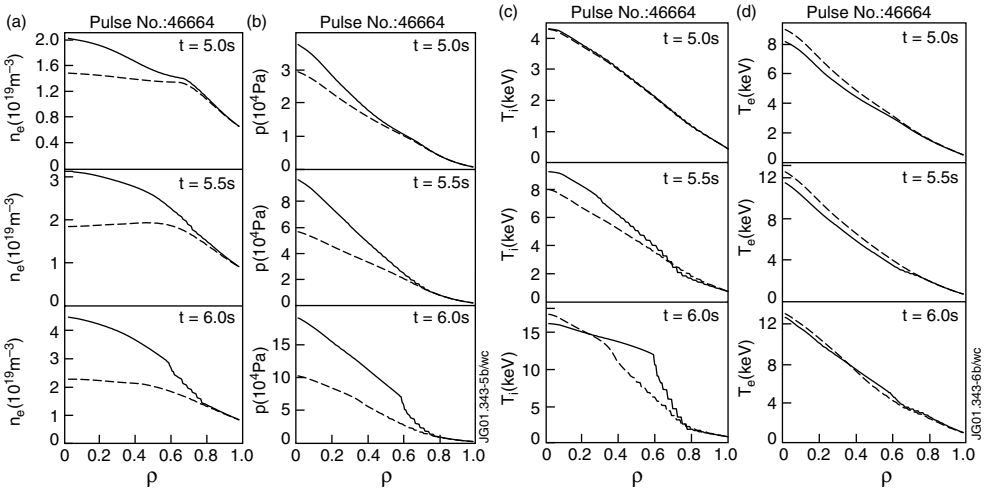

Figure 4. Electron density (*a*), pressure (*b*), ion tmeperature (*c*) and electron temperature (*d*) profiles at three different instants. The solid curve corresponds to the modelling with the NBI particle source, and the dashed one without it.

and smaller pressure. The volume average temperatures are almost the same between the cases, but the ITB is clearly missing in figure 4(*c*) without the NBI particle source (dashed curve).

5. Conclusions

The first results of the application of the Weiland transport model to JET discharges with ITBs are rather encouraging—ITBs are reproduced with prediction errors not much larger than with the extensively validated Bohm/gyro-Bohm semi-empirical transport model. Very

importantly, no numerical fitting parameters exist in the present JETTO implementation of the Weiland model in contrast to the Bohm/gyro-Bohm model. Furthermore, as mentioned earlier, adding some additional edge transport, such as a fraction from the Bohm transport term equation (5) to the terms in equations (8) and (9), the agreement with the experiments will be even better.

In the Weiland model, the importance of the density gradient seems to dominate the effect of the $\omega_{E\times B}$ shearing rate in ITB formation. On the other hand, as found earlier in the analyses with the Bohm/gyro-Bohm transport model, small or negative magnetic shear also plays a crucial role in the ITB physics on top of the $\omega_{E\times B}$ shearing rate [4]. However, magnetic shear effects are not taken into account in this version of the Weiland model nearly as strongly as in the Bohm/gyro-Bohm model. This is an area that needs further work. Moreover, neither model takes into account the rational surfaces of the q-profile which are found to play a role in the ITB formation [13]. Another important task is to improve the numerical stability of the Weiland model with pulses that have ITBs.

Acknowledgments

The authors are grateful to Jan Weiland and Clive Challis for many fruitful discussions.

References

[1] Erba M *et al* 1997 *Plasma Phys. Control. Fusion* **39** 261
[2] Parail V V *et al* 1999 *Nucl. Fusion* **39** 429
[3] Tala T J J *et al* 2000 *Nucl. Fusion* **40** 1635
[4] Tala T J J *et al* 2001 *Plasma Phys. Control. Fusion* **43** 507
[5] Jarmen A, Andersson P and Weiland J 1987 *Nucl. Fusion* **27** 941
[6] Nordman H, Weiland J and Jarmen A 1990 *Nucl. Fusion* **30** 938
[7] Weiland J and Hirose A 1992 *Nucl. Fusion* **32** 151
[8] Strand P, Nordman H, Weiland J and Christiansen J 1998 *Nucl. Fusion* **38** 545
[9] Hinton F L and Hazeltine R D 1976 *Rev. Mod. Phys.* **48** 239
[10] Ohkawa T 1978 *Phys. Lett.* A **67** 35
[11] Hahm T S and Burrell K H 1995 *Phys. Plasmas* **2** 1648
[12] Tresset G *et al* 2001 A dimensionless criterion for characterising internal transport barriers in JET *Nucl. Fusion* submitted
[13] Challis C D *et al* 2001 *Plasma Phys. Control. Fusion* **43** 861

PUBLICATION 3

Impact of different heating and current drive methods on the early *q*-profile evolution in JET

Accepted for publication in Plasma Physics and Controlled Fusion
2002. Vol. 43. 22 p.

http://www.iop.org/journals/ppcf

INSTITUTE OF PHYSICS PUBLISHING PLASMA PHYSICS AND CONTROLLED FUSION

Plasma Phys. Control. Fusion **43** (2002). 22 p. PII: S0741-3335(01)26967-X

Impact of different heating and current drive methods on the early q-profile evolution in JET

T J J Tala[1], V V Parail[2], A Becoulet[3], C D Challis[2], G Corrigan[2], N C Hawkes[2], D J Heading[2], M J Mantsinen[4], S Nowak[5] and contributors to the EFDA-JET work programme[6]

[1] Association Euratom-Tekes, VTT Chemical Technology, PO Box 1404, FIN-02044 VTT, Finland
[2] Euratom/UKAEA Fusion Association, Culham Science Centre, Abingdon, Oxon OX14 3DB, UK
[3] Association Euratom–CEA, CEA-Cadarache, F-13108, St. Paul lez Durance, France
[4] Association Euratom–Tekes, Helsinki University of Technology, FIN-02015 TKK, Finland
[5] Association Euratom–ENEA-CNR, Istituto di Fisica del Plasma, Via Bassini 15, 20133, Milano, Italy

Received 19 July 2001
Published
Online at stacks.iop.org/PPCF/43

Abstract

Transport calculations illustrate that the lower hybrid current drive (LHCD) and off-axis electron cyclotron current drive (ECCD) are the only preheating methods that can create a wide, deeply reversed q-profile, i.e. large negative magnetic shear, on the JET tokamak. Off-axis neutral beam injection (NBI) and off-axis ion cyclotron resonance heating (ICRH) preheating yields a weakly reversed q-profile (small negative magnetic shear), whereas NBI and ICRH on-axis heating as well as ohmic preheating produce a monotonic q-profile in the preheating phase. Here, on-axis power deposition and current drive refers to heating and current drive at or close to magnetic axis and correspondingly, off-axis refers to heating and current drive deposited typically around the half minor radius ($r/a = 0.3$–0.6). The results on LHCD, ICRH and ohmic preheating have been verified in the recent JET experiments. The current drive efficiency scan shows that in the case of LHCD, ECCD and off-axis NBI, the driven current is absolutely crucial to obtain a reversed q-profile and to modify the current profile evolution drastically in the preheating phase. Taking into account only the direct electron heating effect, LHCD does not create a reversed q-profile. The timing scans indicate that the radial location of $q_{\min}$ at the end of the preheating phase is generally quite insensitive to the start time of the preheating, once started 0–2 s after the plasma initiation if the method relies upon the driven current. On the other hand, methods relying only upon electron heating are very sensitive to that. In both cases, the magnitude of the negative magnetic shear, however, seems to be very sensitive to the start time of the preheating.

[6] See Pamela J *et al* 2001 Overview of recent JET results and future perspectives *Fusion Energy 2000 (Proc. 18th Int. Conf. Sorrento, 2000)* (Vienna: IAEA) annex.

0741-3335/01/010001+22$30.00

1. Introduction

Tokamak plasma operation with weak or negative magnetic shear and with an internal transport barrier (ITB) is now regarded as the most promising way to increase fusion performance. A hollow current density profile, i.e. a reversed q-profile (negative magnetic shear), is one of the key conditions that gives rise to the improved core confinement and facilitates the formation of the ITB in advanced tokamak scenarios [1–4].

There are several ways in which magnetic shear s affects transport, including ITB formation and sustainment. With negative magnetive shear $s < 0$, ballooning modes enter the second stable region [5, 6] with complete stability to $n = \infty$ ideal MHD ballooning modes [7]. The negative magnetic shear also reduces the geodesic curvature drive of micro-instabilities, such as ion temperature gradient (ITG) modes, trapped electron modes (TEMs) and high-n ballooning modes [8] and also reduces magnetic stress [9]. Furthermore, it has also been shown that $s < 0$ can reverse the toroidal precession drifts of barely trapped electrons [10]. Even some of the high-k turbulences, such as electron temperature gradient (ETG) turbulence, can be stabilized by a region with negative magnetic shear [11, 12]. In the region where $s \approx 0$, the turbulent vortices, initially linked together by toroidicity, are more easily disconnected than with large values of s, thus giving rise to improved plasma confinement. In JET, the effect of the magnetic shear on the evolution of the ITB has been recently analysed in [13].

In order to have the desired q-profile with all its aforementioned beneficial effects during the high power and plasma performance phase of a tokamak discharge, a successful preparation phase is required to create the appropriate target q-profile. The preparation phase in the context of this work is called the preheating phase and defined as the time between plasma initiation and the large increase in the heating power (called main heating or high power phase), typically having the heating power 3–10 higher than in the preheating phase. The preheating phase lasts typically 2.5–4.0 s in optimized shear (OS) scenarios in JET. It is also the phase when most of the current ramp up occurs. High plasma current is necessary for good confinement, but current ramp up also plays an important role in establishing the appropriate q-profile. The purpose of the preheating phase is to bring the plasma to an optimum state for experiments to be conducted at high power phase which further takes advantage of the created q-profile via the long current diffusion time at high electron temperature in JET. The most important quantity that is to be optimized in the preheating phase is the q-profile. Other plasma parameters that may be of interest to be modified are pressure and plasma rotation. In addition, avoidance of MHD modes, such as the external kink mode, is also an essential part of the preheating phase as these can cause anomalous current penetration or plasma disruption.

The target q-profile is defined to be the q-profile at the end of the preheating phase. In the context of this study, the following definitions for the shapes of the target q-profiles as illustrated in table 1 are used. In table 1, q_0 denotes the value of q on the magnetic axis R_0 and q_{95} is the corresponding value at 95% of the poloidal flux ($\psi/\psi_{\max} = 0.95$).

There are several ways to modify the q-profile in the preheating phase, i.e. to create the target q-profile. The method by which to obtain a reversed q-profile is in principle simple—either to drive off-axis co-current, on-axis counter-current or alternatively to increase the electron temperature in order to slow down the current diffusion from the plasma edge to the

Table 1. Definitions for the shape of the q-profile.

Monotonic q-profile	$q_{\min} = q_0$
Weakly reversed q-profile	$q_{\min} < q_0 < q_{95}$
Deeply reversed q-profile	$q_0 > q_{95}$

centre during the current ramp-up phase. In DIII-D and TFTR, the negative central shear plasmas are formed in the preheating phase with a high power co- or counter neutral beam injection (NBI) together with fast current ramp up [1, 14, 15]. The applicability of electron cyclotron resonance heating (ECRH) and electron cyclotron current drive (ECCD) in the modification of the q-profile has also been demonstrated in DIII-D [12, 16]. Early neutral beam preheating during the current ramp-up is also used in JT-60U to produce the reversed q-profile [3, 17]. In the ASDEX Upgrade, the q-profile is modified in the preheating phase with NBI alone or with a combination of NBI and co- or counter ECCD [4]. In JET, the preheating phase normally consists either of lower hybrid current drive (LHCD) or ion cyclotron resonance heating (ICRH).

Recent JET experiments with motional Stark effect (MSE) measurements show that LHCD preheating can create a deeply reversed q-profile, while ICRH off-axis preheating creates a weakly reversed q-profile and a monotonic q-profile is created by ohmic preheating. Moreover, the recent results on JET also confirm that high performance plasmas with only a moderate heating power can be reached with a reversed q-profile whereas with a monotonic q-profile, more power is needed to trigger the ITB and reach the same performance [18]. However, it still not clear what the optimum target q-profile should be—deeply reversed, weakly reversed or monotonic. In order to assess and optimize how much off-axis current one can or should drive, which radial location to drive it, and where to deposit the external electron heating power so that the desired target q-profile could be achieved, detailed modelling of the current density profile evolution is required. The modelling should also test and compare other preheating and current drive methods with those already used in the experiments on JET.

Detailed modelling of the preheating phase, including the comparison of different heating methods during that phase, is lacking at present. Combined kinetic and transport modelling of LHCD and ECCD has been recently analysed in [19]. In this work, complex current profile control scenarios have been studied, concentrating on the predictive modelling of the establishment of the ITB and the control of the ITB with LHCD and ECCD in the main heating phase. The effect of NBI power deposition and current evolution on the ITB formation has been studied in [20]. It was found that, aside from the total input power, the details in power deposition and current density profiles play an essential role in determining the ITB formation threshold power. However, neither of these studies concerned or compared the effect of different heating methods on the q-profile evolution in the preheating phase.

In the present work, the current profile evolution during the preheating phase in JET has been calculated with the JETTO transport code [21] assuming neoclassical electrical conductivity. The following preheating methods are considered and compared: ohmic, LHCD, on-axis and off-axis ICRH, on-axis and off-axis NBI as well as ECCD. The basic principle used in this study is that the power deposition and external current density profiles are calculated in a self-consistent way. Consequently, the codes to calculate the power deposition profiles are coupled to JETTO to allow a self-consistent simulation cycle between the transport and power deposition (plus current density) calculation with time. This means that all the plasma profiles (such as T_e, T_i, n_e, q, B_ϕ, B_θ, I_p, Z_{eff} etc) are given as input from JETTO to the heating codes and correspondingly, the heating codes return the power deposition and externally driven current density profiles back to JETTO so that the transport calculation can further proceed. At present there are LHCD, NBI and ECCD modules coupled to JETTO, but no ICRH module has been found that would calculate the power deposition profiles roughly within the same time scale as the transport calculations are performed. Thus, ICRH power deposition profiles are calculated by a separate code.

This paper is organized in the following way. Section 2 introduces the transport model and the modelling of the different heating methods, i.e. the calculation of the power deposition

and current density profiles self-consistently with transport. In section 3, experimental results on the effect of different preheating methods on the q-profile evolution in the preheating phase are presented. In addition, experimentally measured q-profiles are compared with the calculated ones. Predictive transport modelling with different preheating methods are analysed in section 4. The preheating methods are compared with each other and current drive efficiency and the effect of varying the duration of the preheating phase are illustrated. The conclusions with a summary are discussed in section 5.

2. Modelling of transport and different heating methods

The current density evolution in JETTO transport code [21] is calculated according to the Faraday equation assuming neoclassical electrical conductivity [22]. All the external current sources, such as LH and NB driven current as well as current driven by ECCD, in addition to ohmic and bootstrap current, are taken into account.

The heat transport model is an empirical transport model which is based on a combination of a Bohm and a gyro-Bohm type of anomalous transport. The model has been tested against several different plasma discharges performed on DIII-D, TFTR, JT-60U, ASDEX-U, START and JET in L mode and against many different plasma shots performed on JET in H mode [23–26]. Recently, it has been amended to include an empirical ITB formation threshold condition found in JET [13]. The set of the heat transport coefficients with the ITB threshold condition can be written in the following form:

$$\chi_{\mathrm{e}} = 1.0\chi_{\mathrm{gB}} + 2.0\chi_{\mathrm{B}} + \chi_{\mathrm{neo-al}} \tag{1}$$

$$\chi_{\mathrm{i}} = 0.5\chi_{\mathrm{gB}} + 4.0\chi_{\mathrm{B}} + \chi_{\mathrm{i}}^{\mathrm{neo}} \tag{2}$$

where

$$\chi_{\mathrm{gB}} = 5 \times 10^{-6}\sqrt{T_{\mathrm{e}}}\left|\frac{\nabla T_{\mathrm{e}}}{B_{\phi}^{2}}\right| \tag{3}$$

$$\chi_{\mathrm{B}} = \chi_{\mathrm{B}_0} \times \Theta(-0.14 + s - 1.47\omega_{E\times B}/\gamma_{\mathrm{ITG}}) \tag{4}$$

with

$$\chi_{\mathrm{B}_0} = 4 \times 10^{-5} R\left|\frac{\nabla(n_{\mathrm{e}}T_{\mathrm{e}})}{n_{\mathrm{e}}B_{\phi}}\right| q^{2}\left(\frac{T_{\mathrm{e}}(0.8\rho_{\max}) - T_{\mathrm{e}}(\rho_{\max})}{T_{\mathrm{e}}(\rho_{\max})}\right) \tag{5}$$

and

$$\chi_{\mathrm{neo-al}} = \frac{c^{2}v_{\mathrm{th}}}{\omega_{\mathrm{pe}}^{2}qR}\epsilon. \tag{6}$$

In (3)–(6), T_{e} and T_{i} are the electron and the ion temperatures, respectively, n_{e} is the electron density, B_{ϕ} the toroidal magnetic field, c the speed of light, v_{th} and ω_{pe} are the electron thermal velocity and plasma frequency and R is the major radius and ϵ the inverse aspect ratio. All the units appearing in (1)–(6) are in SI units except T_{i} and T_{e} whose units are eV. $\chi_{\mathrm{i}}^{\mathrm{neo}}$ is the neoclassical term for the ion heat transport [27]. $\chi_{\mathrm{neo-al}}$ represents transport arising from ETG modes and has a similar form that proposed by Ohkawa [28]. Recently, this form of ETG transport has been supported by nonlinear gyrokinetic calculations and was found to match experiments reasonably well [29].

The Θ-function multiplying the Bohm transport in (4) is the Heaviside step function with the controlling parameter given by the ITB formation threshold condition found in [13]. When the argument x in the step function $x = -0.14 + s - 1.47\omega_{E\times B}/\gamma_{\mathrm{ITG}}$ changes its sign, the ITB

either forms ($\Theta(x < 0) = 0$) or collapses ($\Theta(x > 0) = 1$). $\omega_{E\times B}$ stands for the flow shearing rate defined as

$$\omega_{E\times B} = \left| \frac{RB_\theta^2}{B_\phi} \frac{\partial}{\partial \Psi} \frac{E_\mathrm{r}}{RB_\theta} \right|$$

corresponding to [30] (Ψ is the poloidal flux, E_r is the radial electric field and B_θ is the poloidal magnetic field) and γ_ITG is the linear growth rate of the ITG instability, defined as $\gamma_\mathrm{ITG} = v_\mathrm{th,i}/R$ with $v_\mathrm{th,i}$ being the ion thermal velocity. Physically, the Bohm-type of anomalous transport χ_B (in (1) and (2)) is fully suppressed in regions where the condition $-0.14 + s - 1.47\omega_{E\times B}/\gamma_\mathrm{ITG} \leqslant 0$ is fulfilled, and the internal transport barrier forms. In the preheating phase, the contribution from the magnetic shear s is clearly the dominant term in the ITB threshold condition because $\omega_{E\times B}$ is small with a small input power, especially in the absence of NBI. Recent experiments on JET have also verified that ITBs in the preheating phase are controlled mainly by s, having an ITB existing roughly in regions where $s \lesssim 0$. On the contrary, in the main heating phase there are often two ITBs at the same time, and the outer one is controlled not only by s, but by the $\omega_{E\times B}$ shearing rate and rational surfaces of q [13, 18, 31, 32].

The particle transport is not modelled, but the density is taken from the experiments except in the case of NBI when the density varies with time in the preheating phase and can be much larger than with other preheating methods. Therefore, the amount of externally driven current, like NBI driven current, decreases. The particle diffusion coefficient for the NBI preheated plasmas is defined as $D \propto \chi_\mathrm{e}\chi_\mathrm{i}/(\chi_\mathrm{e} + \chi_\mathrm{i})$. The initial and boundary conditions for the ion and electron temperatures as well as the plasma current are taken from the experiment. Also, experimental values for Z_eff and P_rad are used.

Toroidal velocity is calculated from the momentum balance equation using the torque from neutral beam injection as the source term. The anomalous toroidal viscosity coefficient is assumed to be equal to the ion heat transport coefficient given in (2). There is experimental evidence on JET, and other tokamaks, that in the NB heated plasmas, the toroidal viscosity coefficient coincides with the ion heat diffusion coefficient, both radially (at least inside $r/a = 0.8$) and as a function of time [33]. However, the contribution from the toroidal rotation is almost negligible in the preheating phase, especially for plasmas without NBI. The poloidal rotation is assumed to be neoclassical.

The most critical assumption in the transport model, especially when investigating the q-profile evolution during the preheating phase, is the initial q-profile. Normally no MSE magnetic measurements are available at the beginning or at the time of the preheating phase on JET and consequently, the initial q-profile must be taken from the EFIT [34] calculation that uses magnetics only. Therefore, in order to reach the maximum accuracy and consistency in the calculation of the q-profile evolution, the simulations must be started immediately after the plasma initialisation (plasma initialization at $t \approx 0.5$, simulation started at $t \approx 0.5$–1.0 s). As a consequence, the inaccuracy in the q-profile evolution coming from the initial q-profile is minimized. In addition, this procedure ensures that the calculated current has the longest time to evolve with neoclassical conductivity in order to reach the maximum consistency with neoclassical theory.

The power deposition and current density profiles of LHCD are calculated with the fast ray tracing code (FRTC) [35]. FRTC includes a fast ray-tracing package and the calculation of the power deposition and current density profiles by iteration between the evaluation of the quasi-linear diffusion coefficient and a one-dimensional (1D) Fokker–Planck equation for the electron distribution function. A comprehensive study of its properties was reported in [36]. FRTC is coupled to JETTO, thus allowing self-consistent simulations between transport

and lower hybrid (LH) power and current calculation. The coupled JETTO/FRTC code was validated in [23].

In order to calculate the NBI power deposition and current density profiles, the NBI code PENCIL [37] is used. PENCIL is also coupled to JETTO. It solves a simplified Fokker–Planck equation that is used to describe the fast ion dynamics. Fast ion self-collisions and the effects of toroidal electric field on the fast ion dynamics are neglected. The resulting bounce averaged Fokker–Planck equation is then solved using an eigenfunction expansion in the pitch angle variable. On-axis/off-axis power deposition profiles are produced by an appropriate selection between the normal and tangential PINIs, normal PINIs producing NBI power perpendicular to the toroidal direction (on-axis power deposition) and tangential PINIs at angles smaller than 90° with respect to the toroidal direction (off-axis power deposition).

The calculation of ECRH and ECCD is done with the three-dimensional (3D) code ECWGB [38]. The code has been recently coupled to JETTO. ECWGB calculates the propagation and absorption of the electron cyclotron waves injected as collimated microwave gaussian beams in toroidal geometry. The ECRH power absorbed and the ECCD current generated by highly collimated gaussian beams are evaluated using the equilibrium from JETTO and the relativistic treatment of the wave propagation and driven current. In addition, the effects of the trapped particles are taken into account. The frequency of the electron cyclotron waves is assumed to be 110 GHz and the poloidal and toroidal angles can be steered to radially change the location of the power absorption and the amount of the generated current.

The only heating method that is not dealt with in a self-consistent way in JETTO is ICRH. The power deposition profiles for electrons and ions are calculated with the ICRH code PION [39]. The PION code calculates ion cyclotron resonance frequency (ICRF) heating power deposition profiles by taking into account the time evolution of the distribution functions of the resonating ions. In the simulations, hydrogen minority scheme (hydrogen concentration typically 2–4%) is applied with frequencies in the range of 42–51 MHz to obtain on-axis and off-axis power deposition. The driven ICRH current has been assessed with the 3D Monte-Carlo code FIDO [40] and was found to be negligible for the chosen ICRH scheme.

3. A comparison between the experimental and simulated target q-profiles

Different preheating methods can produce very distinct target q-profiles. The temporal evolution of the main plasma parameters for three different preheating scenarios in typical JET OS experiments is shown in figure 1. Most of the plasma parameters were the same for all the three discharges, i.e. the toroidal field B_ϕ was 2.58 T, the inductive plasma current was ramped up at about 0.37 MA s^{-1} and the average density and $Z_{\rm eff}$ were roughly the same. This current ramp rate was applied after an initial fast rise at plasma initialization between $t = 0.0$–1.0 s. What was distinct between the three pulses was the preheating method; one of them was with LHCD preheating (pulse No 51466), the second one with off-axis ICRF hydrogen minority preheating (pulse No 51470) and the third one with ohmic preheating (pulse No 51456). Consequently, the electron temperatures and current density profiles evolved in different ways. Also shown in figure 1(c) is another LHCD discharge (pulse No 51976) which had similar $I_{\rm p}$, $n_{\rm e}$, LH power and other plasma parameters, but the toroidal magnetic field was 3.45 T. The preheating phase lasted from $t = 1.0$ s until $t = 4.2$ s when diagnostics NBI was added for the MSE measurements.

The target q-profiles just after the end of the preheating phase at $t = 4.4$ s for these three different preheating methods are illustrated in figure 2. The q-profiles have been reconstructed with EFIT equilibrium code using the MSE measurements as the constraints for EFIT [41]. The q-profiles inside $R = 3.6$ m are different between the three cases; LHCD and off-axis

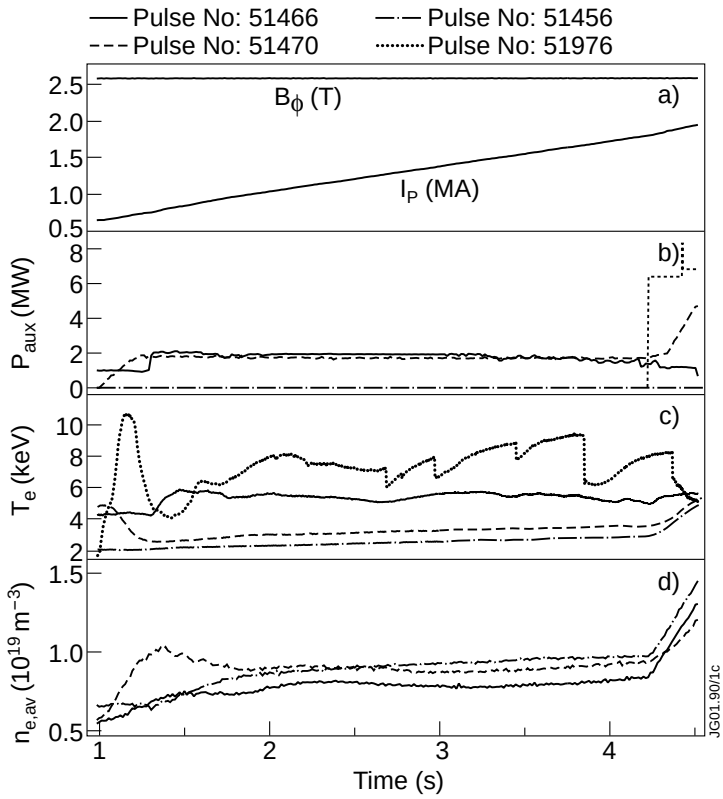

Figure 1. (a) Time traces of plasma current and magnetic field; (b) external heating powers; (c) central electron temperatures (electron cyclotron emission measurements) and (d) average electron densities for three discharges with different preheating methods. The full curve refers to the pulse with LHCD preheating; the broken curve with ICRF preheating and the dash–dotted curve with ohmic preheating. The NBI power (short dashed curve in (b)) started at $t = 4.2$ s is the same for all the three discharges. The dotted curve in (c) is another LHCD preheated pulse with higher B_ϕ.

ICRF preheating created a weakly reversed q-profile, but with a difference of 10 cm in the radial location of $q_{\min}$ whereas Ohmic preheating produced a monotonic q-profile. Also shown in figure 2 is the other LHCD preheated discharge with higher magnetic field. This discharge yielded a deeply reversed q-profile inside $R = 3.5$ m. The electron temperature data for this discharge (shown in figure 1(c), dotted curve) illustrates the sawtooth-like behaviour often seen in pulses with LHCD preheating. This sawtooth-like behaviour is an experimental indicator on magnetic reconnections which are associated with deeply reversed q-profiles [31]. This type of target q-profiles with large negative magnetic shear have been routinely produced with LHCD preheating during the last experimental campaign on JET. Even dozens of discharges with the observation of zero current density in the plasma core region created by LHCD have been recently reported in JET [42].

In order to make a comparison between the q-profiles reconstructed with EFIT using MSE measurements as constraints and the q-profile evolution calculated according to neoclassical resistivity, JETTO transport code has been run in an interpretative way. This means that only the Faraday equation for the current density is solved and all the other plasma parameters,

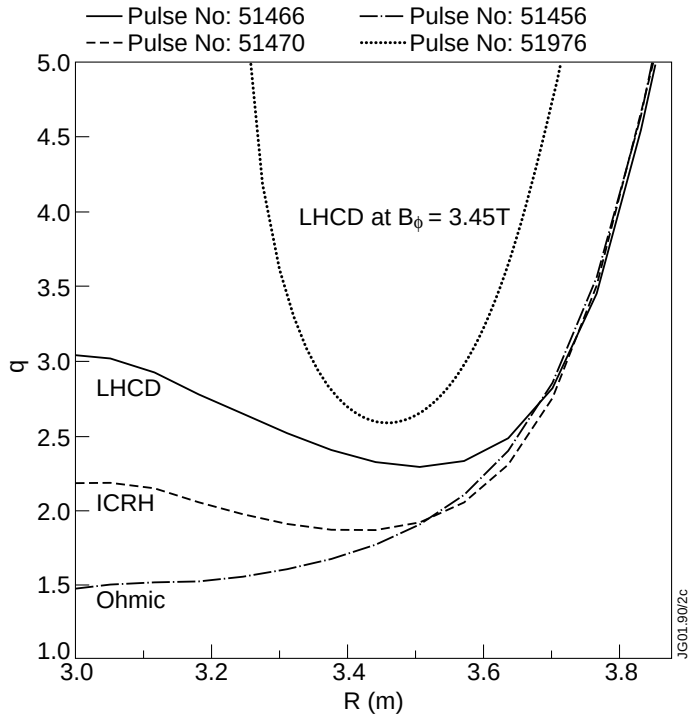

Figure 2. q-profiles at the end of the preheating phase at $t = 4.4$ s for the different preheating schemes. The full curve corresponds to LHCD preheating, the broken one to ICRF preheating and the dash–dotted one to ohmic preheating. The dotted curve is the other LHCD preheated discharge at higher magnetic field and with a better plasma initialization.

such as temperatures, densities, total plasma current, magnetic field, $Z_{\rm eff}$ etc, are taken from the experiments. The simulations are started after plasma initialization at $t = 1.0$ s.

The result of the comparison just after the end of the preheating phase at $t = 4.4$ s when the MSE measurements are available is presented in figure 3 for the same preheating method scan discharges as shown in figure 2. The agreement between EFIT and the neoclassical prediction is relatively good in the case of LHCD. The location of $q_{\rm min}$ is reproduced accurately within 5 cm which is well within the accuracy of the EFIT+MSE reconstruction and also, the magnetic shear is roughly the same elsewhere except in the core region. Neo-classical resistivity predicts a flat q-profile (in the limit of a weakly reversed or monotonic q) for ICRF preheated discharge whereas EFIT tends to produce a weakly reversed q-profile. Nevertheless, quantitatively the q-profiles also seem to be quite similar in the case of ICRF preheating, i.e. the nearly zero shear region is as wide (except the core again) in both cases. In the ohmic preheating, the difference between the electron temperature measurements by Lidar Thomson scattering and electron cyclotron emission (ECE) was significant. As a consequence, the modelling results depend on the $T_{\rm e}$ measurements used. The q-profile calculated with $T_{\rm e}$ measurements from ECE (broken curve) are in much better agreement with EFIT outside $R = 3.3$ m whereas the q-profile calculated with $T_{\rm e}$ measurements from Lidar (dash–dotted curve) is closer to the EFIT one inside $R = 3.3$ m.

The largest discrepancy between EFIT and neoclassical theory is the core region inside $R = 3.15$ m, as seen for each preheating method in figure 3. The number of trapped

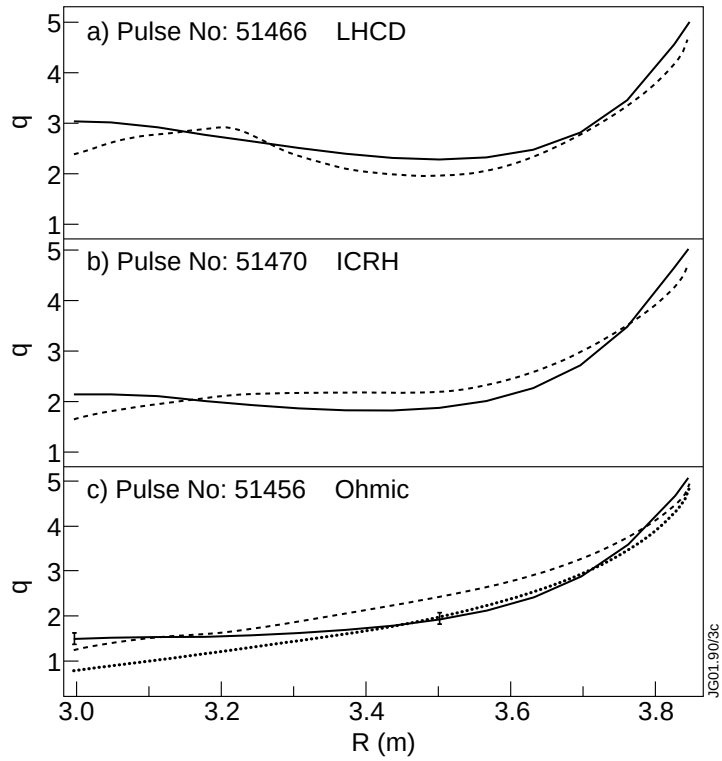

Figure 3. EFIT and calculated q-profiles at the end of the preheating phase at $t = 4.4$ s for: (a) LHCD; (b) ICRF; and (c) ohmic preheating schemes. The full curves correspond to q-profiles reconstructed with EFIT and the broken curves are the calculated ones. The dash–dotted curve in (c) is calculated by using Lidar T_e measurements instead of T_e from ECE. Also shown in (c) are the estimated error bars at two radii in the reconstruction of the q-profile with EFIT + MSE.

particles decreases significantly inside this region and thus, because of the increased electrical conductivity, the neoclassical calculations always generate a dip in the q-profile in the plasma centre. The EFIT solution with prescribed polynomials do not produce this feature. When the classical Spitzer conductivity instead of the neoclassical one is assumed, the agreement between the q-profiles calculated with EFIT and JETTO is not as good. The magnitude of the Spitzer conductivity is a factor of 2–3 larger than the neoclassical one and consequently, it tends to create far too large values for q inside $R = 3.6$ m although it does not create the dip in the q-profile as the neoclassical conductivity does. The earlier experimental results on JET have also demonstrated that neoclassical conductivity is more consistent with experiments than the Spitzer conductivity [43].

The neoclassical conductivity calculated by JETTO is in a very good agreement with the conductivity calculated by a neoclassical transport code NCLASS [44]. The difference in the conductivity is about 2–4% between JETTO and NCLASS, which treats the neoclassical theory in a more sophisticated way and with fewer simplifying approximations than JETTO [21]. Moreover, the comparison of results from the two codes indicates that the difference in the magnitude of the bootstrap current is within 5% outside $R = 3.15$ m and inside that radius it is of the order of 5–20%. The largest difference is found in the cases with a deeply reversed q where the value of q in the centre exceeds 20.

In general, the largest uncertainties in the neoclassical JETTO calculations of the q-profile evolution are the initial q-profile problem already discussed in section 2 and the electron temperature measurements. The initial q from EFIT with magnetics only at $t = 1.0$ s was in each three cases shown in figure 3 very monotonic (large positive magnetic shear). By using a flat initial q-profile instead of the EFIT one, target q-profiles at $t = 4.4$ s slightly closer to EFIT + MSE profiles in the case of ICRH and ohmic preheating can be obtained with JETTO. The other source of error are the electron temperature measurements which determine the neoclassical conductivity. The error in T_e measurements is typically of the order 10–20% in the early preheating phase of the plasma discharge and in some cases the difference between Lidar and ECE is significant, as was the case in the discharge with ohmic preheating as shown in figure 3.

4. Effects of different preheating methods on q-profile evolution

A comparison of the electron temperature profiles between the experiments and predictive JETTO calculations during the preheating phase is presented in figure 4. The three discharges (Pulses No 51456, 51466 and 51470) are the same ones as already presented in figures 1, 2 and 3. The start time of the simulations is at $t = 1.0$ s. The agreement between the measured and calculated T_e profiles is well within the accuracy of the measurements of T_e ($\approx$20%) for all heating methods and at any time during the preheating phase. The difference between the experiment and the simulation tends to be slightly larger in the case of LHCD. This is presumably due to the larger inaccuracies in the modelling of LH power deposition and current density profiles than in the modelling of ICRF power deposition or simulations without any external heating as in the ohmic case.

4.1. ICRF preheating

In hydrogen minority ICRF preheating, the time evolution of T_e and q depends on the location of the ion cyclotron resonance. The power deposition, electron temperature and q-profiles for three different resonance locations are illustrated in figure 5. All the basic plasma parameters as well as the initial and boundary conditions for T_e are taken from the pulse No 51897, which has a preheating phase similar to 51976. The simulations start at $t = 1.0$ s. 5 MW of on-axis ICRF preheating creates a monotonic target q-profile (although s is close to zero) whereas different off-axis power deposition profiles produce a weakly reversed target q-profile if the heating starts immediately after the plasma initialization. Otherwise, if the start of the heating is delayed by more than 1 s, a reversed q-profile is not achieved. The same conclusion on ICRF preheating could be drawn from the q-profiles reconstructed with EFIT using MSE measurements as constraints in section 3. $q_{\min}$ is located at the peak of the power deposition, however not outside $R = 3.35$ m. With the hydrogen minority heating scheme, about 80% of the ICRH power (5 MW) goes to electrons. Modelling indicates that in order to create a deeply reversed q-profile with ICRF preheating, either the power deposition profile should be narrower or the slowing down time of the fast ions colliding with the electrons should be shorter (both options are difficult in practice).

4.2. LHCD preheating

In order to separate the effects of the electron heating and the current drive on the q-profile evolution in the case of LHCD preheating, an LH current drive efficiency scan is performed. The LH driven current calculated by FRTC is multiplied throughout the simulations either

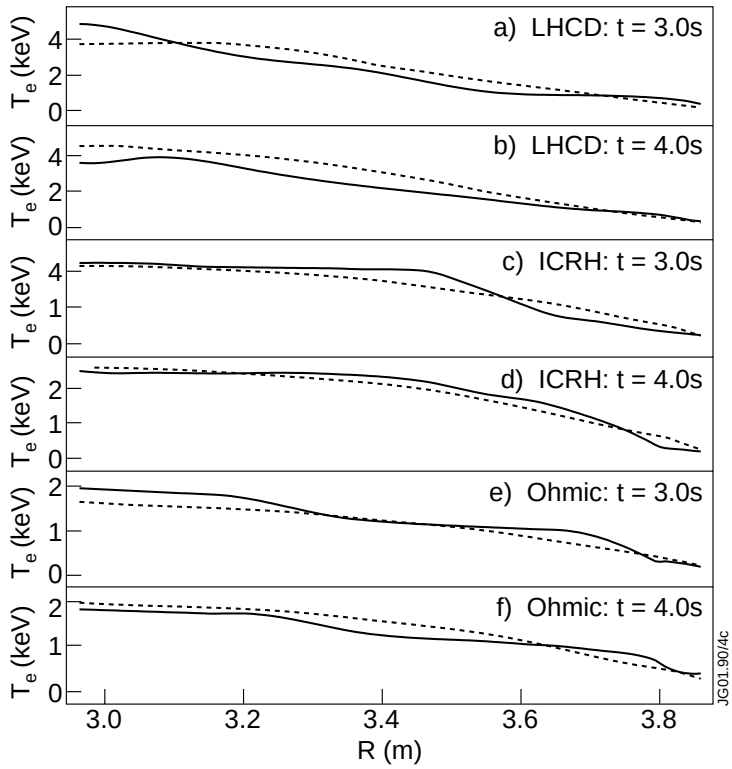

Figure 4. T_e profiles at $t = 3.0$ s and at $t = 4.0$ s for: (a) and (b) LHCD; (c) and (d) ICRF; and (e) and (f) ohmic preheating schemes. The full curves correspond to the measured T_e profiles and the broken curves are the calculated ones.

by 1.0, 0.5, 0.25 or 0.0 with 1.0 corresponding to the actual current evaluated by the ray-tracing code and 0.0 corresponding to the case with the LH heating only. All the basic plasma parameters as well as the initial and boundary conditions for T_e are taken again from the pulse No 51897. LH power is 3 MW and the driven LH current 400–800 kA (depends on time) in the case with the actual LH current calculated by FRTC (multiplication by 1.0). In the other cases the driven LH current decreases roughly with the multiplication factor. The simulations start at $t = 1.0$ s, and the modelling results of the main profiles at the end of the preheating phase at $t = 5.0$ s are presented in figure 6.

The LH current efficiency scan shows that the driven current seems to be absolutely crucial in order to create a reversed q-profile. As shown in figure 6, the q-profile is monotonic if the LH driven current is fully neglected (dotted curve). However, taking into account only 25% of the calculated LH current (dash–dotted curve) seems to be enough to reverse the q-profile. Moreover, the experimental results provide an additional, although indirect, verification of the importance of the LH driven current. If the power deposition profiles of LH (in figure 6(b), full or broken curves) and hydrogen minority off-axis ICRH (in figure 5(a), broken or dash–dotted curves) are compared, they can be regarded as being qualitatively similar during the preheating phase on JET, i.e. the power deposition profiles are very wide and are deposited mostly at radii $r/a \approx 3.1$–3.5 m. Consequently, having assumed a negligible contribution from the LH driven current, the q-profile evolution should be fairly similar in plasmas with LH and ICRF preheating at the same power level. However, the experimental results, such

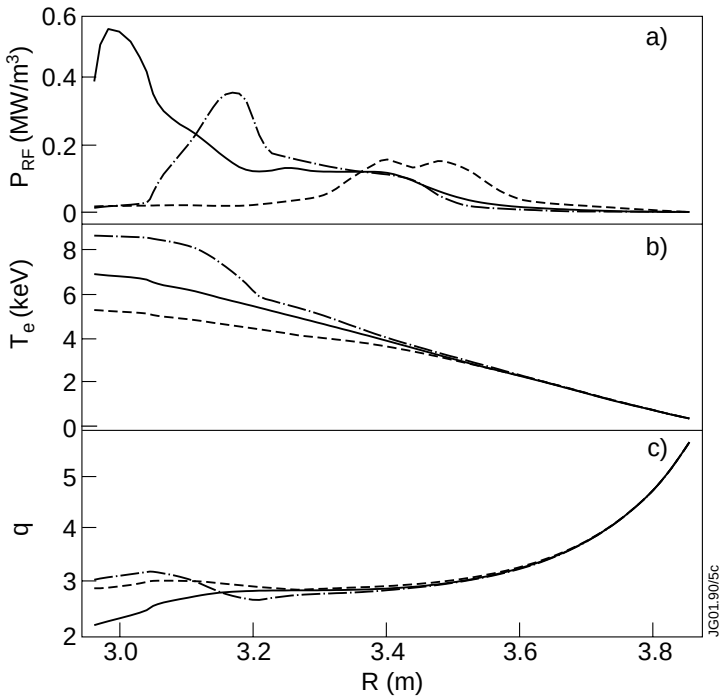

Figure 5. (a) The power deposition profiles (to electrons); (b) T_e profiles; and (c) the target q-profiles for the three different locations of the ion cyclotron resonance at the end of the preheating phase at $t = 5.0$ s.

as shown for example in figure 2, indicate significantly different target q-profiles at the end of the preheating phase; a deeply or weakly reversed q with LHCD and a weakly reversed q with ICRH. To sum up, both the LH current drive efficiency scan and the distinct experimental behaviour of the q-profile with LHCD and off-axis ICRF preheating emphasize the significance of the role of the LH driven current in the modification of the q-profile.

4.3. NBI preheating

The role of particle transport becomes more important in the case of NBI preheating since the external current drive is inversely proportional to density. Furthermore, additional gas puffing must be used in order to avoid excessive shine through of the beams due to too low density. The simulation results of NBI preheating are shown in figure 7. Again, the plasma parameters from the pulse No 51897 are used, but now particle transport is also modelled and gas puffing used in order to exceed the minimum density limit for NBI system to operate safely. The input power is 5 MW and the driven NBI current is of the order of 130–180 kA both with on-axis and off-axis cases.

As seen in figure 7, 5 MW of NBI on-axis preheating creates a monotonic q-profile whereas 5 MW of NBI power deposited off-axis weakly reverses the target q-profile. Similarly to LHCD, without taking into account the externally driven NB off-axis current (dash–dotted curve), a reversed target q-profile cannot be achieved. In the case of off-axis NBI, the q-profile is more strongly reversed between $t = 2.0$ s and $t = 4.0$ s, but after $t = 4.0$ s the rising density decreases the NB driven off-axis current and consequently, plasma current starts to

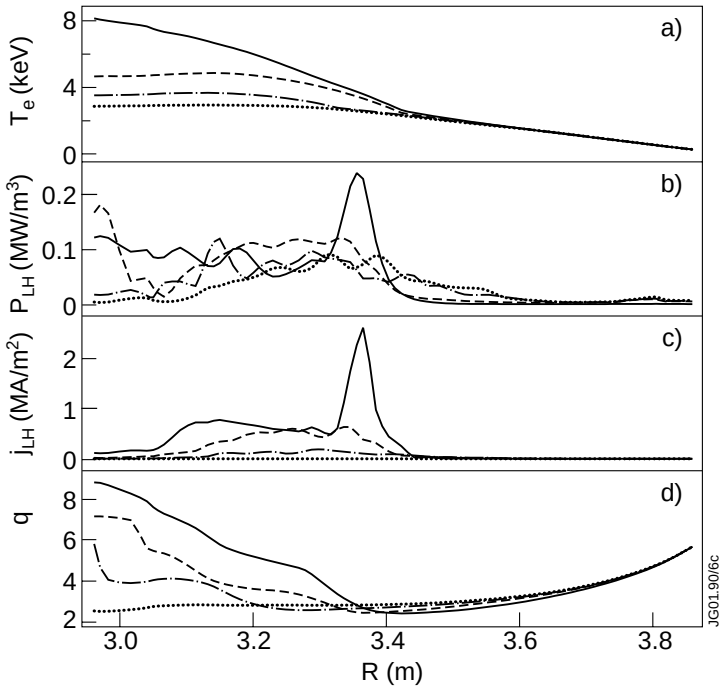

Figure 6. (a) Electron temperature; (b) LH power deposition profiles; (c) LH driven current; and (d) the target q-profiles at $t = 5.0$ s. The calculated LH current is multiplied either by 1.0 (full curves), 0.5 (broken curves), 0.25 (dash–dotted curves) or by 0.0 (dotted curves).

accumulate in the plasma centre. The off-axis power deposition profile shown in figure 7(a) (broken curve) is the most off-axis power deposition profile that is achievable with the present JET NBI system (only tangential beams are used). Therefore, the maximum radius for $q_{\min}$ with NBI preheating is $R = 3.35$ m. Since the density is low in the preheating phase, the shine-through effect decreases the launched power by 15–20%, and additionally, only 45–55% of the absorbed power goes to electrons. Accordingly, the effective heating power that goes to electrons is less than half of the launched NBI power.

In order to complete the analysis of the NBI preheating, counter on-axis NBI preheating is also studied. The simulation results show that at the early phase of the preheating phase ($t \approx 2$ s), the q-profile is deeply reversed, but the radius of $q_{\min}$ is quite small ($R = 3.2$ m). In the early phase the NB driven negative on-axis current is about -300 kA. However, after 2 s the NB current drive efficiency starts to decrease due to increasing density and q becomes less reversed and finally after $t = 4$ s q becomes monotonic.

4.4. ECCD preheating

In ECCD preheating, the location of the power deposition and current density profiles is determined mainly by the frequency of the electron cyclotron waves and the magnetic field in the plasma, which are both fixed quantities and usually do not vary much during the experiment. On the other hand, the amount of absorbed power of the total launched power and the amount of the driven current depend strongly on the electron temperature and density. The absorbed power increases with increasing T_e and n_e whereas the driven ECCD current increases with increasing

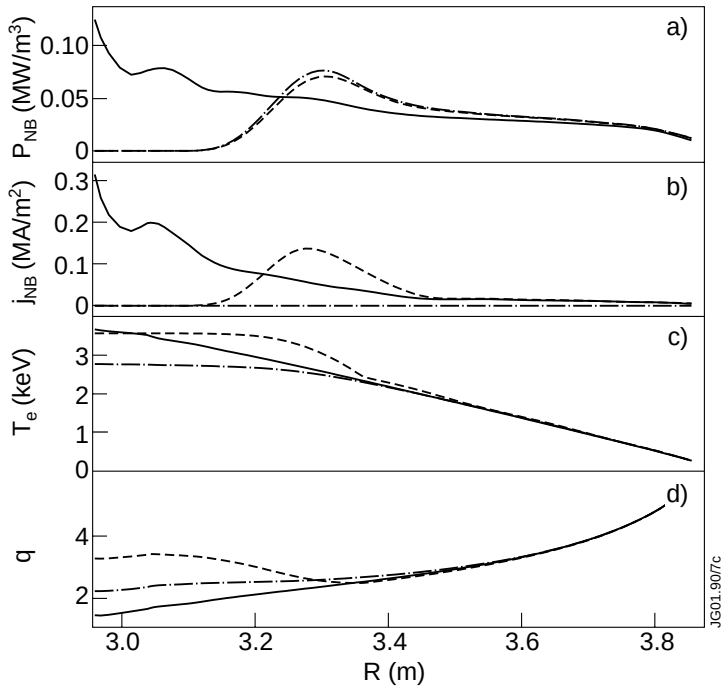

Figure 7. (a) Power deposition profiles (to electrons); (b) NB driven current density profiles; (c) T_e profiles; and (d) the target q-profiles for on-axis (full curve) and off-axis (broken curve) NBI preheating scenarios at $t = 5.0$ s. The dashed–dotted curve is the same off-axis scenario, but neglecting the NB driven current.

T_e, but decreases with increasing n_e. Z_{eff} can also vary significantly in the preheating phase and increasing Z_{eff} decreases ECCD efficiency. These well known dependences are much more pronounced in the preheating phase where the density is typically very low (of the order of 1×10^{19} m^{-3}) and the electron temperature varies from 2 keV up to 15 keV.

Three different off-axis ECCD preheating scenarios are compared in figure 8. Similarly to other preheating methods, the plasma parameters are taken from pulse No 51897 and the input power is 5 MW. Different locations of the ECCD power deposition profiles are obtained by changing the poloidal angle of the launched waves. The toroidal angle is fixed at 15° with respect to the perpendicular direction. The difference between the electron temperatures in (c) and (d) and correspondingly between q-profiles in (e) and (f) is a consequence of the used transport model. In (c) and (e), the transport model is the same as presented in section 2 and used everywhere in this paper, but in (d) and (f), the option of having reduced transport, i.e. an ITB when $s < 0$ is ignored ($\Theta(x) = 1$ all the time). As already discussed in section 2, there is a lot of experimental evidence to assume reduced transport when $s \lesssim 0$ in the preheating phase and thus, the reason for using the different transport model is to test the sensitivity of the q-profile evolution to the applied transport model.

As shown in figure 8(e), deeply or weakly reversed target q-profiles are achieved with ECCD preheating, depending on the radial location of the peak in the power deposition profile. q_{min} is located at the same radius as the peak in the power deposition profile. A weakly reversed target q with the radius of q_{min} as far as $R = 3.6$ m can be produced with ECCD. If no reduced transport is assumed, the electron temperatures are smaller (in (d)), but the q-profiles are

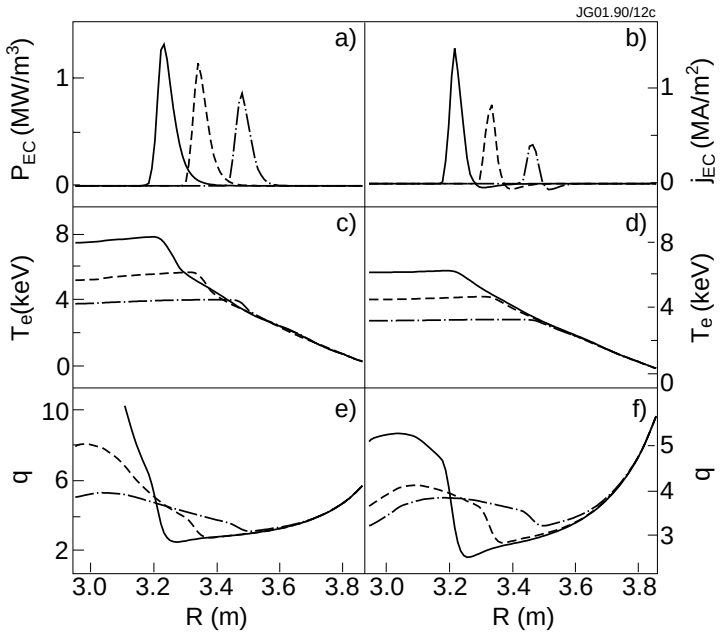

Figure 8. (a) ECCD power deposition profiles; (b) ECCD driven current density profiles; (c) T_e profiles with standard transport model; (d) T_e profiles with modified transport model; (e) the target q-profiles with standard transport model; and (f) the target q-profiles with modified transport model for three different off-axis ECCD preheating scenarios at $t = 5.0$ s.

still weakly reversed (shown in figure 8(f)), however not deeply reversed any longer as with ITBs in figure 8(e). This indicates that the calculated q-profile evolution is sensitive to the transport model, but on the other hand, the results with using the very conservative estimate for electron heat transport (no ITB model) also indicate that ECCD is a very efficient tool to modify the q-profile evolution in the preheating phase. It is also worth noting the difference in the q-profiles in the core between figures (e) and (f); in (e) s is negative everywhere inside $q_{\min}$ whereas in (f) s is only locally negative around the peak of the ECCD power deposition profile. Another point worth mentioning is the amount of absorbed power and driven ECCD current. In the innermost case (full curves), almost full power absorption is reached (98%), but in the middle one (dashed curves) only about 94% is absorbed and in the outermost case only 90% of the launched power is absorbed in the plasma. The corresponding figures of merit for the driven ECCD current are 160 kA, 120 kA and 70 kA, respectively. Still, this amount of the driven ECCD current plays an important role in the evolution of the q-profile in the preheating phase. Using ECRH (heating only, toroidal launching angle zero) does not create a deeply reversed target q-profile with any location of the power deposition profile (weakly reversed target q-profiles are still possible).

It is not possible to apply on-axis ECCD for all B_ϕ at a fixed frequency (110 GHz) of the electron cyclotron waves. In order to assess the ability of the counter on-axis ECCD to modify the q-profile evolution in the preheating phase, a similar preheating phase but with a toroidal magnetic field $B_\phi = 3.7$ T is used. A deeply reversed q-profile can be achieved with counter on-axis ECCD, however, the region of the negative shear is clearly narrower than in most of the off-axis cases, as being located always inside $R = 3.3$ m. The ECCD driven current is much larger than in the off-axis cases, reaching nearly -300 kA. Moreover, the calculation indicates

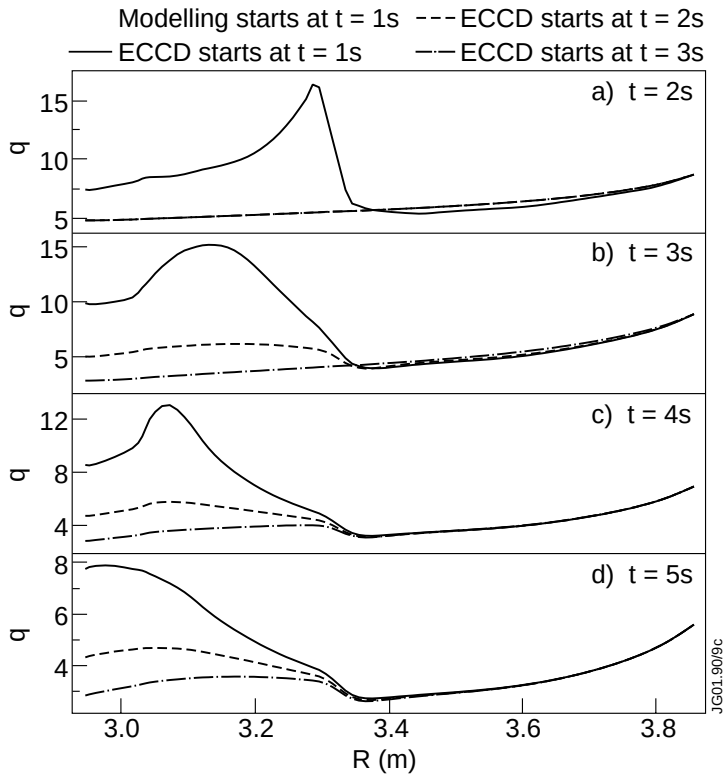

Figure 9. (a) q-profiles at $t = 2.0$ s; (b) at $t = 3.0$ s; (c) at $t = 4.0$ s; and (d) at $t = 5.0$ s for three different instants when ECCD preheating is switched on. ECCD starts either at $t = 1.0$ s (full curve), at $t = 2.0$ s (broken curve) or at $t = 3.0$ s (dash–dotted curve).

that the central electron temperature can reach 20 keV, by far higher than ever achieved on JET.

The effect of the start time of the ECCD preheating is investigated in figure 9. As can be seen, it plays a major role. Delaying ECCD by 1 s does not produce a deeply reversed target q-profile and delaying it by 2 s creates almost a monotonic q-profile. Nevertheless, the location of $q_{\min}$ remains almost unchanged. Other preheating methods give similar timing scan results; the deepness of the reversed q is very sensitive to the start time of the preheating whereas the location of $q_{\min}$, if it still exists, does not vary much.

4.5. Comparison of different preheating methods

The target q-profiles at $t = 4.0$ s and $t = 5.0$ s produced by the different preheating methods are compared in figure 10. In the simulations, the main plasma parameters and the initial and boundary conditions for T_e are taken from the pulse No 51897. The external heating power is 5 MW except in the case of LHCD when the power is 3 MW. Thus, the simulations are identical except in terms of the heating and current drive methods.

The preheating methods can be divided into three categories in terms of the created target q-profile. LHCD and ECCD form category 1 as being the only methods which can produce deeply reversed q-profiles. Quantitatively the q-profiles produced by LHCD and ECCD look quite similar. However, the central values of q are distinct. With LHCD, q tends to increase

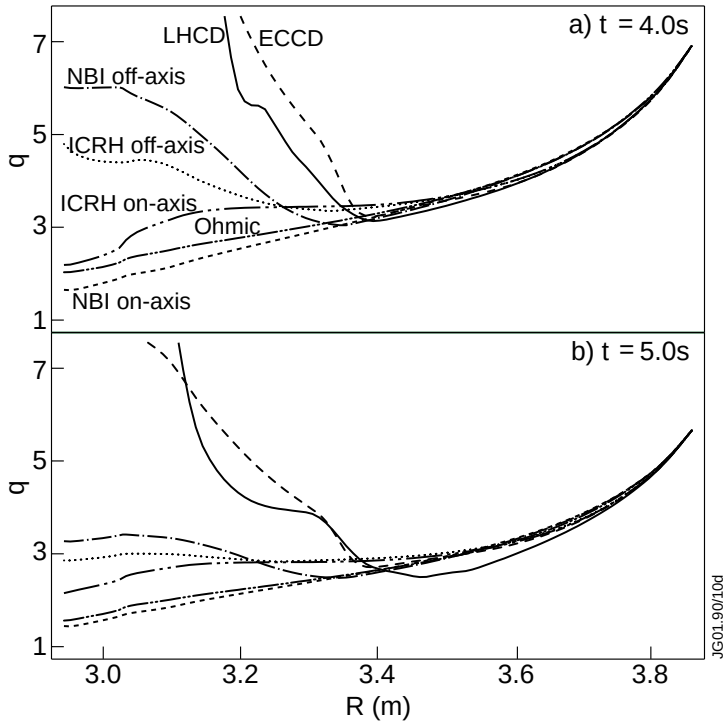

Figure 10. (a) Target q-profiles produced with different preheating methods at $t = 4.0$ s; and (b) at $t = 5.0$ s. Category 1, LHCD (full curve) and ECCD (broken curve); category 2, off-axis NBI (dash–dotted curve) and off-axis ICRH (dotted curve); category 3, on-axis NBI (short dashed curve), on-axis ICRH (long double dot–dashed curve) and ohmic (short double dot–dashed curve).

to very high values, such as $q_0 \approx 30$–50 whereas in the case of ECCD, q_0 remains between 10 and 20. This difference arises mainly from the amount of driven off-axis current; LHCD driven current is of the order of 500–900 kA whereas ECCD current is only 70–160 kA. Large off-axis current can transiently drive the total current density in the core to zero, as has been recently observed in JET [42]. Category 2 consists of off-axis NBI and off-axis ICRH heating which create weakly reversed q-profiles with $q_{\min}$ located inside $R = 3.4$ m. On-axis NBI, on-axis ICRH and ohmic preheating belong to category 3 as they can only create monotonic target q-profiles.

In the simulations shown in figure 10, the initial q-profile was taken from EFIT without MSE measurements, the latter being never available at $t = 1.0$ s. EFIT always gives either a flat or monotonic q-profile; for pulse No 51897 it turned out to be flat. Therefore, in order to test the sensitivity of the target q-profiles at $t = 4.0$ s or $t = 5.0$ s to the initial q, the same simulations, as illustrated figure 10, with reversed and monotonic initial q-profiles were performed. The methods in categories 1 and 3 turned out to be insensitive to the initial q, giving similar results as shown in figure 10 independently of the initial q-profile. However, the methods in category 2 tended to give more reversed target q-profiles in the case of a reversed initial q and flatter or monotonic q-profiles in the case of a monotonic initial q. As a consequence, the simulation results of the preheating methods in category 1 and 3 can be regarded as robust results as being almost independent of the initial q-profile whereas somewhat larger uncertainties in the results with the methods in category 2 remain. Variations within the accuracy of the measurements in the initial T_e do not affect significantly the target q-profile.

The sensitivity of the q-profile evolution to the uncertainties in the power deposition profiles is an important issue. In the case of NBI and ICRH, the sensitivity can be indirectly inferred by comparing the q-profiles calculated with on-axis and different off-axis power deposition profiles shown in figures 5(a) and 7(a). As can be seen from the relatively small difference in the target q-profiles between the two extreme cases (on-axis versus off-axis) in figures 5(c) and 7(c), the q-profile evolution cannot be very sensitive to small uncertainties coming from the modelling of the power deposition profiles with PION and PENCIL. In the case of LHCD, artificially shifting the power deposition profile either by 10 cm outwards or inwards does not have a significant effect on the target q-profile at $t = 5.0$ s. On the other hand, as already shown in figure 6, the q-profile evolution is very sensitive to the magnitude of the LH driven current. However, assuming only a 50% accuracy in the magnitude of the LH driven current changes neither the location of $q_{\min}$ nor qualitatively the shape of the target q-profile very much, as shown in figure 6(d). Quantitatively the changes are within 30% as shown in figure 6(d) as the difference between the full and broken curves. Besides, the assumption of only 50% accuracy in the ray-tracing calculation of the LH driven current with FRTC can be regarded as a very conservative estimation. Ray tracing in the frequency range of the electron cyclotron waves is generally regarded as a robust and reliable method. Consequently, no large uncertainties arising from the modelling of ECCD are expected.

One could argue why the preheating phase is so long, typically being from $t = 1.0$ s until $t = 3.5$–5.0 s. The main reason is that, for example, at $t = 2.5$ s the total plasma current is only about 1.2 MA and as a consequence, the values of q, even $q_{\min}$ are well above three. As already discussed in section 2, there is strong evidence that the integer surfaces of q (especially $q = 3.0$, $q = 2.0$ and $q = 1.0$) play a key role in triggering the outer ITB in the main heating phase [31, 32, 45]. Thus, starting the main heating too early at $t = 2$–3 s would yield a longer period of full heating without ITB which generally is not desirable. In addition, at $t = 2$ s or $t = 3$ s the q-profile is still evolving strongly due to the external heating and current drive and the shape of the q is not necessarily the desired one.

The power deposition profiles (electron channel) and the electron temperature profiles for the same preheating method scan, as shown in figure 10, are compared in figure 11. The very localized nature of the ECCD power deposition profile can be easily seen as the highest peak among the power deposition profiles from the different preheating methods. The two separate peaks in the LHCD power deposition profiles are from the different absorption mechanisms in the single pass and multi pass regimes of lower hybrid waves. NBI preheating and ohmic preheating produce clearly smaller electron temperatures than the other methods. With equal heating power, LHCD would create significantly higher T_e compared with the other ones.

5. Summary and conclusions

The preheating phase in JET has been studied in a very detailed way. The main emphasis was to modify the q-profile evolution in the preheating phase. JETTO transport code was used to model the current diffusion and heat transport. Separate codes to calculate the power deposition and current density profiles of LHCD, ECCD and NBI have been coupled to JETTO to allow a self-consistent calculation cycle between transport and heating and current drive evaluation. Different preheating methods were compared and the role of externally driven current versus direct electron heating in the q-profile evolution was discussed.

The different preheating methods could be divided into three categories in terms of the produced target q-profiles. LHCD and ECCD formed category 1 since they were the only methods which created deeply reversed target q-profiles in JET. Category 2 consisted of off-axis NBI and off-axis ICRH preheating which produced weakly reversed q-profiles with $q_{\min}$

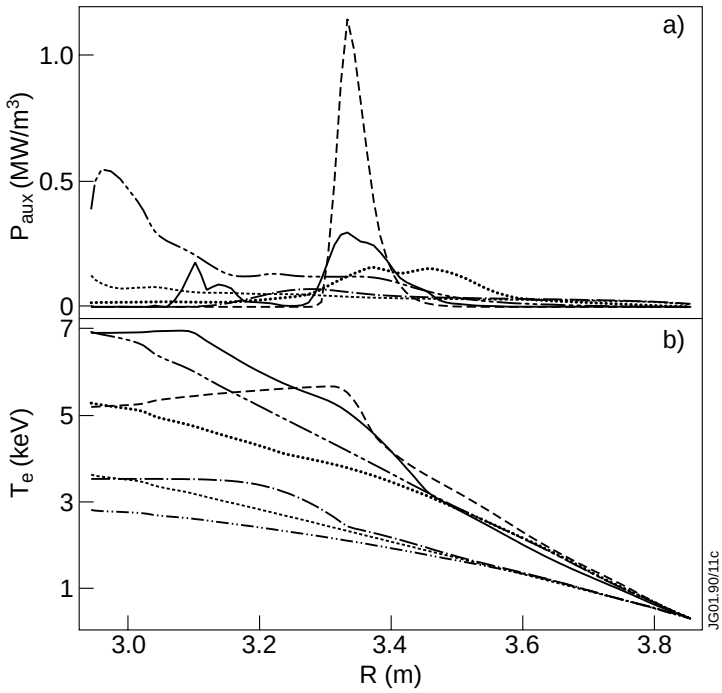

Figure 11. (a) Power deposition profiles (electron channel); and (b) electron temperature profiles at $t = 5.0$ s for the same cases as shown in figure 10.

located inside $R = 3.4$ m. On-axis NBI and on-axis ICRH and ohmic preheating belonged to category 3 as they created only monotonic target q-profiles. Experimental results on LHCD, ICRH and ohmic preheating on JET verified the predictive modelling results.

The current driven by LHCD and ECCD was found to be a crucial factor in producing deeply reversed target q-profiles in the preheating phase. Also, the NBI driven current turned out to be very important in the off-axis NBI preheating scheme. Other important factors affecting the q-profile evolution in the preheating phase were found to be the width of the power deposition profile and the start time of the preheating with respect to plasma initialization. A narrow off-axis power deposition profile was able to slow down the ohmic current diffusing from the plasma periphery to the centre much more efficiently than a wide one. Moreover, the earlier was the preheating started, the more was the current diffusion slowed down. Since ICRF preheating has wider power deposition profiles than ECRH and it also has an additional slowing down time of the fast ions colliding with the electrons ($\approx$0.5 s in JET) that is missing in the ECRH scheme, it is understandable that ECRH preheating (even without any ECCD current) turned out to be a more efficient tool with which to modify the q-profile evolution in the preheating phase than ICRH.

How well the desired target q-profile can be sustained later in the main heating phase depends on the applied heating and current methods and the power levels. Bootstrap current and its alignment with the external current drive becomes an important issue. Recent experimental results on the q-profile evolution in the main heating phase on JET can be found in references [18, 41, 46–48]. Detailed modelling of the q-profile evolution and a comparison between different heating methods in the main heating phase is beyond the scope of this paper and it is left for future publications although it is known to be a key issue in order to be able to

understand better the physics of the 'advanced' tokamak scenarios. Furthermore, in the main heating phase hybrid effects of two or more heating methods can provide excellent tools with which to modify and control the q-profile evolution. One example is a combination of LHCD with off-axis ECCD where the local off-axis increase in the electron temperature could control the damping of LH waves and thus the location of a large amount of the driven LH current. ECCD efficiency may also improve in the presence of an LH tail due to fast electrons. The combination of LHCD and ECCD has been recently modelled in [19]. Other very interesting hybrid effects to sustain the achieved target q-profile in the main heating phase would be a combination of LHCD with some on-axis counter current drive method, such as counter NBI, counter ECCD or counter fast wave current drive (FWCD).

There is one serious issue in the modelling that has not been touched in this paper. It is the sawtooth-like behaviour shown in T_e in figure 1. It is associated with the negative magnetic shear in the core region and the reason for these events are believed to be the neoclassical or double tearing modes [50] or the resistive interchange modes [51]. Similar oscillations have been also observed on Alcator C-Mod [51]. The possible redistribution of the current has not been taken into account in the modelling of the q-profile evolution. This sawtooth-like behaviour does not lead to a full redistribution of the current which could be modelled and for the present, there is no model in JETTO for the possible partial current redistribution caused by these events.

It is not yet known what the optimum target q-profile is. Naturally it depends on what the aim of the experiment is, but some general rules can be drawn. The optimum target q-profile should provide the largest sustainable improvement in the fusion performance while it should also provide MHD stable plasma and good confinement. It should be also sustainable in the main heating phase by non-inductive current drive aligned well with bootstrap current (pressure gradient). Moreover, it should assist the ITB to form as wide as possible in r/a (broad T_i, T_e and n_e profiles) and with moderate gradients. This implies that q_{min} should be also located as far off-axis as possible and preferably also having an integer value of q ($q = 2$ or $q = 3$) close to it, as has been reported in [31, 32, 45].

Each shape of the q-profile, deeply reversed, weakly reversed and monotonic q, has advantages and disadvantages with respect to plasma performance, MHD stability, confinement and steady-state operation. The advantages of a deeply reversed q-profile are a low power threshold to form an ITB at a wide radius [18] and a reduction of various types of turbulence, such as ETG and TEM as discussed in detail in section 1. The disadvantage is that the steady-state is not reached before the performance is lost presumably due to global pressure driven modes or some MHD activity near low-order rational surfaces of q in the core region [18]. In addition, impurity accumulation in the plasma core seems to be a serious issue with a deeply reversed q-profile with peaked density profiles [49]. The advantages of the operation with a weakly reversed q are the absence of low-order rational q-surfaces in the core and thus the disconnection of turbulent vortices linked together with toroidicity. Higher power threshold to obtain improved performance and the absence of some turbulence stabilizing mechanisms that are based on the large negative magnetic shear can be listed as drawbacks with a weakly reversed q. With monotonic q, the advantage is that it can be presumably sustained (remain frozen) most easily in the very long steady-state plasmas. However, the power threshold to form an ITB is clearly the highest among these cases and the stability with respect to many branches of turbulence (TEM, ETG, etc) is the poorest. The future experiments and modelling should be directed towards further understanding of the link between the q-profile and the performance, the evolution of the ITBs, confinement, MHD stability as well as turbulence suppression.

The experimental results on the q-profile evolution on other tokamaks in the preheating phase are not identical to the present modelling results. On DIII-D, JT-60U and ASDEX-U,

NBI on-axis preheating is used as the standard method to obtain a reversed q-profile whereas the present calculations showed that the reversed target q-profile cannot be created in JET (except transiently for a period of less than 1 s immediately after switching on NBI heating). This is due to the larger volume and the larger major radius on JET than on the other tokamaks; the power density is much smaller and the relative radius that is covered by NBI preheating is also smaller in JET. The same difficulty concerns basically all the methods based on on-axis heating and current drive in JET. On the other hand, the long current diffusion time because of the large major radius allows the off-axis methods to work efficiently on JET if either the power deposition profile is narrow or the driven current large.

The importance of the preheating phase in the preparation of the plasma in 'advanced' tokamak scenarios in order to improve fusion performance is obvious in JET. Due to the long current diffusion time, optimizing the q-profile in the preheating phase gives rise to enhanced performance in the high power phase by improving both confinement and MHD stability as well as obtaining a large fraction of well-aligned bootstrap current. In ITER, the current diffusion time is huge during the burn phase. Therefore, in order to improve and optimize fusion performance in ITER, very careful plasma preparation, especially optimizing the q-profile is required. As a consequence, preheating techniques and analyses similar to that presented in this paper should be considered for ITER in future.

Acknowledgments

The authors like to thank Wayne Houlberg for his great efforts in the installation of the NCLASS code that is now coupled with JETTO code. The authors are also grateful to Emmanuel Joffrin and Marc Beurskens for many fruitful discussions. This work has been conducted under the European Fusion Development Agreement within Task Force S2 and H.

References

[1] Levinton F M *et al* 1995 *Phys. Rev. Lett.* **75** 4417
[2] Strait E J *et al* 1995 *Phys. Rev. Lett.* **75** 4421
[3] Koide Y *et al* 1998 *Plasma Phys. Control. Fusion* **40** 641
[4] Wolf R C *et al* 2000 *Phys. Plasmas* **7** 1839
[5] Turnbull A D, Taylor T S, Lin-Liu Y R and St. John H 1995 *Phys. Rev. Lett.* **75** 718
[6] Staebler G M *et al* 1998 *Plasma Phys. Control. Fusion* **40** 569
[7] Kessel C, Manickam J, Rewoldt G and Tang W M *et al* 1994 *Phys. Rev. Lett.* **72** 1212
[8] Diamond P H *et al* 1997 *Phys. Rev. Lett.* **78** 1472
[9] Shaing K C, Aydemir A Y, Houlberg W A and Zarnstorff M C 1998 *Phys. Rev. Lett.* **80** 5353
[10] Beer M A *et al* 1997 *Phys. Plasmas* **4** 1792
[11] Dorland W, Jenko F, Kotschenreuther M and Rogers B N 2000 *Phys. Rev. Lett.* **85** 5579
[12] Doyle E J *et al* 2000 *Proc. 18th IAEA Fusion Energy Conference (Sorrento, Italy, 4–10 October, 2000)* IAEA-CN-77/EX6/2
[13] Tala T J J *et al* 2001 *Plasma Phys. Control. Fusion* **43** 506
[14] Greenfield C M *et al* 1999 *Nucl. Fusion* **39** 1723
[15] Greenfield C M *et al* 2000 *Phys. Plasmas* **7** 1959
[16] Prater R *et al* 2000 *Proc. 18th IAEA Fusion Energy Conference (Sorrento, Italy, 4–10 October, 2000)* IAEA-CN-77/EX8/1
[17] Fujita T *et al* 2000 *Proc. 18th IAEA Fusion Energy Conference (Sorrento, Italy, 4–10 October, 2000)* IAEA-CN-77/EX4/1
[18] Challis C D *et al* 2002 *Plasma Phys. Control. Fusion* submitted
[19] Dumont R, Giruzzi G and Barbato E 2000 *Phys. Plasmas* **7** 4972
[20] Lopez-Bruna D, Carreras B A and Newman D E 2000 *Nucl. Fusion* **40** 1825
[21] Genacchi G and Taroni A 1988 JETTO: A free boundary plasma transport code (basic version), *Rapporto* ENEA RT/TIB 1988(5)

[22] Hirhsman S P, Hawryluk R J and Birge B 1977 *Report* PPPL-1326
[23] Tala T J J *et al* 2000 *Nucl. Fusion* **40** 1635
[24] Parail V V *et al* 1999 *Nucl. Fusion* **39** 429
[25] Erba M *et al* 1997 *Plasma Phys. Control. Fusion* **39** 261
[26] Erba M *et al* 1996 Validation of a new mixed Bohm/gyro-Bohm transport model on discharges of ITER date-base *Report* JET-R(96)07, JET Joint Undertaking
[27] Hinton F L and Hazeltine R D 1976 *Rev. Mod. Phys.* **48** 239
[28] Ohkawa T 1978 *Phys. Lett.* A **67** 35
[29] Jenko F *et al* 2000 *Phys. Plasmas* **7** 1904
[30] Hahm T S and Burrell K H 1995 *Phys. Plasmas* **2** 1648
[31] Challis C D *et al* 2001 *Plasma Phys. Control. Fusion* **43** 861
[32] Joffrin E *et al* 2001 MHD internal transport barrier triggering in low positive shear scenario in JET *Nucl. Fusion* submitted
[33] de Esch H P L, Stork D and Weisen H 1990 *Proc. 17th European Physical Society Conf. on Controlled Fusion and Plasma Physics (Amsterdam, The Netherlands, 25–29 June, 1990)* (ECA vol 14B) p 90
[34] Lao L *et al* 1985 *Nucl. Fusion* **25** 1611
[35] Esterkin A R and Piliya A D 1996 *Nucl. Fusion* **36** 1501
[36] Heikkinen J A *et al* 1999 *Plasma Phys. Control. Fusion* **41** 1231
[37] Challis C D *et al* 1989 *Nucl. Fusion* **29** 563
[38] Nowak S, Lazzaro E and Ramponi G 1996 *Phys. Plasmas* **3** 4140
[39] Eriksson L-G, Hellsten T and Willen U 1993 *Nucl. Fusion* **33** 1037
[40] Carlsson J, Eriksson L-G and Hellsten T 1994 *Proc. Joint Varenna–Lausanne Workshop 'Theory of Fusion Plasmas'* (Bologna: Editrice Compositorei) p 351
[41] Hawkes N C *et al* 2002 *Plasma Phys. Control. Fusion* submitted
[42] Hawkes N C *et al* 2001 Observation of zero current density in the core of JET discharges with lower hybrid heating and current drive *Phys. Rev. Lett.* submitted
[43] Ward D J 1994 *Plasma Phys. Control. Fusion* **36** 673
[44] Houlberg W A *et al* 1997 *Phys. Plasmas* **4** 3231
[45] Joffrin E *et al* 2002 *Plasma Phys. Control. Fusion* submitted
[46] Litaudon X *et al* 2002 *Plasma Phys. Control. Fusion* submitted
[47] Hogeweij G M D *et al* 2002 *Plasma Phys. Control. Fusion* submitted
[48] Mailloux J *et al* 2001 to appear in *Proc. 28th European Physical Society Conf. on Controlled Fusion and Plasma Physics (Madeira, Portugal, 18–22 June, 2001)*
[49] Dux R *et al* 2002 *Plasma Phys. Control. Fusion* submitted
[50] Hender T *et al* 2002 *Plasma Phys. Control. Fusion* submitted
[51] In Y *et al* 2000 *Nucl. Fusion* **40** 1463

PUBLICATION 4

Observation of Zero Current Density in the Core of JET Discharges with Lower Hybrid Heating and Current Drive

Physical Review Letters 2001. Vol. 87, No. 11,
pp. 115001-1–115001-4.

Observation of Zero Current Density in the Core of JET Discharges with Lower Hybrid Heating and Current Drive

N. C. Hawkes,[1] B. C. Stratton,[2] T. Tala,[3] C. D. Challis,[1] G. Conway,[4] R. DeAngelis,[5] C. Giroud,[6] J. Hobirk,[4] E. Joffrin,[6] P. Lomas,[1] P. Lotte,[6] J. Mailloux,[1] D. Mazon,[6] E. Rachlew,[7] S. Reyes-Cortes,[8] E. Solano,[9] and K-D. Zastrow[1]

[1]*Euratom/UKAEA Fusion Association, Culham Science Centre, Abingdon, Oxfordshire, OX14 3DB, United Kingdom*
[2]*Princeton Plasma Physics Laboratory, P.O. Box 451, Princeton, New Jersey 08543*
[3]*Association Euratom-Tekes, VTT Chemical Technology, Espoo, P.O. Box 1404, Finland*
[4]*Max-Planck-Institut für Plasmaphysik, Euratom Association, 85740, Garching, Germany*
[5]*Association Euratom-ENEA sulla Fusione, CRE Frascati, Roma, Italy*
[6]*Association Euratom-CEA, CEA-Cadarache, F-13108 St. Paul lez Durance, France*
[7]*Euratom-NFR, Department of Physics 1, Royal Institute of Technology, SE 10044, Stockholm, Sweden*
[8]*Euratom/IST Association, Centro de Fusao Nuclear, 1049-001, Lisboa, Portugal*
[9]*Association EURATOM-CIEMAT para Fusion, CIEMAT, Madrid, Spain*
and EFDA CSU JET, Abingdon,OX14 3EA, United Kingdom

(Received 16 April 2001; published 22 August 2001)

Simultaneous current ramping and application of lower hybrid heating and current drive (LHCD) have produced a region with zero current density within measurement errors in the core ($r/a \leq 0.2$) of JET tokamak optimized shear discharges. The reduction of core current density is consistent with a simple physical explanation and numerical simulations of radial current diffusion including the effects of LHCD. However, the core current density is clamped at zero, indicating the existence of a physical mechanism which prevents it from becoming negative.

DOI: 10.1103/PhysRevLett.87.115001 PACS numbers: 52.55.Fa

Tokamak experiments [1–3] have shown that heat and particle confinement in the plasma core can be improved by the presence of an internal transport barrier (ITB), motivating extensive study of plasma regimes with ITBs. (Reference [3] contains additional references to experimental work.) An important parameter determining the stability and confinement of the plasma is the safety factor, q, defined as the change of toroidal flux with poloidal flux, $\partial\Phi/\partial\psi$. ITBs can form most easily when the magnetic shear [$s \equiv (r/q)(dq/dr)$] is low or negative in the core region of the discharge [1–3]. The equilibrium state of the plasma current density profile, $j(R, Z)$, in an inductively driven discharge is peaked at the magnetic axis, where the temperature is highest and the resistivity is therefore lowest, resulting in positive shear everywhere in the plasma. [R is the major radius of the torus and Z is the distance from the plasma equatorial plane. In the following, $j(R, Z = 0)$ is denoted $j(R)$.] A standard technique for transiently obtaining low or negative shear is to inject neutral beam or radio frequency heating early in the discharge while the plasma current is ramping up. The heating increases the current diffusion time by decreasing the plasma resistivity, leading to $j(R)$ profiles that are flat or hollow due to current accumulation in the outer region of the plasma. In the JET tokamak, this results in q profiles that are approximately flat [$(q_0 - q_{\min}) < 0.5$], with $q > 1$ everywhere, or low shear. During a subsequent high-power heating phase, ITBs often form near integer values of q, particularly $q = 2$ [3]. Recently, q profiles that are more strongly reversed [$0.5 < (q_0 - q_{\min}) < 2$] have been obtained in JET by application of off-axis lower hybrid heating and current drive (LHCD) during the current ramp-up, hereafter referred to as the LHCD prelude. In this scenario, the ITBs are not always linked to integer q values and the power threshold for ITB formation is lower than in standard optimized shear (OS) discharges [3]. An electron ITB can form early in the LHCD prelude, well before the high-power phase.

This Letter presents an observation of zero current density within measurement errors in the core ($r/a \leq 0.2$) of JET OS plasmas with a LHCD prelude. The magnetic field pitch angle in the plasma is measured by the motional stark effect (MSE) technique [4]. The MSE polarimeter observes D_α emission from energetic atoms injected with velocity $\mathbf{v}_b$ by the heating neutral beams. This emission is split into Stark components by the Lorentz electric field, $\mathbf{v}_b \times \mathbf{B}$, seen by the atoms due to their motion through the tokamak magnetic field, $\mathbf{B}$. The JET MSE polarimeter [5,6] measures the polarization angle of the π lines of the Stark spectrum, which are polarized parallel to the local electric field. The magnetic field pitch angle, $\gamma = \tan^{-1}(B_z/B_\phi)$, where B_z and B_ϕ are the vertical and toroidal components of $\mathbf{B}$, is deduced from the measured polarization angle of the D_α emission, γ_{m}, and is used as a constraint on magnetic equilibrium reconstructions. The statistical accuracy of the γ_{m} measurement is typically $\pm 0.1°$. The overall measurement error is typically $\pm 0.2°$–$0.3°$ when calibration uncertainties are included.

Figure 1 shows the time evolution of the plasma current, the LHCD and neutral beam injection (NBI) power levels, and the electron temperature, T_e, at two radii in a discharge that exhibited extreme shear reversal. This discharge had

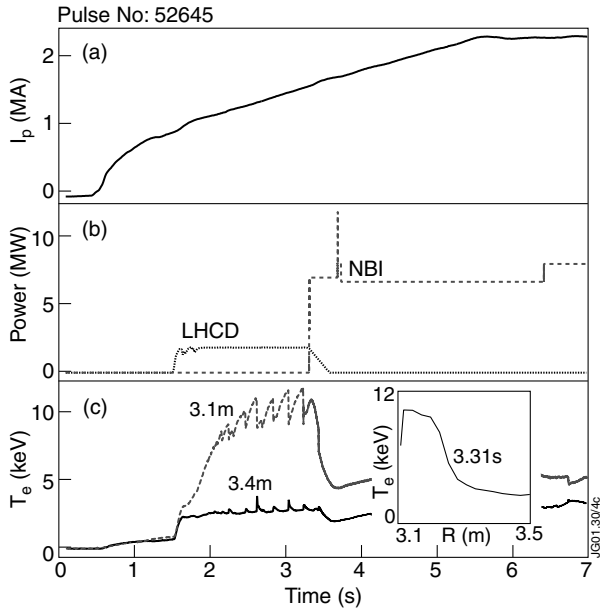

FIG. 1. Time evolution of a JET discharge (No. 52645) that exhibited flat γ_m near the plasma axis at the end of the LHCD prelude. (a) Plasma current, (b) LHCD and NBI power levels, and (c) electron temperature at two radii (solid line: $R = 3.4$ m; dashed line: $R = 3.1$ m) showing sawtoothlike behavior associated with reversed shear.

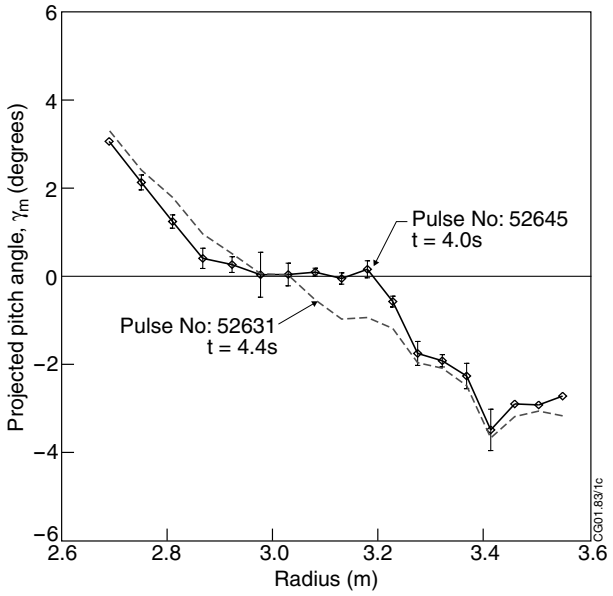

FIG. 2. Polarization angle, γ_m, measured with the MSE polarimeter at the end of the LHCD prelude in two similar discharges. Shot 52645 has a flat region of zero γ_m around the magnetic axis, indicating zero current density in this region, while shot 52631 does not show this effect.

a toroidal magnetic field, B_ϕ, of 2.6 T and plasma current, I_p, of 2.2 MA during the flattop. The LHCD power was 1.9 MW and the launcher was phased to drive current in the same direction as the plasma current (co-current drive). The T_e data show the sawtoothlike behavior often seen in discharges with a LHCD prelude and which is associated with shear reversal [3]. The core T_e shows a significant gradient (-100 keV m^{-1}), indicating that an electron ITB exists early in the LHCD prelude.

Figure 2 shows the MSE polarimeter measurement of the γ_m profile 4.0 s into the discharge, shortly after the end of the LHCD pulse and early in the NBI pulse. γ_m is flat over a region of $r/a \leq 0.2$ around the plasma axis and is zero within measurement errors. The fact that γ_m becomes zero over an extended region indicates that there is a portion of the plasma where $j(R)$ is zero within measurement errors. This feature in the γ_m profile has been seen on a large number of discharges with a LHCD prelude. In general, it is not possible to obtain MSE measurements at earlier times because the density is too low to permit neutral beam injection. However, in a few discharges, short beam pulses were injected as early as 2.5 s, during the time that a clear ITB was apparent in the T_e profiles. In these cases a flat region was again found to be present in the γ_m profile. In such a discharge, when the LHCD was not applied, no flat region in γ_m was measured and no sawtoothing behavior was present on T_e. Figure 2 also shows the γ_m profile measured in a discharge with a LHCD prelude that does not show the flat region near the plasma axis or evidence of a transport barrier in T_e. The formation of the flat region in γ_m during the LHCD prelude is sensitive to unresolved details of the evolution of $j(R)$ and n_e in the first 1 s of the discharge.

The radial component of the plasma electric field, E_r, can contribute to γ_m [7]. The magnitude of this effect was estimated for this discharge by using the value of E_r obtained from the radial force balance equation for carbon impurity ions and charge exchange spectroscopy measurements of the carbon ion temperature, density, and toroidal flow speed. A neoclassical estimate of the poloidal velocity is used [8]. At the time of the profiles shown in Fig. 2 the effect of plasma E_r changes the measured γ_m by $\sim 0.2°$ (due mainly to the toroidal rotation term). A correction was applied to remove this effect from the profiles.

Under the usual discharge conditions of a positive current density everywhere in the plasma, the equilibrium can be described by the Grad-Shafranov equation with the flux surfaces labeled by the normalized poloidal flux, ψ [9]. However, for a plasma with zero current density over a particular region, ψ is also constant in this region. In this situation, ψ is not a monotonic, univalued variable and the equilibrium cannot be accurately reconstructed using the γ_m profile as a constraint in a magnetic equilibrium code which uses ψ as the independent variable. However, the vertical component of the magnetic field, B_z, can be estimated from γ. The value of γ is obtained from the measured pitch angle, γ_m, using an expression based on the full JET neutral beam and MSE polarimeter geometry [5]. This analysis shows that, like γ_m, B_z is near zero over the range $2.9 < R < 3.2$ m. The fact that B_z falls to

zero away from the plasma axis implies that there is a surface that encloses a significant region of zero total current. Since the MSE measurements extend across the diameter of this region, but do not give full coverage in the vertical direction, it is possible that opposed currents of equal magnitude could be flowing in the upper and lower parts of this region, giving, for example, two magnetic axes. However, there is no evidence from the soft x-ray camera data that the plasma has such a structure (the emission profiles are flat within errors) and we therefore conclude that the plasma current is zero across the whole of this region. Assuming, then, that the equilibrium is axisymmetric, the profile of $j(R)$ can be estimated from Ampère's law in a cylindrical geometry (r, θ, z) with θ being the poloidal angle.

Figure 3a shows the $j(R)$ profile calculated in this way from the γ_m profile of Fig. 2 (shot 52645). The current density in the plasma core is zero within an uncertainty of ± 0.2 MA m^{-2} derived from the γ_m measurement errors. This analysis was applied to other discharges that exhibited the flat γ_m region, and the zero core current is consistently seen. In general, measured γ_m profiles which exhibit the flat region do not appear to be consistent with negative values of the core $j(R)$. By ignoring the flat γ_m region, it was possible to obtain an approximate magnetic equilibrium reconstruction using the γ_m profile outside the zero-angle region as a constraint in the EFIT magnetic equilibrium reconstruction code [9]. The q profile obtained in this way was then modified by the difference between the calculated and measured values of B_z to obtain the approximate q profile shown in Fig. 3b. Because q becomes extremely large as $j(R)$ approaches zero, the rotational transform, $\iota = 1/q$, shown in Fig. 3c is a more appropriate description of these equilibria.

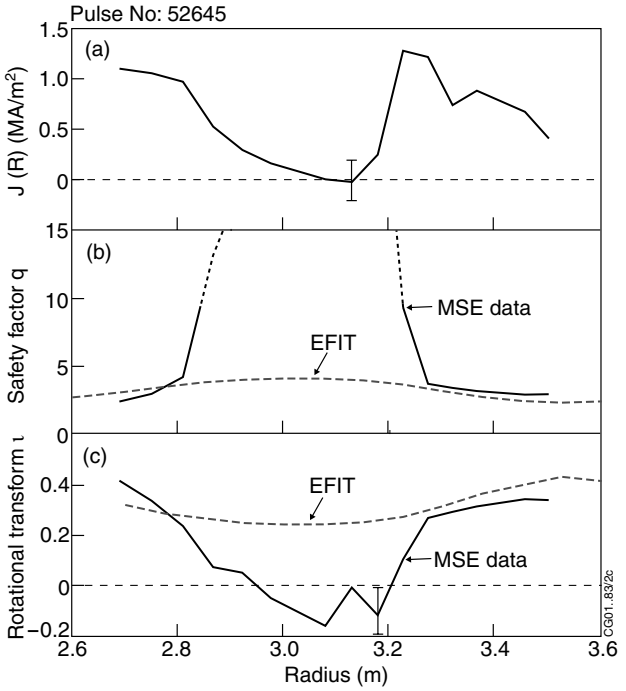

FIG. 3. (a) Current density profile, $j(R)$, derived from the MSE γ_m profile shown in Fig. 2 (No. 52645). (b) Solid lines: safety factor profile, $q(R)$, derived from γ_m measurement and approximate equilibrium solution for the outer region; dashed lines: approximate equilibrium solution for the outer region. (c) Profiles of $\iota = 1/q$ from γ_m measurement and approximate equilibrium solution.

A region of zero or even negative $j(R)$ in the core can exist because the total flux, and therefore the total current, in the core of a highly conductive plasma cannot be rapidly modified due to slow radial diffusion of the parallel electric field [10,11]. This can be seen from the following expression, obtained by combining the radial derivative of Faraday's law with the time derivative of Ampère's law in cylindrical geometry and then eliminating the axial electric field using Ohm's law:

$$\frac{\partial j_{\mathrm{tot}}}{\partial t} = \mu_0^{-1}\left(\frac{\partial^2}{\partial r^2} + \frac{1}{r}\frac{\partial}{\partial r}\right)\eta_{\parallel}(j_{\mathrm{tot}} - j_{\mathrm{ext}}).$$

Here, j_{tot} is the total parallel current density, j_{ext} is the externally driven (noninductive) parallel current density, and $\eta_{\parallel}$ is the parallel resistivity. Initially the external current drive is switched off ($j_{\mathrm{ext}} = 0$) and the Ohmic current density, $j_{\mathrm{tot}} - j_{\mathrm{ext}}$, is nearly zero in the core and does not have a strong gradient. When the external off-axis current drive turns on, regions of positive radial curvature on either side of the peak in j_{ext} transiently decrease j_{tot}. With sufficient external current, this effect can locally drive the current density to zero or even negative. This situation can persist for many seconds in hot JET plasmas due to the long current diffusion time.

This effect can be seen in a simulation of the evolution of the flux surface averaged current density, $J(R)$, in this discharge performed using the JETTO transport code [12] with the assumption of neoclassical resistivity. Measured values of the densities, temperatures, Z_{eff}, plasma current, and magnetic field were used. The simulation was started at 1.0 s and the initial q profile was taken from an EFIT equilibrium constrained by external magnetic measurements only. The LHCD power deposition and generated current density are sensitive to the input temperature and density profiles, and the ray tracing is sensitive to the poloidal magnetic field, B_θ, so the fast ray tracing code [13] used to calculate the power deposition was run inside JETTO to provide a self-consistent model [14]. The beam-driven current is calculated with the PENCIL code [15] which is self-consistently coupled to JETTO.

Figure 4 shows the simulated $J(R)$ profiles at two times: (4a) during the LHCD prelude (3.0 s) and (4b) immediately after the LHCD prelude (4.0 s), when the MSE measurements were made. The contributions to the total current due to LHCD, Ohmic current, bootstrap current, and beam-driven current are shown. Figure 4a shows the region of zero $J(R)$ in the core region ($r/a \leq 0.2$) created in response to the strong off-axis LHCD. Note the wide region of negative Ohmic current due to the effect

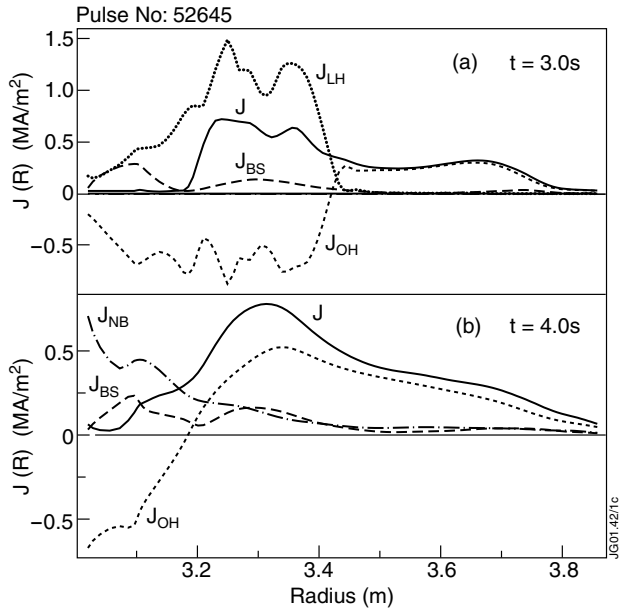

FIG. 4. JETTO code simulation of $J(R)$ in discharge shown in Figs. 1–3 at two times: (a) during the LHCD prelude (3.0 s; $J_{\mathrm{NB}} = 0$) and (b) immediately after the LHCD prelude (4.0 s; $J_{\mathrm{LH}} = 0$), when MSE measurements were made. The contributions to the total current due to LHCD (J_{LH}), Ohmic current (J_{OH}), bootstrap current (J_{BS}), and beam-driven current (J_{NB}) are shown. The region of zero core $J(R)$ due to LHCD is clearly seen in (a). The $J(R)$ profile shown in (b) is consistent with the $j(R)$ profile deduced from MSE measurements (Fig. 3a).

described above. As seen in Fig. 4b, the region of zero current begins to fill in after the LHCD turns off, leaving a small region of zero current density similar to that deduced from the MSE measurements (Fig. 3a). Shrinking of the region of zero current is significantly enhanced by the on-axis current driven by the neutral beams present at 4.0 s (Fig. 4b) but not at 3.0 s (Fig. 4a). The modeling is qualitatively consistent with the MSE measurements. The primary sources of uncertainty in the modeling are uncertainties in the measured input parameters, particularly the initial q and T_e. The resistivity, LHCD deposition, and bootstrap current profile calculations are not valid in the regime where the toroidal current vanishes [this situation is avoided by enforcing $q(r) < 60$]. However, the fact that this condition is attained in the code is a confirmation of the mechanism suggested as responsible for the zero axis current, while the profiles away from the zero current region will still be valid.

An examination of measured γ_{m} profiles in many discharges with an LHCD prelude does not show clear evidence that the core $j(R)$ falls below zero, while the physical explanation and modeling discussed above indicate that this is possible. This observation suggests that a separate physical mechanism acts to prevent a negative core $j(R)$. The sawtoothlike MHD modes present during the LHCD prelude occur at the steep shear region, not in the zero current density region. It is possible that these modes could redistribute current from the periphery of the zero $j(R)$ region, preventing formation of a negative $j(R)$ region, but this has not yet been studied experimentally. The effect of these modes on $j(R)$ could be studied in a future experiment by correlating them with the time evolution of the γ_{m} profile.

A plasma regime with a region of zero core $j(R)$ suggests other interesting experiments. For example, it would allow neoclassical theory [16] to be tested in conditions of near zero B_θ. It would also allow the dependence of the $\mathbf{E} \times \mathbf{B}$ shearing rate on $\partial B_\theta / \partial r$ [17], and its effect on the ion thermal diffusivity, to be studied in a unique regime.

The authors thank Yu. Baranov, V. Drozdov, T. S. Hahm, T. Hender, W. Houlberg, S. Jardin, V. Parail, and J. Wesson for useful discussions. This work was funded by the European Fusion Development Agreement, Euratom, the UK Department of Trade and Industry, and the U.S. Department of Energy (Contract No. DE-AC02-76-CH03073).

[1] F. M. Levinton *et al.,* Phys. Rev. Lett. **75**, 4417 (1995).
[2] E. J. Strait *et al.,* Phys. Rev. Lett. **75**, 4421 (1995).
[3] C. D. Challis *et al.,* Plasma Phys. Controlled Fusion **43**, 861 (2001).
[4] F. M. Levinton *et al.,* Phys. Rev. Lett. **63**, 2060 (1989).
[5] N. C. Hawkes *et al.,* Rev. Sci. Instrum. **70**, 894 (1999).
[6] B. C. Stratton *et al.,* Rev. Sci. Instrum. **70**, 898 (1999).
[7] M. C. Zarnstorff *et al.,* Phys. Plasmas **4**, 1097 (1997).
[8] Y. B. Kim *et al.,* Phys. Fluids B **3**, 2050 (1991).
[9] L. Lao *et al.,* Nucl. Fusion **25**, 1611 (1985).
[10] Ya. I. Kolesnichenko *et al.,* in *Reviews of Plasma Physics,* edited by B. B. Kadomtsev (Plenum, New York, 1992), Vol. 17, pp. 1–191.
[11] P. I. Strand and W. A. Houlberg, Phys. Plasmas **8**, 2782 (2001).
[12] G. Genacchi and A. Taroni, ENEA Report No. ENEA RT/TIB 1988(5), 1988 (unpublished).
[13] A. R. Esterkin and A. D. Piliya, Nucl. Fusion **36**, 1501 (1996).
[14] T. Tala *et al.,* Nucl. Fusion **40**, 1635 (2000).
[15] C. D. Challis *et al.,* Nucl. Fusion **29**, 563 (1989).
[16] Z. Lin *et al.,* Phys. Plasmas **4**, 1707 (1997).
[17] E. J. Synakowski *et al.,* Phys. Plasmas **4**, 1736 (1997).

PUBLICATION 5

Modelling of optimized shear scenarios with LHCD for high performance experiments on JET

Nuclear Fusion 2000. Vol. 40, No. 9, pp. 1635–1649.

Modelling of optimized shear scenarios with LHCD for high performance experiments on JET

T.J.J. Tala[a], F.X. Söldner[b], V.V. Parail, Yu.F. Baranov, A. Taroni[b]
JET Joint Undertaking, Abingdon, Oxfordshire, United Kingdom

J.A. Heikkinen, S.J. Karttunen
Association Euratom–Tekes, VTT Chemical Technology, Espoo, Finland

Abstract. Modelling of LHCD with transport calculations is performed with the JETTO transport code, which has been upgraded by implementing the Fast Ray Tracing Code to calculate self-consistent LH power deposition profiles. Heat and particle transport models that are able to reproduce the experimental JET temperature and density profiles are used in JETTO for predictive high performance modelling. Application of 3.5 MW LHCD power provides an inverted q profile across 50–70% of the plasma radius whereas, without LHCD, the q profile is monotonic during the flat-top phase. The results predict that the fusion power is about 60% higher for high performance DT plasmas in the optimized shear scenario with 3.5 MW LHCD applied during the high performance phase than without LHCD at $B_t = 3.4$ T and $I_p = 3.9$ MA on JET. In addition, the width of the internal transport barrier (ITB) is 0.25–0.30 m larger and the ITB can be sustained for a longer time with LHCD.

1. Introduction

Advanced steady state tokamak operation with pressure and current profile control has become now one of the main goals of magnetic confinement fusion research. Rapid progress in performance has been made in recent experiments with this approach. Internal transport barriers (ITBs) have improved core energy confinement. Improvement of MHD stability with reversed central magnetic shear also gives access to higher β values, resulting in large bootstrap currents. Thus, moderate external current drive should be sufficient to supplement the bootstrap currents for steady state operation. The key to sustained high performance in the advanced steady state tokamak operation mode is a continuous control of pressure and current profiles.

Improved core confinement in a tokamak plasma is achieved by current profile modifications in high performance experiments [1]. The current profile can be modified with early heating by ICRH or LHCD during the current rampup phase. The modified current profile together with a steep pressure gradient gives rise to reduced transport which manifests itself as a further peaking of the temperature and density profiles with steep gradients typically at $r/a = 0.5$–0.7. These ITBs have a large influence on plasma core confinement and thereby significantly enhance tokamak performance [2–4]. This operation mode in JET where one of the key elements is the ITB is called the optimized shear (OS) scenario. At present it is considered to be the most promising approach towards steady state tokamak operation.

The operation mode with ITBs characteristic of the OS regime combined with an edge transport barrier of the high confinement H mode regime is called the double barrier (DB) mode. It has resulted in a fusion gain Q higher by a factor of 2 than those in conventional sawtoothing steady state ELMy H mode plasmas [5]. In DT discharges the DB mode has produced a fusion gain of $Q = 0.4$, and high performance has been sustained for four energy confinement times in the DB mode in a DD plasma. Recently, the DB mode has been routinely established in the gas box divertor configuration on JET.

Advanced tokamak scenario modelling with an optimized magnetic shear configuration that exhibits an ITB was performed by transport simulations recently in Ref. [6]. The authors of that article explored the capability of off-axis electron cyclotron current drive to control the hollow current profile in the OS operation mode. The evolution of the thermal and the particle ITBs with a monotonic or slightly reversed q profile and large $\boldsymbol{E} \times \boldsymbol{B}$ rotation shear

[a] *Permanent address:* Association Euratom–Tekes, VTT Chemical Technology, Espoo, Finland.
[b] *Present address:* European Commission, Brussels, Belgium.

produced mainly by NBI and ICRH was studied in Ref. [7].

In this work, the performance perspectives of the profile controlled OS scenario are investigated and optimized with the JETTO transport code modelling calculations, using LHCD for current profile control. With LHCD, hollow current density profiles and a wider reduced magnetic shear region can be achieved [1]. Thus LHCD can provide wider ITB during the high performance phase. However, high performance OS experiments with LHCD have not been performed on JET. It is therefore important to investigate how LHCD affects the formation and sustainability of the ITB. With a direct influence on the magnetic shear and an indirect one through the electron heating, LHCD can influence the transport coefficients. The LH power deposition depends sensitively on the temperature and density profiles. Accordingly, self-consistent calculation of transport and LH ray tracing including wave absorption is required.

The JETTO transport code [8] has been upgraded by adding the Fast Ray Tracing Code (FRTC) [9], which is run inside JETTO. Lower hybrid current density and power deposition profiles can be modelled by using either the coupled JETTO/FRTC code, the stand-alone Baranov's ray tracing code (noted in this article as BRTC) [10] or experimental profiles of JET discharges. The self-consistent LH power deposition profiles produced by the JETTO/FRTC code can be thus compared with stand-alone ray tracing results or with the experimental results. In the following simulations, self-consistent current profile control with long pulse LHCD during the high performance phase calculated by JETTO/FRTC is applied, producing a significant amount of off-axis current.

The JETTO transport model is based on an empirical transport model which has been developed on JET and validated against several JET discharges [11–13]. The heat and particle transport models are further tested for OS discharges with L and ELMy H mode plasma edge, with the main emphasis on the formation and the expansion of the ITB. The transport model in Ref. [7] differs in some details from the model used in our transport calculations. In the study reported in Ref. [7], the reproduction of the JET OS pulses Nos 40542 and 40847 was found to be as good as the reproduction of those two pulses with our transport model.

The article is structured in the following way. Section 2 gives a brief characterization and summary of the experiments in the OS regime on JET. The transport model used in the transport calculations is described and tested in Section 3. The current profile control with LHCD is the topic of Section 4. The LH power deposition profiles calculated by the coupled JETTO/FRTC code are presented and compared with the profiles calculated by the stand-alone ray tracing code. The improvements in the ITB formation with LHCD for OS plasmas are also discussed. The high performance steady state discharges, including the analysis of different current rampup schemes, in the OS scenario regime with JETTO modelling calculations are demonstrated in Section 5. The main plasma profiles and the parameters predicted by the modelling calculations with LHCD applied during the high performance phase are given and the MHD stability analysis is illustrated. Finally, the summary and the conclusions follow in Section 6.

2. Optimized shear experiments

The OS discharge pulse No. 40847 has achieved the second highest neutron production rate in JET deuterium discharges staying only 5% below the record, also obtained with an OS pulse. Pulse No. 40847 represents the standard scenario of the high performance OS discharge on JET, including the typical sequence of the different confinement regimes. The characteristic time evolution of the main plasma parameters for this pulse is shown in Fig. 1.

The discharge is initiated with a fast plasma current rampup and an early X point formation at $t = 0.8$ s. A short application of LHCD during the early current rampup phase $t = 0.4$–1.2 s assists in forming the required target q profile. ICRH is used for pre-heating from $t = 3$ s to $t = 5$ s to slow down the current inward diffusion. High power heating with NBI and ICRH rises up to a maximum from $t = 5.0$ s to $t = 5.4$ s. An ITB is formed in this pulse at $t = 5.3$ s. The peripheral plasma remains in L mode until $t = 6.76$ s when a transition to an ELM-free H mode occurs. The ion heat conductivity falls close to the neoclassical level in the plasma core. The region of reduced heat conductivity expands gradually with the expansion of the ITB during the L mode phase. The ion heat conductivity is further reduced also in the peripheral region during the ELM-free H mode phase. MHD stability is maintained near the marginal stability limit with a real time power

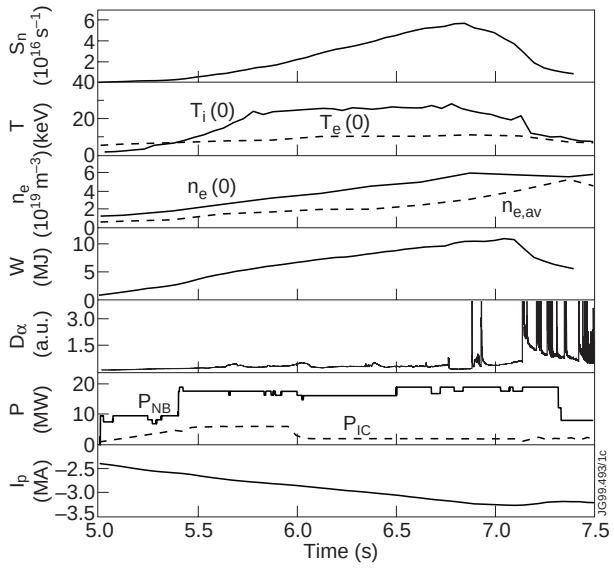

Figure 1. Time traces of the neutron rate S_n, the central ion T_i and electron T_e temperatures, the electron density n_e, the diamagnetic energy W, D_α signal, the heating powers P_{NB} and P_{IC} and the plasma current I_p for the OS discharge (pulse No. 40847) with an ITB and a long lasting L mode edge. The ITB appears at $t = 5.3$ s and the plasma edge experiences an L–H transition at $t = 6.76$ s.

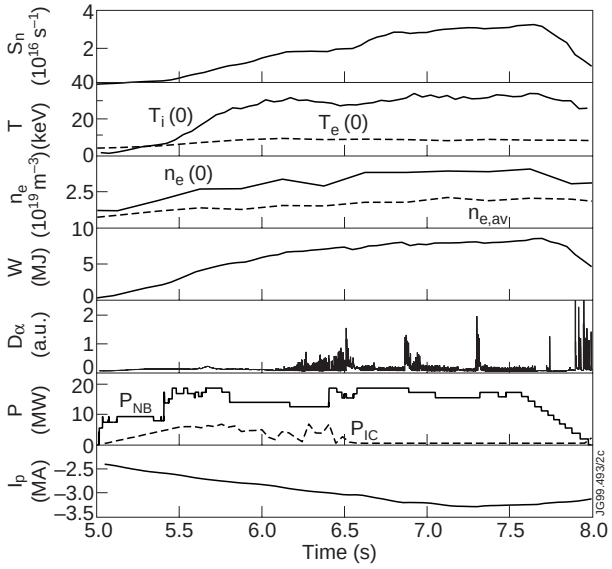

Figure 2. As in Fig. 1, but for the OS discharge (pulse No. 40542) with an ITB and ELMy H mode edge. The ITB appears at $t = 5.4$ s and the plasma edge experiences an L–H transition at $t = 6.1$ s. The DB mode exists until $t = 7.5$ s when the heating is turned down.

control. At $t = 6.88$ s a first ELM marks the transition to an ELMy H mode phase. During this last phase the performance decreases and the ITB decays.

JET pulse No. 40542 represents a discharge in the DB mode. Internal and external transport barriers are superposed in the OS scenario with the plasma edge in ELMy H mode. The discharge approaches steady state conditions in its temperature and density profiles. High performance with an H factor $H^{89\text{-P}} \approx 2$ has been maintained for four energy confinement times. An ITB is formed in this pulse at $t = 5.4$ s. The peripheral plasma remains in L mode until $t = 6.2$ s when a transition to an ELMy H mode occurs. The H mode adds an edge transport barrier (ETB) to the persisting ITB. Both transport barriers co-exist for the remaining phase of high power heating until the NBI power is ramped down from $t = 7.5$ s onwards. Only this ends the high performance steady state phase. The time traces for this pulse are illustrated in Fig. 2.

The ion heat conductivity χ_i falls to the neoclassical level in the plasma core. The region of reduced heat conductivity expands gradually out to two thirds of the plasma minor radius during the L mode phase. The extent of the improved core is maintained during the H mode phase. The ion heat conductivity is further reduced by a factor of 3 in the peripheral region during ELMy H mode.

The electron heat conductivity χ_e is also reduced over the whole plasma cross-section and shows an ITB at the same location, as seen from the ion heat conductivity profile. The reduction in electron heat conductivity, however, is much smaller than that in ion heat conductivity. Inside the ITB, χ_e drops typically by a factor of 5, while χ_i falls by more than an order of magnitude.

MHD stability calculations show a gradual rise of the beta limit after the pressure profile broadening with the transition to ELMy H mode. The marginal stability limit for pressure driven kink modes then increases up to $\beta_N \approx 3$.

3. Description of the JETTO transport model

In this work, we will use as the basic model an empirical transport model developed at JET and tested against several different plasma discharges on DIII-D, TFTR, JT-60, ASDEX Upgrade, START and JET in L mode and against many different plasma discharges on JET in H mode [11, 12]. It is

based on a combination of a Bohm and a gyro-Bohm type of anomalous transport, and the set of transport coefficients can be written in the following form:

$$\chi_e = 1.0\chi_{gB_e} + 2.0\chi_B \tag{1}$$

$$\chi_i = 0.2\chi_{gB_i} + 4.0\chi_B + \chi_i^{neo} \tag{2}$$

$$D = [w_1 + (w_2 - w_1)\rho_{eff}]\frac{\chi_e\chi_i}{\chi_e + \chi_i} \tag{3}$$

where

$$\chi_{gB_{e,i}} = 5 \times 10^{-6}\sqrt{T_{e,i}}\left|\frac{\boldsymbol{\nabla}T_{e,i}}{B_t^2}\right| \tag{4}$$

$$\chi_B = 4 \times 10^{-5} R \left|\frac{\boldsymbol{\nabla}n_eT_e}{n_eB_t}\right| q^2 \times \left(\frac{T_e(0.8\rho_{max}) - T_e(\rho_{max})}{T_e(\rho_{max})}\right). \tag{5}$$

In Eqs (4) and (5), T_e and T_i are the electron and the ion temperatures, respectively, n_e is the electron density, B_t the toroidal magnetic field, R the major radius and q the safety factor. χ_i^{neo} is the neoclassical term for the ion heat transport. The nonlocality in the Bohm transport appears in the last term where ρ_{eff} is the flux surface label defined by $\rho_{eff} = \sqrt{\Phi/\pi B_t}/a_{eff}$ with a_{eff} being the radius of the circle covering the same area as the elongated plasma. ρ_{max} is the value of ρ_{eff} at the separatrix in L mode and on top of the barrier in H mode and Φ is the toroidal magnetic flux. All the quantities appearing in Eqs (1)–(8) are expressed in SI units except the temperatures T_e and T_i whose units are electronvolts. w_1 and w_2, which are multipliers to the particle diffusion coefficient, are the only coefficients that are varied in the model in Eqs (1)–(5). The boundary temperatures for the ions and electrons are taken from the experiment. Modelling of the boundary particle transport is not a well understood problem and we have solved it by assuming that the recycling coefficient at the separatrix is equal to one and then using the experimental particle flux through the separatrix to determine the particle losses from the plasma. The initial q profile is calculated by EFIT and Z_{eff} is taken from the TRANSP analysis.

The model for triggering the ITB is introduced with a step function switching off the Bohm transport when a control parameter exceeds a certain value [13]. The suppression condition of this dimensionless control parameter and the modified Bohm transport can be thus written as

$$s - \alpha_{e,i}\Omega < 0 \tag{6}$$

where

$$\Omega = \frac{\omega_{E\times B}}{\gamma} \propto \frac{R\left|\frac{(RB_\theta)^2}{B}\frac{\partial}{\partial\Psi}\left(\frac{\boldsymbol{\nabla}n_iT_i}{en_iRB_\theta}\right)\right|}{v_{thi}} \tag{7}$$

$$\chi_{B_{e,i}} = \chi_B\Theta(s - \alpha_{e,i}\Omega) \tag{8}$$

where s is the magnetic shear, Ω the ratio of shear in poloidal plasma rotation to instability growth rate, Ψ the poloidal magnetic flux, B_θ the poloidal magnetic field, e the electron charge and $\gamma = v_{thi}/R$ the characteristic growth rate of the drift type of plasma turbulence, with α_e and α_i being the numerical weighting factors for shear in plasma rotation Ω for electrons and ions, respectively. The Θ function multiplying the modified Bohm transport in Eq. (8) is the normal Heaviside step function with the controlling parameter given by Eq. (6). The physical meaning of the step function is that in regions where the argument $s - \alpha_{e,i}\Omega < 0$, the Bohm type of anomalous transport is fully suppressed, i.e. $\Theta = 0$, which then leads to the formation of the ITB. The contributions from the toroidal and poloidal velocities to the radial electric field and Ω are omitted in this model because of the difficulties in modelling the toroidal velocity and due to the lack of measurements of the poloidal rotation on JET [14]. A model which takes into account all three terms in the radial electric field is under construction for the JETTO transport code and the preliminary results are published in Ref. [15]. In consequence, there are four numerical parameters to be fitted with the experimental data, the coefficients α_e and α_i for triggering the ITB as well as the earlier defined w_1 and w_2 in the particle transport.

The model has been tested in the OS regime against both the ITB formation in L mode and ITB formation with ELMy H mode discharges on JET. In Fig. 3, we have reproduced one steady state ITB pulse with first L mode edge till $t = 6.2$ s and then later with ELMy H mode edge (pulse No. 40542, which was already illustrated in Section 2, Fig. 2). In particular the heat transport model can describe the temporal evolution of $T_{e,av}$ and $T_{i,av}$ mostly within the experimental error bars, but despite some further development of the particle transport model moderate uncertainties still persist in it. The differences in the time traces at around $t \approx 6.2$ s are related to the difficulties that the model has in following the rapid L–H transition at the plasma edge. After the delayed response to the L–H transition the transport model reproduces the experiment again nearly within the error bars after $t = 6.5$ s. In this analysis, the values $\alpha_e = 0.0$ and $\alpha_i = 1.9$ were chosen for electrons

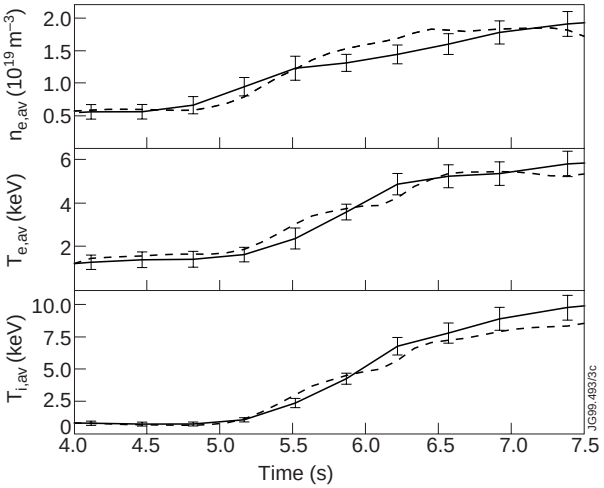

Figure 3. Reproduction of JET deuterium discharge No. 40542. The solid curves with error bars correspond to the experiment and the dashed curves are given by our transport model. The time evolution of the volume averaged electron density and the average electron and ion temperatures are shown.

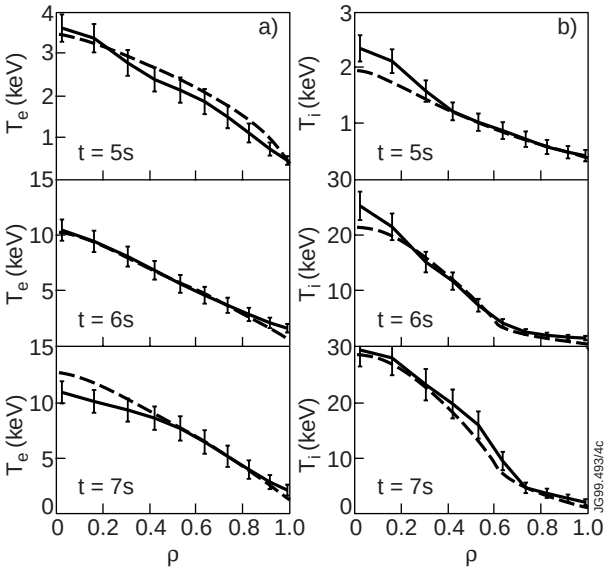

Figure 4. Radial profiles of (a) the electron and (b) the ion temperatures for the reproduction of JET deuterium discharge No. 40542. The solid curves correspond to the experiment and the dashed curves are given by our transport model.

and ions, respectively, as well as $w_1 = 0.8$ (core) and $w_2 = 0.3$ (edge) for the multipliers to the particle transport.

To quantify the agreement between the modelling and the experiments, a statistical approach to simulation results is applied according to the equations

$$m_Y = \left(\sum_{i=1}^{K} \frac{\sum_{j=1}^{N} (Y_{exp}(x_j) - Y(x_j))/Y(x_j)}{N} \right) /K \tag{9}$$

$$\Delta_Y^2 = \sum_{i=1}^{K} Z_i/K \tag{10}$$

where Z_i is defined as

$$Z_i = \frac{\sum_{j=1}^{N} (Y_{exp}(x_j) - Y(x_j) - m_{Y,i})/Y(x_j)^2}{N}. \tag{11}$$

The calculated quantity m_Y symbolizes the modelling offset of the quantity Y, which can be in our case either n_e, T_e or T_i, and the quantity Δ_Y^2 stands for the variance between the experimental measurement and the modelling result of the quantity Y. The inner summation from 1 to N is over the radial grid points ($N = 51$) and the outer summation is over 15 ($K = 15$) time points evenly distributed within the time interval of the simulation. $m_{Y,i}$ is the value of m_Y without the sum over the time range K at the ith time step. $Y_{exp}(x_j)$ is the measured value of the given quantity at the radial point x_j and $Y(x_j)$ is the calculated value at the same point. Consequently, m_Y and Δ_Y^2 characterize the time average modelling offset and the time average modelling variance compared with the measurement over the whole duration of the simulation.

The radial profiles of the electron and ion temperatures as a function of $\rho = r/a$ at $t = 5.0$ s, $t = 6.0$ s and $t = 7.0$ s are presented in Figs 4(a) and (b), respectively. The central ion temperature is underestimated at $t = 5.0$ s and $t = 6.0$ s, but otherwise the profiles are in good agreement with the experiment, mostly within the error bars. In Fig. 5, the density and pressure profiles are shown at the same three instants. The modelling results are well within the error bars in H mode, but in L mode the model tends to overestimate the density. The calculated modelling offsets and modelling standard deviations for T_e, T_i and n_e are presented in Table 1. The standard deviations for the heat transport Δ_{te} and Δ_{ti}, calculated over the whole simulation period (from $t = 4.0$ s up to $t = 7.5$ s), are clearly smaller than the standard deviation of n_e when using the model with $\alpha_i = 1.9$ and $\alpha_e = 0$. Positive modelling offsets in Table 1 indicate that those quantities are

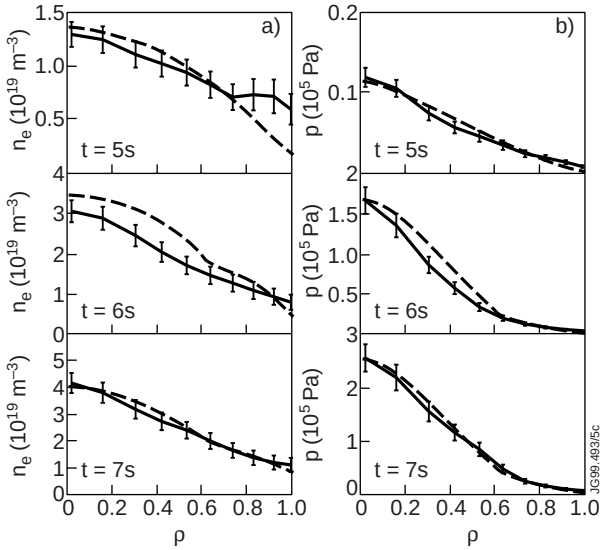

Figure 5. As in Fig. 4, but for (a) density and (b) pressure.

underestimated on average over the whole time range by the transport calculation.

The power deposition profiles of NBI and ICRH are calculated by TRANSP and shown in Fig. 6 at $t = 5.0$ s, $t = 6.0$ s and $t = 7.0$ s. The maximum power for NB heating is about 18 MW and for ICRH about 7 MW. The standard Monte Carlo model was used for calculating the NB power deposition profiles. For the calculation of the ICRH power deposition profiles, the bounce averaged Fokker–Planck code [16] was applied in TRANSP calculations. A comprehensive study of the use of that ICRH module inside TRANSP with OS plasmas and the analysis of ICRH for JET high performance plasmas is made in Refs [17, 18]. The frequency of the applied ion cyclotron hydrogen minority heating scheme (minority concentration 2–3%) was 51 MHz. The diamagnetic energy of the TRANSP analysis for this pulse is almost identical to the experimentally measured diamagnetic energy. Accordingly this can be regarded as an indirect proof of the goodness of the NBI and ICRH power deposition profiles because about 50% of W_{dia} comes from the contribution of the fast particles produced by NBI and ICRH.

The time evolution of the footpoint of the ITB is shown in Fig. 7. The dashed curve corresponds to the radius of the ITB observed in experiment (pulse No. 40542) and the solid curve is calculated by the transport model. The radial expansion of the ITB with time can be reproduced within 6 cm of the measured one by the model even if it tends to

Table 1. Modelling offsets m_{Te}, m_{Ti} and m_{ne} and the modelling standard deviations Δ_{Te}, Δ_{Ti} and Δ_{ne} for the best choice of α_i and α_e ($\alpha_i = 1.9$ and $\alpha_e = 0.0$) and the optimum case with $\alpha_i = \alpha_e$ for pulse No. 40542

α coefficients	m_{Te}	m_{Ti}	m_{ne}	Δ_{Te}	Δ_{Ti}	Δ_{ne}
$\alpha_i = 1.9$, $\alpha_e = 0.0$	−0.01	0.11	0.04	0.18	0.19	0.26
$\alpha_i = 1.2$, $\alpha_e = 1.2$	0.02	0.27	0.05	0.19	0.36	0.27

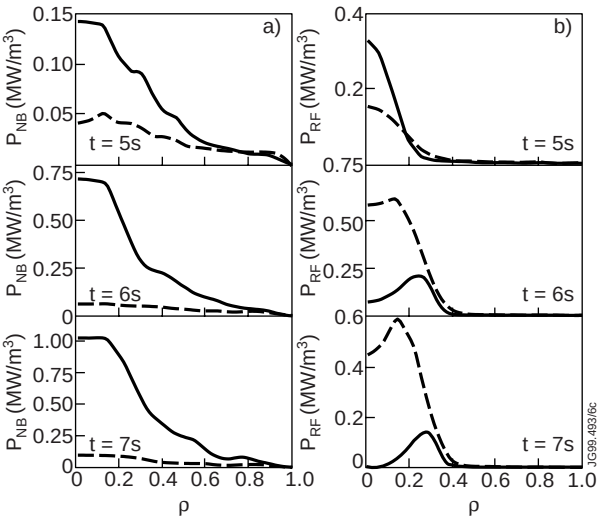

Figure 6. (a) NBI power deposition profiles and (b) ICRH power deposition profiles, both calculated by TRANSP at the same instants as the profiles in Figs 4 and 5. The solid curves correspond to the contribution to the ion heating and the dashed ones to the electron heating.

underestimate slightly the width of the barrier during the steady state phase.

The reason for fixing $\alpha_e = 0$ was that the shear in plasma rotation has only a weak or negligible effect on short wavelength turbulence which is mainly responsible for the electron heat transport. The reproduction is clearly better when $\alpha_e = 0$. The other motivated choice by the physics reasons for α_e would be $\alpha_i = \alpha_e$. In that case the optimum choice according to the modelling calculations is $\alpha_i = \alpha_e = 1.2$. However, the calculated standard deviations in Table 1 in the lower column, especially in Δ_{ti}, confirm the belief that $\alpha_e = 0.0$ was a justified choice.

The sensitivity analysis of the most critical numerical parameter α_i is shown in Fig. 8, where the width

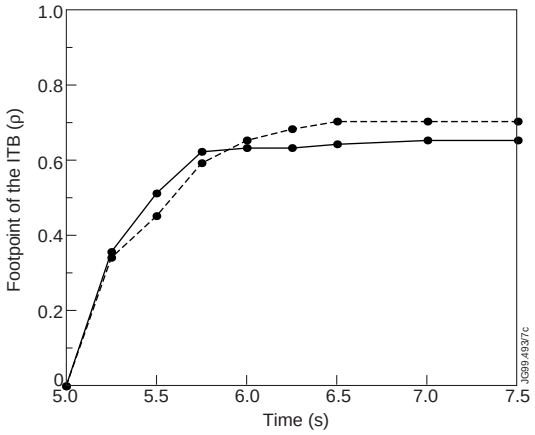

Figure 7. Radial location of the footpoint of the ITB as a function of time. The dashed curve is from pulse No. 40542 and the solid curve is calculated by the transport model.

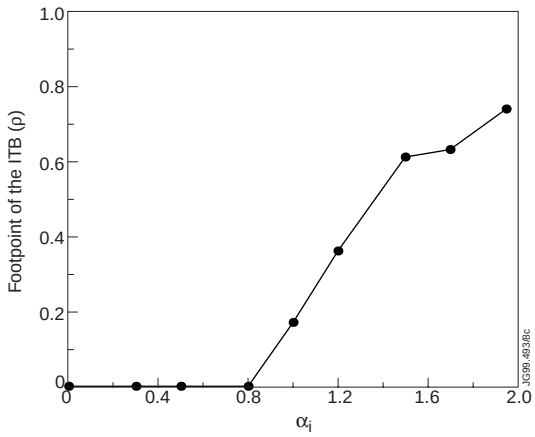

Figure 8. Radial location of the footpoint of the ITB as a function of the weighting factor α_i to shear in plasma rotation for pulse No. 40542 at $t = 7.0$ s.

of the ITB is plotted as a function of α_i at $t = 7.0$ s. As can be seen, the width of the ITB decreases almost linearly with decreasing α_i and the ITB vanishes when $\alpha_i < 0.8$. The same values $w_1 = 0.8$ and $w_2 = 0.3$ were applied during the previous sensitivity analysis. The model is only weakly sensitive to the values of w_1 and w_2 according to a comprehensive sensitivity analysis in the range of $w_1 = [0.2, 2.5]$ and $w_2 = [0.2, 2.5]$.

The most critical assumption in the model is that the initial q profile is taken from EFIT. As shown by Eq. (8), the magnetic shear s, or the q profile has a strong effect on the ITB formation and the width of the barrier. Consequently, the accuracy of the EFIT magnetic reconstruction plays a major role in the modelling calculations. However, by starting the simulation early enough, well before the main heating phase when the current has only about 50–70% of its flat-top value, the current evolution calculated by JETTO should have enough time to evolve in a self-consistent way independently of the initial q profile by EFIT. In all the previous analyses the simulations were started at least 1 s before the main heating phase. The optimum choice for α_i would be 10–20% higher (depending on the pulse) if the simulation was started at the same time as the main heating than in the case with the early start of the simulation. In the future, after validating the new motional Stark effect (MSE) magnetic measurements on JET, EFIT will produce more accurate q profiles.

4. Current profile control and improved ITB formation with LHCD

Lower hybrid current drive has been shown to be the most efficient of the various methods for non-inductive current drive in tokamaks so far and it has been used for current profile control in many experiments [19]. It can be applied in particular in off-axis current drive for creating or sustaining hollow current density profiles. Current profile control by LHCD has been explored and experimented with by using various techniques [2, 3, 20–22]. Another means to control the current profile evolution is current rampup, and its effect on optimizing the fusion performance is investigated in Section 5.1. In this section, we concentrate on the questions of modelling of LHCD current profile for high performance OS discharges and the results of modelling of the current profile control during the main heating and fuelling phase. Moreover, the improved ITB formation when applying LHCD during the main heating phase is considered.

4.1. Validation of self-consistently calculated LHCD by JETTO/FRTC

A new ray tracing code, called FRTC [9], has been installed and coupled to the JETTO transport code. The lower hybrid power deposition and current density profiles are calculated in a self-consistent way, i.e. the evolving temperature and density profiles as well

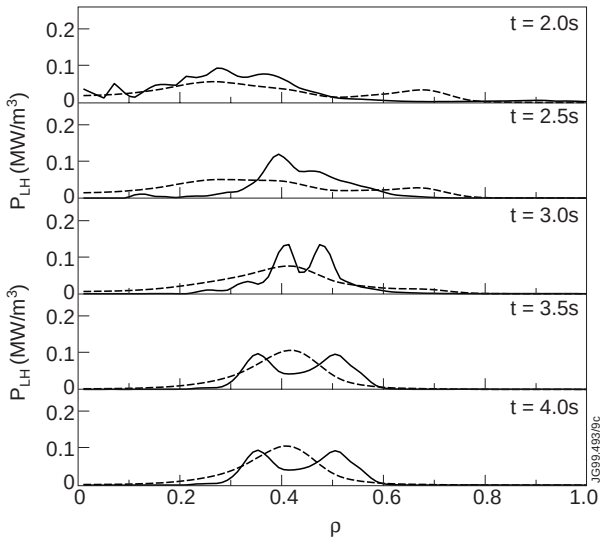

Figure 9. Lower hybrid power deposition profiles calculated by the coupled JETTO/FRTC code (solid curves) and BRTC (dashed curves) for pulse No. 47952.

as the poloidal magnetic field are read directly from JETTO by FRTC at each time step when FRTC is called. The calculated power deposition and current density profiles by FRTC are then used as the source terms for further time steps in JETTO, thus creating a self-consistent transport calculation with current profile control by LHCD. In FRTC, the flux surface averaged quasi-linear diffusion coefficient is found from the power deposition profiles and then used in a 1-D Fokker–Planck equation to calculate the electron distribution function. The equilibrium between the electron distribution and the power deposition is thus achieved by iteration, and finally the driven current can be evaluated. The 1-D Fokker–Planck equation is as in Ref. [23], except in FRTC the collision frequency has the factor $10/(5+Z_{eff})$ instead of $2/(2+Z_{eff})$. This accounts for the important corrections observed with the 2-D Fokker–Planck equations over 1-D solutions, i.e. enhancement of the current drive efficiency by a factor of 2.5 for $Z_{eff} = 1$ and the slight increase of this factor with Z_{eff}.

The power deposition profiles calculated by the coupled JETTO/FRTC code (solid curves) and the profiles that are calculated by BRTC [10] (dashed curves) are compared in Fig. 9 for pulse No. 47952. The maximum input heating powers for this recent LHCD profile control discharge are $P_{LH} = 1.4$ MW and $P_{NB} = 0.9$ MW, and the axial electron and ion temperatures vary between 2.0 and 3.5 keV as well as the axial electron density in the range (1.1–1.7) $\times 10^{19}$ m^{-3}. In each simulation, temperatures, density and I_p were taken from the experiment throughout the pulse and the only transport equation that was solved was the current diffusion equation. Power deposition profiles given by JETTO/FRTC are in a reasonably good agreement with profiles from the stand-alone BRTC, as shown in Fig. 9. That argument can be also strongly motivated by following the time behaviour of the corresponding q profiles presented in Fig. 10. The q profile evolution is almost identical to the LH profiles found by JETTO/FRTC and by BRTC, whereas without LHCD, the q profiles are completely different, i.e. they are flat or monotonic rather than strongly reversed as with LHCD. Since the q profiles calculated by JETTO/FRTC and by BRTC are almost identical, the differences in the power deposition profiles, mostly due to stronger smoothing used in BRTC, do not affect significantly the evolution of the q profile. However, in general it cannot be concluded that the evolution of the q profile is not sensitive to LHCD (see the dotted curves in Fig. 10). Consequently, this can be regarded as an indication of the significant agreement between the LH calculation results of FRTC and BRTC, in spite of differences in the detailed structure in LH power deposition profiles. A more comprehensive study of the properties of FRTC and its power deposition profiles has been done in Ref. [24]. Due to the lack of LHCD experiments during the high performance phase on JET, the corresponding comparison of LH profiles calculated by the two codes under those circumstances could not be accomplished.

Measurement data from the fast electron bremsstrahlung (FEB) diagnostics are not available for pulse No. 47952, and thus the comparison with FRTC calculations could not be made. However, when comparing older LH discharges, pulses Nos 39274 and 39275, FRTC gives more localized power deposition profiles, and the peak of the deposition profile is located closer to the centre of the plasma than with the profiles from the Abel inverted FEB measurements. In addition, Abel inverted FEB profiles are much smoother. The difference between FRTC and Abel inverted FEB calculations can be due to the following three problems. Firstly, FEB diagnostics do not measure fast electrons with energies of less than 133 keV. Secondly, the other problem with FEB measurements is that they also count the X ray emission from the wall produced by the scattering and reflection processes. On the other hand, FRTC does not take into account the spatial diffusion the fast electrons.

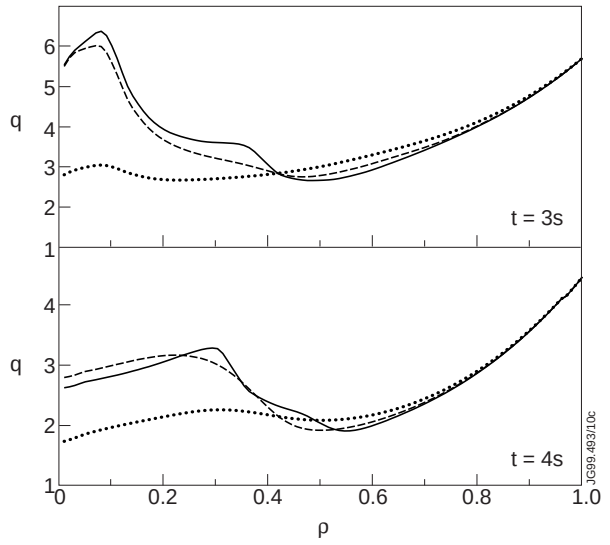

Figure 10. Evolution of the q profile calculated by the coupled JETTO/FRTC code (solid curve), by JETTO with LH power deposition profiles from the stand-alone BRTC (dashed curve) and without LHCD (dotted curves) for pulse No. 47952.

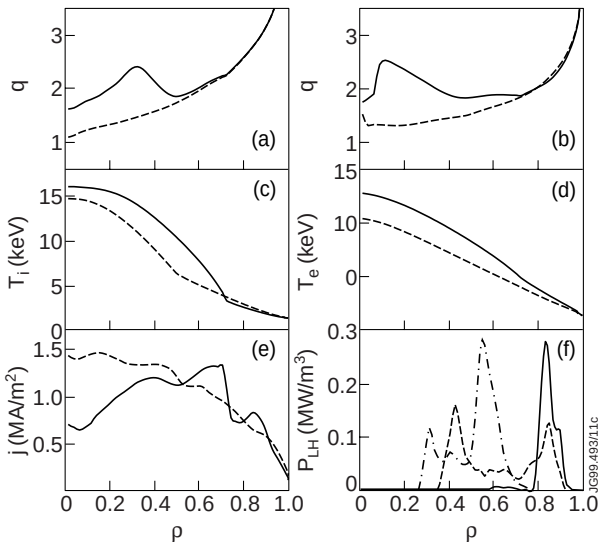

Figure 11. (a) Profiles of q with 3.5 MW LHCD (solid curves) and without LHCD (dashed curves) at $t = 6.0$ s and (b) at $t = 10.0$ s for the high performance OS modelling discharge. (c) The ion and (d) the electron temperature and (e) the current density profiles with (solid curves) and without (dashed curves) LHCD at $t = 10.0$ s. (f) The LH power deposition profiles from JETTO/FRTC at $t = 6.0$ s (chain curve), $t = 8.0$ s (dashed curve) and $t = 10.0$ s (solid curve).

4.2. Improved ITB formation with LHCD

The negative or small magnetic shear s resulting from the hollow or flat current density profile is one of the two key factors suppressing the Bohm transport, as can be seen in Eq. (6). However, it has not been clear how large the effect of LHCD power and the deposition profiles on the formation and location of the internal transport barrier is due to the lack of experiments where LHCD has been applied during the high performance phase on JET. Consequently, this issue was analysed by using the JETTO transport code with self-consistent LHCD deposition profiles from FRTC.

Current profile control with off-axis LHCD has been applied during the high performance phase to freeze the q profile by heating the electrons, thus causing the current diffusion to slow down. Moreover, it provides additional off-axis current peaked at about $\rho = 0.6$–0.8 giving rise to a larger region of low magnetic shear. This dual effect of the current profile control can be seen in Fig. 11. The plasma parameters and initial temperature, density and q profiles are from pulse No. 40542. The input heating powers and power waveform of NBI and ICRH are as shown in Fig. 6 and after that the NBI and ICRH power deposition profiles are kept fixed until $t = 10.0$ s at the level of $P_{NB} = 18$ MW and $P_{RF} = 6.5$ MW. The values of the numerical variables were kept the same as those in Section 3, i.e. $\alpha_e = 0.0$ and $\alpha_i = 1.9$ as well as $w_1 = 0.8$ and $w_2 = 0.3$.

Application of 3.5 MW LH power with power deposition and current density profiles calculated self-consistently by JETTO/FRTC provides an inverted q profile across 50–70% of the plasma radius, whereas the q profile is monotonic without LHCD. The reversed region in the q profile becomes wider from the early main heating phase at $t = 6.0$ s until $t = 10.0$ s, and the changes at the plasma periphery are due to continuous current rampup up to $I_p = 3.9$ MA. Thus, LHCD provides off-axis current drive in these conditions and creates a broad hollow current profile as is seen in Fig. 11(e). Worth mentioning here is the great significance of the amount the bootstrap current, which is about 50% of the total current. The large contribution from the bootstrap current ($\gtrsim$50%) due to the large pressure gradient over a wide region of high density in the core plasma is typical of these high performance OS plasmas according to the modelling calculations.

The radial expansion of the ITB from $\rho \approx 0.5$ to $\rho \approx 0.7$ due to LHCD is seen in Fig. 11(c), where

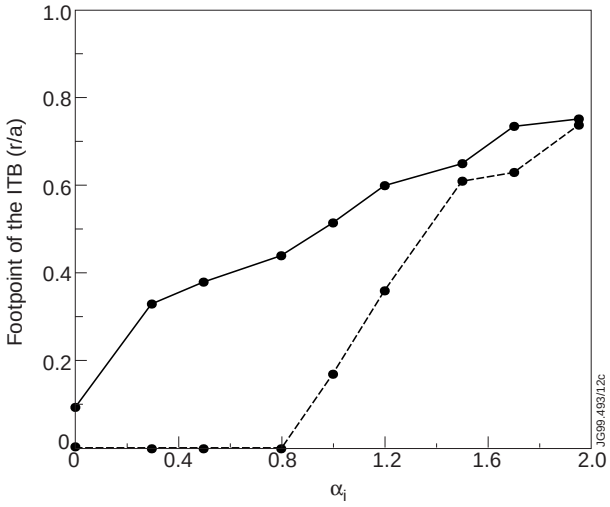

Figure 12. Radial location of the footpoint of the ITB as a function of the weighting factor α_i to shear in plasma rotation at $t = 7.0$ s. The solid curve corresponds to the case with 3.5 MW LHCD and the dashed curve without LHCD (pulse No. 40542).

we have plotted the ion temperature with and without LHCD at $t = 10.0$ s. The electron temperature is also higher with an additional 3.5 MW LHCD, as shown in Fig. 11(d). Thus current diffusion slows down and steady state conditions with a more robust ITB can be sustained for a longer time. The pressure is also higher and the region with high pressure is wider with LHCD. Both these features give rise to the better fusion performance. The pressure in our calculations is of the same order as in the record fusion discharge (DT, hot ion H mode) on JET [25]. The LH power deposition profiles calculated by JETTO/FRTC are shown in Fig. 11(f).

The sensitivity of the formation and location of the ITB to the critical value of $\Theta(s - \alpha_{e,i}\Omega)$ used in our model for turbulence suppression was tested for the same plasma discharge (pulse No. 40542) with the same set of simulation parameters with and without off-axis current profile control by LHCD. In the model, we fixed $\alpha_e = 0.0$ as justified in Section 3, but α_i was varied to find out the sensitivity of the ITB formation and location to the weighting coefficient of the plasma rotation. This is shown in Fig. 12 at $t = 7.0$ s.

For lower values of α_i the stabilizing effect of shear in plasma rotation on the Bohm type of transport diminishes and the transport barrier shrinks. This dependence is significantly weaker with LHCD current profile control due to the wider flat shear region. LHCD therefore does not just provide wider ITBs, but also stiffens the location and reduces radial fluctuations of its location due to slight variations in the shear. A similar curve was also calculated for the case with LH power of 7.0 MW, but this curve does not differ significantly from the one with 3.5 MW power. The case with $\alpha_i = 0.0$ corresponds to the situation where the shear in plasma rotation does not contribute to the barrier formation at all. As is illustrated in Fig. 12, with the only contribution from the magnetic shear the transport barrier would in that case be non-existent without LHCD and very narrow (width ≈ 10 cm) with LHCD. However, the experimental pulse No. 40542, where no LHCD was applied, had an ITB as shown, for example, in Fig. 4. Consequently, the contribution from magnetic shear cannot yield the ITB alone, but the contribution from the shear in plasma rotation has to be taken into account and thus α_i must be greater than 0.

5. High performance OS scenarios

5.1. Effect of the current rampup scheme on the current density profile and ITB

Magnetic configurations which have potential for both achieving high improved confinement factor and high β_N are characterized by broad or hollow current density profiles [26]. There are several methods to create such a configuration. One of the most promising is lower hybrid off-axis current drive, which was presented in Section 4. Another way to generate such a configuration is current rampup.

Current rampup plays an important dual role because it helps to establish a hollow current profile or flat q profile in the inner half of the plasma volume, but it also helps to keep plasma from turning into an H mode too early, presumably by keeping the H mode threshold high through driving high edge currents. Avoiding an early L–H transition is a key factor in building up high core pressure with an ITB [5]. Furthermore, the highest fusion performance in DD plasmas on JET has been obtained when an H mode transition was delayed as long as possible [1, 25].

We have analysed in a predictive way four different current rampup schemes with the JETTO transport code. Either the total plasma current or the current rampup speed is varied, but the other plasma and simulation parameters (except the toroidal

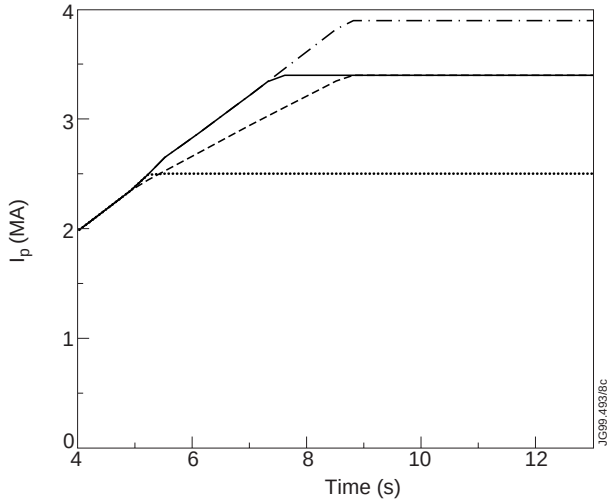

Figure 13. Four different current rampup schemes. The solid curve until $t = 7.5$ s corresponds to the experimental pulse No. 40542. The curves correspond to the following current rampup schemes: fast rampup speed ($dI_p/dt = 0.4$ MA/s) with flat-top value of $I_p = 3.9$ MA, chain curve; fast rampup with $I_p = 3.4$ MA, solid curve; slow rampup ($dI_p/dt = 0.28$ MA/s) with $I_p = 3.4$ MA, dashed curve; $I_p = 2.5$ MA, dotted curve.

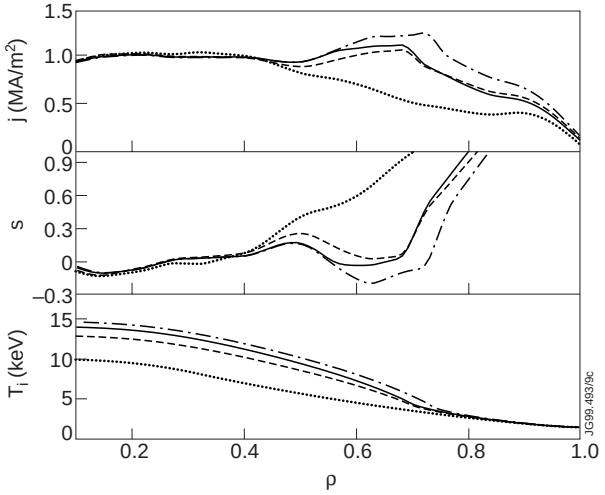

Figure 14. Current density j, magnetic shear s and ion temperature T_i profiles for the four current rampup schemes as presented in Fig. 13 with the same notations for the curves at $t = 10.0$ s.

magnetic field B_t that is varied in accordance with the steady state level of I_p) are kept fixed. The four different current rampup schemes used in this current rampup modelling of JET OS plasmas are presented in Fig. 13.

The current density, the magnetic shear s and the ion temperature profiles for these simulations are shown in Fig. 14 at $t = 10.0$ s when the plasma reaches the steady state level of the plasma current. The initial temperatures, density and q profile at $t = 4.0$ s were taken from pulse No. 40542. The current profiles are almost similar to each other in the core region. However, at radii larger than $\rho \approx 0.5$ they are strongly modified. The centre of the plasma is not affected due to the high electron temperature which effectively prevents current diffusion, whereas in the plasma periphery, the larger the plasma current, the more hollow is the current profile and correspondingly, the smaller is the magnetic shear. What is also interesting is that the faster current rampup (solid curve) with equal flat-top value of the current gives a more hollow current profile and thus smaller magnetic shear than the slower current rampup speed (dashed curve). This gives rise to higher temperature, larger pressure and thus larger fusion power.

The simple conclusion when comparing the different current rampup schemes is that with higher q_a (smaller I_p) shrinking of the ITB is caused by the higher edge shear. Accordingly, the region of low shear increases in size with lower q_a. This can be seen in Fig. 14 where the ITB in the ion temperature is at about $\rho = 0.35$ with $I_p = 2.5$ MA and at about $\rho = 0.73$ with $I_p = 3.9$ MA. Consequently, the best fusion performance for OS plasmas is expected to be obtained with the highest current and with the fastest stable current rampup speed, which was also confirmed on JET during DTE1 [27].

5.2. Fusion performance achieved with combined LHCD and fast current rampup

The starting point for the analysis of the high performance discharges with modelling calculations is the reproduction of pulse No. 40542, but the calculation is extended by 5 s beyond the real JET discharge. Consequently, the main heating phase lasts more than 5 s longer than the experiment and the plasma reaches steady state after $t = 10$ s. The reason for choosing this pulse initially and the main heating and fuelling phase until $t = 7.5$ s is that it has suitable steady-state-like features and benign properties against MHD instabilities. Due to the uncertainties persisting in the particle transport model, the multipliers w_1 and w_2 to the particle diffusion coefficient are varied and the differences in the

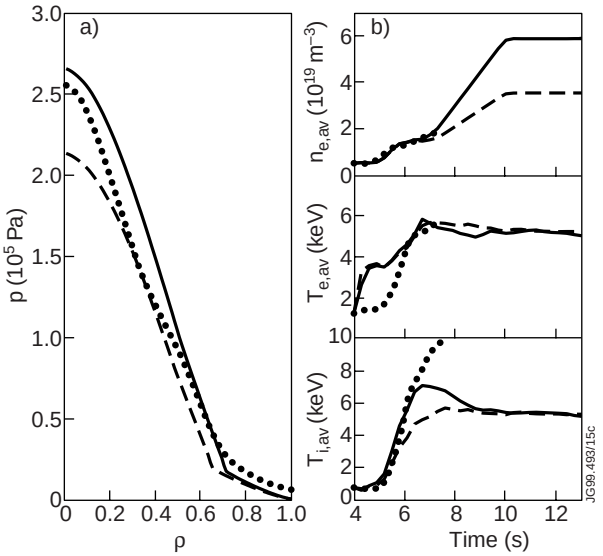

Figure 15. (a) Experimental pressure profile (dotted curve, pulse No. 40542) and two simulated pressure profiles with lower (solid curve) and higher (dashed curve) particle diffusion multipliers w_1 and w_2 at $t = 7.0$ s. (b) Average electron density and the average electron and ion temperatures with the same types of curve as a function of time.

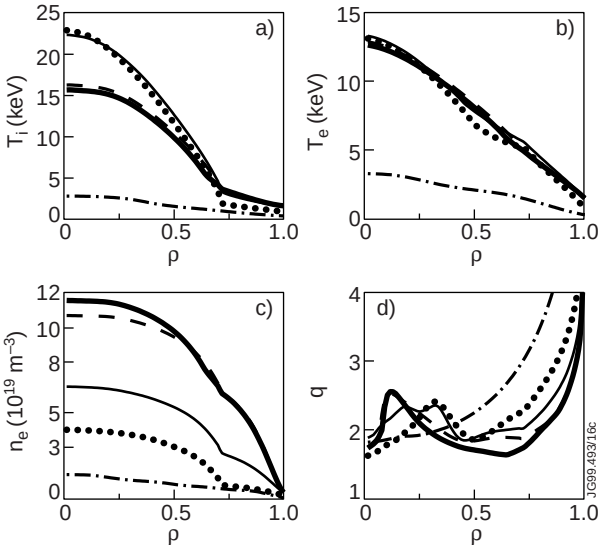

Figure 16. Radial profiles of (a) ion temperature, (b) electron temperature, (c) electron density and (d) q profile at: $t = 4.0$ s, chain curve; $t = 6.0$ s, dotted curve; $t = 8.0$ s, solid curve; $t = 10.0$ s, dashed curve; $t = 13.0$ s, thick solid curve.

performance predictions are illustrated. After a comprehensive sensitivity analysis of w_1 and w_2 in the range of $w_1 = [0.2, 2.5]$ and $w_2 = [0.2, 2.5]$ we show two different sets of w_1 and w_2 with the first set being $w_1 = 0.8$ and $w_2 = 0.3$ (set 1) and the second one $w_1 = 1.6$ and $w_2 = 0.6$ (set 2). Set 1 corresponds to the same values as used in Section 3 and set 2 represents a more conservative choice of w_1 and w_2 in the transport calculation. The plasma current is as for pulse No. 40542 until $t = 7.5$ s and afterwards it is as optimized in Section 5.1, i.e. the flat-top plasma current is 3.9 MA with fast current rampup speed and the toroidal magnetic field is 3.4 T. The heating power and the deposition profiles of NBI and ICRH have been kept fixed since the last experimental deposition profiles calculated by TRANSP. The NBI power deposition profiles did not change significantly according to PENCIL calculations although the density would be more than two times larger at $t = 10.0$ s. The LH power deposition profiles used in the analysis are calculated self-consistently by JETTO/FRTC.

The experimental pressure profile is better reproduced with the model with a lower particle diffusion multiplier (set 1) at $t = 7.0$ s, as shown in Fig. 15(a). The radial location of the ITB ($\rho \approx 0.7$) is well reproduced by the model with smaller w_1 and w_2 whereas the model with larger w_1 and w_2 underestimates the width of the barrier. The pressure is slightly overestimated by the model with set 1 and strongly underestimated by the model with set 2. The time traces of the average electron density and the average electron and ion temperatures are illustrated in Fig. 15(b). The average density yielded by the model with set 1 is about 50% higher than in the model with set 2, partly due to smaller w_1 and w_2, but mostly due to the smaller particle flux out of the plasma in the model with set 1. The differences in temperatures are much smaller between the models, but due to the applied LHCD power of 3.5 MW, the electron temperature in the simulated discharges is significantly higher especially at the beginning of the discharge. The experimental ion temperature is higher at $t \approx 7.5$ s, presumably for two different reasons. Firstly, because in the experiment NBI was turned down but ICRH was turned up again towards $t = 8$ s, whereas in the modelling calculations the powers of NBI and ICRH are on the same level as at $t = 6$ s and, secondly, due to the tendency for the model to underestimate slightly the ion temperature as shown already in Figs 3 and 4.

The evolution of the radial profiles is illustrated in Fig. 16. The ion temperature rises rapidly at the beginning during the low density phase, but due

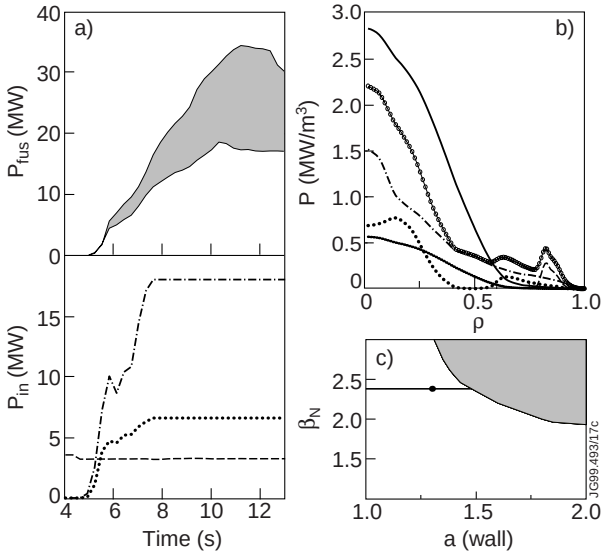

Figure 17. (a) Time evolution of the fusion power calculated by the two different transport models and the input powers (NB, chain curve; RF, dotted curve; LH, dashed curve). (b) Radial profiles of the input heating powers (NB, chain curve; RF, dotted curve; LH, dashed curve; NB+RF+LH, solid curve with circles) and produced fusion (solid curve) and alpha heating powers (densely dotted curve) with the transport model of the smaller particle diffusion coefficient (set 1) at $t = 13.0$ s. (c) MHD stability analysis of the scenario with the largest fusion power at $t = 13.0$ s. The shaded area is unstable with $n = 1$ kink instability as the limiting factor.

to the continuous density rise with beam fuelling it starts to decrease after $t = 7.0$ s. The electron temperature remains fairly constant after $t = 6.0$ s whereas the density rises until $t = 10.0$ s. The quasi-stationary regimes for electron and ion temperatures and densities, the pressure and the location of the ITB are reached at $t = 10$ s. The current diffusion time is around 40–50 s, but before $t = 20$ s it does not affect significantly the profiles or the footpoint of the ITB. The expansion of the ITB occurs mostly between $t = 5.3$ s and $t = 6.0$ s. One reason for the expansion of the ITB with time is the broadening of the low magnetic shear region as shown in Fig. 16(d), which can be explained by the applied $P_{LH} = 3.5$ MW LHCD and the continuous current rampup until $t = 9.5$ s. The magnetic shear is negative inside about 50–70% of the plasma radius. q_{95} is between 3 and 4 and settles during the steady state phase down to 3.1. Worth noticing is also the large contribution (≈50%) from the bootstrap current which is produced in the large pressure gradient region, i.e. in the same region where the footpoint of the ITB is located, thus giving rise to larger current and smaller magnetic shear in that region.

The time evolution of the fusion power is shown in Fig. 17(a) (upper half). The upper curve is obtained with set 1 of the multipliers w_1 and w_2 and the lower one with set 2. By varying w_1 and w_2 in the ranges $w_1 = [0.8, 1.6]$ and $w_2 = [0.3, 0.6]$ (between set 1 and set 2), the shaded area between the two curves for the estimated fusion power is obtained. As can be seen, fusion power in the range 20–30 MW is predicted for $I_p = 3.9$ MA, $B_t = 3.4$ T discharges. Flat-top conditions are obtained at $t \approx 10$ s, after about 5 s from the start of the main heating phase with input heating powers of $P_{NB} = 18$ MW, $P_{RF} = 6.5$ MW (composed of two thirds on-axis and one third off-axis deposition) and $P_{LH} = 3.5$ MW as illustrated in Fig. 17(a) (bottom).

The same two simulations (set 1 and set 2) as shown in Figs 15 and 17 were also performed without LHCD. In each run, the ITB was formed slightly later and its width stayed about 10 cm narrower until $t = 7.0$ s than in the simulation with LHCD. After $t = 7.0$ s the ITB started to shrink and finally, at $t \approx 8$ s, the width of the ITB settled down to $\rho \approx 0.4$. The fusion power was only about 50–60% of the fusion power with LHCD and the average ion temperature about 80%.

The predicted fusion power in fact exceeds clearly the total external input power over the whole plasma core region as shown in Fig. 17(b). The case with the larger fusion power (set 1) is stable against MHD instabilities with a beta value $\beta_N \approx 2.4$ as is seen as a point on the $\beta_N \approx 2.4$ curve in Fig. 17(c) and has a limit of $\beta_N \approx 3$, including wall stabilization with a wall at $r/a = 1.3$ compatible with previous JET results. The most limiting instability is the pressure driven global $n = 1$ kink instability which is a typical limiting factor for the high performance OS discharges in the DB mode on JET [28]. However, this MHD stability analysis does not concern tearing modes nor $q = 2$ 'snakes', which limit the high performance of JET OS plasmas.

Recent experiments on JET have shown that in the DB mode density does not increase with time in the way predicted by our transport model. In experiments density typically saturates at a level of $(4–5) \times 10^{19}$ m^{-3}, whereas the ion temperature continues to rise to 40 keV. However, ion temperatures saturated at the level of 15–20 keV with continuous density rise would be more desirable for reaching the highest fusion performance. The best OS

discharges on JET maintain quasi-steady-state conditions for up to three energy confinement times with neutron yields up to an equivalent of $Q_{DT} \approx 0.4$ at typical $\beta_N \approx 2$ [29]. The effect of the experimentally observed density saturation was not taken into account in our modelling calculations and, as a result, we may overestimate the fusion performance. With L mode plasma edge experiments, density is not saturated, but their problem is the disruptions caused by the pressure driven kink modes [5].

6. Summary and conclusions

LHCD control with transport calculations has been investigated with the JETTO transport code. JETTO has been upgraded by implementing the FRTC code that calculates, coupled with JETTO, LH power deposition and current density profiles. The heat transport model has been further tested in L mode and ELMy H mode with an ITB, and various particle transport models have been used in JETTO to model predictive high performance discharges in the OS DB operation mode. The JETTO transport model has been able to reproduce the formation and evolution of the ITBs in fair agreement, mostly within the experimental error bars, with experiments.

The LH power deposition profiles calculated by JETTO/FRTC are in good agreement with the profiles calculated by BRTC. Evolution of the q profile does not seem to depend on whether the LH power deposition and current density profiles are taken from FRTC or BRTC.

Improved ITB formation with off-axis LHCD calculated by JETTO/FRTC was found in transport calculations. LHCD provided wider ITBs and stiffened their location by reducing the magnetic shear in the OS regime. Current density profiles were hollow, and wider regions with reduced transport due to negative magnetic shear, as well as steady state conditions with more robust ITBs, could be sustained for a longer time. Without LHCD, q profiles were monotonic, whereas application of 3.5 MW LH power provided inverted q profiles across 50–70% of the plasma radius.

Four different current rampup schemes were analysed with JETTO. The total plasma current or the current rampup speed were varied keeping the other plasma parameters fixed. In the core region the current density profiles were not affected, but at larger radii they were strongly modified. ITBs were wider with larger currents and faster current rampup speeds. In conclusion, shrinking of the ITBs is caused by higher edge shear, i.e. higher q_a (smaller I_p). Consequently, the best fusion performance for OS plasmas is expected to be obtained with the highest current and the fastest stable current rampup speed.

The transport modelling results for high performance JET plasma in the OS regime in DB mode at $I_p = 3.9$ MA, $B_t = 3.4$ T predicted a fusion power in the range of 20–30 MW with $Q \approx 0.7$–1. Application of 3.5 MW LHCD was crucial in order to achieve the high performance because without LHCD the fusion power was only about 50–60% of the fusion power with LHCD and the ITB shrank from $\rho \approx 0.7$ to $\rho \approx 0.4$ when LHCD was not applied. Considerable uncertainties still exist, in particular, in the JET particle transport model. The peak performance was analysed to be stable against the kink and ballooning instabilities. However, even if the usually dominating $n = 1$ kink mode was stabilized, the MHD stability analysis did not include neoclassical tearing modes nor $q = 2$ snakes which can affect considerably the transport and lead to a soft rollover and thus limit the performance and the duration of the high performance phase of the OS discharge.

One of the key elements during the high performance phase is the increase and evolution of the density [30]. Steady state conditions were achieved only 5 s after the beginning of the main heating and fuelling phase at $t \approx 10$ s. The limiting factor was the slow fuelling rate from NBI. Higher fuelling rates by additional gas puffing or pellet injection than available from NBI alone would be necessary to raise the core density and the global performance faster [31]. However, until now no ITB with additional gas puffing or pellet injection has been formed or sustained on JET and thus they were not included in the modelling calculations for improving the performance. The recently installed high field side pellet launcher on JET can provide a route to increasing density with pellet fuelling without losing the ITB.

In addition to the fuelling problem, the high performance DT OS discharges on the JET tokamak during DTE1 campaign were limited to less than 5 s duration due to technical restrictions on the high power heating systems and the neutron budget. However, in the light of our modelling results there is a reason to suppose that the high current DT OS pulses could be extended to truly steady state operation with no destruction of the ITB and no significant loss of performance. The key element is the efficient current profile control by LHCD during the high performance phase.

Acknowledgements

The authors are grateful to G. Huysmans for providing them with the MHD stability calculations. The authors also thank A. Piliya and A. Saveliev for implementing the FRTC ray tracing code into JETTO. The NB power deposition profile calculations with PENCIL by A. Bickley are also highly appreciated. Special thanks are also due to D. Heading and G. Corrigan for technical assistance.

References

[1] JET Team (presented by F.X. Söldner), Plasma Phys. Control. Fusion **39** (1997) B353.
[2] Levinton, F.M., et al., Phys. Rev. Lett. **75** (1995) 4417.
[3] Strait, E.J., et al., Phys. Rev. Lett. **75** (1995) 4421.
[4] Gormezano, C., JET Team, Phys. Rev. Lett. **75** (1995) 487.
[5] Söldner, F.X., et al., Nucl. Fusion **39** (1999) 407.
[6] Murakami, M., et al., in Controlled Fusion and Plasma Physics (Proc. 26th Eur. Conf. Maastricht, 1999), Vol. 23J, European Physical Society, Geneva (1999) 1213.
[7] Voitsekhovitch, I., et al., ibid., p. 957.
[8] Genacchi, G., Taroni, A., JETTO: A Free Boundary Plasma Transport Code (Basic Version), Rep. ENEA RT/TIB 1988(5), ENEA (1988).
[9] Esterkin, A.R., Piliya, A.D., Nucl. Fusion **36** (1996) 1501.
[10] Baranov, Yu.F., et al., Nucl. Fusion **36** (1996) 1031.
[11] Erba, M., et al., Plasma Phys. Control. Fusion **39** (1997) 261.
[12] Erba, M., et al., Validation of a New Mixed Bohm/gyro-Bohm Transport Model on Discharges of the ITER Data-Base, Rep. JET-R(96)07, JET Joint Undertaking, Abingdon (1996).
[13] Parail, V.V., et al., Nucl. Fusion **39** (1999) 429.
[14] Baranov, Yu.F., et al., Nucl. Fusion **39** (1999) 1463.
[15] Parail, V.V., et al., in Controlled Fusion and Plasma Physics (Proc. 26th Eur. Conf. Maastricht, 1999), Vol. 23J, European Physical Society, Geneva (1999) 181.
[16] Smithe, D.N., et al., in Radiofrequency Power in Plasmas (Proc. 8th Top. Conf. Irvine, 1989), AIP, New York (1989) 338.
[17] Cottrell, G.A., et al., Nucl. Fusion **39** (1999) 389.
[18] Mantsinen, M.J., et al., Plasma Phys. Control. Fusion **41** (1999) 843.
[19] Ekedahl, A., et al., Nucl. Fusion **38** (1998) 1397.
[20] Hugon, M., et al., Nucl. Fusion **32** (1992) 33.
[21] Moreau, D., et al., in Plasma Physics and Controlled Nuclear Fusion Research 1992 (Proc. 14th Int. Conf. Würzburg, 1992), Vol. 1, IAEA, Vienna (1993) 921.
[22] Gormezano, C., et al., in Applications of Radiofrequency Power to Plasmas (Proc. 12th Top. Conf. Savannah, 1997), AIP, New York (1997) 3.
[23] Karney, C.F.F., Fisch, N.J., Phys. Fluids **22** (1979) 1819.
[24] Heikkinen, J.A., et al., Plasma Phys. Control. Fusion **41** (1999) 1231.
[25] Keilhacker, M., et al., Nucl. Fusion **39** (1999) 209.
[26] Litaudon, X., Plasma Phys. Control. Fusion **40** (1998) A251.
[27] Horton, L.D., et al., Nucl. Fusion **39** (1999) 993.
[28] Huysmans, G.T.A., et al., in Controlled Fusion and Plasma Physics (Proc. 24th Eur. Conf. Berchtesgaden, 1997), Vol. 21A, European Physical Society, Geneva (1997) 21.
[29] Zastrow, K.-D., et al., in Controlled Fusion and Plasma Physics (Proc. 26th Eur. Conf. Maastricht, 1999), Vol. 23J, European Physical Society, Geneva (1999) 217.
[30] Sips, A.C.C., et al., Plasma Phys. Control. Fusion **40** (1998) 1171.
[31] Söldner, F.X., et al., in Controlled Fusion and Plasma Physics (Proc. 26th Eur. Conf. Maastricht, 1999), Vol. 23J, European Physical Society, Geneva (1999) 185.

(Manuscript received 11 October 1999
Final manuscript accepted 14 June 2000)

E-mail address of T.J.J. Tala: tuomas.tala@vtt.fi

Subject classification: H1, Tm; F1, Ti; F2, Ti; B0, Ti

PUBLICATION 6

Role of fast waves in the central deposition of lower hybrid power

In: Plasma Physics and Controlled Fusion 1999. Vol. 41, pp. 1231–1249.

http://www.iop.org/journals/ppcf

Plasma Phys. Control. Fusion **41** (1999) 1231–1249. Printed in the UK PII: S0741-3335(99)03721-5

Role of fast waves in the central deposition of lower hybrid power

J A Heikkinen†, T J J Tala‡, T J H Pättikangas†, A D Piliya§, A N Saveliev§ and S J Karttunen†

† Association Euratom–Tekes, VTT Energy, PO Box 1604, FIN-02044 VTT, Finland
‡ Association Euratom–Tekes, Helsinki University of Technology, Advanced Energy Systems, PO Box 2200, FIN-02015 HUT, Finland
§ A F Ioffe Physical Technical Institute, Politekhnicheskaya ul. 26, 194021, St Petersburg, Russian Federation

Received 26 April 1999, in final form 20 July 1999

Abstract. In tokamaks, lower hybrid (LH) waves are routinely used for current drive and heating of plasmas. The LH waves have two modes of propagation that are called the slow and the fast wave. Usually, the lower hybrid waves are launched as slow waves into a tokamak, but during the propagation part of the wave power can be transformed to fast waves. General characteristics of the mode transformation of slow waves to fast waves are first investigated with a simple quasitoroidal ray-tracing model. Next, the effect of mode transformed LH power on the deposition profiles in a JET-like tokamak is analysed by using the fast ray-tracing code FRTC. When the launched spectrum is at small values of the toroidal refractive index ($1.6 \lesssim n_{\phi 0} \lesssim 2.0$), the contribution of the fast wave to the deposited power is found to be significant and responsible for most of the absorption at the centre. When $n_{\phi 0}$ is large ($n_{\phi 0} \gtrsim 2.2$), the effect of the mode transformed fast waves is small or negligible. At modest central densities ($n_{e0} \sim 0.5 \times 10^{20}$ m^{-3}), the contribution of the fast wave to the power deposition can be more than 50% in the plasma centre. In consequence, the significant amount of wave energy absorbed in the fast mode must be carefully taken into account in modelling LH current drive experiments in the future. At low central densities ($n_{e0} \lesssim 0.3 \times 10^{20}$ m^{-3}), practically no absorption of fast waves occurs.

1. Introduction

Radiofrequency (RF) power in the lower hybrid (LH) range of frequencies plays an important role in profile control and non-inductive current drive of the present tokamak devices. It is well known that RF power in this frequency range can propagate in the form of two wave modes. These modes, called the slow and the fast waves, respectively, are different in their propagation and damping properties, their interaction with alpha particles and other fast ions is distinct, the fast waves do not possess any lower hybrid resonance and have a small $n_\parallel$ shift. In particular, since the Landau damping is much weaker for the fast wave, this mode is expected to provide more central power deposition and current generation in large tokamaks.

The type of wave mode is not, as a rule, conserved in the process of wave propagation. In certain conditions, it is changed via the linear mode conversion. As a result, LH waves excited in a tokamak represent a mixture of both modes regardless of the launching conditions. This feature of lower hybrid heating (LHH) and current drive (LHCD) is taken into account automatically in most modern ray-tracing codes. However, the relative role of the two wave modes has not been investigated in sufficient detail. Also, the possibility of optimizing the

0741-3335/99/101231+19$30.00

launched $n_\parallel$ spectrum with regard to this phenomenon remains an open question. It is important to discuss the characteristic features of the fast–slow (slow–fast) linear mode conversion in a tokamak configuration and make comparisons with the better known case of slab geometry.

The accessibility of LH waves in a slab geometry is often expressed by a lower bound on the launched parallel refractive index $n_{\parallel 0}$ obtained from the well known condition [1]

$$n_{\parallel 0} \geqslant n_{\parallel c} \approx \sqrt{S} + \omega_{pe}^2/\Omega_e^2$$

where

$$S = 1 - \omega_{pi}^2/(\omega^2 - \omega_{ci}^2) - \omega_{pe}^2/(\omega^2 - \omega_{ce}^2)$$

ω_{pe} is the electron plasma frequency, Ω_e is the electron cyclotron frequency and ω is the wave angular frequency.

For $n_{\parallel 0} < n_{\parallel c}$, the slow wave launched by the antenna can transform to a fast wave before reaching the region where $n_{\parallel c}$ is evaluated. The fast wave can then return to outer plasma layers where it is reflected. On the other hand, if $n_{\parallel 0} > n_{\parallel c}$, the slow wave has access to the region where $n_{\parallel c}$ is evaluated. If damping is weak, the slow wave can make multiple passes with a consequent evolution of $n_\parallel$ and with a repeated possibility of transforming to a fast mode at $n_\parallel = n_{\parallel c}$.

The transformation to the fast mode has been known [2–8] to be possible for slow waves that have access to the tokamak plasma centre and launched with a toroidal refractive index $n_{\phi 0}$ spectrum extending below a certain threshold $n_{\phi 0}^\star$ [5, 6] in an interval of poloidal mode numbers m. The implications to power deposition and mode partition in the propagation region have not, however, been studied so far in detail. Moreover, it has been shown [3] that the fast waves resulting from mode transformation would preferentially propagate in the outer plasma layers, which leads to decreased power deposition in the plasma centre.

In the present paper, the characteristics and occurrence of mode transformation and its effect on the power deposition in LHCD are investigated. Both a cylindrical quasitoroidal approximation and a JET-type elongated toroidal configuration are considered. Rays launched in a slow mode are followed to resolve the evolution of the parallel refractive index, the poloidal mode number and the polarization as a function of launching parameters. The fast ray-tracing code FRTC [9] is applied to obtain ensemble-averaged power deposition for a number of launched $n_\parallel$ spectra. In contrast to previous understanding, the fast waves are found to contribute significantly to the power deposition and to constitute even half of the total absorption and most of the central absorption in the JET configuration with relevant $n_{\parallel 0}$ spectra.

In section 2, a general discussion and a short review of the mode transformation problem for the LH waves is given. Section 3 explains the conditions for mode transformation and the adopted ray-tracing equations within a quasitoroidal model. This simple quasitoroidal ray-tracing model includes only the correct propagation properties of LH waves in a torus, but no power absorption is calculated or considered. Section 4 describes the regions of accessibility for the slow and fast waves and the regimes where mode transformation can occur. Section 5 presents the FRTC results for ray ensembles showing the power deposition profiles for both slow and fast wave direct excitations. The results are discussed in section 6.

2. Physics of fast/slow wave transformation

Properties of waves in magnetized plasmas are strongly dependent on their parallel refractive index $n_\parallel$. Therefore, propagation of a wave mode can be analysed conveniently with a given value of this parameter. In a cold plasma, the dispersion relation reads

$$H = A(n_\parallel)n_\perp^4 + F(n_\parallel)n_\perp^2 + C(n_\parallel) = 0 \tag{1}$$

where $n_\perp$ is the perpendicular refractive index of the wave with respect to the magnetic field and the coefficients are defined as $A = S, -F = (S+P)(S-n_\parallel^2) - D^2$ and $C = P[(S-n_\parallel^2)^2 - D^2]$. Here, $P = \epsilon_{zz}$ and $\mathrm{i}D = \epsilon_{xy}$ and $S = \epsilon_{xx}$ with ϵ_{ik} being the element of the cold plasma dielectric tensor in the coordinate system with the z-axis along the magnetic field.

In the LH frequency region, we have $\Omega_\mathrm{i} \ll \omega \ll \Omega_\mathrm{e}$ and typically, $\omega_\mathrm{pe} \gg \omega$ where ω and Ω_i are the wave frequency and the ion cyclotron frequency, respectively. Then the coefficients in equation (1) are given approximately by $A \equiv S \simeq 1 + w - v/M$, $F \simeq v(S - n_\parallel^2 + w)$ and $C \simeq v(vw - n_\parallel^4)$ where $w = \omega_\mathrm{pe}^2/\Omega_\mathrm{e}^2$, $v = \omega_\mathrm{pe}^2/\omega^2$ and $M = m_\mathrm{i}/m_\mathrm{e}$ with m_i and m_e being the ion and the electron mass, respectively.

The LH resonance occurs at the frequency $\Omega_\mathrm{LH} = [\omega_\mathrm{pi}^2\Omega_\mathrm{e}\Omega_\mathrm{i}/(\omega_\mathrm{pi}^2 + \Omega_\mathrm{e}\Omega_\mathrm{i})]^{1/2}$. Below the resonance, at $\omega < \Omega_\mathrm{LH}$, equation (1) has an unambiguous solution $n_\perp(n_\parallel)$ which exists for $n_\parallel > 0$ in the interval $0 < n_\parallel < n_\mathrm{max}$, where $n_\mathrm{max} = (vw)^{1/4}$. This situation is illustrated in figure 1(*a*). The mode described by this root of the dispersion relation is known in the LH frequency region as the fast wave. It represents the high-frequency limit of the fast magnetosonic wave.

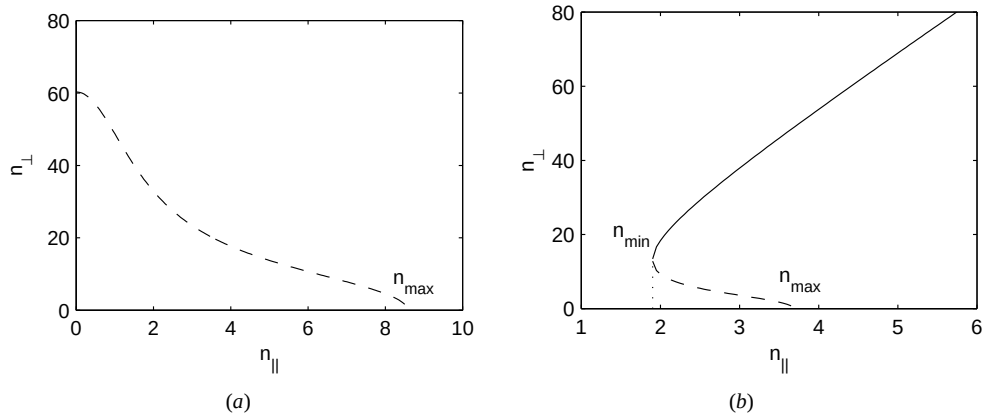

Figure 1. Dispersion curves for the fast wave (dashed curve) and the slow wave (full curve) when (*a*) $\omega < \Omega_\mathrm{LH}$ ($f = \omega/2\pi = 0.6$ GHz) and (*b*) $\omega > \Omega_\mathrm{LH}$ ($f = 3.7$ GHz). A deuterium plasma with $n_\mathrm{e} = 5 \times 10^{19}$ m^{-3} and $B = 3.2$ T is assumed. Since the left-hand side of equation (1) is an even function of both $n_\parallel$ and $n_\perp$, it is sufficient to consider solutions at positive values of these variables.

Above the LH resonance, the solution consists of two branches, as is shown in figure 1(*b*). The upper branch is called the slow wave and the lower branch is the fast wave. The lower branch exists in the interval $n_\mathrm{min} < n_\parallel < n_\mathrm{max}$, where n_min is found from the relation $F^2 - 4AC = 0$ as follows:

$$n_\mathrm{min} = w^{1/2} \pm S^{1/2}. \tag{2}$$

In addition to having different values of $n_\perp$, the slow and fast waves with the same $n_\parallel$ are different in their polarization. In particular, the slow mode is electrostatic at $n_\parallel^2 \gg 1$. In this limiting case, it is also known as the oblique electron plasma wave or the Trivelpiece–Gould mode.

In a weakly inhomogeneous plasma, equation (1) describes the slow and the fast WKB waves. Three different parameter regions exist for these waves at a given frequency ω. Firstly, if $\omega < (\Omega_\mathrm{e}\Omega_\mathrm{i})^{1/2}$, two modes can exist simultaneously in the region $1 < v < v_\mathrm{res}$, where v_res is the value of v at the LH resonance layer. Secondly, if $\omega > (\Omega_\mathrm{e}\Omega_\mathrm{i})^{1/2}$, two modes can exist at

any density $v > 1$. Thirdly, only the fast mode exists at $v > v_{\rm res}$. Considering the dependence of $n_\perp$ on the plasma density, one can see that $n_\perp \to \infty$ at $v \to v_{\rm res}$ (i.e. at $S \to 0$) for the slow wave and $n_\perp$ remains finite for the fast one. The fast mode passes freely through the resonance layer while the slow wave is absorbed or transformed into a hot-plasma mode.

Assume now that the waves are treated using the ray approximation. In the axisymmetrical tokamak geometry, the ray propagation can be considered in the three-dimensional $\{r, \theta, n_\parallel\}$ phase space where r is the 'radial' coordinate labelling the flux surface and θ is the generalized poloidal angle. A ray belongs to one of the mode types which is determined by the initial conditions. This characteristic remains unchanged until the ray reaches the surface $n_\parallel = n_{\rm min}(r, \theta)$ in the phase space where the two roots of the dispersion relation merge or 'intersect'. The normal component of the group velocity vanishes on the surface and its signs are opposite for the two modes in its vicinity. The ray trajectory approaches the conversion surface tangentially and changes its mode label at the touching point, i.e. here it undergoes the linear conversion, see figure 1(*b*). The energy carried by the ray remains unchanged in the event.

The smooth continuous transition between the slow and the fast mode reflects the fact that both belong to the same wave normal surface. In this case, the distinction between the two modes is, in a sense, a matter of convention and depends on the adopted principle of classification. For example, in the variables $\{v_{\rm ph}, \alpha\}$, with α being the angle between the wavevector and the magnetic field, there is only one wave mode described by an unambiguous function $v_{\rm ph}(\alpha)$. This is illustrated by the wave normal surface in figure 2.

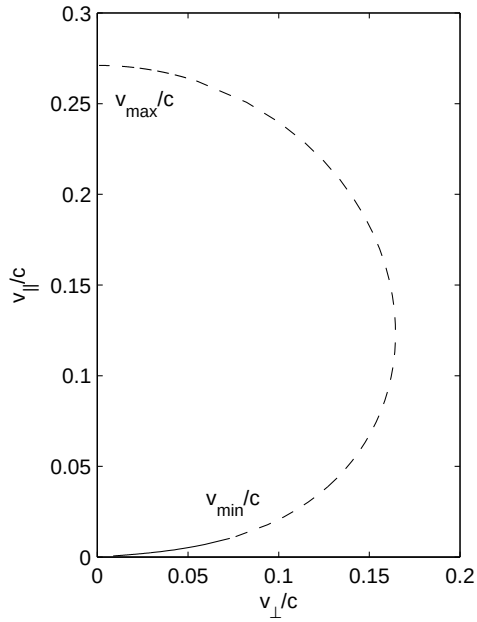

Figure 2. Cross section of the wave normal surface showing the parallel and the perpendicular phase velocity for the fast wave (dashed curve) and the slow wave (full curve) for the parameters of figure 1(*b*). Only one quarter of the cross section having the shape of a figure of eight is shown.

The form and the position of the conversion surface $n_\parallel = n_{\rm min}$ in the phase space are readily understood from equation (2). The function $n_{\rm min}(r, \theta)$ is typically close to unity. It consists

of two branches which merge at the resonance layer. In the absence of the LH resonance, the branches are separated and the lower one having the minus sign lies in the evanescent region.

Consider the conversion process in more detail and begin with the case of the slab geometry discussed intensively in the literature. Suppose that a uniform magnetic field B is in the z-direction and the plasma density $n_{e,i}$ depends only on the x coordinate. Assume also that $\omega < (\Omega_e\Omega_i)^{1/2}$ and the LH resonance layer exists in the plasma. Figure 3(*a*) shows the accessibility regions of the slow and the fast wave in the $\{x, n_\parallel\}$ phase plane. The boundaries of the slow wave domain are the cut-off surface at $v = 1$, the LH resonance layer $v = v_{res}$, and the conversion surface $n_\parallel = n_{min}$. The fast wave region is enclosed by the $n_\parallel = n_{max}(x)$ cut-off and the $n_\parallel = n_{min}(x)$ conversion surfaces. Unlike the slow mode, the fast wave rays can propagate through the LH resonance into the region $v > v_{res}$. The slow and the fast wave domains should be imagined as lying on the opposite sides of a sheet with a transition between them only possible through a cut made along the $n_\parallel = n_{min}$ line.

The rays propagate along horizontal lines in the $\{n_\parallel, x\}$ slab geometry. Therefore, the rays experience the linear conversion if their $n_\parallel$ is in the interval $1 < n_\parallel < n_{GS}$, where $n_{GS} = (1 + w_{res})^{1/2}$ is the maximum value of $n_\parallel$ on the conversion surface and $w_{res} = [(\Omega_e\Omega_i/\omega^2) - 1]^{-1}$. Such rays are locked in the plasma periphery between the edge and the n_{min}-surface and oscillate between these boundaries taking alternatively the form of the slow and the fast mode. Rays having $n_\parallel > n_{GS}$ propagate towards the plasma interior and reach the LH resonance at v_{res}. The inequality $n_\parallel > n_{GS}$ is the well known Golant–Stix condition for accessibility to the LH resonance. The case with no LH resonance within the plasma slab is illustrated in figure 3(*b*).

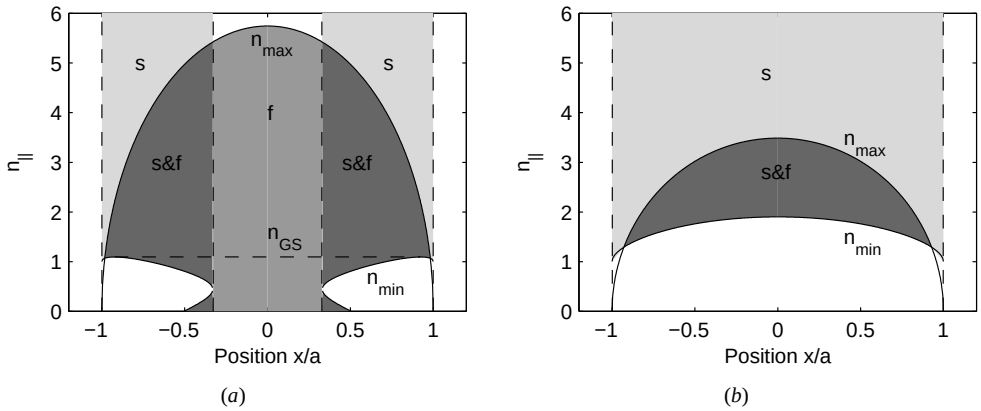

Figure 3. Accessibility regions of the slow (s) and the fast (f) wave in a slab geometry: (*a*) $\omega < \Omega_{LH}$ ($f = \omega/2\pi = 0.6$ GHz, $n_{e0} = 2.2 \times 10^{19}$ m^{-3}) and (*b*) $\omega > \Omega_{LH}$ ($f = 3.7$ GHz, $n_{e0} = 5 \times 10^{19}$ m^{-3}). A deuterium plasma is assumed with the parabolic density profile $n_e(x) = n_{e0}[1 - (x/a)^2]^\beta + n_{e1}$ ($n_{e1} = 1 \times 10^{15}$ m^{-3}, $\beta = 1$, $B = 3.2$ T).

One obvious effect of the toroidal geometry is that $n_\parallel$ is not constant along a ray. As a result, even a ray launched below the Golant–Stix limit can reach the resonance and similarly, a ray having initially $n_\parallel > n_{GS}$ can experience the conversion. In addition, toroidal effects can change the volume and the shape of accessibility regions considerably for both wave modes. The reason lies in the coupling between variations of $n_\parallel$ and the poloidal refractive index n_p [8].

Consider a tokamak with a major radius R_0, minor radius a, poloidal magnetic field B_p and total magnetic field B. Assuming for clarity $(B_p/B)^2$ and a/R_0 to be small, we have

$n_\mathrm{p} = (B/B_\mathrm{p})(n_\parallel - n_{\phi 0})$, where the toroidal refractive index $n_{\phi 0} = c\,\ell/\omega R_0$ is constant along the ray and ℓ is the toroidal mode number. Within the same accuracy, we have $n_\perp = (n_r^2 + n_\mathrm{p}^2)^{1/2}$, where n_r is the radial component of the refractive index. This leads to the condition [8, 10]

$$n_\perp(n_\parallel) \geqslant (B/B_\mathrm{p})|n_\parallel - n_{\phi 0}|. \tag{3}$$

The boundary of the phase-space volume defined by this requirement represents a cut-off surface. Implications of the constraints put on the wave propagation by equation (3) become obvious when both its left-hand and right-hand sides are presented graphically. This is shown in figure 4. In particular, one can see that it is equation (3) rather than the condition $n_\parallel = n_\mathrm{max}$ which actually determines the boundary of the allowed phase space for the fast mode.

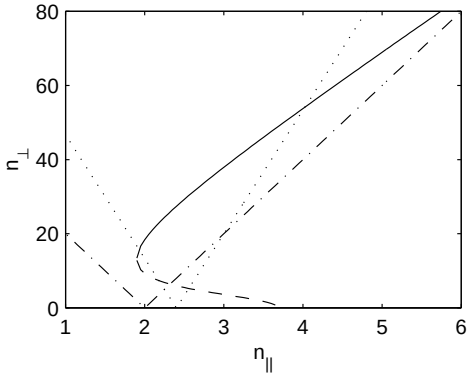

Figure 4. Constraints for the refractive index in a toroidal geometry for the parameters of figure 1(*b*). The dash–dot line shows constraint (3) when $n_{\phi 0} = 2.0$ and $B_\mathrm{p}/B = 0.05$ and the dotted line that when $n_{\phi 0} = 2.4$ and $B_\mathrm{p}/B = 0.03$ ($n_\mathrm{e} = 5 \times 10^{19}$ m^{-3} and $B = 3.2$ T).

From equation (3) a necessary condition for the mode conversion at a given spatial $\{r, \theta\}$ point is readily derived by using the values of $n_\parallel$ and $n_\perp$ at the conversion surface. The result is

$$v^{1/2}(r/qR_0)(w/S)^{1/4} + S^{1/2} + w^{1/2} > n_{\phi 0} \tag{4}$$

where q is the safety factor. The left-hand side of this equation has, as a function of θ, a maximum at the low-field side of the tokamak at $\theta = 0$ and a minimum at $\theta = \pi$. Therefore, the conditions for the mode conversion are most favourable on the low-field side. The conditions also improve with increasing plasma density.

Denoting the maximum value of the left-hand side in equation (4) in the plasma volume as n_c, we obtain the sufficient condition for the absence of mode conversion: $n_{\phi 0} > n_\mathrm{c}$. Under this condition, cut-off always occurs before $n_\parallel$ reaches its limiting value n_min. In this case, the phase-space domains of the two modes are separated by an evanescent region, although they overlap in the coordinate space. Below n_c the domains are connected through a part of the $n_\parallel = n_\mathrm{min}$ surface and mode conversion is possible. It is also clear in figure 4 that the fast wave domain vanishes when $n_{\Phi 0}$ is above the maximum value of n_max. This implies that it is impossible for the mode conversion to occur in this case also.

Evolution of the accessibility conditions with $n_{\phi 0}$ is illustrated in figure 6 where the mode domains are shown in an $\{r, n_\parallel\}$ cross section of the phase space at $\theta = 0$ and $\theta = \pi$, i.e. in the equatorial plane of the tokamak for the case with no LH resonance. It should be noted that the inequality $n_{\phi 0} < n_\mathrm{c}$ is, strictly speaking, the necessary condition for the mode conversion. The answer to the question of whether a real ray actually crosses the conversion surface depends

on the particular solution of the ray equation and cannot be found in advance. One can assume that, due to the stochastic behaviour of the propagation of the small $n_\parallel$ rays, mode conversions are random events which can be treated statistically. This approach is applicable, however, only at a sufficiently low electron temperature where rays survive many reflections before being absorbed. At higher temperatures typical of large tokamaks, the ray-tracing method seems to be, at present, the only reliable tool for investigating mode conversion.

3. Quasitoroidal ray-tracing model

To investigate mode transformations in a simplified geometry, a quasitoroidal axisymmetric tokamak configuration with circular concentric magnetic surfaces is adopted. A magnetic field $\boldsymbol{B} = B_\mathrm{t}\hat{\phi} + B_\mathrm{p}\hat{\theta}$ is assumed, where $\hat{\phi}$ and $\hat{\theta}$ are the unit vectors in the toroidal and poloidal directions, respectively. The toroidal field component is $B_\mathrm{t} = \hat{B}_\mathrm{t}R_0/R$, where $\hat{B}_\mathrm{t} = B_0$ is constant, and R is the major radius coordinate and R_0 its value at the plasma centre. The poloidal component is defined as

$$B_\mathrm{p} = \hat{B}_\mathrm{p}R_0/R$$

where

$$\hat{B}_\mathrm{p} = (\mu_0 I/2\pi)[1 - (1 - r^2/a^2)^{1+\alpha}]/r$$

and I is the total plasma current, r is the minor radius coordinate, a is the minor radius, μ_0 is the vacuum permeability and α is the exponent of the current density profile $j(r) = j_0(1-r^2/a^2)^\alpha$. To describe the wave propagation, a cold plasma is assumed with a radial electron density profile $n_\mathrm{e}(r) = n_{\mathrm{e}0}(1 - r^2/a^2)^\beta + n_{\mathrm{e}1}$. The electron temperature profile was assumed to be $T_\mathrm{e}(r) = T_{\mathrm{e}0}(1 - r^2/a^2)^\gamma + T_{\mathrm{e}1}$.

In the quasitoroidal calculations, we will concentrate on the conditions where the mode transformations occur and we will for the moment ignore the damping of the waves. The damping will be included in section 5, where power deposition is considered.

The wave dispersion is obtained from the zeros of the Hamiltonian in equation (1). The parallel and the perpendicular refractive index components can be obtained from the corresponding toroidal and poloidal mode numbers of the wave which are ℓ and m, respectively. In the given geometry, we find

$$n_\parallel = (\ell/R)(B_\mathrm{t}/B) + (m/r)(B_\mathrm{p}/B) \tag{5}$$

$$n_q = (m/r)(B_\mathrm{t}/B) - (\ell/R)(B_\mathrm{p}/B) \tag{6}$$

with $n_\perp^2 = n_q^2 + n_r^2$. Here, the magnitude of the magnetic field is $B = (B_\mathrm{t}^2 + B_\mathrm{p}^2)^{1/2}$, n_r is the radial component of the refractive index and n_q is the projection of the perpendicular refractive index on the magnetic surface. All the variables here and in what follows are dimensionless: the time has been normalized to ω^{-1} and the length has been normalized to c/ω, where c is the speed of light.

The ray-tracing equations can be written as [4]

$$\mathrm{d}r/\mathrm{d}t = -(\partial H/\partial n_r)/(\partial H/\partial\omega) \tag{7}$$

$$\mathrm{d}\theta/\mathrm{d}t = -(\partial H/\partial m)/(\partial H/\partial\omega) \tag{8}$$

$$\mathrm{d}n_r/\mathrm{d}t = (\partial H/\partial r)/(\partial H/\partial\omega) \tag{9}$$

$$\mathrm{d}m/\mathrm{d}t = (\partial H/\partial\theta)/(\partial H/\partial\omega) \tag{10}$$

which give the rate of change of the polar coordinates r and θ of the ray on the poloidal cross section as well as of the radial refractive index n_r and the poloidal mode number m. Here, the partial derivatives $\partial/\partial n_r$ and $\partial/\partial m$ are obtained from

$$\partial/\partial n_r = (n_r/n_\perp)\partial/\partial n_\perp$$

and

$$\partial/\partial m = (n_q/n_\perp)(B_t/rB)\partial/\partial n_\perp + (B_p/rB)\partial/\partial n_\parallel.$$

The perpendicular refractive index $n_\perp$ is found with the help of n_q and n_r obtained from equations (6) and (9).

The perpendicular refractive index $n_\perp$ solved numerically from the ray-tracing equations can be checked with the help of the solution of equation (1) which is

$$n_\perp^2 = [-F \pm \sqrt{F^2 - 4SC}]/2S. \tag{11}$$

Here, the plus sign corresponds to the slow mode and the minus sign to the fast mode. The values of $n_\perp$ obtained by integrating equations (7)–(10) should coincide with one of the local roots of equation (11).

The wave can propagate only in a region where the expression $F^2 - 4SC$ under the square root is positive, which requirement gives the generalized Golant–Stix condition. A mode transformation happens whenever the ray approaches the point where this expression vanishes, i.e.

$$[(S + P)(n_\parallel^2 - S) + D^2]^2 - 4SP[(S - n_\parallel^2)^2 - D^2] = 0. \tag{12}$$

This region is accessible provided that $-F/2S \geqslant 0$, i.e.

$$(S + P)(S - n_\parallel^2) - D^2 \geqslant 0 \tag{13}$$

which gives a necessary condition for the existence of non-evanescent roots around the mode transformation region. Equation (12) defines surfaces in $(n_\parallel,\ r,\ \theta)$ space, i.e. for each r and θ there can exist real $n_\parallel$ satisfying the condition (12). In a mode transformation, the surface shall be tangential to the ray path at the mode transformation point in phase space.

Mode transformations were investigated by solving equations (7)–(10) for typical launching parameters with the quasitoroidal ray-tracing code (QRTC). The parameters of a JET-like tokamak plasma used in the calculations are presented in table 1 and the parameters of the launched LH spectrum are given in table 2. In simulations with QRTC, the exponent of the current profile was $\alpha = 1$.

Table 1. Plasma parameters in a JET-like tokamak.

Minor radius a (m)	0.95
Major radius R_0 (m)	3.05
Magnetic field B_0 (T)	3.2
Plasma current I (MA)	3.5
Central density n_{e0} (10^{20} m^{-3})	0.6
Edge density n_{e1} (10^{20} m^{-3})	0.001
Exponent of the density profile β	1
Central temperature T_{e0} (keV)	6
Edge temperature T_{e1} (keV)	0.1
Exponent of the temperature profile γ	1.5

In figure 5, the mode polarization is shown along the ray trajectories as well as the mode transformation points. For these example rays, several mode transformations occur—this is partly because the wave damping has been ignored in our quasitoroidal model. Since the slow wave is a backward wave and the fast wave is a forward wave, the radial component of the group velocity of the fast wave is opposite to that of the slow wave at the transformation point. Therefore, whenever the slow wave reaches its transformation point during inward propagation, the fast wave is found to propagate outwards from the transformation point. However, as one

Table 2. Parameters of the lower hybrid spectrum in a JET-like tokamak.

Frequency f (GHz)	3.7
Centre of the spectrum $n_{\phi 0}$	2.0
Width of the spectrum (FWHM) $\Delta n_{\phi 0}$	0.13
Poloidal launching position θ_0 (rad)	± 0.3
Poloidal mode number m_0	0
Radial launching position r_0/a	0.968

can find from figure 5, the fast wave then experiences a reflection from the outer layers with consequent penetration to the plasma centre. The present examples demonstrate how wave partition into fast and slow modes can easily take place for slow modes having access to the plasma centre.

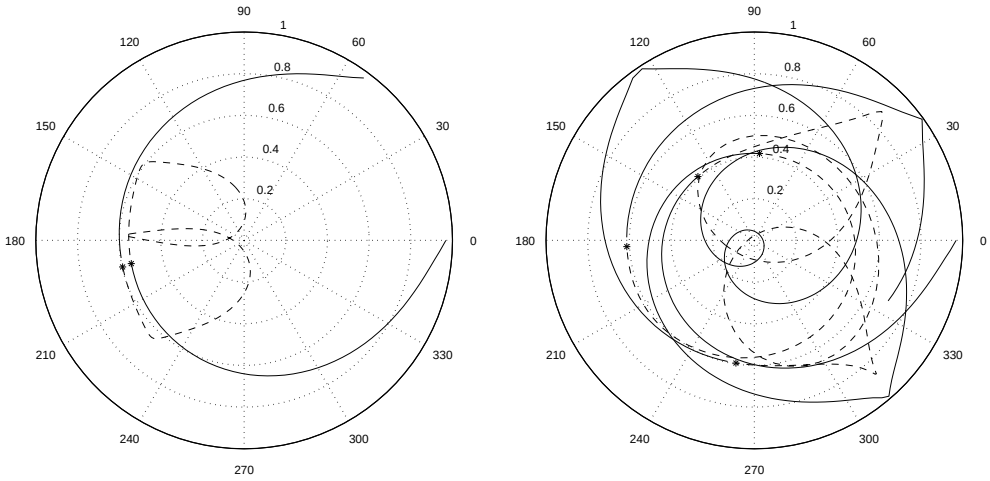

Figure 5. Examples of ray trajectories with transformations (∗) between the slow mode (full curve) and the fast mode (dashed curve) in a JET-like tokamak: (*a*) $n_{\phi 0} = 1.8$ and (*b*) $n_{\phi 0} = 2.0$ ($n_{e0} = 0.5 \times 10^{20}$ m^{-3}, $\theta_0 = 0$).

4. Accessibility conditions for the slow and the fast modes in a torus

In this section we present some numerical results for accessibility conditions in real tokamak plasmas. An exact condition for the coefficients A, F and C of the dispersion relation is written [8, 10] as

$$\left[n_\parallel \sqrt{1 - (B_p/B)^2} - \ell/R \right]^2 \leqslant (B_p/B)^2 n_\perp^2 \tag{14}$$

which is actually just a more accurate version of the simplified equation (3) introduced in section 2.

Figure 6 shows accessibility regions of the slow and the fast waves for different values of the toroidal refractive index $n_{\phi 0}$ in $n_\parallel$–r space along a horizontal radial line through the plasma centre. The plasma parameters are again those of a JET-like tokamak in table 1. The Golant–Stix condition in equation (12) is also depicted. The boundaries shown in figure 6 are

independent of the initial launching parameters m_0 and θ_0, but the actual phase-space region covered by any ray may strongly depend on the chosen initial parameters.

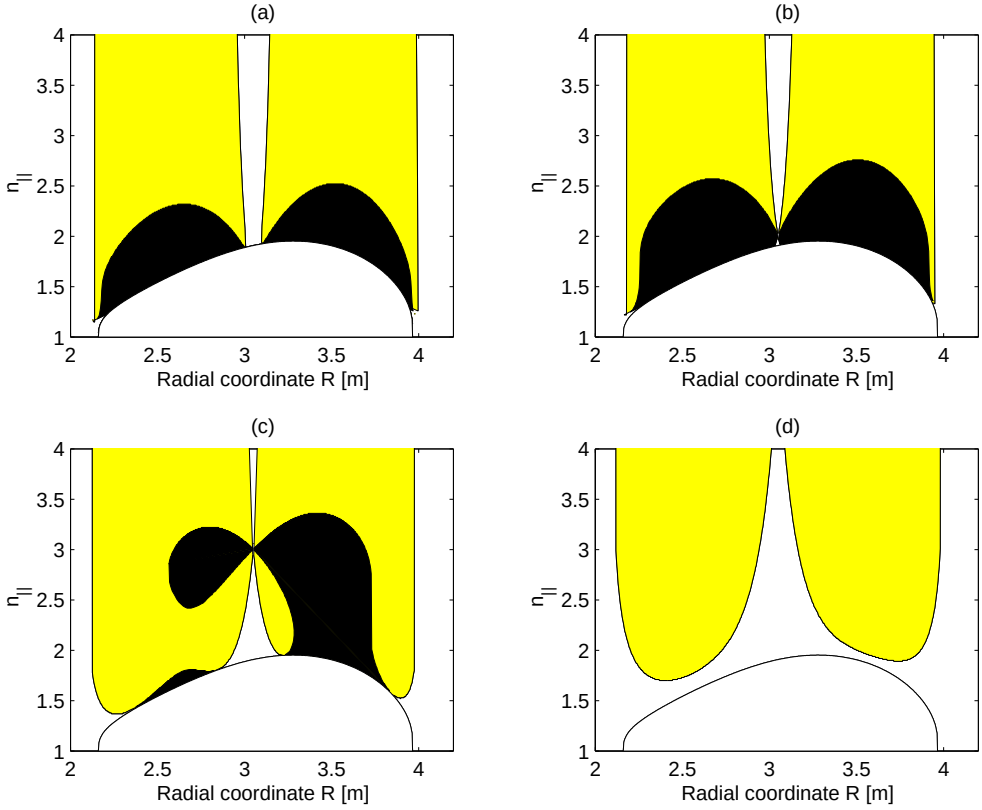

Figure 6. Accessibility regions of the slow wave (grey) and the fast wave (black) in the horizontal plane for a JET-like tokamak. The initial values of the toroidal refractive index are: (*a*) $n_{\phi 0} = 1.6$, (*b*) $n_{\phi 0} = 2.0$, (*c*) $n_{\phi 0} = 3.0$ and (*d*) $n_{\phi 0} = 5.0$ ($n_{e0} = 0.5 \times 10^{20}$ m^{-3}).

The accessibility regions of the slow and the fast waves are found to overlap, but the region of the slow wave is much larger than that of the fast wave. The transformation between the modes is possible only on the Golant–Stix boundary. For sufficiently small toroidal refractive index $n_{\phi 0}$, both the fast and the slow modes appear on this boundary and the transformation is possible. On the other hand, for large $n_{\phi 0} = 5.0$ in figure 6(*d*), the fast mode disappears at the Golant–Stix boundary and no mode transformation is possible. The behaviour obtained is of general nature and implies that the appearance of mode transformations in the plasma interior requires a launched spectrum of $n_{\phi 0}$ to extend below a certain threshold, as noted in [5]. It is of interest to note that the fast waves have access to the plasma centre and do not allow large shift of $n_\parallel$ during propagation.

The values of $n_\parallel$ on the mode transformation surface can be obtained from condition (12) or more simply from equation (2), and here are depicted from equation (2) in r–θ space in figure 7 for two central densities. In order for the ray to reach this surface its $n_\parallel$ has to reduce. The mode transformation surface has a distinct minimum of $n_\parallel$ in the region around $\theta/2\pi = 0.5$, i.e. on the high-field side of the tokamak. Correspondingly, there is a maximum of the surface on the low-field side at $\theta = 0$. In the low-field side, a smaller down shift in $n_\parallel$ is enough to

obtain a mode transformation. Therefore, one could expect that mode transformations occur more often on the low-field side than on the high-field side.

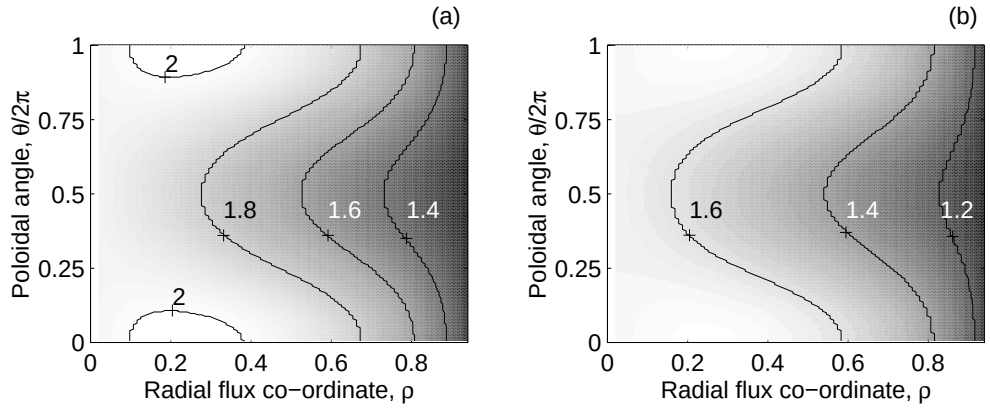

Figure 7. A contour plot of the values of $n_\parallel$ on the mode transformation surface for a JET-like tokamak. The central densities are: (*a*) $n_{e0} = 0.6 \times 10^{20}$ m^{-3} and (*b*) $n_{e0} = 0.3 \times 10^{20}$ m^{-3}.

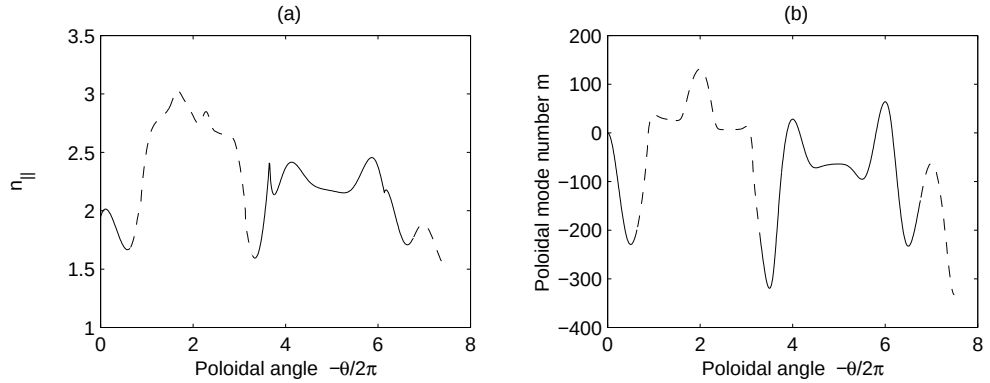

Figure 8. (*a*) The parallel refractive index $n_\parallel$ of the slow wave (full curve) and the fast wave (dashed curve) along a ray as a function of the poloidal angle for a JET-like tokamak. (*b*) The poloidal mode number m along the same ray. Note that this is the same ray as in figure 5(*b*) ($n_{e0} = 0.5 \times 10^{20}$ m^{-3}, $n_{\phi 0} = 2.0$ and $\theta_0 = 0$).

The variation of $n_\parallel$ and the poloidal mode number m along the ray as a function of the poloidal angle θ is shown in figure 8 for the ray we have already presented in figure 5(*b*). The launching point of the ray is at angle $\theta_0 = 0$ and the initial poloidal mode number is $m_0 = 0$. As has been explained in [2], both m and $n_\parallel$ start decreasing for such initial conditions after ray launching. Here, m decreases sufficiently to make $n_\parallel$ so small that a mode transformation occurs at $\theta/2\pi \simeq -0.7$. One can find an estimate for the variation of m from the ray-tracing equations by using the electrostatic approximation [2]

$$\mathrm{d}m/\mathrm{d}\theta = -\frac{\partial H/\partial\theta}{\partial H/\partial m} \approx -n_\parallel R_0 q(r)\left(1 + \frac{\omega_{pe}^2/\Omega_e^2}{S}\right)\frac{(r/R_0)\sin\theta}{1 + (r/R_0)\cos\theta} \qquad (15)$$

where $q(r)$ is the safety factor. Clearly, m reduces for increasing $|\theta|$ when we have $0 < |\theta| < \pi$, and so does $n_\parallel$, which can also be seen in figure 8.

In figure 9, the perpendicular refractive index obtained from ray tracing is depicted for various initial values of the toroidal refractive index. The slow and the fast branches of the dispersion relation along the ray trajectory are also shown. In figure 9(*a*) with $n_{\phi 0} = 1.6$, we find the slow wave to transform to a fast wave at $\theta/2\pi \simeq -0.2$ and $\theta/2\pi \simeq -0.85$, respectively. The transformation back to a slow wave occurs at $\theta/2\pi \simeq -0.3$ and $\theta/2\pi \simeq -0.95$, respectively. At a large value of $n_{\phi 0}$, the transformation does not exist at all in accordance with figure 6.

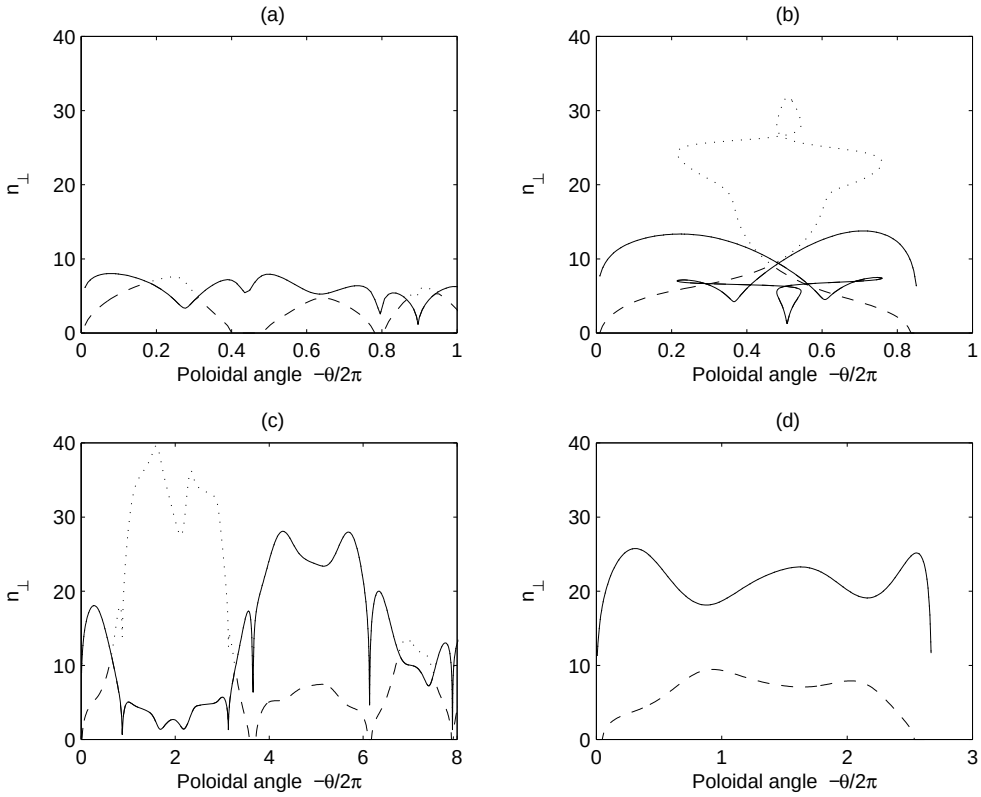

Figure 9. The perpendicular refractive index along a ray (full curve) against the poloidal angle in a JET-like tokamak. The slow branch (dotted curve) and the fast branch (dashed curve) of the dispersion relation are also shown. The initial values of the toroidal refractive index are: (*a*) $n_{\phi 0} = 1.6$, (*b*) $n_{\phi 0} = 1.8$, (*c*) $n_{\phi 0} = 2.0$ and (*d*) $n_{\phi 0} = 2.4$ ($n_{e0} = 0.5 \times 10^{20}$ m^{-3}, $\theta_0 = 0$).

Figure 10 shows the evolution of the perpendicular refractive index at different plasma densities when the toroidal refractive index is $n_{\phi 0} = 2.0$. It seems that the probability of a mode transformation increases when the central density becomes larger. At the lowest central densities below $n_{e0} \simeq 0.3 \times 10^{20}$ m^{-3}, no transformation is found, while at densities above $n_{e0} \simeq 1.0 \times 10^{20}$ m^{-3} the transformation is inevitable. More evidence on enhancement of mode transformation with increasing density will be presented in the following section.

The effect of changing the total current, i.e. changing the edge safety factor $q(a)$, on the fast wave propagation and power deposition was also investigated. The results clearly indicated that the larger the plasma current, i.e. the smaller $q(a)$, the more probable is the mode transformation from the slow to the fast wave. This result can also be deducted from equation (4) where the first term on the left-hand side is larger with smaller q.

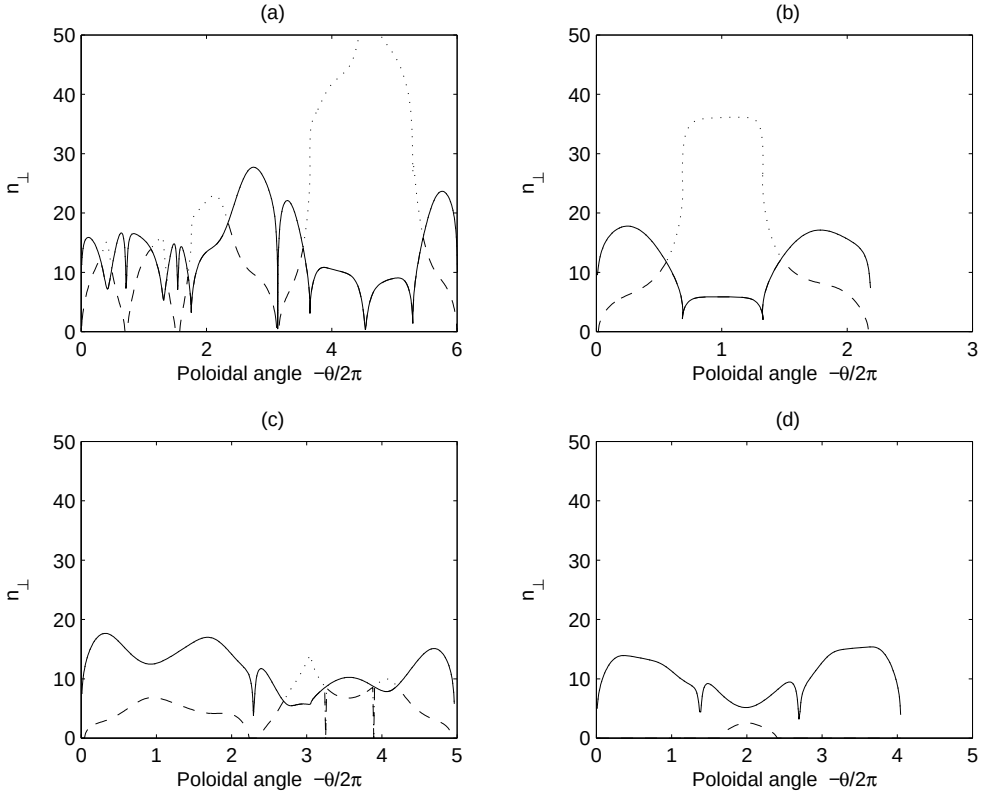

Figure 10. The same as in figure 9, but for different central densities: (*a*) $n_{e0} = 1.0 \times 10^{20}$ m^{-3}, (*b*) $n_{e0} = 0.6 \times 10^{20}$ m^{-3}, (*c*) $n_{e0} = 0.3 \times 10^{20}$ m^{-3} and (*d*) $n_{e0} = 0.1 \times 10^{20}$ m^{-3} ($n_{\phi 0} = 2.0$ and $\theta_0 = 0$).

5. Effect of mode transformation on power deposition

A fast wave has different polarization and smaller $n_\parallel$ during propagation than a slow wave. In general, the electron damping term of a fast wave is similar to that of a slow wave. Assuming that $\omega_{pe}^2/\Omega_e^2 \ll 1$, we find for the imaginary part of the radial refractive index [11]

$$n_{r,i} \simeq n_r \frac{\pi^{1/2}\zeta \exp(-\zeta^2)}{1 + (\Omega_e/\omega_{pe} n_\parallel)^2 (n_\parallel^2 - S)^2} \tag{16}$$

where $n_r \simeq (\omega_{pe}^2/\omega\Omega_e)(n_\parallel^2 - S)^{-1/2}$ and $\zeta = c/(\sqrt{2} v_e n_\parallel)$. For a fast wave, the exponential term is smaller than for a slow wave because the fast wave typically has smaller $n_\parallel$. Since fast waves do not form resonance cones, the weaker absorption disperses the energy in a larger region of plasma. This may improve the penetration, in particular at high densities, where most of the absorption appears to be that of the fast mode.

We now analyse the effect of mode transformation on the power deposition in a JET-like tokamak having the parameters given in tables 1 and 2. In contrast to the previous sections, we now consider a non-circular plasma with elongation $\kappa = 1.74$. We assume that the triangularity is $\delta = 0.4$. The present model for the magnetic equilibrium does not have an X-point. The launched LH power is 6 MW and a deuterium–tritium (50:50) plasma is assumed. The full width of the launched Gaussian spectrum at half maximum is $\Delta n_{\phi 0} = 0.13$.

The power deposition profiles and the current density profiles were calculated with the fast ray-tracing code (FRTC) [9] coupled with the ASTRA transport code. The simulation procedure includes combined ray-tracing and Fokker–Planck calculations. The input RF power is distributed among a number of rays in accordance with the radiated Brambilla spectrum. The rays are traced with canonical ray equations whose Hamiltonian function is given by the left-hand side of the full electromagnetic dispersion relation in the cold plasma approximation. The type of wave mode, specified initially and changing due to the mode transformation, is known at any point of the ray trajectory. The power assigned to individual rays evolves according to Landau and collisional damping. Both the damping rates depend on the current wave polarization that is taken into account in the calculations. For the purpose of this paper, the power depositions into a phase-space volume element from the rays belonging to the fast and slow modes are calculated separately. A one-dimensional model of the Fokker–Planck equation is used with the diffusion coefficient compatible with the assumed damping mechanism. The coefficient is found from the power deposition data. The self-consistent equilibrium between the electron distribution and the power deposition is achieved iterationally. In these calculations, 100 rays were used and fixed density and temperature profiles were assumed with the parameters given in table 1.

The total absorbed power and the power absorbed as a fast wave is illustrated in figure 11. Different values of the toroidal refractive index are considered when the central density is $n_{e0} = 0.5 \times 10^{20}$ m^{-3} and the temperature is $T_{e0} = 6$ keV. As is expected, the amount of mode transformation increases when the initial toroidal refractive index becomes small enough. When we have $1.6 \lesssim n_{\phi 0} \lesssim 2.0$, the contribution of the fast wave to the deposited power is significant and is responsible for the most absorption at the centre. At large values of the toroidal refractive index ($n_{\phi 0} \gtrsim 2.2$), the effect of the fast wave is small.

The observed increase in the fast wave absorption with deceasing toroidal refractive index is in agreement with our results obtained from the quasitoroidal model in section 4. According to figure 6(*d*), the mode transformations are absent at high values of $n_{\phi 0}$ because the fast wave is not accessible. When $n_{\phi 0}$ is large, it was found in figure 9(*d*) that the slow and the fast branches of the dispersion relation are far away from each other, which makes mode transformation unlikely. Furthermore, it is easier for the wave to reach the mode transformation surface of figure 7 if the initial value of the parallel refractive index is not too large.

The effect of the electron temperature on the power deposition profiles is illustrated in figure 12. Here, the LH wave absorption is strongly off-axis because of enhanced Landau damping. The conversion to the fast mode is also reduced, which is caused by the shortened paths of the rays and thus by the reduced probability of the rays to reach the conversion surface. Here, too, the fast wave is responsible for most of the deepest power deposition. As demonstrated in figure 13, the contribution of the fast wave to the deposited power clearly increases with increasing density. At a high central density of $n_{e0} = 0.6 \times 10^{20}$ m^{-3}, most of the central power deposition occurs as a fast wave mode. At low central densities ($n_{e0} \lesssim 0.2 \times 10^{20}$ m^{-3}), all the lower hybrid power is absorbed as a slow wave.

The observed increase in the fast wave deposition with increasing plasma density is in agreement with our discussion in section 2 and with the quasitoroidal results obtained in section 4. The mode transformation surface presented in figure 7 is located at higher values of $n_{\|}$ when the central plasma density is high, which makes a mode transformation more probable. Figure 10 shows that at low densities the fast and the slow branches of the dispersion relation are far away from each other, which makes a mode transformation unlikely. Also, as explained in the context of equation (4), the fast wave has better access to the conversion surface at higher density. However, as is seen in figure 13(*a*), the LH wave penetration is reduced for densities $n_{e0} \gtrsim$

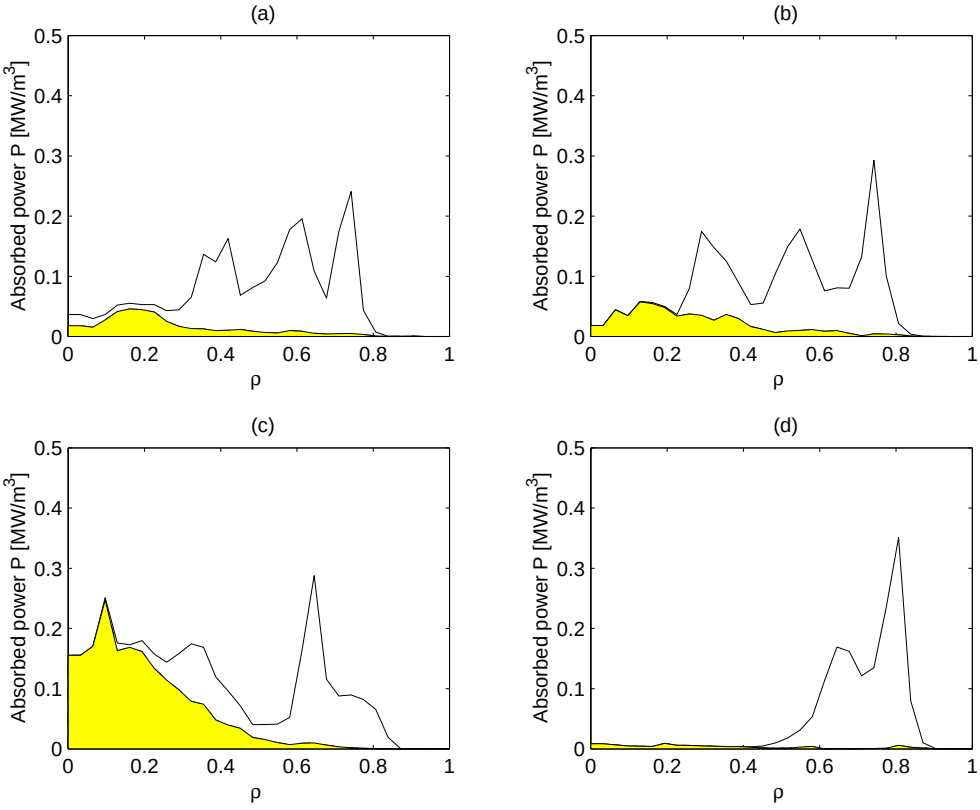

Figure 11. The total absorbed power density and the power density absorbed as a fast wave (shaded) in a JET-like tokamak. The initial values of the toroidal refractive index are: (*a*) $n_{\phi 0} = 1.6$ and (*b*) $n_{\phi 0} = 1.8$, (*c*) $n_{\phi 0} = 2.0$ and (*d*) $n_{\phi 0} = 2.4$ ($n_{e0} = 0.5 \times 10^{20}$ m^{-3}, $T_{e0} = 6$ keV).

1.0×10^{20} m^{-3} which reduces the fast wave contribution as in the case of increased temperature.

It should also be noted that according to equation (15) the variation of m and $n_\parallel$ becomes stronger when ω_{pe}^2/Ω_e^2 becomes larger (provided that $\omega_{pe}^2/\Omega_e^2 \lesssim 1$, as is the case in our examples, except for the highest density $n_{e0} = 1.0 \times 10^{20}$ m^{-3}). Thus, when the density becomes larger (or the magnetic field becomes smaller), the chances increase for the ray to hit the mode transformation surface during propagation.

6. Summary and discussion

The transformation of LH waves from slow waves to fast waves has been investigated in a toroidal configuration. The detailed mechanism of the transformations was first studied with a simple analysis amenable for comparison with the better known slab geometry case. A more detailed analysis was made with a transparent quasitoroidal ray-tracing model. The effect of fast waves on the power deposition profiles in a JET-like configuration was analysed by using the fast ray-tracing code (FRTC).

The effect of the launched spectrum on mode transformation was investigated when the central density was $n_{e0} = 0.6 \times 10^{20}$ m^{-3}. The role of the fast waves is important when the

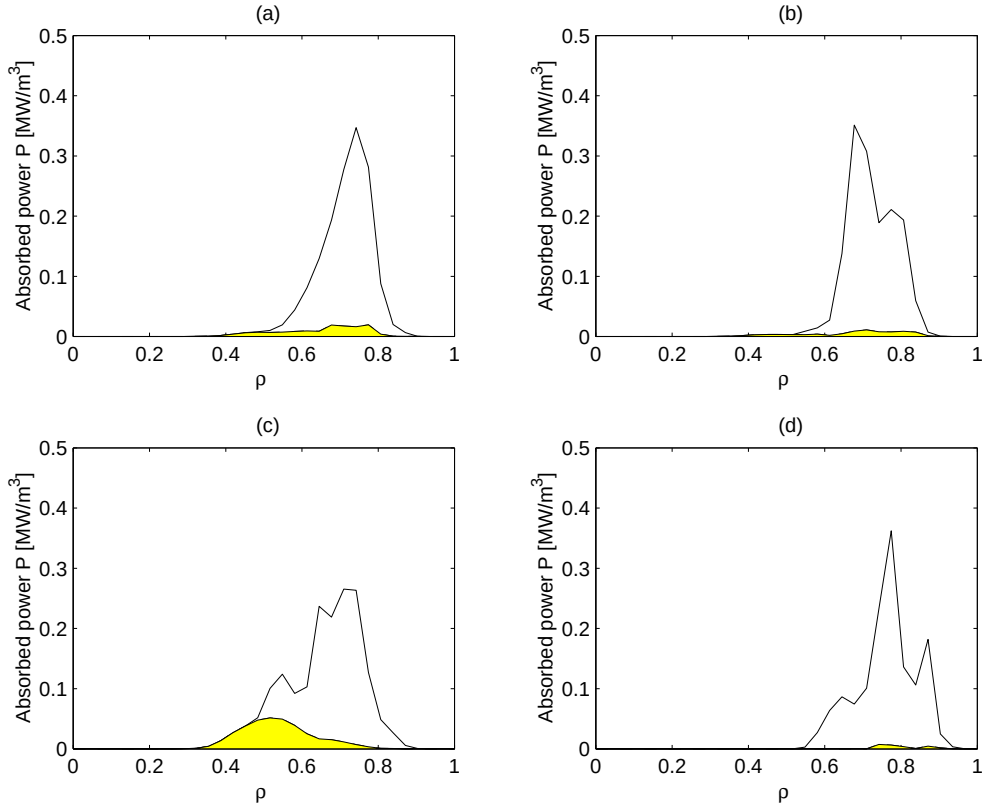

Figure 12. The same as in figure 11 but for a higher temperature of $T_{e0} = 12$ keV.

launched spectrum has small toroidal refractive index $n_{\phi 0}$. If $n_{\phi 0}$ is small ($1.6 \lesssim n_{\phi 0} \lesssim 2.0$), the contribution of the fast wave to the deposited power is found to be even larger than 50% and is responsible for most of the absorption at the centre. On the other hand, if $n_{\phi 0}$ is large ($n_{\phi 0} \gtrsim 2.2$), the effect of the mode transformed fast waves is small or negligible.

The effect of the plasma density was investigated when the toroidal refractive index is $n_{\phi 0} = 2.0$. The contribution of the fast wave to the power deposition also increases with increasing density. At high central densities ($n_{e0} \gtrsim 0.6 \times 10^{20}$ m^{-3}), the contribution of the fast wave to the deposited power can be more than 50%. At low central densities ($n_{e0} \lesssim 0.3 \times 10^{20}$ m^{-3}), practically no absorption of the fast wave occurs. For the highest densities with $\omega_{pe}^2/\Omega_e^2 \gtrsim 1$, the conversion rate is however again reduced because of weakened LH wave penetration and power accessibility to the conversion surface.

Benefits of fast wave for plasma heating and current drive were discussed in [11], where direct launching of fast waves from wave guides was considered. In the present study, the coupling to fast wave occurs via mode transformations. Therefore, the possible advantages of the fast waves are obtained without resorting to a different launching method. Figures 14 and 15 demonstrate the current drive performance of the direct slow and fast wave excitations. In figure 14, the power depositions of the fast and slow wave branches are depicted for various $n_{\phi,0}$ with otherwise similar parameters as in figure 11, but the waves are launched as fast waves. Deepest penetration is found for largest $n_{\phi,0}$ for the fast mode, but here the tunnelling from the antenna across the evanescent layer in the edge plasma becomes more difficult. Comparison

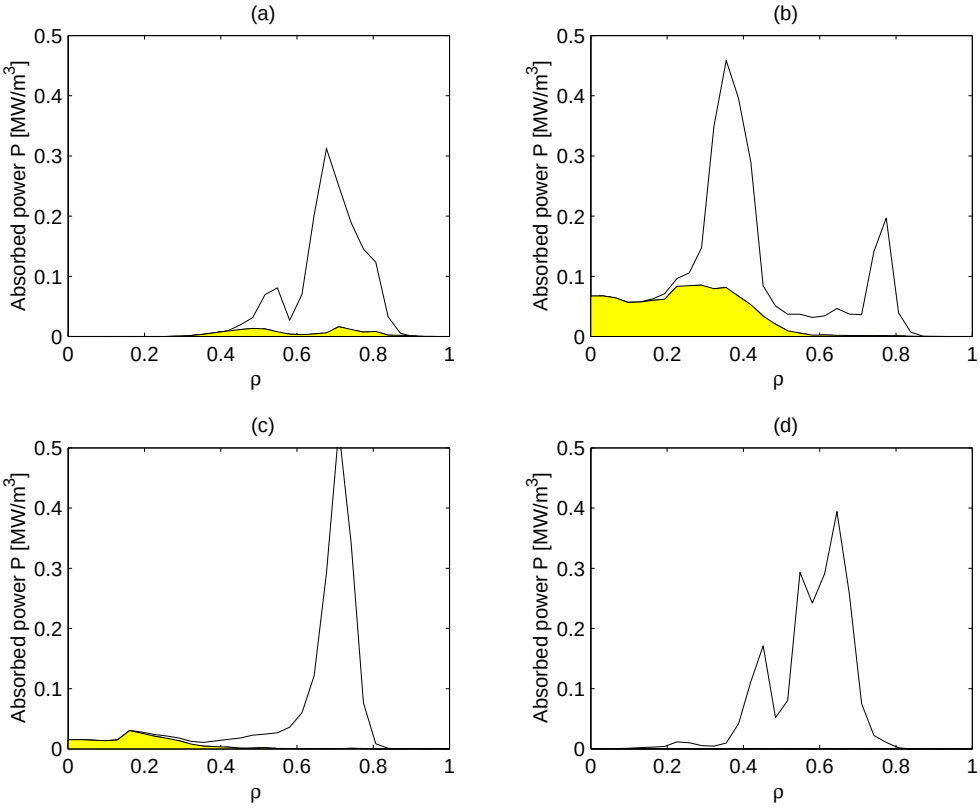

Figure 13. The total absorbed power density and the power density absorbed as a fast wave (shaded) in a JET-like tokamak when $n_{\phi 0} = 2.0$. The central densities are: (*a*) $n_{e0} = 1.0 \times 10^{20}$ m^{-3}, (*b*) $n_{e0} = 0.6 \times 10^{20}$ m^{-3}, (*c*) $n_{e0} = 0.3 \times 10^{20}$ m^{-3} and (*d*) $n_{e0} = 0.1 \times 10^{20}$ m^{-3}.

of figures 11(*c*) and 14(*c*) shows that the relative partition between the fast and slow wave power deposition is very similar. The corresponding driven current profiles in figure 15 show also a fair similarity. Noting the large contribution of the fast wave mode in this case even with a slow wave direct excitation, leads us to conclude that it is possible to achieve some of the advantages of direct fast wave excitation with the present slow wave launchers.

At the highest plasma densities ($n_{e0} \gtrsim 1 \times 10^{20}$ m^{-3}) studied in the present paper, the deposition profiles are off-axis at $\rho \simeq 0.5$–0.8. Thus, neither the fast waves nor the slow waves appear to penetrate to the plasma centre. This demonstrates that the damping of the fast waves can also be strong in the outer plasma layers, thus preventing deep penetration in our examples. As this was found to be a consequence of condition $\omega_{pe}^2/\Omega_e^2 \gtrsim 1$, increasing the magnetic field up to 5 T in a reactor would eliminate this effect for densities around 10^{20} m^{-3}.

The FRTC code has very recently been installed and coupled into the JETTO transport code [12] at JET. FRTC can also be run as a stand-alone version using experimental profiles. Thus, in the future we can use the JET experimental database to simulate the fast wave deposition profiles, and what is even more intriguing are the self-consistent simulations with the coupled JETTO/FRTC transport code. The results of the modelling of LHCD deposition profiles with the coupled JETTO/FRTC code are deferred to future publications.

The significant amount of wave energy in the fast mode must be carefully taken into account in modelling LH current drive experiments. It may have an effect, for instance, on the

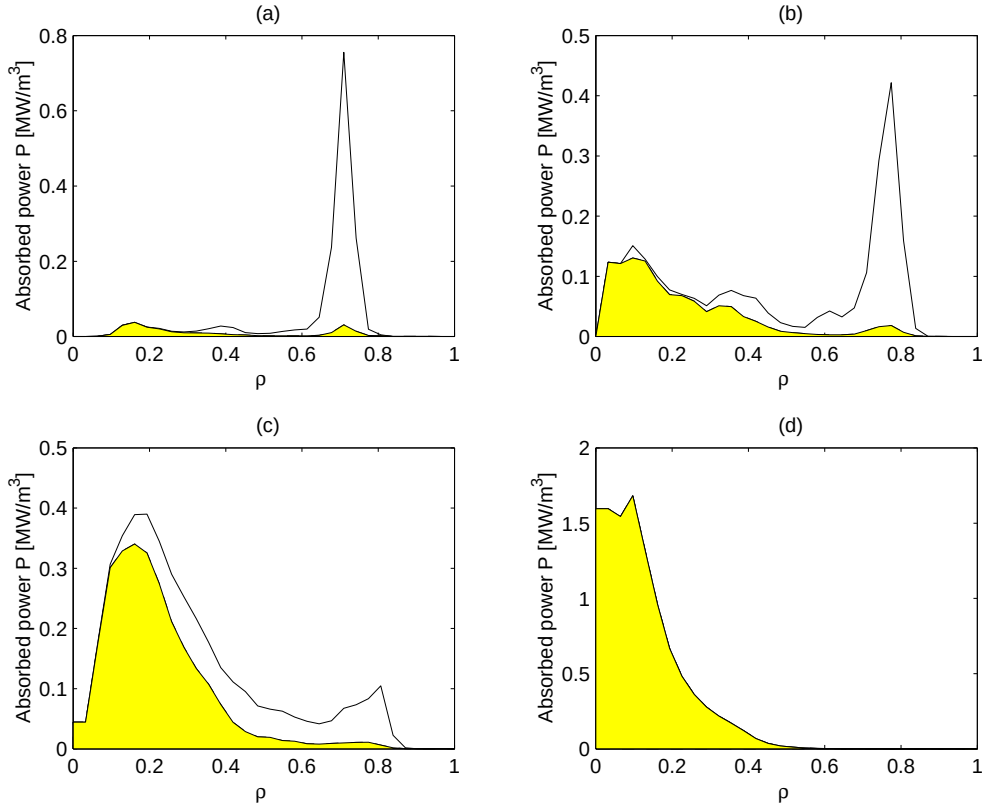

Figure 14. The total absorbed power density and the power density absorbed as a fast wave (shaded) in a JET-like tokamak when the wave is initially launched as a fast wave. The initial values of the toroidal refractive index are: (*a*) $n_{\phi 0} = 1.6$ and (*b*) $n_{\phi 0} = 1.8$, (*c*) $n_{\phi 0} = 2.0$ and (*d*) $n_{\phi 0} = 2.4$ ($n_{\mathrm{e}0} = 0.5 \times 10^{20}$ m^{-3}, $T_{\mathrm{e}0} = 6$ keV).

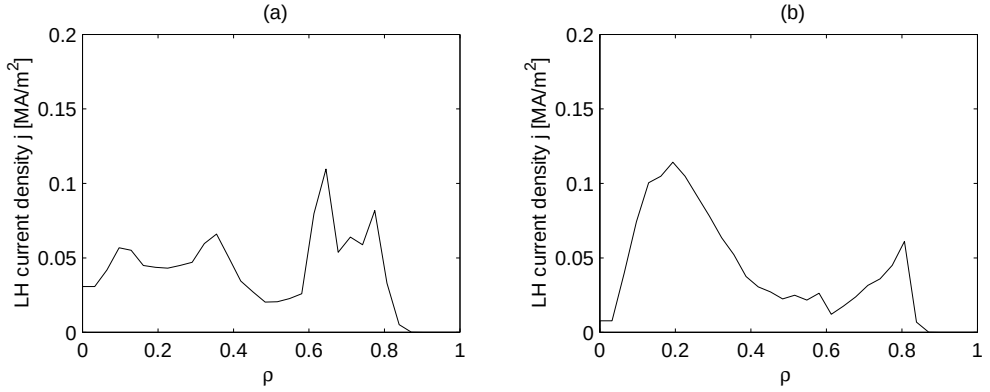

Figure 15. The wave-induced current when the wave is launched (*a*) as a slow wave and (*b*) as a fast wave ($n_{\phi 0} = 2.0$, $n_{\mathrm{e}0} = 0.5 \times 10^{20}$ m^{-3}, $T_{\mathrm{e}0} = 6$ keV).

absorption of the LH waves by alpha particles and fast ions, the diagnostics of the LH waves and various models of the spectral gap problem. Further work is needed to clarify these issues.

Recently, experimental evidence of LHCD on the PBX-M tokamak was demonstrated although the launched spectrum was below the accessibility condition [13]. It was found that in this case the current drive efficiency decreased with decreasing $n_{\phi 0}$. The reason for this seemed to be that a large spectral upshift was necessary before the absorption could occur. Furthermore, it was found that the damping location was not correlated to accessibility, but to upshift, which was largely independent of the original $n_{\phi 0}$.

The validity of the WKB approximation in the lower hybrid range of frequencies has been critically discussed by several authors [14–17]. In the present work, a well established routine for LHCD simulation has been used. The routine is based completely on commonly accepted, although not always well justified, approaches. A detailed discussion of the validity of the WKBJ approximation for LHCD is, however, beyond the scope of this paper.

Acknowledgments

The authors thank an anonymous referee for bringing the recent results on PBX-M [13] to our attention. The authors are grateful to Karin Rantamäki, Lic. Tech., for technical assistance.

References

[1] Stix T H 1992 *Waves in Plasmas* (New York: AIP) p 101
[2] Bonoli P T and Ott E 1982 *Phys. Fluids* **25** 359
[3] Santini F 1985 *Course and Workshop on Applications of RF Waves to Tokamak Plasmas (Varenna, September 1985)* vol 1, ed S Bernabei, U Gasparino and E Sindoni (International School of Plasma Physics 'Piero Caldirola') (Perugia: Monotypia Franchi, Città di Castello) p 251
[4] Valeo E J and Eder D C 1985 *Course and Workshop on Applications of RF Waves to Tokamak Plasmas (Varenna, September 1985)* vol 2, ed S Bernabei, U Gasparino and E Sindoni (International School of Plasma Physics 'Piero Caldirola') (Perugia: Monotypia Franchi, Città di Castello) p 493
[5] Esterkin A R and Piliya A D 1992 *Plasma Phys. Control. Fusion* **34** 1957
[6] Esterkin A R and Piliya A D 1992 *Nucl. Fusion* **32** 927
[7] Kupfer K and Moreau D 1992 *Nucl. Fusion* **32** 1845
[8] Paoletti F, Ignat D W, Kesner J, Bernabei S, Kaita R, Leblanc B, Levinton F M and Luckhardt S C 1994 *Nucl. Fusion* **34** 771
[9] Esterkin A R and Piliya A D 1996 *Nucl. Fusion* **36** 1501
[10] Wégrove J-G 1997 *Proc. 12th Topical Conf. on Radio Frequency Power to Plasmas (Savannah, GA, April, 1997) (AIP Conference Proceedings vol 403)* (New York: AIP) p 141
[11] Theilhaber K and Bers A 1980 *Nucl. Fusion* **20** 547
[12] Genacchi G and Taroni A 1988 JETTO: A free boundary plasma transport code (basic version) *Rapporto* ENEA RT/TIB 1988(5)
[13] Bernabei S, Cardinali A, Giruzzi G, Hoang G T, Ignat D, Kaita R, Okabayashi M, Paoletti F and von Goeler S 1997 *Phys. Plasmas* **4** 125
[14] Brambilla M and Cardinali A. 1982 *Plasma Phys. Control. Fusion* **24** 1187
[15] Esterkin A R, Gusakov E Z, Irzak M A and Piliya A D 1995 *Proc. 22nd European Physical Society Conf. on Controlled Fusion and Plasma Physics (Bournemouth, 3–7 July, 1995) (Europhysics Conference Abstracts vol 19C)* (Geneva: EPS) part IV, p 389
[16] Peysson Y, Sébelin E, Litaudon X and Moreau D 1998 *Nucl. Fusion* **38** 939
[17] Pereverzev G V 1998 *Phys. Plasmas* **5** 3529

Published by

Vuorimiehentie 5, P.O.Box 2000, FIN–02044 VTT, Finland
Phone internat. +358 9 4561
Fax +358 9 456 4374

Series title, number and report code of publication

VTT Publications 467
VTT–PUBS–467

Author(s)
Tala, Tuomas

Title

Transport Barrier and Current Profile Studies on the JET Tokamak

Abstract

One of the crucial problems in fusion research is the understanding of heat and particle transport in plasmas relevant for energy production. The neo-classical theory of tokamak transport is well-established, but it cannot explain experimental results. Instead, the micro-turbulence driven anomalous transport has been found to be dominant in present tokamak experiments.

There are several mechanisms that can locally suppress micro-turbulence and reduce significantly the anomalous transport. These regions of reduced transport are called transport barriers. The presence of Internal Transport Barriers (ITBs) is one of the bases in 'Advanced Tokamak Scenarios'. One of the principal goals in the 'Advanced Tokamak Scenarios' is to improve the fusion power density and confinement with internal transport barriers by controlling the current density profile and maximising the bootstrap current – and ultimately rendering the tokamak compatible with continuous operation.

This thesis reports on studies and modelling of internal transport barriers and current density profiles in the Joint European Torus (JET) tokamak with a fluid transport code. Explanations for the following open questions are sought: what are the mechanisms that govern the formation and dynamics of the ITBs in JET and secondly, how can the current density profile be modified and further, how does it affect ITBs and plasma performance?

On the basis of the empirical study at the ITB transition, the $\omega_{E\times B}$ flow shear and magnetic shear appear as strong candidates in determining the onset time, the radial location and the dynamics of the ITBs in JET. This ITB threshold condition, employed in the semi-empirical Bohm/GyroBohm transport model, has been found to be in good agreement with experimental results in predictive transport simulations. On the other hand, the simulation results from the predictive transport modelling with a theory-based quasi-linear fluid transport model strongly emphasise the importance of the density gradient in the ITB formation.

According to the current density modelling studies, lower hybrid and electron cyclotron current drive are the most versatile current drive methods in terms of the produced q-profile in the preheating phase in JET. With lower hybrid preheating, a core current hole has been found and a physics-based explanation, confirmed by the transport modelling, is given. The predictive transport simulations indicate that application of lower hybrid current drive during the high performance phase can enhance the fusion performance significantly by increasing the ITB radius.

Keywords
nuclear fusion, JET tokamak, plasma transport, heat transport, internal transport barriers, current density, modelling, transport models, flow shear, magnetic shear

Activity unit
VTT Processes, Industrial Physics, Otakaari 3 A, P.O.Box 1404, FIN–02044 VTT, Finland

ISBN	Project number
951–38–5988–6 (soft back ed.) 951–38–5989–4 (URL:http://www.inf.vtt.fi/pdf/)	

Date	Language	Pages	Price
May 2002	English	71 p. + app. 95 p.	D

Name of project	Commissioned by

Series title and ISSN	Sold by
VTT Publications 1235–0621 (soft back ed.) 1455–0849 (URL: http://www.inf.vtt.fi/pdf/)	VTT Information Service P.O.Box 2000, FIN–02044 VTT, Finland Phone internat. +358 9 456 4404 Fax +358 9 456 4374